Topics in General Relativity: naked singularities, and theoretical aspects of gravitational waves from merging compact binaries.

Thesis by
Theocharis A. Apostolatos

In Partial Fulfillment of the Requirements
for the Degree of
Doctor of Philosophy

California Institute of Technology
Pasadena, California
1995
(Defended November, 1994)

Thesis Advisor:
Professor Kip S. Thorne

Στήν Κυριακή

To see and accept the boundaries of the human mind without vain rebellion, and in these severe limitations to work ceaselessly without protest–this is where man's first duty lies.

Build over the unsteady abyss, with manliness and austerity, the fully round and luminous arena of the mind where you may thresh and winnow the universe like a lord of the land.

Distinguish clearly these bitter yet fertile human truths, flesh of our flesh, and admit them heroically: (a) the mind of man can perceive appearances only, and never the essence of things; (b) and not all appearances but only the appearances of matter; (c) and more narrowly still: not even these appearances of matter, but only relationships between them; (d) and these relationships are not real and independent of man, for even these are his creations; (e) and they are not the only ones humanly possible, but simply the most for his practical and perceptive needs.

Within these limitations the mind is the legal and absolute monarch. No other power reigns within its kingdom.

I recognize these limitations, I accept them with resignation, bravery, and love, and I struggle at ease in their enclosure, as though I were free.

I subdue matter and force it to become my mind's good medium. I rejoice in plants, in animals, in man and in gods, as though they were my children. I feel all the universe nestling about me as though it were my own body.

In sudden dreadful moments a thought flashes through me: "This is all a cruel and futile game, without beginning, without end, without meaning." But again I yoke myself swiftly to the wheels of necessity, and all the universe begins to revolve around me once more.

Discipline is the highest of all virtues. Only so may strength and desire be counterbalanced and the endeavors of man bear fruit.

This is how, with clarity and austerity, you may determine the omnipotence of the mind amid appearances and the incapacity of the mind beyond appearances–before you set out for salvation. You may not otherwise be saved.

from "Spiritual Exercises"
by N. Kazantzakis

Acknowledgments

I have been particularly fortunate to be a student of Kip Thorne. Attracted by his excellence in teaching I joined his group and soon realized what a great man and scientist he was. Even when he was overwhelmed by various important obligations, he always was there to give his advice, help, and encouragement, with patience and zeal. His modesty, integrity, and respect to other people have been a great lesson for the rest of my life. I will always remember his noble personality with gratitude and admiration.

I would like to express my appreciation to Caltech in general, for the warm and friendly environment, it provided me for five whole years. I would also like to thank all the members of Kip's group for the pleasant support and especially Eric Poisson, Curt Cutler, and Eanna Flanagan for their scientific advice and friendly help. Shirley Hampton, was a very helpful presence in the working environment too.

Getting to know, being his Teaching Assistant and seeing Professor Don Skelton teaching the lab was a great pleasure for me.

Many thanks to all the Greek friends I met in Caltech, who made my life more interesting and entertaining, especially to Petros Koumoutsakos for his unforgettable great parties and Thales Karagounis.

I feel I owe a lot to my parents Toula and Apostolos Apostolatos, and my beloved sister Chrysa. My deep appreciation for their love and support over the years is the least I can offer them.

Finally, I dedicate this thesis to Kyriaki, the woman who holds a very special place in my heart.

Abstract

Two topics in classical general relativity are discussed: a) The clothing of singularities by event horizons, and b) various issues in the evolution of coalescing compact binaries, as sources of gravitational waves to be detected by the LIGO/VIRGO/GEO ground-based detectors and/or the LISA space-based detector. More specifically:

We investigate a problem related to an important conjecture of classical relativity, namely the existence of a "cosmic censorship" that forbids the formation of naked singularities, and always clothes them with event horizons that causally hide them from the rest of the Universe. Under consideration is the role of rotation in an infinite cylindrical shell consisting of collisionless dust particles, half of which rotate clockwise and half counterclockwise. We show that, although such a shell without any rotation is known to collapse into a line singularity, the presence of an arbitrarily small amount of rotation is sufficient to halt the collapse. Such a shell, starting from a non equilibrium configuration, will "breath" radially, emitting gravitational waves, and will finally settle down to an equilibrium radius at which gravity is balanced by centrifugal forces. This suggests the essential role that rotation might play in halting the gravitational collapse of an elongated distribution of mass and preventing the formation of a naked singularity. However, this is a highly idealized example, and it can, by no means, ensure the validity of the "cosmic censorship" hypothesis.

On a separate topic, we explore the details of how gravitational radiation reaction drives the evolution of a slightly eccentric orbit of a small body around nonrotating supermassive black holes. A combination of analytic and numerical results arise from the solution of the Teukolsky perturbation equation. It is shown that in the fully relativistic situation, as in the Newtonian quadrupole approximation, there is a tendency for circularization of the orbit down to an orbital radius $r_c \simeq 6.6792GM/c^2$, where M is the mass of the black hole, and G and c are Newton's gravitation constant and the speed of light. It is further shown that for radii smaller than r_c the eccentricity increases.

Finally, an attempt is made to understand and construct analytic expressions that, based on the laws of general relativity, approximately describe the simultaneous precession in rapidly spinning black hole and/or neutron star and inspiral binaries with circular orbits. The precession is produced by general relativistic spin-orbit and spin-spin coupling; the inspiral, by gravitational radiation reaction. We derive the corresponding approximate waveforms to be received by the network

of LIGO, VIRGO, and GEO earth-based gravitational-wave detectors. We then go on to investigate the adequateness of various "families of templates," to detect these spin-modulated waveforms by the method of "matching filters," We introduce a "fitting factor" FF as a measure of templates' adequateness, and show the complete inadequateness, for the task of detection, of the "Newtonian template family" (the set of the waveforms derived from the Newtonian, quadrupole approximation formalism). Another template family with an extra parameter is suggested that performs much better.

Contents

Chapter 1

Introduction

The body of this thesis consists of four chapters (2 through 5), each of which is a paper that has been published in or submitted for publication to *Physical Review D*. I have written Chapters 2, 3, and 4 in collaboration with other people, while I am the sole author of chapter 5, and of a previously unpublished appendix to chapter 4.

These four chapters deal with two topics in Classical General Relativity: the "cosmic censorship conjecture," which says that physical systems cannot turn into "naked singularities" after gravitational collapse (chapter 2), and various theoretical issues related with the formation and detection of gravitational waves from compact merging binaries (chapters 3, 4, 5). These four chapters were written largely for experts in the topics they cover. Scientists in other fields will find in the present introductory chapter a schematic nontechnical description of all the following chapters, together with some relevant background information.

1 CYLINDRICAL, RELATIVISTIC GRAVITATIONAL COLLAPSE AND COSMIC CENSORSHIP

A spherically symmetric gravitational collapse is well known [1], from analytic analyses, to end up in a black hole – a region enclosing a spacetime singularity that cannot causally communicate with the external universe (i.e., with "future null infinity"). This is of great physical significance since it means that all the super-high-curvature physics present in the vicinity of the singularity (a region of volume $\sim 10^{-99}$ cm^3), remains well hidden from the world outside, and cannot affect it. In the singularity, classical general relativity is not adequate to describe the structure of spacetime. The laws of quantum gravity must come into play, though nobody knows yet exactly how. If a singularity could be "naked," it would influence the distant word in an unpredictable manner, and raise physicists' hopes of sometime observing phenomena due to Planckian scale physics.

Of course the assumption of absolute spherical symmetry is highly idealized. But studies of perturbations from the Schwarzschild spherically symmetric solution indicate that the produced singularity will still be "clothed" by an absolute event horizon (the boundary of the space that can send signals to future null infinity). Even Kerr black holes (rotating black holes), in numerical studies of strong vacuum perturbations [2] and of highly nonspherical rotating stellar collapse [3], have

turned out to be stable configurations with the formed singularity hidden behind an event horizon. All these indications, together with numerous failed attempts to find examples where a "naked singularity" forms [4, 5, 6], have lent credence to the so called *cosmic censorship conjecture*, first formulated by Roger Penrose in 1969 [7], namely, *that there exists a cosmic censor who forbids the appearance of naked singularities, clothing each one in an absolute event horizon.*

There are three apparent counterexamples to this conjecture. First the Universe itself, since the big bang singularity could in principle be observed. The second one, less secure, has to do with the evaporation of tiny black holes (of the order of a Planck length) and the formation of Planck-scale curvature at the late stage of their evaporation. The third one comes from the work of Choptuik, Abrahams, and Evans [8], in which they show that suitably chosen scalar-field initial data can evolve to form arbitrary high naked curvature, but with correspondingly arbitrarily small total mass. But these have not harmed the validity of the cosmic censorship hypothesis; they have just led to more precise formulations, e.g., taking into consideration the initial state and the type of matter field involved in a realistic situation [9, 10]. The question of whether a physical initial mass distribution much greater than a Planck mass could end up in a naked singularity remains open.

There are well known unphysical configurations where matter collapses to a singularity without any horizon ever forming. In the 1960s, Thorne showed that an infinite cylindrical shell consisting of collisionless dust particles will collapse, according to General Relativity, to form a naked line singularity along its axis [11]. Of course an infinitely cylindrical star is completely beyond imagination, but such an example could provide us intuition on what happens in highly nonspherical situations. For example a prolate spheroid of non-colliding, non-rotating dust particles in Newtonian gravity will eventually form a thin spindle (a phenomenon known as the Lin-Mestel-Shu instability [12]). For such a configuration the approximation of an infinite cylinder is quite accurate at least near the spindle's waist. This example suggests the formation of a naked singularity, in this aspherical case.

Several years ago, Stuart Shapiro and Saul Teukolsky explored numerically the fully relativistic dynamical evolution of such dust-type spheroids, starting from momentarily static configurations, with no pressure or rotation [13]. A thin spindle formed, as in Newtonian gravity, if the initial shape was sufficiently elongated. What was surprising was that the singularity showed up, not just inside the body of the spindle but also at its ends (poles), extending outside the matter along

the spindle axis, without any apparent horizon ever being detected. (When a singularity shows up, the numerical code breaks down, and probing the spacetime geometry arbitrarily far into the future, to definitely rule out the formation of an event horizon, becomes technically impossible.) In such a situation, the concept of "apparent horizon," the boundary of the region of space where gravity makes an outgoing beam of light contract, is a good but weaker candidate to replace the absolute event horizon. Several people [14, 15] have pointed out the possibility that the Shapiro-Teukolsky conclusion may be artificial due to their specific numerical choice of time slicing. They may have reached only a small region of the final spacetime, touching the formed singularity only at its extensions beyond the poles before the code broke down; and both an apparent horizon and an absolute horizon might form in the spacetime region they were unable to explore. On the other hand, the singularities Shapiro and Teukolsky discovered may be truly naked and may have a simple physical origin; namely, nonlinear vacuum gravity forces triggered by the pointed spindle's ends.

Since the examples of Shapiro and Teukolsky were pressureless and nonrotating, they were expected to form singularities (though only inside the matter and inside a horizon) in the same manner as the infinite cylinder example. Now, Tsvi Piran [16] had previously shown by numerical examples that a realistic pressure in cylindrically symmetric configurations can halt the gravitational collapse. The matter bounces, and eventually, after a few radial oscillations and the emission of gravitational waves, it settles down into a nonsingular, equilibrium configuration.

But the role of rotation in cylindrically symmetric systems was unclear. Motivated by this, by the numerical results of Shapiro and Teukolsky and by unpublished analytical calculations done by Thorne in the early 1970s, Kip Thorne and I embarked several years ago on an exploration of whether rotation, like realistic pressure, can halt cylindrical collapse. Our study was concentrated on an idealized model that could be solved analytically and provide us with more insight into realistic gravitationally collapsing objects: an infinitely long cylindrical shell of collisionless dust particles, with rotation. To avoid frame dragging complications without losing the new feature of rotation, we constructed our model with half the dust particles moving rightwards with some net angular momentum per unit mass, and half of them moving leftwards with the same net angular momentum.

Based on this model and Thorne's concept of C-energy [11] (a cylindrical analogue of the Schwarzschild mass function $m(r)$ for spherically symmetric systems), we showed that for any amount of the particles' angular momentum, however

small, there is always an equilibrium radius for the shell, where the centrifugal forces keep it from collapse. This was already known from old (1970) unpublished work of Thorne. If the combination of angular momentum and radius is not the right one to provide a balance between centrifugal and gravitational forces, the infinite cylindrical shell moves toward the equilibrium configuration (either contracting or expanding radially), bouncing back and forth, and finally settling down by emitting gravitational waves. However small the angular momentum of the particles is, the shell will never be able to collapse and form a singularity. The detailed dynamical evolution of such a system was investigated by me, building on the formalism earlier used by Thorne.

If the singularity that Shapiro and Teukolsky discovered is just a continuation of the infinite-cylinder-like singularity forming inside the body of the spindle, then it seems suggestive that an arbitrarily small rotation will make the spindle bounce without forming any naked singularity. If on the other hand their singularity is connected to nonlinear vacuum gravity developing at the spindle's ends, then our simple example doesn't look promising to assure the validity of Penrose's conjecture.

Thorne and I published our analysis and these conclusions in *Phys. Rev. D* **46**, 2435 (1992); our paper appears as chapter 2 of this thesis. Since we completed our paper, Shapiro and Teukolsky have numerically explored the gravitational collapse of rotating prolate spheroids [17]. They constructed these spheroids from equal numbers of corrotating and counterrotating particles in analogy with our model. They found that for moderate and large rotation rates the spheroids end up in black holes. For these cases our simple infinite cylindrical model looks like a good analogue of the spheroid until its polar axis contracts to the same length as the equatorial axis. Rotation impedes the contraction of the equatorial axis, helping this way in the formation of a black hole. But for small amounts of rotation they obtained exactly the same kind of singularities they discovered with their earlier investigations of nonrotating spheroids [17]. In this low-rotating case it is not clear if the rotation effects exceed the numerical errors, thus, leaving the cosmic censorship conjecture yet open. Experts in the field remain sceptical about the numerical results of Shapiro and Teukolsky since in their explorations they cannot probe the spacetime geometry far enough to rule out the formation of an event horizon.

2 GRAVITATIONAL RADIATION AND CIRCULARIZATION OF ELLIPTICAL ORBITS

Chapters 3, 4, and 5 are devoted to gravitational waves from astrophysical sources and their detection. Although the concept of gravitational waves, as linearized perturbations of spacetime geometry traveling on a flat spacetime with the speed of light, dates back to Einstein's 1916 analysis [18], they are still a dream to be detected. In addition to testing one more prediction of General Relativity, gravitational wave astronomy can open a new and valuable window in observational astrophysics. This new window is likely to bring qualitatively new information, since gravitational waves are produced by coherent bulk motions of highly compacted matter and energy, whereas the electromagnetic waves, on which our present knowledge of the Universe is based, are mainly created by incoherent emissions from individual atoms, molecules, and charged particles [19]. Thus, detecting and analyzing cosmic gravitational waves could greatly enhance our understanding of the Universe.

Since the early 1960s, experimentalists have been trying to detect gravitational waves directly by means of huge (a few tons) resonant solid bars [20]. Although more and more sophisticated techniques have been used over the years to reduce the amount of internal thermal noise, increase the sensitivity of the mechanical to electrical transducers, and reach the sensitivity level appropriate for detection ($\sim 10^{-21}$ in strain), no success has yet been scored, that has been widely accepted. One of the great disadvantages of the bar detectors is the narrowness of their frequency band of operation.

A new type of detector, based on laser interferometry, began to be developed in the 1970s. Because of their great potential arm length L, and because their sensitivity against most noise sources scales $\propto 1/L$, the interferometers have the potential to become much more sensitivity than the bars; and, in fact, as of this writing the Caltech prototype interferometer is estimated to have an rms noise level of about half of that for any bar that has ever operated. Not only are these new types of detectors potentially more sensitive, but they can also be much broader in frequency than the bars, giving us the opportunity to observe a source's detailed evolution, through the waves' changes in frequency.

Since the interferometric detectors are approaching the level of sensitivity needed in order to "hear" the whisper of gravitational waves, there is a growing need for theorists to construct models of the possible sources, to give realistic estimates of

their event rates, and to derive ways to extract information from observed waves.

In this spirit, in chapter 3, Eric Poisson, Daniel Kennefick and I have investigated the gravitational-wave-induced evolution of eccentric orbits of binaries consisting of small objects (of the order of $1M_{\odot}$) orbiting around a large Schwarzschild black hole. Our focus is on the influence of that orbital evolution on the waves, which might be detected by the broad-band earth-based interferometric detectors LIGO/VIRGO/GEO (all of which are under construction or in the final stage of their design) and/or the future space-based detector LISA.

Compact merging binaries (binaries of neutron stars and/or black holes) are considered the most promising sources for these detectors (a) because there are expected to exist enough of them, within the range of the detectors, for several or more to be seen each year [21], (b) their waves carry a large amount of information about the binaries' characteristics and geometry, and (c) mainly because they are the best understood of all the suggested sources: they produce gravitational signals that are very clean, throughout the sensitive band of the detectors, without any complications related to the bodies' internal structure. It will be especially helpful, in searching for these binaries, that most of the (complex) features of their gravitational waveforms can be computed analytically. The generic shape of these waves, with all complicating factors (spins, eccentricities, etc.) removed, is the so called "chirp" waveform, a sinusoidal signal that slowly grows in amplitude and frequency (sweeping through the frequency band of the detectors in a time of a few minutes for the LIGO/VIRGO/GEO detectors and a few months or longer for LISA), as the two stars orbit around each other with relativistic velocities, and move closer to each other by losing energy via gravitational radiation [22].

One of the relevant parameters, in gravitational wave emission from binaries, is the eccentricity of the binary's orbit. The dependence of the waves on eccentricity is two-fold: (a) the magnitude of the eccentricity makes the waves asymmetric (i.e., enriches their harmonic content), since in eccentric orbits the objects do not travel with constant angular velocity around each other, and (b) the orientation of the ellipticity is an extra degree of freedom in determining what combination of the wave's two polarizations is measured by each detector on Earth. Of course the assumption of a circular orbit would substantially simplify the problem, and this is what most people, investigating the detectability of the gravitational waves, assume. As a matter of fact, this is often a well justified assumption since in general gravitational radiation reaction tends to circularize the orbit.

My work with Poisson and Kennefick, which is presented in chapter 3 of this

thesis, is focused on the radiation-reaction-induced evolution of slightly eccentric orbits in a Schwarzschild black hole geometry. We examine the evolution not only when the orbiting body is far from the black hole where the field is rather weak and the motion is slow, but in the strong-field regime as well, i.e., near the black hole. In 1964, Phillip Peters derived analytical expressions for the evolution of the eccentricity of a binary, based on the simple Newtonian quadrupole formalism for the orbital motion and wave generation [23]. According to his formulae, the eccentricity continuously decreases during the inspiral.

Now, radiation reaction in general relativity is a very delicate issue. It encompasses both major conceptual and computational difficulties. Gravitational waves are defined as ripples in the curvature of spacetime traveling with the speed of light. As such, they have no meaning as a local field. Additionally they interfere with the curved background where they propagate, they get scattered and they may influence the future evolution of the radiating system; these backscattered waves, in the process of emission, are often referred as *tails* (see [24]) and when gravity is strong, they severely complicate the theory of gravitational radiation reaction.

Fortunately, there is a great amount of literature on perturbative analyses of the gravitational field around a black hole. Newman and Penrose [25] have developed general mathematical tools for such an analysis in an arbitrary spacetime, and Teukolsky [26] and others have specialized these tools to black-hole spacetimes (Schwarzschild and Kerr). In the case of a binary with an extreme ratio of masses, one may think of the small object as a perturbation on the big mass's gravitational field. The relevant differential equation describing the evolution of the gravitational field is the so called Teukolsky equation [26]. In order to compute the gravitational waves emitted from such a binary, one must solve the inhomogeneous Teukolsky equation, with the stress energy tensor of the small object moving on a geodesic orbit [27] as the source term. By imposing the right boundary conditions at infinity and at the black hole's horizon we can obtain the radial part of the perturbative field (while the angular part is given by tensor spherical harmonics, thanks to the spherical symmetry of the Schwarzschild black hole). Finally from the field evolution, we can construct the waveform, and deduce the energy and angular momentum radiated.

In the limit that the mass μ of the inspiraling body is small compared to the black hole's mass M, all the delicate issues of radiation reaction and its sensitivity to tails can be avoided in a simple way. The orbit evolves only a tiny bit during

one orbital period, so radiation reaction effects can be averaged over a period. This enables us to simply infer the evolution of the orbit's semimajor axis and eccentricity from the energy and angular momentum carried off by the waves.

Eric Poisson and I have worked out, independently, the analytic computations involved in solving the Teukolsky equation for a slightly eccentric orbit, in the weak-field, slow-motion approximation (in other words far from the black hole). Our analysis involved a post-Newtonian expansion of the Teukolsky formalism, i.e., an expansion in powers of $(M/r_0)^{1/2}$, where M is the black hole's mass and r_0 is the orbit-averaged Schwarzschild radial coordinate of the small orbiting body. From this fully analytic analysis, we obtained the following results: In zeroth order we obtained the same evolution rate $d\epsilon/dt$ for the orbital eccentricity ϵ as Peters obtained by using just the Newtonian quadrupole formalism (see Ref. [23].) We computed relativistic corrections to this rate up through post$^{1.5}$-Newtonian order, $(M/r_0)^{3/2}$. Daniel Kennefick then computed numerically, from Poisson's and my equations, the rate of evolution of the eccentricity everywhere, including the fully relativistic region near the black hole. Far from the black hole, our analytic solution was in full agreement with Kennefick's numerical solution. Also Poisson and I independently derived analytic expressions for the rate of evolution of the eccentricity in the highly relativistic regime, when r_0 approaches $6M$. (When the orbit falls below $r = 6M$, it becomes unstable, and the orbiting object plunges towards the black hole.) Our analytic expressions were again in full agreement with Kennefick's numerical solution. Our results are presented in chapter 3 of this thesis, which is identical to our paper in *Phys. Rev. D* **47**, 5376 (1993). [Amos Ori was added as an author of the paper after it was written, when we learned that he had independently derived some of these same results.]

The general picture we gained from both our numerical and analytic solutions is the following. Far away from the black hole, the eccentricity evolves in a Newtonian, quadrupolar manner; more energy is radiated in the vicinity of periastron (close to the black hole) than near apastron, thereby making the orbit become more circular. However, there is a critical radius very close to the black hole ($r_c \simeq 6.6792M$) below which radiation reaction meshes with the black hole's strong-field geometry to drive the eccentricity up – though not by an enormous amount.

Of course, one should keep in mind that our analysis is, restricted to small initial eccentricities. After the completion of our paper, Poisson, Cutler, and Kennefick [28] explored numerically the general problem of orbits with arbitrary eccentricity

in a Schwarzschild geometry, and found the same qualitative behavior as in our work. Eccentricity decreases with time, until the orbit reaches some minimum periastron radius, very close to the final stable orbit; then it grows.

These conclusions make us feel safe that, whenever we deal with long lived binaries like those produced by normal stellar evolution, with very unequal masses (our regime of computation) and with initial radii far larger than r_c, we are free to ignore the eccentricity of the orbit; radiation reaction is guaranteed to have circularized the orbit before it reaches the strongly relativistic regime, where the gravitational-wave observations will be made. (For example, the eccentricity decreases by almost a factor of 60 while the orbital radius shrinks from $100M$ down to r_c). This is thought to be the situation for most of the binaries that will be seen by the earth-based LIGO, and presumably is true when the binaries have comparable masses (and our calculations fail), as well as for very unequal masses.

By contrast, when a neutron star or small black hole gets captured into a tightly bound orbit around a supermassive black hole in a dense galactic nucleus, the captured object may not have enough time to lose its eccentricity before it enters the frequency window of the gravity-wave detector [5], in this case the space-based LISA; and it may even remain quite eccentric all the way into r_c and onward to $r = 6M$.

3 SPIN-INDUCED MODULATION OF GRAVITATIONAL WAVES FROM MERGING BINARIES AND SEARCH TEMPLATES FOR THEIR DETECTION

3.1 Motivation

In the previous section we referred to gravitational wave detectors only as a context for our analysis of eccentric orbits, without considering the detectors' noise spectra. Chapters 4, and 5 are more closely related to the actual task of gravitational wave detection, and thus are more closely tied to the detectors' noise. Therefore, I will start with a short description of these detectors and their internal noise, on which the rest of this chapter will rely.

LIGO and VIRGO will be long (3 or 4 kilometers) L-shaped laser interferometers, consisting of four massive ($\sim$ 10 kg) mirrors hung from vibration-isolated

supports, that will eventually be able to detect strain amplitudes of the order of 10^{-21} or smaller. Of course this is such a difficult task that state-of-the-art optics, vacuum systems, seismic isolation, etc. must be used. The first pair of these detectors, by the name LIGO, is already under construction in the USA. Another detector, the VIRGO (a French/Italian collaboration) will follow shortly. GEO (a British/German collaboration), and a Japanese and/or an Australian analogue may follow in the future. By $\sim$ 2001, the 3-detector LIGO/VIRGO network is expected to be in operation. As we have emphasized in the previous section, these detectors, by contrast with the bar detectors, are broad band instruments with a range of frequencies, 10 Hz $\lesssim f \lesssim$ 500 Hz. The LIGO team has published an estimate of the spectrum noise curve [30], as it might look with a few years of improvements beyond the first generation of LIGO detectors. This so called "advanced detector" noise curve is used by theorists as a benchmark for investigations connected to the detection of waves and/or the extraction of information from gravitational wave signals (see for example [31]).

LISA is a proposed space-based gravitational wave antenna, which will consist of a cluster of four spacecraft functioning in effect as an interferometer with a few million kilometer arm length. LISA's design is still in a preliminary stage. Its estimated frequency band will be 0.1 mHz $\lesssim f \lesssim$ 1 Hz. Last month LISA was approved, by the European Space Agency, as the third of two or three *Cornerstone Missions* for the $\sim$2010 time frame. LISA's fate in Europe will depend on whether funds are available for three, or only for two Cornerstone Missions. If it does not move forward in Europe, a vigorous attempt will be made to convince NASA to fly it.

While experimentalists are striving to develop new techniques to build ground-based detectors with super-high sensitivity, which is a major scientific and technical task, a worldwide group of theorists is trying to estimate event rates of possible detectable sources, as well as waveforms corresponding to these sources. The predicted waveforms are essential for detecting the gravitational waves, especially from compact merging binaries of neutron stars and/or black holes. The reason is that the received signals are expected to be hidden behind the detectors' internal noise. In order to extract them from the noise, one must use the technique of "matched filtering." More specifically, the noisy output of each detector must be cross-correlated with a family of previously designed templates, presumed to describe accurately all the possible waveforms, with the cross-correlation weighted by the sensitivity of the interferometer. If a signal is present, the cross-correlation

will turn out high for some specific template. The more accurate the templates are, the more promising this detection process will be.

In principle one could solve, with higher and higher accuracy, the general relativistic equations describing the motion of a binary and its emission of gravitational waves, to get more and more realistic templates, and this has to be done to obtain sufficiently accurate templates to extract all possible information from any detected signal. But in searching for signals, because of restrictions on the computers' speed [32] (since the data analysis must keep up with the incoming data), and the desire not to reduce the statistical significance of any signal discovered, one should make sophisticated choices to reduce the total number of search templates. Once the signal has been detected, the recorded data can then be cross-correlated with the information extraction templates, to extract further details of the signal, not included in the family of search templates.

The parameters determining a hypothetical realistic waveform from a binary are the masses and spins of the two objects, the direction and distance to the binary, its relative orientation with respect to the detector's arms, and the time and orbital phase of the bodies' final coalescence. To span the whole range of these parameters with perfect accuracy would require a huge number of templates. Fortunately, some of them – such as the orientation of the binary (if the orbital plane remains fixed), the distance to the binary, and the time of coalescence – enter into the waveform in such a trivial way that we can construct the templates without any reference to them.

A nice, pictorial way to get a feeling for the problem of constructing the template family is the following. Imagine the multidimensional space of all possible signal waveforms [31], with as many dimensions (~ 17) as the number of parameters they depend on. One then has to fill up the whole volume of interest (only a part of the whole space is potentially detectable, since the signal's frequency must be within the detector's window) with templates represented as points in this space, in a clever way that covers all the possible corners but with a modest template density. Then if a signal arrives, "located" in the vicinity of one of the templates, its cross-correlation with the template will depend on their separation (defined as the square root of the sensitivity-weighted cross-correlation of their difference with itself). The signal/template cross-correlation will be maximum if the separation is zero. If the template family used does not include the exact waveforms of the true signals, then the templates and the signals populate disjoint finite dimensional subspaces of the infinite dimensional space of all (sufficiently

smooth) functions. This cannot be avoided, since the fully relativistic equations have to be solved exactly to obtain perfect templates. But, at least, one can wisely choose templates, located very close to the subspace of the true waveforms.

In the Newtonian quadrupolar approximation to general relativity, the waveforms from a circular binary, whose bodies do not spin, depend on just three parameters: a specific combination of masses called the "chirp mass," $\mathcal{M} \equiv [M_1^3 M_2^3/(M_1+M_2)]^{1/5}$, the orbital phase ϕ_C, and the time t_C of final coalescence. A perfect family of search templates in this case depends only on the two parameters $\mathcal{M}$ and ϕ_C. The third parameter, the time of coalescence t_C, does not show up in the templates; instead it is taken into account directly in the computing process, while performing the cross-correlations via fast Fourier transforms [33]. Moreover for ϕ_C only two values are needed, conventionally chosen to be 0 and $\pi/2$ (see [33]); The cross-correlation with some signal, maximized over ϕ_C, is the square root of the sum of the squares of its values for $\phi_C = 0$ and $\phi_C = \pi/2$. Thus, the templates depend nontrivially on only one parameter, the chirp mass $\mathcal{M}$.

This set of templates is known by the name "Newtonian family" or "Newtonian filter." The members of this family have a characteristic "chirp" form, in which both the amplitude and the frequency grow monotonically with time, at a rate which is faster the larger is $\mathcal{M}$. Near the end of chapter 5, I show that even for binaries with zero spins, this Newtonian template family is **NOT** adequate for gravitational wave searches, since the post-Newtonian corrections to the waveforms' phase are quite large and differ in form from the Newtonian phase. (As we will see later on, the evolving phase is the part of the template that must agree most accurately with that of the signal.) If the binary's objects are spinning, the Newtonian template family is even more inadequate.

3.2 The binaries' spin-induced precession and waveform modulation

In order to check the adequateness of various search-template families, one needs to know how much the true signals are affected by special features of the binaries, most especially by the two bodies' spins, which cause the binary to precess via general relativistic spin-orbit and spin-spin coupling (the "dragging of inertial frames").

In Chapter 4, Curt Cutler, Gerald Sussman, Kip Thorne and I develop the equations describing the general relativistic spin-orbit and spin-spin coupling and explore their consequences. These couplings arise first at post$^{1.5}$- and post^{2}-

Newtonian order respectively. For the sake of simplicity we have kept the Newtonian quadrupole approximation for the orbit, the inspiral rate, and the formation of gravitational waves, and have used the post$^{1.5}$-Newtonian and post^{2}-Newtonian equations only to compute the orbital precession.

Thorne derived precession equations from his previous work with James Hartle [34] on the motion and precession of black holes; and then Sussman did a first quick set of numerical integrations to get a feeling for the precessional effects. For the limiting but interesting case where one of the objects has negligible spin (e.g., a spinning black hole and a nonrotating neutron star), I then derived analytic expressions for the evolution of the orbital plane and Cutler computed the corresponding gravitational waveforms. I showed that, in this case, the total angular momentum $\mathbf{J}$ (the vectorial sum of orbital angular momentum and spin) remains almost fixed in direction and the orbital angular momentum precesses around this almost fixed direction, as Thorne had guessed; and I derived the details of $\mathbf{J}$'s tiny failure to be fixed. The angle between the orbital angular momentum $\mathbf{L}$ and spin $\mathbf{S}$ is constant. Therefore, as $\mathbf{L}$ shrinks with time, via radiation reaction, the cone that $\mathbf{L}$ sweeps opens or closes, depending on the misalignment between $\mathbf{L}$ and $\mathbf{S}$ and the relative magnitudes of $\mathbf{L}$ and $\mathbf{S}$. To this behavior we gave the name *simple precession.*

The situation is more complicated if $\mathbf{L}$ and $\mathbf{S}$ are almost anti-aligned. We didn't manage to derive any analytic expression describing the evolution of $\mathbf{L}$ for this case, so I wrote a code to integrate numerically the corresponding differential equations. Based on these numerical explorations, I deduced the following qualitative behavior. As long as L is much larger than S, the binary undergoes simple precession around $\mathbf{J} = \mathbf{L} + \mathbf{S}$, which is more or less fixed in direction, and the precession cone gradually opens up. When the cone becomes nearly planar, L is approximately the same as S, $\mathbf{L}$ and $\mathbf{S}$ almost cancel each other, the binary loses its gyroscopic stability, the "simple precession" breaks down, and both $\mathbf{L}$ and $\mathbf{S}$ "tumble" in space. Then, when L shrinks to become much smaller than S, this "*transitional precession*" is followed by a simple precession around a new fixed direction, the final direction of $\mathbf{J} = \mathbf{L} + \mathbf{S}$, with the precession cone gradually closing.

The general case of arbitrary masses and spins is even more complicated, since spin-spin interactions come into play. Being unable to solve the relevant differential equations, I numerically integrated them to produce diagrams depicting their behavior. For a few combinations of masses and spin orientations, the diagrams

show ragged precessional evolution for the orbital plane.

Even with the complications of the spin-spin interaction, there are two cases which I was able to explore approximately analytically. (a) If one of the spins is much smaller than the other, we can treat it as a perturbation of the simple precession case. My solution of the corresponding equations leads to an epicyclic motion on top of the precession. (b) If both masses and spins are equal (e.g., two equally spinning neutron stars of $1.4M_\odot$) then the differential equations for the evolution of $\mathbf{L}$ and $\mathbf{S}_1, \mathbf{S}_2$, up to leading orders in $S_{1,2}/L$, turn out to be solvable by means of Jacobian elliptic integrals (see my addendum to chapter 4). The expansion in terms of $S_{1,2}/L$ is justified by the fact that for equal masses, the spins are always much smaller than L: $S_{1,2}/L \lesssim 0.1$ within the range of frequencies where the detectors are sensitive.

Although these spin-orbit and spin-spin couplings are high order post-Newtonian effects, they are potentially in danger of creating a lot of trouble in detecting signals from precessing binaries (and correspondingly can bring a lot of information about a detected binary). The reason is the following. The few tens of precession cycles of $\mathbf{L}$ and consequently of the orbital plane, during the epoch when the gravitational waves are sweeping through the detectors' sensitive window, will induce a modulation, both in amplitude and in phase, in the waveforms; and for some binary orientations, this modulation can be very deep and can have a complicated character that changes with time. In chapter 4 we present diagrammatic ways (derived by Cutler and Thorne) to deduce and understand some of the details of this modulation from the details of the precession.

3.3 Search templates

Chapter 5 (of which I am the sole author) is mainly devoted to exploratory investigations of the possible problems this modulation may produce in attempts to detect signals from precessing merging binaries, using simpler nonmodulated search templates.

I begin by defining a quantitative measure of how well a chosen family of templates fits the shape of a hypothetical waveform. I call this measure the family's "*Fitting Factor*" and denote it FF. Although this FF has been extensively used in one or another form by other people (using simply the name "correlation"), its significance has not previously been brought out. I avoided the generic name "correlation" because the FF is a very specialized type of correlation: it is a

correlation of the normalized [35] signal and a normalized template, weighted by the inverse of the detector's noise spectrum, and maximized over all the templates in the family. The value of FF is between 0 and 1, and it measures the reduction in signal to noise brought about by using a family that does not contain any template identical to the waveform. (A FF value equal to 1 corresponds to a family that does contain a template precisely identical to the hypothetical waveform.) It should be noted here, that it is mainly the evolving phase mismatch between template and signal that can drive the FF to low values, and not the amplitude differences. The FF value, then, is a nice criterion for the adequateness of the family of search templates.

Before I enter into the complications of the modulated signals, I would like to explain the significance and the consequences of the numerical value of FF. A FF of 0.9 means a reduction in signal to noise by 10%, which in turn means a 27% reduction in the event rate, since the event rate goes like the volume of the Universe enclosed in a radius corresponding to the maximum distance that a signal can be detected. On the other hand, this 10% reduction in the signal to noise ratio is analogous to roughly a 10% reduction in length of the interferometers arms, and speaking in real cost, something like 10 million dollars to build 10% longer arms to compensate for this loss. Several people in the field [36, 37] seem not to realize the high cost of such a reduction, and keep talking about "high detectability" for FF values well below 0.9. For example, the Newtonian template family has been considered adequate to detect signals described by the best approximate waveform (without precession) available nowadays, which includes relativistic corrections up through post$^{1.5}$-Newtonian order, even though FF in this case is < 0.6.

Although there is numerical agreement between different people's calculations of their analogue to FF, the interpretation varies. In chapter 5, I examine all the possible combinations of unmodulated signals (with phases accurate up to post^s-Newtonian order) and templates (described by waveforms accurate up to post^t-Newtonian order with $1.5 \geq s \geq t$). The FF values I obtain are rather discouraging, well below 0.9, except for templates with the same accuracy as the signal ($t = s$). This suggests a need to use templates of at least post$^{1.5}$-Newtonian accuracy.

If corrections higher than post$^{1.5}$-Newtonian are proven to be negligible (which seems very unlikely [38]), then templates accurate to post$^{1.5}$-Newtonian order are needed and will be sufficient. This means the addition of just one more parameter to the Newtonian family (the ratio of reduced mass to total mass,

μ/M), if precession-induced modulation is ignored. (The unmodulated post$^{1.5}$-Newtonian waveforms depend on a second new parameter, a combination of the body's spins; but this parameter does not produce qualitatively new effects and thus does not reduce FF significantly.) Although corrections of higher order than post$^{1.5}$-Newtonian are likely to be important, the consortium of researchers who are computing them need several years to complete the calculations [9].

The principal purpose of chapter 5 is to carry out an initial exploratory study of the effects of precession-induced signal modulation on the FF's of unmodulated template families. My conclusions will be a foundation for further research toward the choice of search templates for LIGO.

When the binary's spins are not parallel to the orbital angular momentum, they and the resulting precession introduce a large number of new parameters into the game. The precession of the orbital plane causes a time dependent mixture of polarizations to be received by the ground- or space-based detectors. For the sake of simplicity, in chapter 5 I restrict myself to "simple precession" situations, where analytic expressions for the evolution of the orbital plane are available. Except for the quite singular (and presumably rare) transitional precession, simple precession is a good guide for the general two-spin case. In chapter 5 I show the following: (a) The precession-induced amplitude modulation is not very harmful in reducing the signal-to-noise, but the phase modulation *can* be harmful. (b) The larger the misalignment between **L** and **S** is, the more open the cone of precession is, and the deeper the modulation can be. (c) For some special orientations of the cone of precession, the phase modulation can grow secularly with each precession cycle, then abruptly switch over to nonsecular oscillations, or conversely. The geometries that lead to this behavior during inspiral through the detectors' frequency band are potentially the worst cases, producing the lowest values of FF for unmodulated Newtonian or post-Newtonian templates.

By exploring the effects of all the possible parameters connected with the precession phenomenon, I have arrived at the following general picture.

For the unmodulated Newtonian template family and a Newtonian signal with precession: For neutron star/neutron star binaries with masses of $1.4M_\odot$, and one of them rapidly rotating (assuming an extreme magnitude for the spin, $S_i = M_i^2$), the cone of precession is so narrow, that only for a very small percentage ($< 10\%$) of all possible geometries does the FF value drop below 0.9. By contrast, a binary consisting of a $10M_\odot$ rapidly spinning black hole and a nonrotating $1.4M_\odot$ neutron star, precesses on a much wider cone (because the

ratio of spin to orbital angular momentum is much larger), leading to much lower FF values; for an $\mathbf{S}, \mathbf{L}$ misalignment above 30° there is almost no possibility to obtain a FF above 0.9.

For the unmodulated post$^{1.5}$-Newtonian template family, with all the spin parameters stripped off (see a few paragraphs above), **and a full post$^{1.5}$-Newtonian signal with precession** (based, however on Newtonian orbits): Since an additional parameter is available with this new template family, one should expect more flexibility to fit the modulated signals. This is what actually happens, but it produces only a modest, not large, improvement of the FF's: For the same pair of neutron stars discussed above, the probability for some geometry to give a FF value below 0.9 is still less than 10% (slightly smaller than with the Newtonian template family). For the same black hole/neutron star pair as before, there is now a modestly larger probability to find a geometry with a FF above 0.9. This probability is quite small for a large misalignment angle ($\sim 140°$), but increases substantially for small misalignment angles; for example, $\simeq 25\%$ probability for $FF > 0.9$ when the misalignment angle is 30°. These results suggest that it will be necessary to include at best one modulational parameter in LIGO's search templates.

Finally, in the Appendix of chapter 5 I extend my calculations for the FF, to the space-based detector LISA. This extension is straightforward since the shape of LISA's noise spectrum is about the same as LIGO's, only shifted to much lower frequencies (0.1 mHz - 1 Hz) [40]. Since the equations describing the precession of the orbital plane depend only on the ratio of masses and the product of total mass times frequency, Mf, binaries with masses 5 orders of magnitude larger than the masses of the binaries considered for the LIGO-type detectors should produce almost the same FF's, if the same types of templates are used. I have verified this conjecture for the example of a maximally rotating $10^6 M_\odot$ black hole and a non rotating $1.4 \times 10^5 M_\odot$ black hole, with an $\mathbf{S}, \mathbf{L}$ misalignment angle of 30°. This binary produced almost the same FF's (for all the possible geometries) as the corresponding $1.4 M_\odot - 10 M_\odot$ BH/NS binary with the same misalignment angle, and the Newtonian template family.

This work should be regarded as just the first step in a quantitative attempt to define what standards an "adequate family of templates" should fulfill, and to explore issues that are important for the ultimate choices of LIGO's and LISA's search templates.

Bibliography

[1] J. R. Oppenheimer, and H. Snyder, *Phys. Rev.* **56**, 455 (1939).

[2] R. F. Stark, and T. Piran, *Phys. Rev. Lett.* **55**, 891 (1985).

[3] E. Seidel, *Phys. Rev. D* **44**, 950 (1991).

[4] R. M. Wald, *Ann. Phys* **82**, 548 (1974).

[5] P. S. Jang, and R. M. Wald, *J. Math. Phys.* **18**, 41 (1977).

[6] G. W. Gibbons, S. W. Hawking, G. T. Horowitz, and M. J. Perry, *Commun. Math. Phys.* **88**, 295 (1983).

[7] R. Penrose, *Rev. del Nuovo Cimento* **1**, 252 (1969).

[8] M. W. Choptuik, *Phys. Rev. Lett.* **70**, 9 (1993); A. M. Abrahams, C. R. Evans, *Phys. Rev. Lett.* **70**, 2980 (1993).

[9] R. P. Geroch, and G. Horowitz, in *General Relativity, an Einstein Centenary Survey*, ed. S. W. Hawking and W. Israel (Cambridge: Cambridge University Press, 1979).

[10] R. Penrose, in *General Relativity, an Einstein Centenary Survey*, ed. S. W. Hawking and W. Israel (Cambridge: Cambridge University Press, 1979).

[11] K. S. Thorne, unpublished Ph.D. thesis, Princeton University, 1965; available from University Microfilms Inc., Ann Arbor, Michigan. In chapter 4, and more quantitatively in chapter 7, Thorne introduces, for cylindrical systems the concept of C-energy, as an analogue of the Schwarzschild mass for spherically symmetric systems. C-energy incorporates all the expected features of an energy-like quantity. (a) It is localizable and locally measurable; (b) near the symmetry axis, when gravitational waves are absent, it reduces to proper mass per unit length; (c) it is carried away by gravitational waves; and (d)

among all momentarily static, cylindrical configurations of perfect fluid with a fixed number of baryons per unit coordinate length, the configurations of hydrostatic equilibrium extremize the C-energy per unit length.

[12] C. C. Lin, L. Mestel, and F. H. Shu, *App. J.* **142**, 1431 (1965).

[13] L. Shapiro, and S. A. Teukolsky, *Phys. Rev. Lett.* **66**, 994 (1991).

[14] T. A. Apostolatos and K. S. Thorne, *Phys. Rev. D* **46**, 2435 (1992).

[15] R. M. Wald, *Phys. Rev. D* **44**, 3719 (1992).

[16] T. Piran, *Phys. Rev. Lett.* **41**, 1085 (1978).

[17] S. L. Shapiro and S. A. Teukolsky, *Phys. Rev. D*, **45**, 2006 (1992).

[18] A. Einstein, *Preuss. Akad. Wiss. Berlin, Sitzungsberichte der Physikalischmathematischen Klasse*, 688 (1916).

[19] K. S. Thorne, in *300 Years of Gravitation*, ed. S. W. Hawking and W. Israel (Cambridge University Press, Cambridge, 1987), pp. 330-458.

[20] J. Weber, *Phys. Rev.*, **117**, 306 (1960).

[21] E. S. Phiney, *Astrophys. J.* **380**, L17 (1991).

[22] K. S. Thorne, to be published in *Proceedings of the Eighth Nishinomiya-Yukawa Symposium on Relativistic Cosmology*, ed. M. Sasaki (Universal Academy Press).

[23] P. C. Peters, *Phys. Rev.* **136**, B1224 (1964).

[24] E. Poisson, *Phys. Rev. D* **47**, 1497 (1993).

[25] E. T. Newman, and R. Penrose, *J. Math. Phys.* **7**, 863 (1966).

[26] S. A. Teukolsky, *Astrophys. J.* **185**, 635 (1973).

[27] Here we assume that the small object moves on a geodesic orbit. In general for a radiating system this is not correct, but for an extreme ratio of masses this is a reasonable assumption, since the ratio of inspiral timescale to the orbital period scales like the ratio of masses. Thus, the orbit remains adiabatically geodesic up to some limiting radius which we have taken into consideration in

our analysis (for a ratio of masses $1 : 10^6$, the adiabatic approximation breaks down at $r = 6.002M$).

[28] C. Cutler, D. Kennefick, and E. Poisson, *Phys. Rev. D* **50**, 3816 (1994).

[29] G. Quinlan and S. L. Shapiro, *Astrophys. J.*, **321**, 199 (1987).

[30] A. Abramovici *et al.*, *Science* **256**, 325 (1992).

[31] C. Cutler, and E. Flanagan, *Phys. Rev. D* **49**, 2658 (1994).

[32] To give a feeling for the computer power needed to perform the cross-correlations of all the templates with noisy output, Thorne has estimated that for a family of $\sim 10^5$ templates and output sampled at 20 or 40 kHz, a ~ 10 Gflop machine will be needed. This is possible, though expensive, even today. This estimate can be derived from the relevant formulae of Ref. [33].

[33] B. F. Schutz, in *The detection of gravitational waves* ed. D. G. Blair (Cambridge University Press, Cambridge, 1991), pp. 406-452.

[34] K. S. Thorne, and J. B. Hartle, Rev. D **31**, 1815 (1985).

[35] By normalized signals and templates here, we mean signals and templates constructed to give a unity cross-correlation with themselves.

[36] K. Kokkotas, A. Kròlak, G. Schäfer *Proceedings of the Moriond 94 Workshop.*

[37] R. Balasubramanian, and S. V. Dhurandhar, *Phys. Rev. D*, in press.

[38] C. Cutler, and E. Flanagan, *Phys. Rev. D*, in preparation.

[39] M. Will, to be published in *Proceedings of the Eighth Nishinomiya-Yukawa Symposium on Relativistic Cosmology*, ed. M. Sasaki (Universal Academy Press).

[40] K. Danzmann, A. Rüdiger, R. Schilling, W. Winkler, J. Hough, G. P. Newton, D. Robertson, N. A. Robertson, H. Ward, P. Bender, J. Faller, D. Hils, R. Stebbins, C. D. Edwards, W. Folkner, M. Vincent, A. Bernard, B. Bertotti, A. Brillet, C. N. Man, M. Cruise, P. Gray, M. Sandford, R. W. P. Drever, V. Kose, M. Kühne, B. F. Schutz, R. Weiss, and H. Welling, "LISA: Proposal

for a Laser-Interferometer Gravitational Wave Detector in Space," unpublished proposal submitted to the European Space Agency in May 1993; available as document MPQ 177 from the Max-Planck-Institut für Quantenoptik, 8046 Garching bei München, Germany.

Chapter 2

Rotation halts cylindrical, relativistic gravitational collapse. [Co-authored with Kip S. Thorne]

(Originally appeared in Phys. Rev. D **46**, 2435 (1992).)

Abstract

It is shown, in a simple analytic example, that an infinitesimal amount of rotation can halt the general relativistic gravitational collapse of a pressure-free cylindrical body. The example is a thin cylindrical shell (a shell with translation symmetry and rotation symmetry), made of counter-rotating dust particles. Half of the particles rotate about the symmetry axis in one direction with (conserved) angular momentum per unit rest mass α, and the other half rotate in the opposite direction with the same α. It is shown, using C-energy arguments, that the shell can never collapse to a circumference smaller than $C = 8\pi\alpha\Lambda$, where Λ is the shell's non-conserved mass per unit proper length. Equivalently, if $R \equiv |\partial/\partial\phi||\partial/\partial z|$ is the product of the lengths of the rotational and translational Killing vectors at the shell's location and λ is the shell's conserved rest mass per unit Killing length z, then the shell can never collapse smaller than $R = 4\alpha\lambda$. It is also shown that after its centrifugally-induced bounce, the shell will oscillate radially and will radiate gravitational waves as it oscillates, the waves will carry away C-energy, and this loss of C-energy will force the shell to settle down to a static, equilibrium radius.

1 INTRODUCTION AND SUMMARY

1.1 Motivation

A recent numerical solution of the Einstein field equations by Shapiro and Teukolsky[1] suggests that it may be possible for a naked singularity to form in the gravitational collapse of a highly nonspherical body, in violation of Penrose's[2] cosmic censorship conjecture. The Shapiro-Teukolsky solution describes the collapse of a prolate spheroid of dust particles, all of which initially are at rest. Near the endpoint of their collapse, the dust particles form a thin spindle that is imploding radially. If the spindle is so long that its poloidal circumference exceeds $4\pi M$ (where M is its mass and we set Newton's gravitation constant and the speed of light to unity), then in accord with the hoop conjecture[3, 4] no apparent horizon forms around the spindle at least up to the termination of the numerical solution; and in apparent violation of cosmic censorship, naked singularities appear to be forming in the vacuum just beyond the spindle's two pointed ends. The growth of these singularities forces the numerical integration to terminate.

It is not surprising that the collapse forms a singularity, since the dust spindle is more or less a finite-length version of an infinitely long dust cylinder, and it has long been known that collapsing infinite dust cylinders form naked singularities.[3, 5, 6] What *is* a bit surprising is that the Shapiro-Teukolsky singularity appears to be forming most rapidly in the vacuum just beyond the spindle's end rather than inside the spindle, where the dust resides. We shall discuss the significance of this below.

The cosmic censorship conjecture (the impossibility of naked singularities) is generally thought to be correct only for *realistic* gravitational collapse—collapse with rotation and realistic amounts of pressure. It therefore is of interest to ask whether the Shapiro-Teukolsky collapse would still produce a naked singularity if the collapsing body were endowed with rotation and/or a realistically stiff equation of state.

In this paper we investigate the effects of rotation in the idealized limit of an infinitely long spindle, i.e., an infinite cylinder. We show analytically that the centrifugal forces associated with an arbitrarily small amount of rotation, by themselves, without the aid of any pressure, can halt the collapse and prevent a singularity from forming[7]. Elsewhere Piran[8] has shown in specific numerical examples, that realistic pressure (pressure p such that $\gamma \equiv d\ln p/d\ln n > 1$ where n is the number density of conserved baryons) can also halt cylindrical collapse.

These results make it seem likely that also in the Shapiro-Teukolsky case of a finite-length spindle, an arbitrarily small amount of rotation and/or a realistic pressure will halt the spindle's radial collapse. If so, however, this by no means would *guarantee* an absence of naked singularities. The reason is as follows:

The fact that the singularity appears to be forming most rapidly in the vacuum just beyond the spindle's end suggests that the vacuum part of the singularity might be spacelike with respect to the singularity in the dust interior, or might even precede it causally. If so, then a realistic but tiny rotation or pressure in the spindle's imploding matter would make itself felt too late to influence the vacuum singularity. The imploding matter might bounce, but the vacuum singularity, causally oblivious of the bounce, would still form in precisely the same manner as if there were no rotation or pressure. The singularity presumably would be created by nonlinear gravity that is triggered by the sharp spacetime curvature that occurs near the bouncing spindle's pointed ends.

We must emphasize that this scenario is pure speculation. The Shapiro-Teukolsky numerical solution is by no means accurate enough nor carried to late enough times to reveal (i) whether the vacuum singularity is spacelike with respect to the interior dust singularity, nor (ii) whether a horizon forms around the vacuum singularity at late times.

1.2 Collapsing shell of counter-rotating dust

The system whose collapse is analyzed in this paper is a thin cylindrical shell made of pressure-free counter-rotating dust. Half of the dust particles orbit around the symmetry axis in a right-handed direction with angular momentum per unit rest mass α, and the other half orbit in the opposite, left-handed direction with angular momentum per unit rest mass $-\alpha$, so there is vanishing total angular momentum. This counter-rotation guarantees that there will be no dragging of inertial frames and thereby simplifies the analysis. (It seems likely on intuitive grounds that, as for our counter-rotating shell, so also for shells with net angular momentum, an arbitrarily small amount of rotation will cause the collapsing shell to bounce. However, we have not attempted to analyze shells with net angular momentum.)

In our analysis we describe the counter-rotating shell mathematically by Israel's thin-shell junction conditions[9] (Sec. 2.2). In the vacuum interior and exterior of the shell, the Einstein-Rosen canonical cylindrical coordinates[10, 11] (t, r, z, ϕ) are

introduced and the line element takes the form

$$ds^2 = e^{2(\gamma-\psi)}(-dt^2 + dr^2) + e^{2\psi}dz^2 + r^2e^{-2\psi}d\phi^2 \ . \qquad (2.1)$$

Here $\psi = \psi(t,r)$ is a gravitational field whose static part is an analog of the Newtonian potential and whose ripples represent gravitational waves; $\gamma = \gamma(t,r)$ is a metric function that will play an important role in the details of our analysis (Secs. 2—4) but is irrelevant for our discussion of the results (Sec. 1); t is the coordinate time; r is the coordinate radius; $\partial/\partial z$ and $\partial/\partial\phi$ are the Killing vector generators of translational symmetry along the cylinder and rotational symmetry around the symmetry axis; z is the Killing coordinate length with $-\infty < z < +\infty$; and ϕ is angle around the axis with $0 \le \phi \le 2\pi$. Here and throughout we set Newton's gravitation constant and the speed of light to unity. Notice that r has the geometric meaning $r = |\partial/\partial z||\partial/\partial\phi| =$ (product of lengths of the two Killing vectors), and that the circumference around the symmetry axis is $2\pi re^{-\psi}$.

We restrict attention to shells whose mass per unit length is small enough that, at some initial moment of time they do *not* close space up around themselves radially (Subsection 1.4). This implies (Appendix A) that they will never close space up radially, and correspondingly r always increases monotonically as one travels radially outward from the symmetry axis ($r = 0$) to the shell and then onward; i.e., r varies over the range $0 \le r < \infty$.

We shall use the following parameters to characterize the shell: (*i*) the angular momentum per unit rest mass of its particles, $\pm\alpha$; (*ii*) its coordinate radius $R =$ (value of r on shell); (*iii*) the value ψ_s of ψ on the shell; (*iv*) $\mathcal{R} = Re^{-\psi_s} =$ (circumference of shell)$/2\pi$; (*v*) $u \equiv \alpha/\mathcal{R} \equiv v/\sqrt{1-v^2}$ where $\pm v$ is the velocity of orbital motion of the dust particles as measured by an observer who rides on the shell and orbits neither rightward nor leftward, and where $\pm u$ is the dust particles' corresponding linear momentum per unit rest mass as measured by these observers; $\lambda \equiv dm/dz \equiv$ (shell's total rest mass per unit Killing length); and $\Lambda \equiv \lambda e^{-\psi_s} =$ (shell's total rest mass per unit proper length).

Of these parameters, α, $\mathcal{R}$, u, v, and Λ are unaffected by a rescaling of the Killing coordinate length z [i.e. by $z \to$ const $\times\, z$; Eq. (2.15) below], and in fact they are locally measurable with no ambiguity. By contrast, R and λ are scale-dependent and thus are not locally measureable; however, their dynamical changes (doublings, halvings, ...) are readily measureable locally. The parameters α and λ are conserved as the shell evolves and emits gravitational waves, but the other parameters change.

1.3 Nearly Newtonian shell

M If the shell's rest mass per unit proper length Λ and linear momentum per unit rest mass u are very small compared to one, $\Lambda \ll 1$ and $u \ll 1$ (in geometrized units where the speed of light and Newton's gravitation constant are equal to unity), and if the gravitational waves initially are very weak, so (with an appropriate choice of z-scaling) $|\psi| \ll 1$ everywhere except at extremely large radii, then the shell and its evolution will be very nearly Newtonian. More specifically, $\Lambda \simeq \lambda$ will be conserved as will be α; and the shell's radius $\mathcal{R} \simeq R$ will obey the rather obvious equation of motion

$$\mathcal{C} = \frac{\Lambda}{2}\left(\frac{d\mathcal{R}}{dt}\right)^2 + \mathcal{C}_{\rm MS}(\mathcal{R}) \, . \tag{2.2}$$

Here $\mathcal{C}$ is the shell's conserved energy per unit length and

$$\mathcal{C}_{\rm MS}(\mathcal{R}) = \Lambda\frac{\alpha^2}{2\mathcal{R}^2} + \Lambda^2 \ln \mathcal{R} + \text{const} \tag{2.3}$$

is the energy the shell would have if it were radially momentarily static. (We use the symbol $\mathcal{C}$ because these energies are the Newtonian limits of the shell's relativistic "C-energy".) Note that $\mathcal{C}_{\rm MS}(\mathcal{R})$ plays the role of an effective potential for the shell's radial motion (Fig. 2.1).

From the shape of the effective potential, it should be clear that the shell oscillates back and forth between a maximum radius $\mathcal{R}_{\rm max}$ and a minimum radius $\mathcal{R}_{\rm min}$, whose values depend on its initial conditions. At $\mathcal{R}_{\rm max}$, gravity overwhelms the centrifugal force and pulls the shell inward; at $\mathcal{R}_{\rm min}$, the centrifugal force overwhelms gravity and pushes it outward.

General relativity insists that these nearly Newtonian oscillations produce very weak gravitational waves which carry off energy. As a result, $\mathcal{R}_{\rm max}$ decreases a bit from one oscillation to the next and $\mathcal{R}_{\rm min}$ increases a bit, until finally the shell settles down into equilibrium at the minimum of its effective potential $\mathcal{C}_{\rm MS}(\mathcal{R})$. The equilibrium radius is clearly

$$\mathcal{R}_{\rm eq} = \alpha/\sqrt{\Lambda} \, . \tag{2.4}$$

From this simple analysis it is obvious that (i) if $\alpha = 0$ (no counter-rotation), then the shell collapses to a Newtonian singularity, $\mathcal{R} = 0$, but (ii) an arbitrarily small amount of angular momentum per unit mass, α, causes any collapsing shell to bounce and thereby prevents a singularity from forming.

As we shall see, in full general relativity the shell behaves qualitatively the same as this, though the quantitative details are different.

In our relativistic analysis we shall find it convenient to think about the equilibrium configuration from a different viewpoint than Eq. (2.4). We shall ask the question, "If the shell at some moment of time has a rotational linear momentum per unit rest mass $u = \alpha/\mathcal{R}$, then how large must its rest mass per unit length Λ be in order for its inward gravitational force to precisely counterbalance its outward centrifugal force?" The answer is easily seen from Eq. (2.3) to be

$$\Lambda_{\rm eq} = u^2 \ . \tag{2.5}$$

1.4 Static and momentarily static, relativistic shell

Gravitational radiation causes severe complications in the theory of a fully relativistic cylindrical shell. A useful tool for cutting through those complications is the concept of a *momentarily static and radiation-free* (MSRF) shell, i.e., a configuration which, at some chosen moment of coordinate time t, (i) has no gravitational radiation ($\partial\psi/\partial t = \partial^2\psi/\partial t^2 = 0$ everywhere), and (ii) has its shell momentarily radially at rest ($dR/dt = 0$ and thus also $d\mathcal{R}/dt = 0$ since $\mathcal{R} = Re^{-\psi_s}$).

As we shall see in Sec. 3, a MSRF shell is characterized fully (at the chosen time t) by the scale-invariant parameters α = (angular momentum per unit rest mass), Λ = (rest mass per unit proper length), and $\mathcal{R}$ = (circumference)/2π. From these we can construct two dimensionless parameters, e.g., Λ and $u = \alpha/\mathcal{R}$ = (linear momentum per unit rest mass). In Fig. 2.2 we plot Λ upward and u rightward. There are two special lines in this Λ-u plane. The upper line, $\Lambda_{\rm max}(u)$, is given by

$$\Lambda_{\rm max} = \frac{1}{4\sqrt{1+u^2}} \tag{2.6}$$

or equivalently

$$\frac{\Lambda_{\rm max}}{\sqrt{1-v^2}} = \frac{1}{4} \ , \tag{2.7}$$

where $\pm v$ is the speed of orbital motion of the shell's particles as measured by an observer at rest on the shell (cf. Subsection 1.2), so $\Lambda/\sqrt{1-v^2}$ is their total mass (rest mass plus kinetic energy) per unit proper length, as measured by that observer. Any MSRF shell above this upper line, $\Lambda > \Lambda_{\rm max}(u)$, i.e., any MSRF shell with total mass per unit proper length greater than 1/4, is so massive that it closes space up around itself radially (see Appendix B for a proof). (In the language of Appendix A, the spacetime has character $D^{(-)}$ outside the shell.)

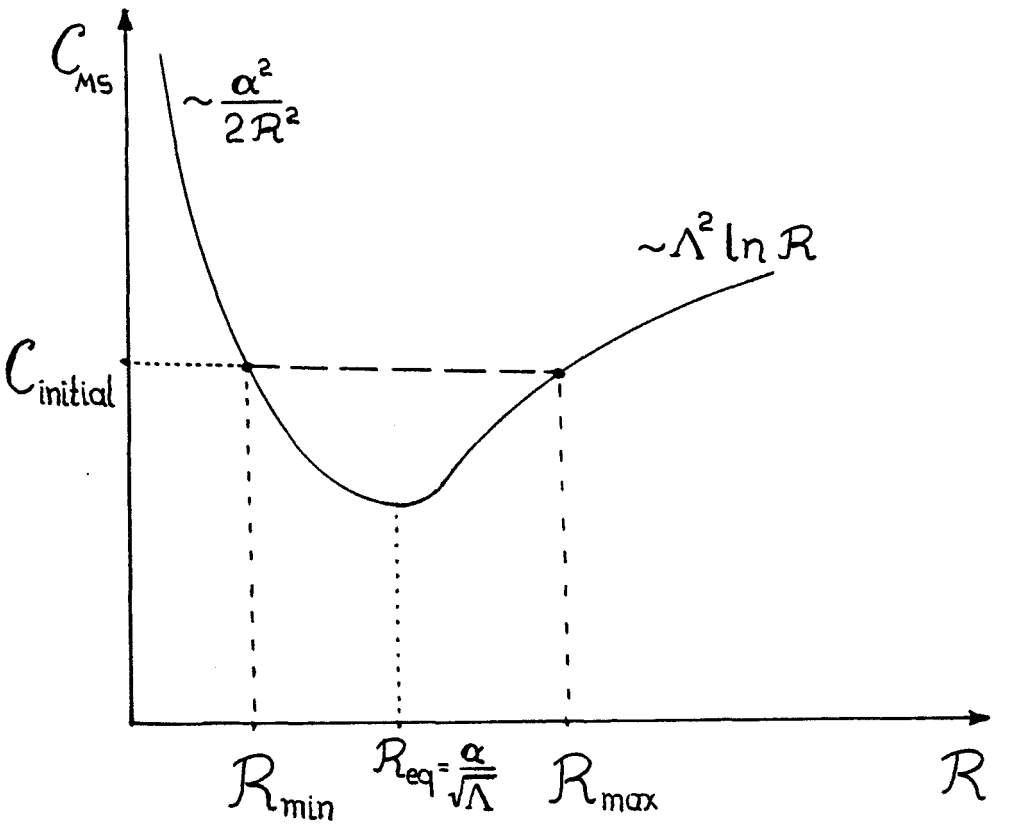

Figure 2.1: The energy per unit length $\mathcal{C}$ for a cylindrical, Newtonian shell of counterrotating dust, plotted as a function of the shell's radius $\mathcal{R}$. For a dynamical shell, $\mathcal{C}$ is conserved (dashed line) as the shell bounces back and forth between the radii $\mathcal{R}_{\rm min}$ and $\mathcal{R}_{\rm max}$. The effective potential $\mathcal{C}_{\rm MS}(\mathcal{R})$ in which it moves is given by Eq. (2.3).

In this paper, we are seeking insight into the collapse of bodies around which spacetime is asymptotically flat, not closed, so we constrain our analysis to MSRF shells below the upper line of Fig. 2.2, $\Lambda < \Lambda_{\max}$.

The lower line $\Lambda_{eq}\,(u)$ in Fig. 2.2 represents MSRF shells that are in equilibrium–i.e., shells that, when evolved to the future of the chosen initial time t, never change their radii R or $\mathcal{R}$ and never develop any gravitational radiation and thus always remain static. At small u this $\Lambda_{eq}(u)$ has the Newtonian form (2.5), $\Lambda_{eq} \simeq u^2$. The precise formula for $\Lambda_{eq}(u)$ is (Sec. 3)

$$\Lambda_{eq} = \frac{u^2\sqrt{1+u^2}}{(1+2u^2)^2}\,. \tag{2.8}$$

At $u < 0.8836$, $\Lambda_{eq}(u)$ increases with increasing u (cf. Fig. 2.2) because larger u means larger centrifugal forces and requires larger mass to produce enough gravity to hold the shell together. At $u > 0.8836$, $\Lambda_{eq}(u)$ decreases with increasing u because larger u means larger total mass per unit rest mass and thus less rest mass is needed to produce enough total mass to hold the shell together.

It turns out (Sec. 3) that any MSRF shell with $\Lambda < \Lambda_{eq}(u)$ begins to expand when released from its initial state, because its gravity is too weak to counterbalance its centrifugal forces; and similarly any MSRF shell with $\Lambda > \Lambda_{eq}(u)$ [but $\Lambda < \Lambda_{\max}(u)$] begins to contract when released.

1.5 Dynamical relativistic shell

In Secs. 3—7, we use the concept of C-energy to prove that a fully relativistic, cylindrical shell evolves dynamically in the same qualitative manner as a nearly Newtonian one. More specifically, we place the shell in an initial MSRF configuration that is arbitrary (arbitrary values of $\mathcal{R}$, u, Λ) except that $\Lambda < \Lambda_{\max}(u)$ so it does not close up space radially around itself. We then select a radius r_0 that is arbitrarily large and evaluate the total amount of C-energy $\mathcal{C}_0$ inside r_0. As the shell evolves dynamically, emitting gravitational waves, this total C-energy $\mathcal{C}_0$ will be conserved until the waves reach r_0 (which means for an arbitrarily long time), and then as the waves carry C-energy outwards through r_0 (Sec. 6), $\mathcal{C}_0$ will begin to decrease.

During the shell's arbitrarily long evolution with fixed $\mathcal{C}_0$, it conserves its values of α, λ, and $\psi_0 =$ (value of ψ at r_0), while $\psi(r,t)$ and $R(t)$ evolve dynamically.

In Sec. 5 we prove that $\mathcal{C}_0$ at any moment of time t consists of a *positive* contribution associated with the shell's radial velocity dR/dt and with the gravitational

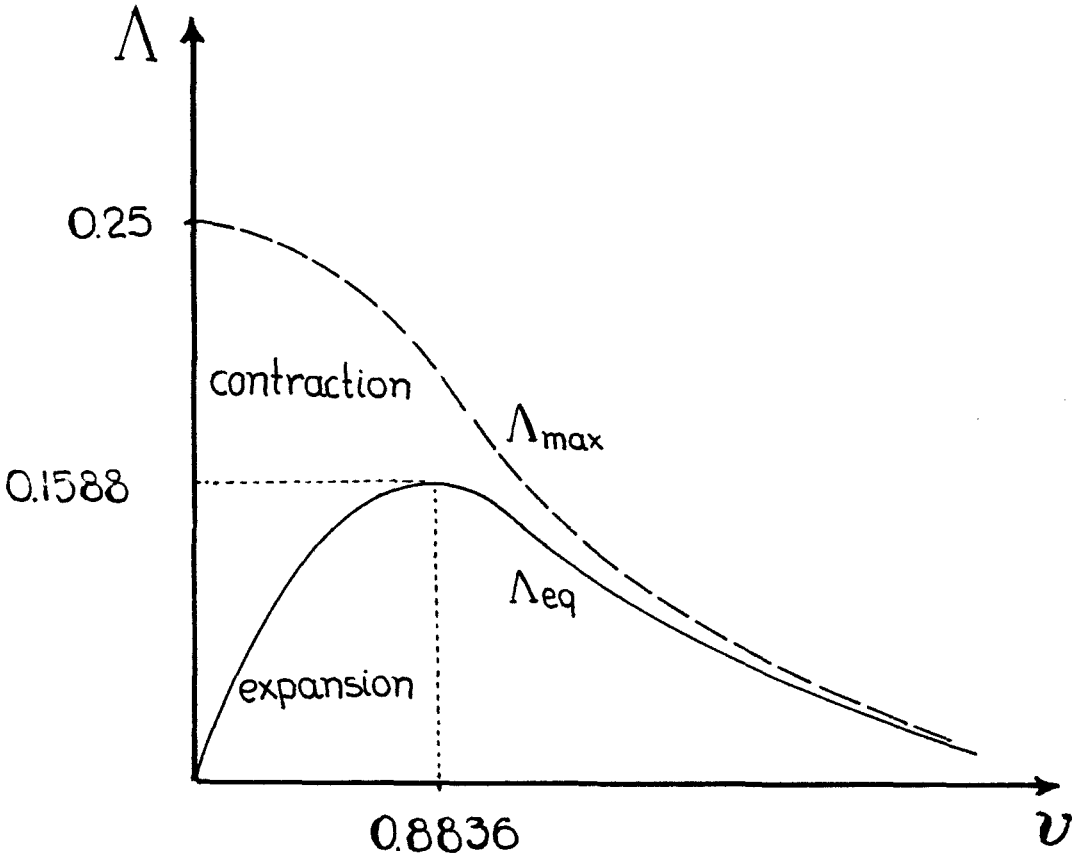

Figure 2.2: The dimensionless parameter space for momentarily static and radiation free (MSRF) shells.

waves it has emitted, plus the contribution $\mathcal{C}_{\rm MSRF}(R)$ that the configuration would have if it were MSRF and had the the same shell radius R as it actually has:

$$\mathcal{C}_0 = \mathcal{C}_{\rm MSRF}(R) + (\text{positive kinetic and GW energy}) . \tag{2.9}$$

In Secs. 3 and 4 we derive the somewhat complicated functional form of $\mathcal{C}_{\rm MSRF}(R)$ and show that it has the following properties: (*i*) $\mathcal{C}_{\rm MSRF}(R)$ has the same qualitative form as the Newtonian $\mathcal{C}_{\rm MS}(\mathcal{R})$ (Fig. 2.1): It has a single minimum at a radius $R_{\rm eq}$, and it increases monotonically as one moves away from that minimum toward either decreasing or increasing shell radii R. (*ii*) In the Newtonian limit $\mathcal{C}_{\rm MSRF}(R)$ becomes $\mathcal{C}_{\rm MS}(R)$ [Eq. (2.3)]. (*iii*) $\mathcal{C}_{\rm MSRF}(R)$ reaches the largest value, 1/8, that any shell's C-energy can have without closing the universe up radially, as R approaches r_0 from below and as it approaches

$$R_{\rm abs\ min} = 4\alpha\lambda \tag{2.10}$$

from above.

These properties of $\mathcal{C}_{\rm MSRF}(R)$, together with relation (2.9) and the conservation of $\mathcal{C}_0$, imply the following dynamics for the shell: (*i*) Once released from its initial MSRF radius, the shell must oscillate back and forth in R, emitting gravitational waves, and finally settle down into an equilibrium state. (*ii*) If the shell's initial radius R_i is larger than the minimum point $R_{\rm eq}$ of $\mathcal{C}_{\rm MSRF}(R)$, then the shell can never oscillate out to a radius R larger than R_i; and if $R_i < R_{\rm eq}$, then it can never oscillate to a smaller R than R_i. (*iii*) No matter what the initial state may be, so long as the shell initially does not close space up radially, the centrifugal force always keeps its radius R larger than $R_{\rm abs\ min} = 4\alpha\lambda$, and correspondingly keeps $\mathcal{R}$ = circumference/2π larger than

$$\mathcal{R}_{\rm abs\ min} = 4\alpha\Lambda . \tag{2.11}$$

(Recall that λ and α are conserved during the evolution; $\Lambda = \lambda e^{-\psi_s}$, however, will generally vary.) From Eqs. (2.10) and (2.11), it is clear that an arbitrarily small angular momentum α prevents the shell from collapsing to a singularity[7].

1.6 Organization of this paper

In the body of this paper, we derive the results described above.

We lay foundations for our derivation in Sec. 2. In Sec. 2.1 and Appendix A, we discuss the requirement that spacetime not be closed up radially, and then

relying on that requirement, we introduce our spacetime coordinates t, r, z, ϕ and corresponding metric coefficients ψ and γ, we write down the vacuum Einstein field equations for the shell's interior and exterior, and we introduce the concept of C-energy. Then in Sec. 2.2 we introduce the parameters that describe the shell and write down, in the form of thin-shell junction conditions, the Einstein field equations that govern the shell's coupling to the spacetime metric and its dynamical evolution.

In Sec. 3, we analyze the structures of momentarily static and radiation free (MSRF) configurations, and prove that among all MSRF configurations, the ones in equilibrium are those that minimize the C-energy with respect to variations of the shell's radius R.

In Sec. 4, we show that the C-energy of MSRF configurations, as a function of shell radius R, has the same qualitative form as in Newtonian theory (Fig. 2.2).

In Sec. 5, we show that the C-energy of a dynamical configuration is always greater than that of a MSRF configuration that has the same shell radius R, i.e. that the C-energy can be written in the form (2.9) used above in our discussion of dynamical evolution.

In Sec. 6, we show that gravitational waves always carry C-energy away from the shell, toward $r = \infty$.

In Sec. 7, we recapitulate: The properties of the C-energy, as derived in Secs. 3—6, are precisely the underpinnings needed to validate the discussion of shell dynamics given above, in Sec. 1.5. Therefore, it must be that the shell can neither collapse to a line singularity nor explode to infinity, but instead must undergo damped oscillations and end up in an equilibrium configuration of finite radius.

2 FOUNDATIONS FOR THE ANALYSIS

2.1 Radial non-closure, coordinates, metric, and vacuum field equations

It is well known[10, 11] that in any cylindrically symmetric spacetime with vanishing net momentum density along the Killing directions $\partial/\partial z$ and $\partial/\partial\phi$, one can introduce coordinates $(\bar{t}, \bar{r}, z, \phi)$ in which the line element takes the form

$$ds^2 = e^{2(\bar{\gamma}-\psi)}(-d\bar{t}^2 + d\bar{r}^2) + e^{2\psi}dz^2 + \beta^2 e^{-2\psi}d\phi^2 \ . \qquad (2.12)$$

Here $\bar{\gamma}$, ψ, and β are functions of $\bar{t}$ and $\bar{r}$. In vacuum, but not generally inside matter, the quantity $\beta = |\partial/\partial z||\partial/\partial\phi|$ obeys the Einstein field equation

$$\beta_{,\bar{t}\bar{t}} - \beta_{,\bar{r}\bar{r}} = 0 \,, \tag{2.13}$$

where commas denote partial derivatives. (This equation is the content of $R^z_z + R^\phi_\phi = 0$, where R^ν_μ is the Ricci tensor.) In Appendix A it is shown that, if (as we shall assume) space *initially* is *not* closed up radially by the shell's mass, then *everywhere* in the spacetime $\vec{\nabla}\beta$ is spacelike and is directed away from the symmetry axis. This together with Eq. (2.13) permits us, throughout the spacetime, to perform a conformal transformation in the $(\bar{t}, \bar{r})$ plane to new (t, r) coordinates such that $\beta = r$:

$$ds^2 = e^{2(\gamma-\psi)}(-dt^2 + dr^2) + e^{2\psi}dz^2 + r^2e^{-2\psi}d\phi^2 \,. \tag{2.14}$$

These are the coordinates discussed in Sec. 1.2.

Because the Einstein equation takes the form (2.13) only in vacuum and not on the shell itself, the conformal transformation turns out to be discontinuous across the shell. More specifically, although z, ϕ, $r = |\partial/\partial z||\partial/\partial\phi|$ and $\psi = \frac{1}{2}\ln|\partial/\partial z|$ (being Killing-defined quantities) are continuous across the shell, the time coordinate t and the metric function γ are discontinuous.

The Killing coordinate length z is defined only up to an arbitrary multiplicative factor. It should be obvious that a rescaling of z produces the following changes in other quantities:

$$z \to e^\mu z, \quad \psi \to \psi - \mu, \quad r \to e^{-\mu}r, \quad t \to e^{-\mu}t, \tag{2.15}$$

where μ is an arbitrary constant; and correspondingly,

$$\lambda \to e^{-\mu}\lambda, \quad R \to e^{-\mu}R \,. \tag{2.16}$$

In the vacuum inside and outside the shell, the metric coefficients $\psi(t, r)$ and $\gamma(t, r)$ satisfy the Einstein field equations[10, 11]

$$\psi_{,tt} - \frac{1}{r}(r\psi_{,r})_{,r} = 0 \,, \tag{2.17}$$

$$\gamma_{,r} = r[(\psi_{,t})^2 + (\psi_{,r})^2] \,, \tag{2.18}$$

$$\gamma_{,t} = 2\psi_{,t}\psi_{,r} \,. \tag{2.19}$$

Smoothness of the spacetime geometry on the symmetry axis $r = 0$ requires that

$$\gamma = 0 \text{ and } \psi \text{ finite at } r = 0. \tag{2.20}$$

We shall sometimes refer to ψ as the *gravitational-wave field* since it satisfies the wave equation (2.17) and it governs distortions of the geometry along the polarization axes (z and ϕ directions) in the usual "transverse-traceless" manner[13] (a weak ripple $\delta\psi$ in ψ produces fractional metric perturbations $\delta g_{zz}/g_{zz} = \delta\psi$, $\delta g_{\phi\phi}/g_{\phi\phi} = -\delta\psi$ that are confined to the transverse plane and are equal and opposite along the two transverse directions).

The quantity γ and the C-energy $\mathcal{C}$ are monotonic functions of each other,[11, 12]

$$\mathcal{C} = \frac{1}{8}(1 - e^{-2\gamma}) . \tag{2.21}$$

2.2 Description of the shell

The evolution of the shell will be characterized by $R(\tau)$, where R is the value of the radial coordinate r at the shell's location and τ is the proper time of an observer riding with the shell, but not rotating with the shell's particles. We sometimes will use $\mathcal{R} = Re^{-\psi_s}$ = circumference/2π to describe the shell's location, instead of R; here ψ_s is the value of ψ at the shell.

As an aid in analyzing the shell's properties and motion, it will be helpful to introduce the proper reference frame of an observer riding on the shell. This frame's orthonormal tetrad is the following:

$$\begin{aligned}
\vec{e}_\tau &\equiv \frac{d}{d\tau} \equiv \vec{u} = \text{4-velocity of the shell} \\
&= X_\pm \frac{\partial}{\partial t_\pm} + V \frac{\partial}{\partial r} , && (2.22) \\
\vec{e}_n &\equiv \frac{d}{dn} \equiv \vec{n} = \text{outward unit vector normal to shell} \\
&= X_\pm \frac{\partial}{\partial r} + V \frac{\partial}{\partial t_\pm} , && (2.23) \\
e_{\hat{z}} &\equiv \frac{1}{e^{\psi_s}} \frac{\partial}{\partial z} , && (2.24) \\
e_{\hat{\phi}} &\equiv \frac{1}{re^{-\psi_s}} \frac{\partial}{\partial \phi} . && (2.25)
\end{aligned}$$

Here

$$V \equiv \frac{dR}{d\tau} \tag{2.26}$$

and

$$X_\pm \equiv \frac{dt_\pm}{d\tau} = \sqrt{e^{-2(\gamma_\pm - \psi_s)} + V^2} \ . \tag{2.27}$$

The subscripts + and − are used to denote quantities evaluated on the outer and inner faces of the shell. (Recall that t and γ are discontinuous across the shell.)

As was discussed in Sec. 1.2, the shell is made of counter-rotating particles with conserved angular momenta per unit rest mass $\pm\alpha$, and with linear velocities $\pm v$ as measured in the shell's rest frame (2.22)–(2.25) and linear momenta per unit rest mass

$$\pm u = \frac{\pm v}{\sqrt{1-v^2}} = \pm\frac{\alpha}{\mathcal{R}} = \pm\frac{\alpha}{Re^{-\psi_s}} \ . \tag{2.28}$$

The shell's conserved rest mass per unit Killing length z is λ, and correspondingly its total mass per unit proper area as measured in its own rest frame (2.22)–(2.25) is

$$\sigma = \frac{\lambda}{2\pi R}\frac{1}{\sqrt{1-v^2}} = \frac{\lambda\sqrt{1+u^2}}{2\pi R} \ . \tag{2.29}$$

By their orbital motion, the particles create a surface stress $S^{\hat\phi\hat\phi} = T$ whose ratio to their surface energy density $S^{\tau\tau} = \sigma$ is

$$\frac{T}{\sigma} = \frac{S^{\hat\phi\hat\phi}}{S^{\tau\tau}} = \left(\frac{p^{\hat\phi}}{p^\tau}\right)^2 = \frac{u^2}{1+u^2} \tag{2.30}$$

[where $p^{\hat\phi} = \pm u$ is a particle's linear momentum per unit rest mass and $p^\tau = 1/\sqrt{1-v^2} = \sqrt{1+u^2}$ is its total mass per unit rest mass as measured in the shell's rest frame]. By combining Eqs. (2.29) and (2.30) we see that

$$T = \frac{\lambda u^2}{2\pi R\sqrt{1+u^2}} \ . \tag{2.31}$$

The shell's full surface stress-energy tensor is

$$\mathbf{S} = \sigma\vec{u}\otimes\vec{u} + T\vec{e}_{\hat\phi}\otimes\vec{e}_{\hat\phi} \ . \tag{2.32}$$

Israel[9] has shown that the Einstein field equations for a thin shell reduce to

$$K^+_{\alpha\beta} - K^-_{\alpha\beta} = 8\pi(S_{\alpha\beta} - \frac{1}{2}S^\mu_\mu\gamma_{\alpha\beta}) \ , \tag{2.33}$$

where $K^\pm_{\alpha\beta}$ is the extrinsic curvature of the shell's outer (inner) face and $\gamma_{\alpha\beta}$ is the metric of its world sheet. For our thin shell, the zz component of these junction

conditions reduces to a jump condition on the normal derivative of the gravitational wave field,

$$\psi_{+,n} - \psi_{-,n} = -\frac{2\lambda}{R\sqrt{1+u^2}} \; ; \tag{2.34}$$

the $\phi\phi$ component, after use of Eq. (2.34), reduces to a jump condition for $X = dt/d\tau$ and therefore [cf. Eq. (2.27)] for the time coordinate t and the metric function γ

$$X_+ - X_- = -4\lambda\sqrt{1+u^2} \; ; \tag{2.35}$$

and the $\tau\tau$ component reduces to an equation of motion for the shell

$$\begin{aligned} A \equiv \frac{d^2R}{d\tau^2} \;\; &= \;\; V\psi_{s,\tau} - R[(\psi_{s,\tau})^2 + (\psi_{-,n})^2] + X_- \frac{\psi_{-,n}}{1+u^2} \\ &\quad - \frac{X_-\lambda}{R(1+u^2)^{3/2}} + \frac{X_-X_+u^2}{R(1+u^2)} \; . \end{aligned} \tag{2.36}$$

(In deriving Eq. (2.36), the vacuum field equations (2.17)–(2.19) and the junction conditions (2.34), (2.35) have been used.)

In summary, Eq. (2.36) governs the motion of the shell; Eqs. (2.17)–(2.19) and (2.20) govern the evolution of the metric functions $\gamma(r,t), \psi(r,t)$; and the junction conditions (2.34), (2.35) match the metric functions across the shell. Among the various functions that we use, r, z, ϕ, ψ, $\psi_{,\tau}$ are continuous and t, γ, $\psi_{,n}$, X are discontinuous across the shell.

3 MOMENTARILY STATIC AND RADIATION-FREE CONFIGURATIONS

If the configuration, at some moment of time t, is momentarily static ($V = dR/d\tau = 0$) and radiation-free ($\psi_{,t} = \psi_{,tt} = 0$), i.e., MSRF, then it will have the following properties: (i) In the vacuum outside the shell the vacuum field equations (2.17)–(2.19) imply

$$\psi \;\; = \;\; \psi_s - \kappa \ln(r/R) \text{ at } r > R \; , \tag{2.37}$$

$$\gamma \;\; = \;\; \gamma_+ + \kappa^2 \ln(r/R) \text{ at } r > R \; , \tag{2.38}$$

where κ and ψ_s are constants. This is the *Levi-Civita line-mass solution* to the Einstein equations.[14] (ii) In the vacuum interior, the field equations imply a similar logarithmic form for ψ and γ, and the boundary conditions (2.20) at $r = 0$

imply a vanishing value of κ and correspondingly

$$\psi = \psi_s\,, \quad \gamma = 0 \ \text{ at } r < R\,, \tag{2.39}$$

which means that spacetime is flat and Minkowskiian inside the shell. (*iii*) The jump condition (2.34) on the normal derivative of ψ, together with Eqs. (2.23), (2.34), (2.35) and (2.39), implies that the value of the parameter κ is

$$\kappa = \frac{2\Lambda}{(1 - 4\Lambda\sqrt{1+u^2})\sqrt{1+u^2}} \tag{2.40}$$

(where $\Lambda = \lambda e^{-\psi_s}$ is the rest mass per unit proper length; cf. Sec. 1.2). (*iv*) The jump condition (2.35) on $X_\pm$, together with expressions (2.27) and (2.39), implies that

$$\gamma_+ = -\ln(1 - 4\Lambda\sqrt{1+u^2})\,. \tag{2.41}$$

In order that space not be closed radially by the shell's mass, it must be that $\Lambda\sqrt{1+u^2} < 1/4$ (see Appendix B for a proof and Sec. 1.4 for discussion); correspondingly, γ_+ is real and positive, and κ is positive. (*v*) The equation of motion (2.36) for the shell, when combined with $V = 0$, $\psi_{-,n} = 0$, $\Lambda = \lambda e^{-\psi_s}$, and Eqs. (2.27) and (2.41), takes the form

$$A = \frac{d^2R}{d\tau^2} = \begin{pmatrix}\text{positive}\\ \text{quantity}\end{pmatrix} \times [\Lambda_{\text{eq}}(u) - \Lambda]\,, \tag{2.42}$$

where $\Lambda_{\text{eq}}(u) \equiv u^2\sqrt{1+u^2}/(1+2u^2)^2$; cf. Eq. (2.8).

Therefore, if the rest mass per unit proper length Λ is greater than Λ_{eq}, then the MSRF shell starts contracting, and if Λ is lower than Λ_{eq}, it starts expanding.

In our analysis of dynamical shells (Sec. 1.5 above) a central role is played by C-energy. For a MSRF configuration with shell radius R and with the Killing coordinate z so normalized that

$$\psi_0 \equiv \psi(r_0) = 0 \tag{2.43}$$

[cf. Eq. (2.15)], the total C-energy inside some fixed radius $r_0 > R$ is given by

$$\mathcal{C}_{\text{MSRF}}(R) = \frac{1}{8}(1 - e^{-2\gamma_0}) \tag{2.44}$$

[Eq. (2.21)], where

$$e^{\gamma_0} = \frac{y^{-\kappa^2}}{1 - 4\lambda y^\kappa\sqrt{1 + (\alpha/r_0)^2 y^{-2-2\kappa}}}\,, \tag{2.45}$$

$$y = R/r_0 < 1 \ , \tag{2.46}$$

$$\kappa = \frac{2\lambda y^\kappa}{[1 - 4\lambda y^\kappa \sqrt{1 + (\alpha/r_0)^2 y^{-2-2\kappa}}]\sqrt{1 + (\alpha/r_0)^2 y^{-2-2\kappa}}} \tag{2.47}$$

cf. Eqs. (2.37)–(2.42) and (2.28).

A MSRF configuration will be nearly Newtonian if its mass per unit proper length Λ is small and its dust particles orbit around the axis with a small velocity,

$$\Lambda = \lambda e^{-\psi_s} = \lambda y^\kappa \ll 1 \ , \tag{2.48}$$

$$u = \frac{\alpha}{R e^{-\psi_s}} = \frac{\alpha}{r_0} y^{-1-\kappa} \ll 1 \ . \tag{2.49}$$

If, in addition, the Newtonian potential difference between $r = r_0$ and $r = R$ is small

$$\Lambda \ln(r_0/r) \ll 1 \ , \tag{2.50}$$

then throughout the region $r \lesssim r_0$ the configuration's gravity can be approximated by Newtonian theory, and the relativistic equations (2.43)–(2.47) reduce to

$$\kappa = 2\lambda \ , \tag{2.51}$$

$$\mathcal{C}_{MSRF} = \lambda + 2\lambda^2 + \frac{\lambda\alpha^2}{2R^2} + \lambda^2 \ln\left(\frac{R}{r_0}\right) \ . \tag{2.52}$$

Since, in this Newtonian situation, $\lambda \simeq \Lambda$ and $R \simeq \mathcal{R}$, expression (2.52) for the C-energy $\mathcal{C}_{MSRF}(R)$ is the same as Eq. (2.3) for the Newtonian energy per unit length $\mathcal{C}_{MS}(\mathcal{R})$.

A relativistic MSRF configuration will be in permanent, static equilibrium if and only if $A = d^2R/d\tau^2 = 0$, i.e., if and only if $\Lambda = \Lambda_{\rm eq}(u)$; cf. Eqs. (2.42) and (2.8), Fig. 2.2, and the discussion in Sec. 1.4.

An alternative, equivalent criterion for equilibrium involves C-energy: Choose an arbitrary radius r_0 and for concreteness adjust the scale of z [Eq. (2.15)] so that proper length and Killing length coincide at r_0, i.e. so Eq. (2.43) is satisfied. Then *among all MSRF configurations with fixed α and λ and with $R < r_0$, the ones that are in equilibrium are those that extremize $\mathcal{C}_{\rm MSRF}$ with respect to variations of R. Moreover, every one of these extrema is a minimum of $\mathcal{C}_{\rm MSRF}$.* (In Sec. 4 we shall prove that for the situations of interest in this paper, there is precisely one minimum.)

These properties of equilibria can be proved as follows:

Since $\mathcal{C}_{\rm MSRF} = \frac{1}{8}(1 - e^{-2\gamma_0})$ is a monotonically increasing function of γ_0, it suffices to prove these properties for γ_0 instead of $\mathcal{C}_{\rm MSRF}$. Consider the first-order change $d\gamma_0$ of γ_0 caused by a change dR of R. Equation (2.38) implies that

$$d\gamma_0 = d\gamma_+ + 2\kappa \ln(r_0/R)d\kappa - \kappa^2 dR/R \,, \tag{2.53}$$

where by (2.37) and (2.43)

$$\ln(r_0/R)d\kappa = \kappa dR/R + d\psi_s \,, \tag{2.54}$$

and by (2.40), (2.41), with $\Lambda = \lambda e^{-\psi_s}$ and $u = \alpha/Re^{-\psi_s}$,

$$d\gamma_+ = -2\kappa d\psi_s - 2\kappa u^2 dR/R \,. \tag{2.55}$$

By combining Eqs. (2.53), (2.54), (2.55) we obtain

$$d\gamma_0 = \kappa(\kappa - 2u^2)dR/R \,, \tag{2.56}$$

so γ_0 is extremized if and only if $\kappa = 2u^2$. By virtue of Eq. (2.40) for κ, this is equivalent to $\Lambda = \Lambda_{\rm eq}(u)$. Thus, the equilibria are the MSRF configurations that extremize γ_0, as claimed.

To show that these equilibria actually minimize γ_0, we compute the second order change $d^2\gamma_0$ produced by dR when $\Lambda = \Lambda_{\rm eq}(u)$, i.e., when $\kappa = 2u^2$. Equation (2.56) implies that

$$d^2\gamma_0 = \kappa \frac{dR}{R}(d\kappa - 4u\, du) \,. \tag{2.57}$$

By combining with Eqs. (2.54), (2.40), (2.8), $\Lambda = \lambda e^{-\psi_s}$, and $u = \alpha/Re^{-\psi_s}$ and performing a series of manipulations, we bring this into the form

$$\begin{aligned} d^2\gamma_0 \;=\; & 2u^2 \left(\frac{dR}{R}\right)^2 \frac{1+2u^2}{\ln(r_0/R)} \Bigg[1 - [1 - 4u^2 \ln(r_0/R)] \\ & \times \frac{1 + 2u^2 \ln(r_0/R)(1+2u^2)}{1 + 2u^2 \ln(r_0/R)[1 + 4u^2 + u^2/(1+u^2)]}\Bigg] \,. \end{aligned} \tag{2.58}$$

The last fraction is obviously less than unity, and this implies that $d^2\gamma_0$ is positive and thus γ_0 and hence $\mathcal{C}_{\rm MSRF}$ is minimized by the equilibrium configurations. *QED.*

4 QUALITATIVE FORM OF C-ENERGY FOR MSRF CONFIGURATIONS

Of special interest for analyzing the dynamical evolution of a shell (Sec. 1.5) is the form of $\gamma_0(R)$ and thence $\mathcal{C}_{\rm MSRF}(R)$, when the outer radius r_0 is chosen arbitrarily

large and the shell's initial configuration is MSRF with some specific initial values $\mathcal{R}_i$ of $\mathcal{R}$ and Λ_i of Λ. In this case the initial configuration has a mass per unit Killing length λ and a value κ_i of κ given by [cf. Eqs. (2.43), (2.37), (2.40), (2.28), and $\Lambda = \lambda e^{-\psi_s}$, $\mathcal{R} = Re^{-\psi_s}$]

$$\lambda = \Lambda_i (r_0/\mathcal{R}_i)^{\kappa_i/(1+\kappa_i)} , \tag{2.59}$$

$$\kappa_i = \frac{2\Lambda_i}{(1 - 4\Lambda_i\sqrt{1+\alpha^2/\mathcal{R}_i^2})\sqrt{1+\alpha^2/\mathcal{R}_i^2}} . \tag{2.60}$$

Since $r_0/\mathcal{R}_i$ is arbitrarily large and κ_i is positive, λ is also arbitrarily large. With λ being arbitrarily large and $\propto r_0^{\kappa_i/(1+\kappa_i)}$, it becomes fairly straightforward to deduce the qualitative form of $\gamma_0(R)$ and thence $\mathcal{C}_{\rm MSRF}(R)$:

These two functions of R are given explicitly by Eqs. (2.43)–(2.47). By examining these equations one can show[15] that the only places where $\gamma_0 \to \infty$ (for r_0 arbitrarily large) are at $R \to r_0$ and $R \to 4\lambda\alpha$. Since γ_0 is always positive and the only extrema of $\gamma_0(R)$ are minima (cf. Sec. 3) , this implies that as R varies from $R_{\rm abs\ min} = 4\lambda\alpha$ to r_0, $\gamma_0(R)$ decreases from ∞ to a single, unique minimum at some $R = R_{\rm eq}$, and then increases to ∞ at $R = r_0$. Correspondingly, $\mathcal{C}_{\rm MSRF}(R)$ [Eq. (2.44)] decreases monotonically from its maximum allowed value of 1/8 at $R_{\rm abs\ min} = 4\lambda\alpha$ to a minimum at $R_{\rm eq}$ and then increases monotonically back to 1/8 at $R = r_0$. This is the qualitative behavior that we stated and used in discussing the dynamics of a shell in Sec. 1.5.

5 C-ENERGY OF DYNAMICAL CONFIGURATIONS

We are now ready to prove that *the C-energy of a dynamical configuration is always greater than that of a MSRF configuration that has the same α, λ, R and $\psi_0 \equiv \psi(r_0) = 0$, but different V, $\psi(r)$, and $\psi_{,t}(r)$* [Eq. (2.9)]. Since $\mathcal{C}_0$ is a monotonically increasing function of γ_0, it suffices to prove that γ_0 has this property, or equally well that $e^{-\gamma_0}$ is always smaller for a dynamical configuration than for the corresponding MSRF one. In our proof we shall denote $\dot{\psi} \equiv \psi_{,t}$ and $\psi' \equiv \psi_{,r}$.

Proof: We proceed in two steps. *First*, we hold the dynamical configuration's $\psi(r)$ and $\dot{\psi}(r)$ fixed and vary only its shell velocity V. From the junction condition (2.35), Eq. (2.27), and $\Lambda = \lambda e^{-\psi_s}$, it follows that

$$e^{-\gamma_+} \le e^{-\gamma_-} - 4\Lambda\sqrt{1+u^2} , \tag{2.61}$$

with the equality holding if and only if $V = 0$. Combining this with the field equation (2.18) and boundary condition (2.20), we learn that, when V is varied, $e^{-\gamma_0}$ takes on an absolute maximum value at $V = 0$. The value of that maximum is

$$e^{-\gamma_0}|_{V=0} = I \equiv J(K - 4\Lambda\sqrt{1+u^2}) \,, \tag{2.62}$$

where

$$K \equiv e^{-\gamma_-} = \exp\left[-\int_0^R r(\dot{\psi}^2 + \psi'^2)\, dr\right] \,, \tag{2.63}$$

$$J \equiv \exp\left[-\int_R^{r_0} r(\dot{\psi}^2 + \psi'^2)\, dr\right] \,. \tag{2.64}$$

In our *second* step, we hold $V = 0$ and ask how $e^{-\gamma_0} = I$ changes as we vary $\psi(r)$ and $\dot{\psi}(r)$. It is straightforward to compute the first order change δI of I around any configuration [any $\psi(r)$ and $\dot{\psi}(r)$], with α, λ, R, $V = 0$, r_0, $\psi_0 \equiv \psi(r_0) = 0$, and $\dot{\psi}_0 \equiv \dot{\psi}(r_0) = 0$ held fixed, and with $\Lambda = \lambda e^{-\psi_s}$, $u = \alpha e^{\psi_s}/R$ and the junction condition (2.34) imposed. The result is

$$\delta I = -2I\int_R^{r_0} \left(r\dot{\psi}\delta\dot{\psi} - (r\psi')'\delta\psi\right) dr - 2JK\int_0^R \left(r\dot{\psi}\delta\dot{\psi} - (r\psi')'\delta\psi\right) dr \,, \tag{2.65}$$

which implies that I is extremal ($\delta I = 0$) if and only if $\dot{\psi} = 0$ and $(r\psi')' = 0$, i.e. if and only if the configuration is MSRF. In fact, the extremum of I is a maximum, as one can show by computing its second variation [using in the computation the fact that the junction conditions (2.34), (2.35) must be satisfied by the perturbed configuration as well as the MSRF one]:

$$\begin{aligned} \delta^2 I \;=\; & -2I\int_R^{r_0} r(\delta\dot{\psi}^2 + \delta\psi'^2)\, dr - 2JK\int_0^R r(\delta\dot{\psi}^2 + \delta\psi'^2)\, dr \\ & -4J(\delta\psi_s)^2 \frac{\Lambda}{(1+u^2)^{3/2}}\left[1 + 2u^2 + \frac{4\Lambda\sqrt{1+u^2}}{1 - 4\Lambda\sqrt{1+u^2}}\right] < 0 \,. \end{aligned} \tag{2.66}$$

To recapitulate, in our first step we found that, when V is varied with $\dot{\psi}(r)$ and $\psi(r)$ held fixed at any values one wishes, then $e^{-\gamma_0}$ reaches an absolute maximum, $e^{-\gamma_0} = I$, at $V = 0$. Then in the second step we found that when V is held equal to zero and $\dot{\psi}(r)$ and $\psi(r)$ are varied, $e^{-\gamma_0} = I$ reaches an absolute maximum when $\dot{\psi}(r)$ and $\psi(r)$ assume their MSRF values. Therefore, among all configurations with fixed α, λ, R, and $\psi_0 = 0$, the MSRF has the absolute maximum value of $e^{-\gamma_0}$ and the absolute minimum C-energy $\mathcal{C}_0$. *QED*.

This extremal property of the C-energy, together with the properties of $\mathcal{C}_{\rm MSRF}(R)$ derived in Secs. 3 and 4, are all that we needed in Sec. 1.5 to infer the qualitative, dynamical evolution of the shell—with one exception: We also needed the

fact that the gravitational waves emitted by the shell's oscillations carry away C-energy. This we prove in the next section.

6 C-ENERGY OUTFLOW

The rate of change of the C-energy $\mathcal{C} = \frac{1}{8}(1 - e^{-\gamma})$ inside a radius r is given by

$$\mathcal{C}_{,t} = \frac{1}{8}e^{-\gamma}\gamma_{,t} = \frac{1}{4}e^{-\gamma}\psi_{,t}\psi_{,r} \ , \tag{2.67}$$

cf. Eq. (2.19). We shall now show that at any radius $r \gg R$, $\psi_{,t}\psi_{,r}$ is negative and thus $\mathcal{C}_{,t} < 0$, which means that the waves carry away C-energy.

The general outgoing-wave solution of the wave equation (2.17) is

$$\psi = \Re \int_0^\infty A(\omega)e^{-i\omega t}H_0^{(1)}(\omega r)\, d\omega \ , \tag{2.68}$$

where $\Re$ denotes the real part and $H_m^{(1)}(x)$ is the Hankel function of the first kind. Therefore,

$$\psi_{,t} = \Re \int_0^\infty -i\omega A(\omega)e^{-i\omega t}H_0^{(1)}(\omega r)\, d\omega \ , \tag{2.69}$$

and

$$\psi_{,r} = \Re \int_0^\infty -\omega A(\omega)e^{-i\omega t}H_1^{(1)}(\omega r)\, d\omega \tag{2.70}$$

Using the limit $H_m^{(1)}(x) \xrightarrow{x\gg 1} \sqrt{2/\pi x}\exp[i(x - m\pi/2 - \pi/4)]$, we see that

$$H_1^{(1)}(\omega r) \xrightarrow{\omega r\gg 1} -iH_0^{(1)}(\omega r) \ , \tag{2.71}$$

which implies that the contributions from all frequencies $\omega \gg 1/r$ satisfy $\psi_{,t} = -\psi_{,r}$ and thence $\psi_{,t}\psi_{,r} < 0$ as was to be proved. But what about contributions from $\omega \lesssim 1/r$? Because ψ is always finite and $\int_0^{x_0} x^n H_0^{(1)}(x)dx$ converges only for $n > -1$, it is always the case that as $\omega \to 0$, $A(\omega) \sim \omega^n$ with $n > -1$. This implies that the low-frequency, $\omega \lesssim 1/r$, contributions to $\psi_{,t}$ and $\psi_{,r}$ are

$$\psi_{,t}(\omega \lesssim 1/r) \sim \psi_{,r}(\omega \lesssim 1/r) \sim \frac{1}{r^{2+n}} \ , \tag{2.72}$$

which are negligible compared to the $O(1/\sqrt{r})$ contributions from $\omega \gg 1/r$ when r is sufficiently large. Thus, for large r the waves necessarily carry C-energy outward through radius r ($\mathcal{C}_{,t} \equiv \frac{1}{4}e^{-\gamma}\psi_{,t}\psi_{,r} < 0$). *QED*.

7 CONCLUSIONS

In Secs. 3—6 we have derived all the properties of the C-energy that were needed, in Sec. 1, to infer the dynamical evolution of a thin, cylindrical shell of counter-rotating dust: By giving the dust particles arbitrarily small amounts of angular momentum per unit mass, we guarantee that centrifugal forces will convert the shell's collapse into a bounce, thereby preventing formation of a singularity. After its bounce, the shell will oscillate radially, and then as gravitational waves carry away C-energy, it will settle down into a static, equilibrium state.

ACKNOWLEDGEMENTS

One of the authors (KST) thanks Richard Bonham for hospitality in the southern Selous Game Preserve, Tanzania, where much of this paper was written. This research was supported in part by the National Science Foundation Grant AST88-17792.

APPENDIX A: RADIAL NONCLOSURE OF SPACE

In this appendix we show that, if the space around an initial, MSRF configuration is not closed radially, then throughout the shell's spacetime to the future of the initial configuration, we can introduce coordinates (t, r, z, ϕ) in which the line element takes the canonical form (2.1) with $0 \leq r < \infty$.

The proof begins by introducing coordinates $(\bar{t}, \bar{r}, z, \phi)$ in which the line element takes the form (2.12). Such coordinates are permitted throughout any cylindrically symmetric spacetime with vanishing net momentum density along the Killing directions.[10, 11]

Following Thorne[11], we define the *character* of spacetime at any event to be $D^{(+)}$ if $\vec{\nabla}\beta$ is spacelike and points away from the symmetry axis, $D^{(-)}$ if $\vec{\nabla}\beta$ is spacelike and points toward the symmetry axis, $D^{(01)}$ if $\vec{\nabla}\beta$ is timelike and points toward the future, and $D^{(01)}$ if $\vec{\nabla}\beta$ is timelike and points toward the past. [Recall that $\beta = |\partial/\partial z||\partial/\partial\phi|$; cf. Eq. (2.12).] The vacuum field equation $\beta_{,\bar{t}\bar{t}} - \beta_{,\bar{r}\bar{r}} = 0$ [Eq. (2.13)] implies that spacetime can change character only on radial null surfaces, which Thorne[11] calls *critical surfaces*, or across the nonvacuum dust

shell.

The nature of the character change across any critical surface is constrained by the geometric optics focusing equation for radial null geodesics (Eq. (22.37) of MTW[4]). This equation implies that β can never have a minimum along any ingoing or outgoing radial null geodesic; and this, in turn, implies that the only kinds of (vacuum) critical surfaces that can ever exist are these: An outgoing null surface with spacetime character $D^{(-)}$ in the past and $D^{(0\downarrow)}$ in the future or with $D^{(0\uparrow)}$ in the past and $D^{(+)}$ in the future, and an ingoing null surface with character $D^{(+)}$ in the past and $D^{(0\downarrow)}$ in the future or with $D^{(0\uparrow)}$ in the past and $D^{(-)}$ in the future.

The nature of any character change across the dust shell is constrained by the junction condition for the $\phi\phi$ component of the extrinsic curvature [generalization of Eq. (2.35) to the case where spacetime is not necessarily $D^{(+)}$ on both sides of the shell]. This junction condition says

$$\beta_{+,n} - \beta_{-,n} = -4\lambda\sqrt{1+u^2} < 0 \; . \tag{2.73}$$

Since $\beta_{,\tau}$ is continuous across the shell and $\vec{\nabla}\beta = \beta_{,\tau}\vec{e}_\tau + \beta_{,n}\vec{e}_n$ (where the notation is that of Sec. 2.2, generalized to the case where the spacetime character is not necessarily $D^{(+)}$ everywhere), Eq. (2.73) implies that, as one moves from the shell's interior to its exterior (its "$-$" side to its "$+$" side), the only allowed character changes are $D^{(+)}$ to any other character, and $D^{(0\uparrow)}$ or $D^{(0\downarrow)}$ to $D^{(-)}$.

By hypothesis, there is an initial MSRF configuration in which space is not radially closed. The fact that this configuration is momentarily static implies that nowhere on its spacelike hypersurface can spacetime have character $D^{(0\uparrow)}$ or $D^{(0\downarrow)}$; radial nonclosure means the character must be $D^{(+)}$ far outside the shell; and smoothness of spacetime near the symmetry axis implies character $D^{(+)}$ there. These constraints on character, together with the constraints on character change listed in the preceding two paragraphs, imply that on the initial hypersurface the character is everywhere $D^{(+)}$.

As the spacetime evolves forward off the initial hypersurface, the only way any change of character could occur would be if a future directed, ingoing or outgoing critical surface were to be created at some moment at the shell's location. By examining various hypothetical character changes across such a critical surface and across the shell to its future, one discovers that there are no patterns of character change that satisfy the above constraints. Therefore, the spacetime character must remain $D^{(+)}$ throughout the future of the initial hypersurface . *QED.*

APPENDIX B: RADIAL NONCLOSURE FOR MSRF CONFIGURATIONS

Inside any MSRF configuration, spacetime is flat and therefore, in the notation of Sec. 2.2 and Appendix A, $\beta_{-,n} = e^{\psi_s}$. This, together with $\Lambda = \lambda e^{-\psi_s}$ and the junction condition (2.73), implies that

$$e^{-\psi_s}\beta_{+,n} = 1 - 4\Lambda\sqrt{1+u^2}\,. \tag{2.74}$$

In order for space to be radially non-closed outside the shell, the character must be $D^{(+)}$ there rather than $D^{(-)}$ (these are the only possibilities for a MSRF configuration, cf. Appendix A); this corresponds to the requirement that $\beta_{+,n}$ must be positive and not negative; and this, by virtue of Eq. (2.74), corresponds to $\Lambda\sqrt{1+u^2} < 1/4$. Thus, for a MSRF configuration space will be radially nonclosed (character $D^{(+)}$ everywhere) if $\Lambda\sqrt{1+u^2} < 1/4$, and radially closed (character $D^{(-)}$ outside the shell) if $\Lambda\sqrt{1+u^2} > 1/4$.

Bibliography

[1] S. L. Shapiro and S. A. Teukolsky, Phys. Rev. Lett. **66**, 994 (1991).

[2] R. Penrose, Revista del Nuovo Cimento **1**, special number, 252 (1969).

[3] K. S. Thorne, in *Magic Without Magic: John Archibald Wheeler*, ed. J. Klauder (Freeman, San Francisco, 1972), p. 231.

[4] C. W. Misner, K. S. Thorne, and J. A. Wheeler, *Gravitation* (Freeman, San Francisco, 1973), Box 32.3.

[5] K.S. Thorne, Comm. Astrophys. Space Sci., **2**, 191 (1970).

[6] F. Echeverria, paper in preparation.

[7] The conclusion that an infinitesimal amount of counterrotation will cause a thin, cylindrical dust shell to bounce was derived analytically by one of the authors (Thorne) in the early 1970s. T. L. Anderson and T. A. Morgan followed up Thorne's research by constructing numerical solutions to the equations of evolution for such a collapsing, bouncing shell. Thorne, Anderson, and Morgan announced their results in T. L. Anderson, T. A. Morgan and K. S. Thorne, Bull. Amer. Phys. Soc. **B17**, 516 (1972), but they never published the details. This paper presents a proof of Thorne's bounce result, as part of a much more thorough, C-energy based analysis of the dynamics of the thin shell recently worked out by Apostolatos.

[8] T. Piran, Phys. Rev. Lett. **41**, 1085 (1978).

[9] W. Israel, Nuovo Cimento **44B**, 1, and **48b**, 463; see also Sec. 21.13 of Ref. [4].

[10] A. Einstein and N. Rosen, J. Franklin Inst. **223**, 43 (1937).

[11] K. S. Thorne, unpublished Ph.D. thesis, Princeton University, 1965; available from University Microfilms Inc., Ann Arbor, Michigan.

[12] K. S. Thorne, Phys. Rev. **138**, B251 (1965). Note: The definition of C-energy used in this reference was $\mathcal{C} = \gamma/4$; in Ref. [11] the definition was changed to the one used in the present paper, $\mathcal{C} = (1/8)(1 - e^{-2\gamma})$. Because the two definitions are monotonic functions of each other, the analysis in the present paper would work with either definition.

[13] Ref. [4], chapter 35.

[14] T. Levi-Civita, Rend. Acc. Lincei **28**, 101 (1919).

[15] As $R \to r_0$ from below (as $y \to 1$ from below), Eq. (2.47) buffers κ [which is always positive since space is radially nonclosed, cf. Eq. (2.40) and Appendix B] into $4\lambda y^\kappa \simeq 1$, i.e. into $\kappa \simeq \ln(4\lambda)/\ln(y^{-1})$. Correspondingly [cf. Eq. (2.45)], as $y \to 1$, $\gamma_0 \to \infty$. At what other values of y, in the region $y < 1$, will $\gamma_0 \to \infty$? Equation (2.56) with $u = (\alpha/r_0)y^{-1-\kappa}$, implies that $\gamma_0 \to \infty$ only where $\kappa \to \infty$. But Eq. (2.47) with $y < 1$ implies that $\kappa \to \infty$ only when the term in square brackets goes to zero, which means only when $R \to 4\alpha\lambda$ from above.

Chapter 3

Gravitational radiation from a particle in circular orbit around a black hole. III: Stability of circular orbits under radiation reaction. [Co-authored with Daniel Kennefick, Amos Ori, and Eric Poisson]

(Originally appeared in Phys. Rev. D **47**, 5376 (1993).)

Abstract

We use the Teukolsky perturbation formalism to show that: (i) a particle in circular motion around a nonrotating black hole remains on a circular orbit under the influence of radiation reaction; and (ii) circular orbits are stable only if the orbital radius is greater than a critical radius $r_c \simeq 6.6792M$, where M is the mass of the black hole. A circular orbit is stable if, when slightly perturbed so that it acquires a small eccentricity, radiation reaction decreases the eccentricity; a circular orbit is unstable if radiation reaction increases the eccentricity. Our analysis is restricted by four major assumptions: (i) the black hole is nonrotating, (ii) the eccentricity is always small, (iii) the gravitational perturbations are linear, and (iv) the adiabatic approximation (that radiation reaction takes place over a timescale much larger than the orbital period) is valid. On the other hand, our analysis is not limited to weak-field, slow-motion situations; it is valid for particle motion in strong gravitational fields.

1 INTRODUCTION AND SUMMARY

1.1 Motivation

A particle of mass μ, which interacts with the gravitational field of an isolated object of mass M, does not, in general, move on a spacetime geodesic. This is due to the fact that the combined system emits gravitational waves; the problem of radiation reaction—to determine the influence of this emission on the motion of the particle—is a difficult one in general relativity.

Gravitational radiation reaction has a well-known electromagnetic analogue: A charged particle, accelerated by an electric field, does not move according to the Lorentz equations of the motion, because of the emission of electromagnetic waves. There are difficult conceptual problems associated with radiation reaction in electromagnetism [1]; however, these conceptual problems are not a serious impediment to computations, at least when radiation reaction is a small effect. The use of half retarded minus half advanced potentials, together with the rejection of runaway solutions on physical grounds, provide a well-defined calculational basis for most applications [2].

In contrast with the electromagnetic case, the problem of gravitational radiation reaction is plagued with conceptual *and* calculational difficulties, which are mostly due to the non-local character of the problem. Non-locality enters in essentially two different ways: (i) As a consequence of the principle of equivalence, a gravitational wave can be identified as such only in a region of spacetime larger than several wavelengths [3], which precludes the construction of a local radiative field. And (ii) due to the fact that gravitational waves are in general scattered by the curvature of spacetime, waves emitted at one time may influence the motion of the particle at some later time [4]; these *tails* in the waves can produce noticeable effects, most especially if curvature is large.

In order to gain insight into the general problem of gravitational radiation reaction, it is important to look at simple special cases for which the above problems can be addressed. To study such a simple case is the main purpose of this paper.

The question of radiation reaction is most pressing in the context of the late evolution of compact binary systems [5], since the waves generated by such systems are the most promising for detection by kilometer-size interferometric detectors [6]. Extraction of the information encoded in the waves will require an accurate calculation of the expected waveforms [7]; these theoretical waveforms are used as matched filters through which the detected signal is processed [8]. Radiation re-

action governs the rate at which the wave frequency increases with time, as the compact objects spiral together toward coalescence. During the last stages of evolution, when the waves are most interesting for detection, the wave frequency sweeps from approximately 10 Hz to several hundred Hz in just a few minutes, during which the waves oscillate about 10^4 times. It is therefore essential to incorporate radiation reaction, to a fractional accuracy of at least 10^{-4}, into the calculation of the theoretical waveforms [7]. Thus, the practical importance of radiation reaction in the evolution of compact binary systems provides more motivation for the work presented here.

Also of interest are the last stages of evolution, under radiation reaction, of a solar-mass compact object orbiting a galactic, supermassive black hole. Such a binary system could be observed with an eventual space-based interferometric detector, which would operate between 10^{-4} Hz and 10^{-1} Hz [9]. Because we consider small mass ratios (see subsection 1.2 below), the results presented in this paper are directly relevant to these sources.

Most of the work devoted so far to gravitational radiation reaction, in particular for the two-body problem, has been restricted to weak-field, slow-motion situations [3, 10, 11, 12, 13]. Lincoln and Will [12] have calculated, using post-Newtonian theory, the orbital motion of a binary system at post$^{5/2}$-Newtonian order, which only incorporates radiation reaction at leading order. These calculations are not accurate enough for the purpose of constructing matched filters for interferometric detectors [7]. Higher-order corrections to the post-Newtonian, radiation-reaction force have recently been calculated by Iyer and Will [13].

By comparison, very little has been done for strong-field situations. Gal'tsov [14] has laid the foundations for strong-field radiation-reaction calculations in the case of particle motion in the field of a Kerr black hole. His formalism is based on the notion of a local, gauge-dependent radiation-reaction force. However, Gal'tsov's only explicit calculation of this force was also restricted to weak-field, slow-motion situations. Finn, Ori, and Thorne [15] have studied the strong-field transition between inspiral and plunge motion in Kerr; however, their analysis does not require a detailed knowledge of radiation-reaction effects. In this paper, we present concrete results on radiation reaction in strong-field situations.

1.2 The problem, method of solution, and approximations

We study the effects of radiation reaction on the bound motion of a particle of mass μ in the geometry of a Schwarzschild black hole of mass M. Two quantities are of fundamental interest: the orbit's averaged radius r_0, and the orbit's eccentricity ε. The radius r_0 denotes the averaged value of the orbit's Schwarzschild radial coordinate; the maximal value of the orbital radius defines the eccentricity: $r_{\rm max} = r_0(1+\varepsilon)$. More precise definitions of r_0 and ε will be given in Sec. 2. We shall suppose that both the eccentricity ε and the mass ratio μ/M are much smaller than unity. However, we do not suppose that the radius r_0 is large, so our analysis includes strong-field situations.

We adopt the Teukolsky perturbation formalism [16], and consider the linear gravitational perturbations associated with the motion of the particle. The perturbations are described in terms of the complex Weyl scalar Ψ_4, which becomes radiative at large distances from the source. The rates of loss of orbital energy E, and orbital angular momentum L, due to gravitational radiation, can be calculated by solving the Teukolsky equation.

The *secular* evolution (the evolution over timescales much larger than the orbital period) of r_0 and ε can be determined from the knowledge of $\dot{E}$ and $\dot{L}$, where an overdot denotes time differentiation followed by an average over several orbital periods. In particular, the following relations can be derived (Sec. 2): $\dot{r_0} = \dot{r_0}(r_0, \dot{L})$, and $\dot{\varepsilon} = \dot{\varepsilon}(\varepsilon, r_0, \dot{E}, \dot{L})$. We shall use the perturbation formalism to calculate the rates of loss of energy and angular momentum. These calculations are performed (i) analytically, for the special case of weak fields and slow motions; and (ii) numerically, for the general case.

Our calculations are restricted to small eccentricities, $\varepsilon \ll 1$. The work presented in this paper can therefore be interpreted as a stability analysis: A circular orbit with radius r_0 is slightly perturbed and acquires a small eccentricity ε. The orbit evolves because of radiation reaction; the sign of $\dot{\varepsilon}$ determines whether the perturbed orbit is driven more circular, or more eccentric. Circular orbits are thus *stable* if $\dot{\varepsilon} < 0$, and are *unstable* if $\dot{\varepsilon} > 0$. Previous studies have shown that circular orbits are always stable in weak-field, slow-motion situations [11, 12]; our own study confirms this, and also determines whether this remains true in strong-field situations.

Recently, and independently of us, Tanaka *et al.* [17] numerically calculated

the gravitational waveforms, and the fluxes of energy and angular momentum at infinity, for orbits with *arbitrary* eccentricities. The differences between their analysis and ours are significant. Tanaka *et al.* are mostly concerned with what can be observed at infinity, and are not much concerned with radiation reaction. In particular, they do not calculate the fluxes of energy and angular momentum at the black-hole horizon, which we do here, and which is important for radiation reaction. We have become aware of the work by Tanaka *et al.* very shortly before submitting this paper for publication.

Our calculations are also restricted to small mass ratios. This condition comes from two requirements: (i) that the gravitational perturbations be small enough to be linear, which implies $\mu/M \ll 1$, and (ii) that the *adiabatic approximation* be valid. The adiabatic approximation supposes that radiation reaction takes place over a timescale which is much larger than the orbital period. We shall show below (Sec. 4.6) that this implies a restriction on μ/M; this restriction is not severe at large distances, but becomes $\mu/M \ll (1 - 6M/r_0)^{3/2}$ for r_0 approaching $6M$. The adiabatic approximation must therefore break down at $r_0 = 6M$, where, even without radiation reaction, circular orbits become unstable.

The adiabatic approximation is a fundamental feature of our analysis. It allows us to suppose that, over timescales comparable to the orbital period, the motion of the particle is, in fact, geodesic; non-geodesic behavior becomes noticeable only over much larger timescales. Moreover, the motion is also strictly periodic, and, consequently, the gravitational waves have a well-resolved frequency spectrum; the waves' frequencies change appreciably only over timescales much larger than the orbital period. Our problem is therefore one for which we first determine the rates of loss of energy and angular momentum for the slightly eccentric, geodesic motion of a particle around a Schwarzschild black hole, and then use these rates to infer the slow evolution of the orbit.

1.3 The results

Our analysis first allows us to prove that, if the particle's orbit is strictly circular ($\varepsilon = 0$), then radiation reaction produces a strictly circular evolution. In other words, *circular orbits remain circular under radiation reaction.* Previous proofs of this statement were restricted to weak-field, slow-motion situations [11, 12]; our proof is valid both for weak and strong fields.

If the eccentricity is small but not identically zero, our analysis shows that

radiation reaction (i) *decreases* the eccentricity if r_0 is larger than a certain critical value r_c, and (ii) *increases* the eccentricity if r_0 is smaller than r_c. Thus circular orbits are *stable* if $r_0 > r_c$, and *unstable* if $r_0 < r_c$. The point $r_0 = r_c$ corresponds to $\dot{\varepsilon}$ changing sign; we have estimated numerically that

$$r_c/M \simeq 6.6792. \tag{3.1}$$

Our results are most conveniently presented in terms of the dimensionless quantity $c(r_0)$, defined as

$$c(r_0) = \frac{r_0}{\dot{r}_0}\frac{\dot{\varepsilon}}{\varepsilon} = \frac{d\ln\varepsilon}{d\ln r_0}, \tag{3.2}$$

and which can be interpreted as the ratio of the *inspiral timescale* $r_0/|\dot{r}_0|$ (the timescale over which the orbital radius r_0 changes appreciably) over the *circularization timescale* $\varepsilon/|\dot{\varepsilon}|$ (the timescale over which the eccentricity changes appreciably). By virtue of the adiabatic approximation, both timescales are much larger than the orbital period. A plot of $c(r_0)$, obtained numerically, is given in Fig. 1.

For large r_0 (weak-field, slow-motion), $c(r_0)$ can be calculated analytically (Sec. 5.1), and takes the form

$$c(r_0) = \frac{19}{12}\Big[1 - \frac{3215}{3192}v^2 + \frac{377}{152}\pi v^3 + O(v^4)\Big], \tag{3.3}$$

where $v = (M/r_0)^{1/2} \ll 1$ acts as a post-Newtonian expansion parameter. The leading-order term of Eq. (3.3) corresponds to a Newtonian calculation of the orbit, together with the use of the quadrupole formula to determine $\dot{r}_0$ and $\dot{\varepsilon}$ [11]. The first-order correction (at post-Newtonian, v^2, order) corresponds to post-Newtonian corrections to the orbital motion. The second-order correction (at post$^{3/2}$-Newtonian, v^3, order) corresponds to effects due to the propagation of the gravitational waves in the field of the black hole—effects associated with the tails of the waves.

For values of r_0 approaching $6M$ (highly relativistic situation; Sec. 5.2), $c(r_0)$ behaves according to

$$c(r_0 \to 6M) \sim -\frac{1}{4}(1 - 6M/r_0)^{-1}, \tag{3.4}$$

and therefore grows to arbitrarily large, negative values. This behavior is a consequence of the fact that circular orbits, even without radiation reaction, become unstable at $r_0 = 6M$. We recall that the limit $r_0 \to 6M$ must be taken with care, in view of the adiabatic approximation; orbits arbitrarily close to $r_0 = 6M$ can be considered at the price of taking μ/M sufficiently small.

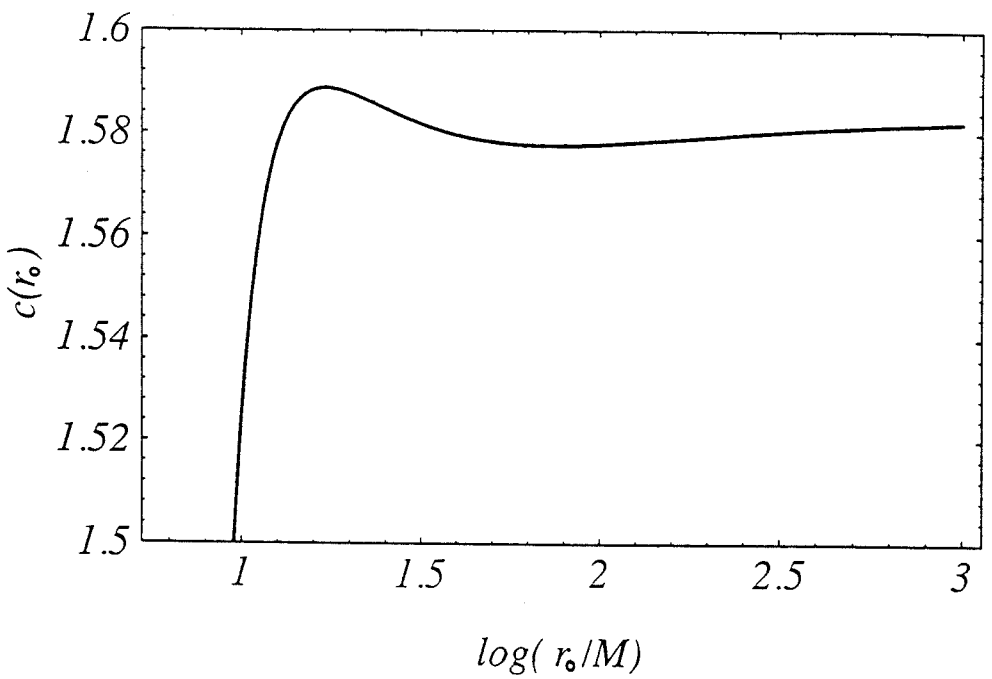

Figure 3.1: A plot of $c(r_0)$, as defined in Eq. (3.2), as a function of $\log r_0/M$. Shown is the range $10 \lesssim r_0/M < 1000$, in which $c(r_0)$ has the most interesting behavior. For $r_0/M > 1000$, $c(r_0)$ is well approximated by Eq. (3.3), and approaches the value $19/12 \simeq 1.5833$ as r_0 tends to infinity. The function $c(r_0)$ changes sign at $r_0 = r_c \simeq 6.6792M$, and approaches minus infinity when $r_0 \to 6M$, in a way well described by Eq. (3.4).

Eqs. (3.3) and (3.4) are derived analytically, and imply that $c(r_0)$ must change sign at some radius $r_0 = r_c$. We have therefore provided an *analytical proof* that circular orbits are stable in the range $r_0 > r_c > 6M$ only. However, a numerical calculation is necessary to show that $c(r_0)$ changes sign only once, and to determine the value of r_c, Eq. (1.1).

The complete evolution of the eccentricity, so long as it remains small, can be obtained by integrating Eq. (3.2). It is most convenient to parametrize the evolution with r_0, and to express the eccentricity in terms of the function $\gamma(r_0; r_i)$, defined as

$$\gamma(r_0; r_i) = \ln \frac{\varepsilon(r_0)}{\varepsilon(r_i)} = \int_{r_i}^{r_0} \frac{c(r_0')}{r_0'} dr_0', \tag{3.5}$$

where r_i is some initial radius. If r_0 and r_i are both much larger than $6M$, then Eqs. (3.3), (3.5) imply

$$\gamma(r_0; r_i) \simeq \alpha(r_0/M) - \alpha(r_i/M), \tag{3.6}$$

where

$$\alpha(x) = \frac{19}{12}\Big[\ln x + \frac{3215}{3192}x^{-1} - \frac{377}{1288}\pi x^{-3/2}\Big]. \tag{3.7}$$

If, on the other hand, r_0 is very close to $6M$, but $r_i \gg 6M$, then Eqs. (3.4), (3.5) imply

$$\gamma(r_0; r_i) \simeq -\frac{1}{4}\ln(r_0/6M - 1). \tag{3.8}$$

The behavior of $\gamma(r_0; r_i)$, for r_i arbitrarily fixed to $100M$, is depicted in Fig. 2. From this curve one can easily infer the corresponding $\gamma(r_0; r_i)$ for $r_i < 100M$.

As one sees from Fig. 2, during the weak-field, slow-motion phase of the orbital evolution, the eccentricity is reduced by many orders of magnitude—the orbit becomes essentially circular. The eccentricity reaches a minimum value when $r_0 = r_c$, and then starts increasing. Eventually, if the mass ratio μ/M is arbitrarily small and the adiabatic approximation holds, the orbit shrinks to a radius r_0 for which the eccentricity becomes equal to its initial value; in general this occurs very close to $6M$, as is indicated on the graph. For reasonable mass ratios, however, the eccentricity has not increased by much by the time the adiabatic approximation breaks down. As an example, consider a solar-mass object spiraling around a $10^6 M_\odot$ galactic black hole; this example is particularly relevant to space-based gravitational-wave detectors [9]. For $\mu/M = 10^{-6}$, the adiabatic approximation becomes invalid in the vicinity of $r_0 = r_1$, where $r_1/M = 6.002$; our numerical results then imply $\varepsilon(r_1)/\varepsilon(r_c) \simeq 4.0$. For such binary systems, the inspiral time from $r_0 = r_c$ to $r_0 = r_1$ is of the order of two years. For $\mu/M = 10^{-8}$, the ratio of the eccentricities is only increased by a factor of two.

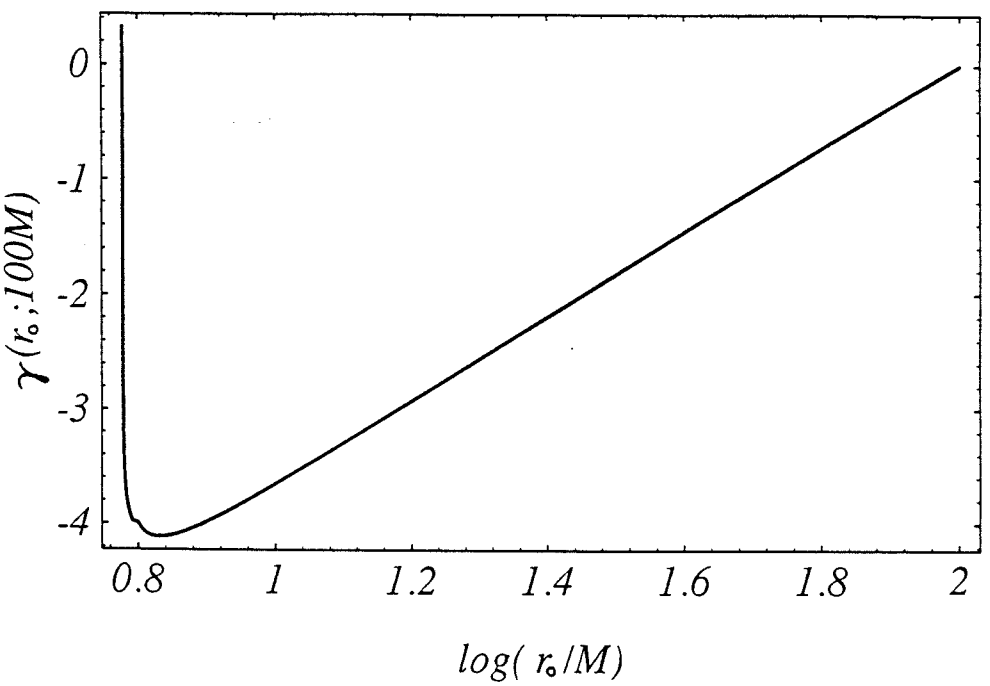

Figure 3.2: A plot of $\gamma(r_0, r_i)$, as defined in Eq. (3.5), for $r_i = 100M$, as a function of $\log r_0/M$. The curve may be continued, both to the left and to the right, using the analytical estimates (1.6) – (1.8). For example, $\gamma(1000M; 100M) \simeq 3.6392$. The function $\gamma(r_0; r_i)$ has a minimum at $r_0 = r_c \simeq 6.6792M$, and grows to plus infinity when $r_0 \to 6M$. Horizontal lines intersect the curve at two distinct points ($r_0 = r_1$ and $r_0 = r_2$) for which the eccentricity is equal, $\varepsilon(r_1) = \varepsilon(r_2)$.

1.4 Organization of the paper

The remainder of this paper is devoted to deriving the results quoted in the preceding subsection. We begin with a precise formulation of the problem in Sec. 2. We first provide definitions for the quantities r_0 and ε, and then derive the evolution equations $\dot{r}_0 = \dot{r}_0(r_0, \dot{L})$, $\dot{\varepsilon} = \dot{\varepsilon}(\varepsilon, r_0, \dot{E}, \dot{L})$. Two conditions which ensure that $\dot{\varepsilon} \propto \varepsilon$ are imposed, and are justified in later sections. The first condition is that, for circular motion, gravitational waves carry energy and angular momentum in such a way that $\dot{E}/\dot{L} = \Omega = (M/r_0{}^3)^{1/2}$; the second condition is that corrections to $\dot{E}$ and $\dot{L}$, due to nonvanishing eccentricity, are second order in ε. The fact that $\dot{\varepsilon} \propto \varepsilon$ implies that circular orbits remain circular under radiation reaction; the stability of circular orbits depends on the sign of the proportionality factor.

We present a brief summary of the Teukolsky perturbation formalism [16] in Sec. 3. First, the inhomogeneous Teukolsky equation, and its formal solution, are described in detail. Then we explain the method for extracting, from the solution, the gravitational waveforms, and the rates at which the waves carry energy and angular momentum. The section is concluded with a proof, valid for arbitrarily strong fields, that $\dot{E}/\dot{L} = \Omega$ for circular orbits.

The calculations relevant for slightly eccentric motion are presented in Sec. 4. The first step consists of integrating the radial and azimuthal geodesic equations; the integration is carried out to second order in the eccentricity. This calculation is presented in subsection 4.1, and subsection 4.2 offers an overview of the remaining steps. The form of the results obtained for $r(t)$ and $\phi(t)$ allows us, in subsection 4.3, to (i) identify the frequency spectrum of the gravitational waves, (ii) witness important simplifications, and (iii) prove that corrections to $\dot{E}$ and $\dot{L}$ are second order in the eccentricity. All of this may be achieved without performing detailed calculations; instead, all computations are kept at a schematic level. These schematic calculations are pushed even further, in subsection 4.4, to derive expressions for $\dot{r}_0$ and $\mu\dot{\varepsilon}/\varepsilon$; this allows us to witness more cancellations, which greatly simplify the problem. The detail of the remaining calculations are presented in subsection 4.5. Conditions on μ/M, which ensure the validity of the adiabatic approximation, are formulated in subsection 4.6.

We present our analytical and numerical results in Sec. 5. We first consider the weak-field, slow-motion ($r_0 \gg 6M$) limit of our formalism, and derive post-Newtonian expansions for the quantities of interest. This analysis yields Eq. (3.3) above. We then consider the highly relativistic ($r_0 \to 6M$) limit of the formalism, which is also tractable analytically. This analysis yields Eq. (3.4) above. In sit-

uations where r_0 is neither very large nor very close to $6M$, our equations must be integrated numerically, which we describe next. Our numerical analysis yields Eq. (3.1) above, as well as the graphs presented in the Figures.

We conclude in Sec. 6 with a recapitulation of our fundamental results, and a discussion of our approximations.

Throughout the paper we use geometrized units in which the speed of light and the gravitational constant are set equal to unity. Most of the paper is essentially self-contained, except for Sec. 5, which relies heavily on previous papers in this series. These previous papers are concerned with purely circular orbits; paper I [18] is devoted to analytical methods, while paper II [19] is devoted to numerical methods. Both analytical and numerical methods are utilized in this paper.

2 FORMULATION OF THE PROBLEM

2.1 Definition of r_0 and ε

Timelike geodesics in the Schwarzschild geometry obey the following equations:

$$\begin{aligned} dt/d\tau &= \tilde{E}/f, \\ d\phi/d\tau &= \tilde{L}/r^2, \\ (dr/d\tau)^2 + V(\tilde{L},r) &= \tilde{E}^2, \end{aligned} \tag{3.9}$$

where τ is the particle's proper time; $\tilde{E} = E/\mu$ and $\tilde{L} = L/\mu$ are, respectively, the specific orbital energy and angular momentum. We have also introduced $f = 1 - 2M/r$, and $V(\tilde{L},r)$ is the effective potential for radial motion,

$$V(\tilde{L},r) = f(1 + \tilde{L}^2/r^2). \tag{3.10}$$

We suppose that the motion takes place in the equatorial plane, $\theta = \pi/2$, and near a minimum of the potential $V(\tilde{L},r)$. We *define* the radius $r = r_0$ to be the position of this minimum; since $\partial V/\partial r|_{r=r_0} = 0$, we have

$$\tilde{L}^2 = M^2[v^2(1 - 3v^2)]^{-1}, \tag{3.11}$$

where $v = (M/r_0)^{1/2}$. Radial motion corresponds to small oscillations about $r = r_0$.

We *define* the eccentricity ε so that $r = r_0(1+\varepsilon)$ is a turning point of the radial motion, at which $\tilde{E}^2 = V(\tilde{L},r)$. This equation can be expanded in powers of ε, which yields

$$(1 - 3v^2)\tilde{E}^2 = (1 - 2v^2)^2 + v^2(1 - 6v^2)\varepsilon^2 - 2v^2(1 - 7v^2)\varepsilon^3 + O(\varepsilon^4). \tag{3.12}$$

Eq. (3.11) implies $r_0 = r_0(\tilde{L})$, while Eq. (3.12) implies $\varepsilon = \varepsilon(\tilde{L},\tilde{E})$.

2.2 Radiation reaction—evolution of r_0 and ε

The results of subsection 2.1 imply that the knowledge of the rates of loss of energy and angular momentum, due to gravitational radiation, is sufficient to determine the evolution of both r_0 and ε. We are interested in the *secular* evolution of these quantities—the evolution over timescales much larger than the orbital period. The secular evolution is well defined, and can be unambiguously calculated. In contrast, the short-term evolution is not so well defined, due to the fact that gravitational waves cannot be localized in a region of spacetime smaller than a few wavelengths [3]. To perform a time averaging over several orbital periods is therefore a fundamental feature of our calculations. We shall henceforth denote by an overdot the operation of time differentiation followed by an average over several orbital periods; thus $\dot{\psi} = \langle d\psi/dt \rangle$, for any quantity ψ.

An evolution equation for r_0 is obtained by using Eq. (3.11) to calculate $\mu \dot{r_0} = (dr_0/d\tilde{L})\dot{L}$, which yields

$$\mu \dot{r_0} = 2(1-3v^2)^{3/2}[v(1-6v^2)]^{-1}\dot{L}. \tag{3.13}$$

Similarly, one may use Eqs. (3.11) and (3.12) to calculate $\mu\dot{\varepsilon} = (\partial\varepsilon/\partial\tilde{E})\dot{E} + (\partial\varepsilon/\partial\tilde{L})\dot{L}$, which yields

$$\begin{aligned} \mu\dot{\varepsilon} \;=\; & \frac{1}{\varepsilon}\frac{(1-2v^2)(1-3v^2)^{1/2}}{v^2(1-6v^2)}\Big\{\Big[1+\frac{v^2(1-6v^2)}{2(1-2v^2)^2}\varepsilon^2+O(\varepsilon^3)\Big]\dot{E} - \\ & -\Big[1-\frac{1-12v^2+18v^4}{(1-2v^2)(1-6v^2)}\varepsilon^2+O(\varepsilon^3)\Big]\Omega\dot{L}\Big\}, \end{aligned} \tag{3.14}$$

where $\Omega = v/r_0 = (M/{r_0}^3)^{1/2}$.

The rate of loss of orbital energy is equal to minus the rate at which gravitational waves carry energy. We therefore write $\dot{E} = -\dot{E}^{(\mathrm{GW})}$, and expand $\dot{E}^{(\mathrm{GW})}$ in powers of the eccentricity:

$$\dot{E}^{(\mathrm{GW})} = \dot{E}^{(0)} + \varepsilon\dot{E}^{(1)} + \varepsilon^2\dot{E}^{(2)} + O(\varepsilon^3); \tag{3.15}$$

$\dot{E}^{(0)}$ corresponds to circular motion. Similarly, we write $\dot{L} = -\dot{L}^{(\mathrm{GW})}$, and

$$\dot{L}^{(\mathrm{GW})} = \dot{L}^{(0)} + \varepsilon\dot{L}^{(1)} + \varepsilon^2\dot{L}^{(2)} + O(\varepsilon^3). \tag{3.16}$$

In Secs. 3.3 and 4.3 below, we will show that

$$\dot{E}^{(0)} = \Omega\dot{L}^{(0)}, \quad \dot{E}^{(1)} = \dot{L}^{(1)} = 0, \tag{3.17}$$

which implies that the lowest-order corrections to $\dot{E}^{(\mathrm{GW})}$ and $\dot{L}^{(\mathrm{GW})}$ are second order in the eccentricity.

Substitution of Eqs. (3.16) and (3.17) into (3.13) implies

$$\mu\dot{r_0} = -2M(1-3v^2)^{3/2}[v^4(1-6v^2)]^{-1}\dot{E}^{(0)} + O(\varepsilon^2); \tag{3.18}$$

the evolution of r_0 is therefore dominated by the circular limit of Eq. (3.13), and corrections due to the small eccentricity can be ignored.

Substitution of Eqs. (3.15), (3.16), and (3.17) into (3.14) yields important cancellations, and the final answer is

$$\mu\dot{\varepsilon} = -\varepsilon(1-2v^2)(1-3v^2)^{1/2}[v^2(1-6v^2)]^{-1}[g(v)\dot{E}^{(0)}+\dot{E}^{(2)}-\Omega\dot{L}^{(2)}]+O(\varepsilon^2), \tag{3.19}$$

where

$$g(v) = \frac{2-27v^2+72v^4-36v^6}{2(1-2v^2)^2(1-6v^2)}. \tag{3.20}$$

Thus the calculation of $\mu\dot{\varepsilon}$ requires the computation of $\dot{E}^{(\mathrm{GW})}$ and $\dot{L}^{(\mathrm{GW})}$, accurately to second order in the eccentricity. Due to the crucial relations (3.17), $\mu\dot{\varepsilon}$ is itself *linear* in the eccentricity.

Eqs. (3.17) are therefore the key to the proof that circular orbits remain circular under radiation reaction, since Eq. (3.19) implies $\dot{\varepsilon}(\varepsilon = 0) = 0$. The problem of determining the evolution of r_0 and ε is now equivalent to that of calculating $\dot{E}^{(0)}$, and the pieces of $\dot{E}^{(2)}$ and $\dot{L}^{(2)}$ which do not cancel out when the combination $\dot{E}^{(2)} - \Omega\dot{L}^{(2)}$ is constructed.

3 THE PERTURBATION FORMALISM

This section contains a brief summary of the relevant equations. More detail can be found in paper I [18], and in the references quoted herein.

3.1 The Teukolsky equation

The stress-energy tensor associated with the motion of a particle perturbs the gravitational field of a Schwarzschild black hole. The gravitational perturbations are described by the Weyl scalar $\Psi_4 = -C_{\alpha\beta\gamma\delta}n^\alpha\bar{m}^\beta n^\gamma\bar{m}^\delta$, where $C_{\alpha\beta\gamma\delta}$ is the Weyl tensor, $n^\alpha = \frac{1}{2}(1,-f,0,0)$, and $\bar{m}^\alpha = (0,0,1,-i\csc\theta)/\sqrt{2}r$; throughout we denote complex conjugation with an overbar. At large distances, Ψ_4 describes outgoing gravitational waves; at the black-hole horizon, Ψ_4 describes ingoing waves.

The Weyl scalar can be decomposed into Fourier-harmonic components according to

$$r^4\Psi_4 = \int_{-\infty}^{\infty} d\omega \sum_{\ell m} R_{\omega\ell m}(r)\,{}_{-2}Y_{\ell m}(\theta,\phi)e^{-i\omega t}, \tag{3.21}$$

where ${}_sY_{\ell m}(\theta,\phi)$ are spin-weighted spherical harmonics [20]; the sums over ℓ and m are restricted to $-\ell \le m \le \ell$ and $\ell \ge 2$. The radial function $R_{\omega\ell m}(r)$ satisfies the inhomogeneous Teukolsky equation [16],

$$\left[r^2 f\frac{d^2}{dr^2} - 2(r-M)\frac{d}{dr} + U(r)\right] R_{\omega\ell m}(r) = -T_{\omega\ell m}(r), \tag{3.22}$$

with

$$U(r) = f^{-1}\left[(\omega r)^2 - 4i\omega(r-3M)\right] - \lambda, \tag{3.23}$$

where $\lambda = (\ell-1)(\ell+2)$.

The source term in Eq. (3.22) is calculated from the particle's stress-energy tensor $T^{\alpha\beta}(x) = \mu\int d\tau\, u^\alpha u^\beta \delta^{(4)}[x - z(\tau)]$, where x is the spacetime point, $z(\tau)$ the particle's trajectory with tangent $u^\alpha = dz^\alpha/d\tau$, and τ is the particle's proper time. The first step is to construct the projections ${}_0T = T_{\alpha\beta}n^\alpha n^\beta$, ${}_{-1}T = T_{\alpha\beta}n^\alpha \bar{m}^\beta$, and ${}_{-2}T = T_{\alpha\beta}\bar{m}^\alpha \bar{m}^\beta$. Then one calculates the Fourier-harmonic components ${}_sT_{\omega\ell m}(r)$ according to

$${}_sT_{\omega\ell m}(r) = \frac{1}{2\pi}\int dt d\Omega\, {}_sT\, {}_s\bar{Y}_{\ell m}(\theta,\phi)e^{i\omega t}, \tag{3.24}$$

where $d\Omega$ is the element of solid angle. The source is

$$\begin{aligned} T_{\omega\ell m}(r) \;=\; & 2\pi\{2[\lambda(\lambda+2)]^{1/2} r^4\, {}_0T_{\omega\ell m}(r) + 2(2\lambda)^{1/2} r^2 f\mathcal{L} r^3 f^{-1}\, {}_{-1}T_{\omega\ell m}(r) + \\ & + r f\mathcal{L} r^4 f^{-1}\mathcal{L} r\, {}_{-2}T_{\omega\ell m}(r)\}, \end{aligned} \tag{3.25}$$

where $\mathcal{L} = f d/dr + i\omega$.

The inhomogeneous Teukolsky equation (3.22) can be integrated by means of a Green's function [21]. The solution at large radii is

$$R_{\omega\ell m}(r\to\infty) \sim \mu\omega^2 Z^H_{\omega\ell m} r^3 e^{i\omega r^*}, \tag{3.26}$$

where $r^* = r + 2M\ln(r/2M-1)$, and the solution near the black-hole horizon is

$$R_{\omega\ell m}(r\to 2M) \sim \mu\omega^3 Z^\infty_{\omega\ell m} r^4 f^2 e^{-i\omega r^*}. \tag{3.27}$$

The amplitudes $Z^{H,\infty}_{\omega\ell m}$ are defined by

$$Z^{H,\infty}_{\omega\ell m} = \frac{1}{2i\mu\omega^2 Q^{\rm in}_{\omega\ell}}\int_{2M}^{\infty} dr\, \frac{R^{H,\infty}_{\omega\ell}(r) T_{\omega\ell m}(r)}{r^4 f^2}, \tag{3.28}$$

where the functions $R^H_{\omega\ell}(r)$ and $R^\infty_{\omega\ell}(r)$ are solutions of the *homogeneous* Teukolsky equation. $R^H_{\omega\ell}(r)$ is the solution with boundary conditions corresponding to ingoing waves at the black-hole horizon, $R^H_{\omega\ell}(r \to 2M) \sim (\omega r)^4 f^2 e^{-i\omega r^*}$; $R^H_{\omega\ell}(r)$ represents a superpostion of ingoing and outgoing waves at large radii, $R^H_{\omega\ell}(r \to \infty) \sim Q^{\rm in}_{\omega\ell}(\omega r)^{-1} e^{-i\omega r^*} + Q^{\rm out}_{\omega\ell}(\omega r)^3 e^{i\omega r^*}$. $R^\infty_{\omega\ell}(r)$ is the solution with boundary conditions corresponding to outgoing waves at infinity, $R^\infty_{\omega\ell}(r \to \infty) \sim (\omega r)^3 e^{i\omega r^*}$; $R^\infty_{\omega\ell}(r)$ represents a superposition of ingoing and outgoing waves at the horizon.

The amplitudes $Z^{H,\infty}_{\omega\ell m}$ satisfy the identities

$$\bar{Z}^{H,\infty}_{-\omega,\ell,-m} = (-1)^\ell Z^{H,\infty}_{\omega\ell m}, \tag{3.29}$$

which we now derive. We use the fact that $u^\theta = 0$, which implies ${}_s\bar{T} = (-1)^s {}_sT$; substitution into Eq. (3.24), using ${}_sY_{\ell,-m}(\theta,\phi) = (-1)^{s+\ell} {}_s\bar{Y}_{\ell m}(\theta,\phi)$, then yields ${}_s\bar{T}_{-\omega,\ell,-m}(r) = (-1)^\ell {}_sT_{\omega\ell m}(r)$. It follows from this and Eq. (3.25) that $\bar{T}_{-\omega,\ell,-m}(r) = (-1)^\ell T_{\omega\ell m}(r)$. The homogeneous Teukolsky equation is invariant under complex conjugation followed by $\omega \to -\omega$, so $\bar{R}^{H,\infty}_{-\omega,\ell}(r) = R^{H,\infty}_{\omega\ell}(r)$ and $\bar{Q}^{\rm in}_{-\omega,\ell} = Q^{\rm in}_{\omega\ell}$. Eq. (3.29) finally follows from Eq. (3.28).

3.2 Waveforms; energy and angular momentum fluxes

At large distances, the two fundamental polarizations of the gravitational waves, h_+ and $h_\times$, can be obtained from Eqs. (3.21) and (3.26); they are

$$h_+ - ih_\times = \frac{2\mu}{r} \sum_{\ell m} {}_{-2}Y_{\ell m} \int_{-\infty}^{\infty} d\omega \, Z^H_{\omega\ell m} e^{-i\omega u}, \tag{3.30}$$

where $u = t - r^*$ represents retarded time. The transverse traceless gravitational-wave tensor is

$$h^{\rm TT}_{ab} = (h_+ - ih_\times) m_a m_b + (h_+ + ih_\times) \bar{m}_a \bar{m}_b. \tag{3.31}$$

The rates at which gravitational waves carry energy and angular momentum to infinity can be calculated from the Isaacson stress-energy tensor [22], which is constructed from $h^{\rm TT}_{ab}$. An alternative but equivalent method involves reading off the multipole moments of the radiative field, as defined by Thorne [23], and using the relevant equations of Ref. [23] to calculate $\dot{E}^\infty$ and $\dot{L}^\infty$. To present the results, we now specialize to the case considered in this paper, in which the frequency spectrum of the waves is characterized by a discrete set of distinct frequencies ω_k. Then

$$Z^H_{\omega\ell m} = \sum_k Z^{Hk}_{\ell m} \delta(\omega - \omega_k), \tag{3.32}$$

and

$$\dot{E}^{\infty} = \frac{\mu^2}{4\pi}\sum_{\ell mk}{\omega_k}^2|Z^{Hk}_{\ell m}|^2, \tag{3.33}$$

$$\dot{L}^{\infty} = \frac{\mu^2}{4\pi}\sum_{\ell mk}\frac{m}{\omega_k}{\omega_k}^2|Z^{Hk}_{\ell m}|^2. \tag{3.34}$$

The rates at which the black hole absorbs energy and angular momentum can be calculated along similar lines [24]. From $\Psi_4(r \to 2M)$ one recovers the gravitational-wave tensor, from which the Isaacson stress-energy tensor is calculated. The calculation of the fluxes then reproduces the results of Teukolsky and Press [25], which were derived in a completely different manner:

$$\dot{E}^{H} = \frac{\mu^2}{4\pi M^2}\sum_{\ell mk}\alpha^k_\ell|Z^{\infty k}_{\ell m}|^2, \tag{3.35}$$

$$\dot{L}^{H} = \frac{\mu^2}{4\pi M^2}\sum_{\ell mk}\frac{m}{\omega_k}\alpha^k_\ell|Z^{\infty k}_{\ell m}|^2, \tag{3.36}$$

for

$$Z^{\infty}_{\omega\ell m} = \sum_k Z^{\infty k}_{\ell m}\delta(\omega-\omega_k). \tag{3.37}$$

We have introduced

$$\alpha^k_\ell = \frac{2^{12}[1+4(M\omega_k)^2][1+16(M\omega_k)^2]}{[\lambda(\lambda+2)]^2+144(M\omega_k)^2}(M\omega_k)^8. \tag{3.38}$$

The total rates of loss of energy and angular momentum are then $\dot{E}^{(\mathrm{GW})} = \dot{E}^{\infty}+\dot{E}^{H}$, and $\dot{L}^{(\mathrm{GW})} = \dot{L}^{\infty}+\dot{L}^{H}$.

3.3 Proof that $\dot{E}^{(0)} = \Omega\dot{L}^{(0)}$

For circular motion, the particle's stress-energy tensor is proportional to $\delta(\phi-\Omega t)$. Eqs. (3.24) and (3.25) then imply $T_{\omega\ell m} \propto \delta(\omega-m\Omega)$—the wave frequency ω is a harmonic of the orbital frequency Ω. Eq. (3.28) further implies $Z^{H,\infty}_{\omega\ell m} \propto \delta(\omega-m\Omega)$, so that we can write

$$Z^{H,\infty}_{\omega\ell m} = A^{H,\infty}_{\ell m}\delta(\omega-m\Omega), \tag{3.39}$$

which is a special case of Eqs. (3.32) and (3.37), with $\omega_k = m\Omega$. Eqs. (3.33)–(3.36) then yield

$$\dot{E}^{\infty} = \Omega\dot{L}^{\infty} = \frac{\mu^2}{4\pi}\sum_{\ell m}(m\Omega)^2|A^H_{\ell m}|^2, \tag{3.40}$$

and

$$\dot{E}^H = \Omega \dot{L}^H = \frac{\mu^2}{4\pi M^2} \sum_{\ell m} \alpha_\ell |A^\infty_{\ell m}|^2, \tag{3.41}$$

where $\alpha_\ell = \alpha^k_\ell(\omega_k = m\Omega)$. Finally, Eqs. (3.40) and (3.41) imply $\dot{E}^{(0)} = \Omega \dot{L}^{(0)}$. Notice that the proof does not require the explicit calculation of $A^{H,\infty}_{\ell m}$. The key to the proof is the observation that for a mode of given m and ω_k, $\dot{E}^{\infty,H}/\dot{L}^{\infty,H} = \omega_k/m$. This property is very general and holds for arbitrary fields; cf. Ref. [26].

4 GRAVITATIONAL WAVES FROM SLIGHTLY ECCENTRIC MOTION

4.1 First step—slightly eccentric motion

The first step of the calculation consists of solving the geodesic equations for slightly eccentric orbits. We begin with the radial equation. Eqs. (3.9) imply

$$(dr/dt)^2 + U(\tilde{E}, \tilde{L}, r) = 0, \tag{3.42}$$

where

$$U(\tilde{E}, \tilde{L}, r) = (f/\tilde{E})^2[V(\tilde{L}, r) - \tilde{E}^2]. \tag{3.43}$$

Our strategy is to expand $r(t)$ according to

$$r(t) = r_0[1 + \varepsilon \xi^{(1)}(t) + \varepsilon^2 \xi^{(2)}(t) + O(\varepsilon^3)], \tag{3.44}$$

and to similarly expand $U(\tilde{E}, \tilde{L}, r)$, using Eqs. (3.11) and (3.12). Collecting terms of equal order in ε yields (i) a differential equation for $\xi^{(1)}(t)$,

$$(d\xi^{(1)}/dt)^2 = {\Omega_r}^2(1 - \xi^{(1)\,2}), \tag{3.45}$$

where

$$\Omega_r = \Omega(1 - 6v^2)^{1/2} \tag{3.46}$$

is the *radial frequency*—the fundamental frequency of radial motion; and (ii) a linear differential equation for $\xi^{(2)}(t)$,

$$\frac{1}{{\Omega_r}^2}\frac{d\xi^{(1)}}{dt}\frac{d\xi^{(2)}}{dt} + \xi^{(1)}\xi^{(2)} = -\frac{1 - 7v^2}{1 - 6v^2} + \frac{2v^2}{1 - 2v^2}\xi^{(1)} + \frac{1 - 11v^2 + 26v^4}{(1 - 2v^2)(1 - 6v^2)}\xi^{(1)3}. \tag{3.47}$$

Eq. (3.45) can be integrated to give

$$\xi^{(1)}(t) = \cos \Omega_r t, \tag{3.48}$$

where the time origin is chosen so that $r(t = 0) = r_0(1 + \varepsilon)$. Substitution of Eq. (3.48) into (3.47) then yields, after integration,

$$\xi^{(2)}(t) = q_1(v)(1 - \cos\Omega_r t) + q_2(v)(1 - \cos 2\Omega_r t), \tag{3.49}$$

where $q_1(v) = (1 - 7v^2)(1 - 6v^2)^{-1}$, and $q_2(v) = (1 - 11v^2 + 26v^4)[2(1 - 2v^2)(1 - 6v^2)]^{-1}$.

Integration of the azimuthal equation proceeds along similar lines. Eqs. (3.9) imply

$$d\phi/dt = (\tilde{L}/\tilde{E})(f/r^2), \tag{3.50}$$

which may be expanded in powers of ε using Eqs. (3.11), (3.12), (3.44), (3.48), and (3.49). Integration then yields

$$\phi(t) = \Omega_\phi t - \varepsilon p_1(v)\sin\Omega_r t + \varepsilon^2 p_2(v)\sin\Omega_r t + \varepsilon^2 p_3(v)\sin 2\Omega_r t + O(\varepsilon^3), \tag{3.51}$$

where $p_1(v) = 2(1 - 3v^2)[(1 - 2v^2)(1 - 6v^2)^{1/2}]^{-1}$, $p_2(v) = 2(1 - 3v^2)(1 - 7v^2)[(1 - 2v^2)(1 - 6v^2)^{3/2}]^{-1}$, $p_3(v) = (5 - 64v^2 + 250v^4 - 300v^6)[4(1 - 2v^2)^2(1 - 6v^2)^{3/2}]^{-1}$; and

$$\Omega_\phi = \left[1 - \frac{3(1 - 3v^2)(1 - 8v^2)}{2(1 - 2v^2)(1 - 6v^2)}\varepsilon^2\right]\Omega \tag{3.52}$$

is the *azimuthal frequency*—the fundamental frequency of azimuthal motion. That $\Omega_\phi \neq \Omega_r$ reflects the fact that eccentric orbits in Schwarzschild are not closed.

4.2 The remaining steps—an overview

The next steps of the calculation consist of (i) substituting the results of the preceding subsection into the expression for the particle's stress-energy tensor,

$$T^{\alpha\beta} = \mu\frac{u^\alpha u^\beta}{r^2 u^t}\delta[r - r(t)]\delta(\cos\theta)\delta[\phi - \phi(t)]; \tag{3.53}$$

(ii) constructing the projections ${}_sT$, and (iii) expanding to second order in the eccentricity. In particular, we must expand $r - r(t)$ about $r - r_0$, thereby introducing derivatives of the radial δ-function; and expand $\phi - \phi(t)$ about $\phi - \Omega_\phi t$, which introduces derivatives of the azimuthal δ-function.

The next task is to obtain the Fourier-harmonic components ${}_sT_{\omega\ell m}(r)$, using Eq. (3.24). The integration over ϕ implies that the derivatives of $\delta(\phi - \Omega_\phi t)$ are integrated by parts, and the n-th derivative of $\delta(\phi - \Omega_\phi t)$ is therefore equivalent to $(im)^n\delta(\phi - \Omega_\phi t)$.

Once the source to the Teukolsky equation has been evaluated using Eq. (3.25), we calculate $Z^{H,\infty}_{\omega\ell m}$ using Eq. (3.28). Since the source has support only at $r = r_0$, the integral can be performed analytically, and involves several integrations by parts. As a result, $Z^{H,\infty}_{\omega\ell m}$ can be expressed as a function of (i) r_0, (ii) the functions $R^{H,\infty}_{\omega\ell}(r)$ and their derivatives at $r = r_0$, and (iii) the coefficient $Q^{\rm in}_{\omega\ell}$.

In weak-field, slow-motion situations (r_0 large), the analytical techniques developed in paper I [18] may be used to calculate, approximately, $R^{H}_{\omega\ell}(r)$ and $Q^{\rm in}_{\omega\ell}$. The result is an analytical expression for $Z^{H}_{\omega\ell m}$, valid for $r_0 \gg 6M$. Since $\dot{E}^H/\dot{E}^\infty$ and $\dot{L}^H/\dot{L}^\infty$ are of order v^8 and hence very small [14, 27], the weak-field, slow-motion calculation does not require the computation of $Z^{\infty}_{\omega\ell m}$.

In a strong-field situation, $R^{H,\infty}_{\omega\ell}(r)$ and $Q^{\rm in}_{\omega\ell}$ must be obtained, for a given value of r_0, by numerically integrating the homogeneous Teukolsky equation. The result is then a numerical expression for $Z^{H,\infty}_{\omega\ell m}$, valid for that value of r_0.

Once $Z^{H,\infty}_{\omega\ell m}$ has been obtained, we observe that the continuous sum over ω reduces to a discrete sum, as in Eqs. (3.32) and (3.37). We then calculate $\dot{E}^{(\rm GW)}$ and $\dot{L}^{(\rm GW)}$ with the help of Eqs. (3.33)–(3.36). Finally, Eqs. (3.18) and (3.19) are used to calculate $\dot{r}_0$ and $\dot{\varepsilon}/\varepsilon$.

4.3 Frequency spectrum, simplifications, and proof that $\dot{E}^{(1)} = \dot{L}^{(1)} = 0$

Each step of the calculation, as outlined in the preceding subsection, would require an extremely long and tedious computation if some remarkable simplifications did not occur along the way. These simplifications arise because: (i) The gravitational waves possess a frequency spectrum characterized by a discrete set of frequencies. As in the circular case, the waves have frequencies equal to the harmonics of the azimuthal frequency, $\omega = m\Omega_\phi$. However, a small eccentricity also implies the existence of *side bands* [28], at $\omega = m\Omega_\phi \pm \Omega_r$, and $\omega = m\Omega_\phi \pm 2\Omega_r$. (ii) The calculation of $\dot{E}^{(\rm GW)}$ and $\dot{L}^{(\rm GW)}$ includes a time averaging, which causes a large number of terms to vanish. In particular, all $O(\varepsilon)$ terms average out, as do most $O(\varepsilon^2)$ terms. And (iii) the calculation of $\dot{\varepsilon}/\varepsilon$ only requires the computation of $\dot{E}^{(2)} - \Omega\dot{L}^{(2)}$, which also generates important cancellations.

We now look more closely into the nature of the waves' frequency spectrum. The calculation of ${}_sT_{\omega\ell m}(r)$ was outlined in subsection 4.2. After the angular integration has been performed, it is clear from Eqs. (3.48), (3.49), (3.51), and (3.53) that the next step is to integrate over time terms which are proportional to:

(i) $e^{i(\omega-m\Omega_\phi)t}$; (ii) $e^{\pm i\Omega_r t}e^{i(\omega-m\Omega_\phi)t}$; and (iii) $e^{\pm 2i\Omega_r t}e^{i(\omega-m\Omega_\phi)t}$. It is also clear that the terms with dependence (i) are dominantly $O(\varepsilon^0)$, while the terms with dependence (ii) are dominantly $O(\varepsilon)$, and the terms with dependence (iii) are dominantly $O(\varepsilon^2)$. Correspondingly, time integration yields terms which are proportional to: (i) $\delta(\phi-m\Omega_\phi)$, with magnitude $O(\varepsilon^0)$; (ii) $\delta(\phi-m\Omega_\phi\pm\Omega_r)$, with magnitude $O(\varepsilon)$; and (iii) $\delta(\phi-m\Omega_\phi\pm 2\Omega_r)$, with magnitude $O(\varepsilon^2)$. Finally, Eqs. (3.25), (3.28), and (3.30) imply that the gravitational waves possess the frequency spectrum described previously.

Our schematic considerations can be pushed further. It is indeed clear from the results obtained thus far that $Z^{H,\infty}_{\omega\ell m}$ must have the following structure (we momentarily remove the H,∞ subscripts for the sake of clarity):

$$\begin{aligned} Z_{\omega\ell m} &= A_{\ell m}\delta(\omega-\omega_m) - \tfrac{1}{2}B^-_{\ell m}\delta(\omega-\omega_-)\varepsilon - \tfrac{1}{2}B^+_{\ell m}\delta(\omega-\omega_+)\varepsilon + \\ &\quad + C_{\ell m}\delta(\omega-\omega_m)\varepsilon^2 + D^-_{\ell m}\delta(\omega-\omega_-)\varepsilon^2 + D^+_{\ell m}\delta(\omega-\omega_+)\varepsilon^2 + \\ &\quad + E^{-2}_{\ell m}\delta(\omega-\omega_{-2})\varepsilon^2 + E^{+2}_{\ell m}\delta(\omega-\omega_{+2})\varepsilon^2 + O(\varepsilon^3), \end{aligned} \tag{3.54}$$

where $\omega_m = m\Omega_\phi$, $\omega_\pm = m\Omega_\phi \pm \Omega_r$, and $\omega_{\pm 2} = m\Omega_\phi \pm 2\Omega_r$. The various coefficients of the δ-functions are expected to be complicated functions of (i) r_0, (ii) $R^{H,\infty}_{\omega\ell}(r)$ and their derivatives at $r = r_0$, and (iii) $Q^{\rm in}_{\omega\ell}$. All these coefficients *can* be calculated with the help of the equations presented in this and the preceding section; however, we shall now show that only a small number actually *need* be calculated.

Substitution of Eq. (3.54) into (3.33)–(3.36), using (3.32) and (3.37), yields

$$\begin{aligned} \dot{E}^\infty &= \frac{\mu^2}{4\pi}\sum_{\ell m}{\omega_m}^2\Big[|A^H_{\ell m} + \varepsilon^2 C^H_{\ell m}|^2 + \Big(\frac{\omega_-}{\omega_m}\Big)^2|\tfrac{1}{2}B^{H-}_{\ell m}|^2\varepsilon^2 + \\ &\qquad + \Big(\frac{\omega_+}{\omega_m}\Big)^2|\tfrac{1}{2}B^{H+}_{\ell m}|^2\varepsilon^2 + O(\varepsilon^3)\Big], \end{aligned} \tag{3.55}$$

$$\begin{aligned} \Omega_\phi \dot{L}^\infty &= \frac{\mu^2}{4\pi}\sum_{\ell m}{\omega_m}^2\Big[|A^H_{\ell m} + \varepsilon^2 C^H_{\ell m}|^2 + \frac{\omega_-}{\omega_m}|\tfrac{1}{2}B^{H-}_{\ell m}|^2\varepsilon^2 + \\ &\qquad + \frac{\omega_+}{\omega_m}|\tfrac{1}{2}B^{H+}_{\ell m}|^2\varepsilon^2 + O(\varepsilon^3)\Big], \end{aligned} \tag{3.56}$$

$$\begin{aligned} \dot{E}^H &= \frac{\mu^2}{4\pi M^2}\sum_{\ell m}\alpha_\ell\Big[|A^\infty_{\ell m} + \varepsilon^2 C^\infty_{\ell m}|^2 + \frac{\alpha^-_\ell}{\alpha_\ell}|\tfrac{1}{2}B^{\infty-}_{\ell m}|^2\varepsilon^2 + \\ &\qquad + \frac{\alpha^+_\ell}{\alpha_\ell}|\tfrac{1}{2}B^{\infty+}_{\ell m}|^2\varepsilon^2 + O(\varepsilon^3)\Big], \end{aligned} \tag{3.57}$$

$$\begin{aligned} \Omega_\phi \dot{L}^H &= \frac{\mu^2}{4\pi M^2}\sum_{\ell m}\alpha_\ell\Big[|A^\infty_{\ell m} + \varepsilon^2 C^\infty_{\ell m}|^2 + \frac{\alpha^-_\ell}{\alpha_\ell}\frac{\omega_m}{\omega_-}|\tfrac{1}{2}B^{\infty-}_{\ell m}|^2\varepsilon^2 + \\ &\qquad + \frac{\alpha^+_\ell}{\alpha_\ell}\frac{\omega_m}{\omega_+}|\tfrac{1}{2}B^{\infty+}_{\ell m}|^2\varepsilon^2 + O(\varepsilon^3)\Big], \end{aligned} \tag{3.58}$$

where $\alpha_\ell = \alpha_\ell^k(\omega_k = \omega_m)$ and $\alpha_\ell^\pm = \alpha_\ell^k(\omega_k = \omega_\pm)$. These results teach us that the coefficients $D_{\ell m}^{H,\infty\pm}$ and $E_{\ell m}^{H,\infty\pm 2}$ are irrelevant to our calculation; their contributions vanish after the time averaging has been carried out. More simplifications arise below.

Eqs. (3.55)–(3.58) imply that corrections to $\dot{E}^{(\mathrm{GW})}$ and $\dot{L}^{(\mathrm{GW})}$, due to nonvanishing eccentricity, are second-order in ε. Thus $\dot{E}^{(1)} = \dot{L}^{(1)} = 0$, as was first written in Eq. (3.17). The proof that circular orbits remain circular under radiation reaction is now complete.

4.4 Calculation of $\dot{r}_0$ and $\mu\dot{\varepsilon}/\varepsilon$

The calculation of $\dot{r}_0$ is almost complete. Explicit expressions for $A_{\ell m}^{H,\infty}$ will be given in subsection 4.5; these may be used together with Eqs. (3.40) and (3.41) to calculate $\dot{E}^{(0)}$, which is then substituted in Eq. (3.18).

The calculation of $\mu\dot{\varepsilon}/\varepsilon$ requires the computation of $\dot{E}^{(0)}$ and $\dot{E}^{(2)} - \Omega\dot{L}^{(2)}$. In Eqs. (3.55)–(3.58), a number of terms are *explicitly* second-order in the eccentricity; others are $O(\varepsilon^2)$ only *implicitly*, by virtue of the fact that $\Omega_\phi = \Omega(1 - \Delta\Omega\varepsilon^2)$, where $\Delta\Omega$ can be read off from Eq. (3.52). To make all dependence on ε explicit, we now adapt our notation so that $\omega_\pm = m\Omega \pm \Omega_r$, and write $\omega_m{}^2|A_{\ell m}^{H,\infty}|^2 = (m\Omega)^2|A_{\ell m}^{H,\infty}|^2 + O(\varepsilon^2)$. It follows that the quantity $\dot{E}^{(2)} - \Omega\dot{L}^{(2)} + \Delta\Omega\dot{E}^{(0)}$ only requires the calculation of the coefficients $B_{\ell m}^{H,\infty\pm}$. With the help of Eq. (3.19), we finally obtain

$$\mu\dot{\varepsilon}/\varepsilon = -\frac{(1-2v^2)(1-3v^2)^{1/2}}{v^2(1-6v^2)}[\Gamma - h(v)\dot{E}^{(0)}], \tag{3.59}$$

where $\Gamma = \Gamma^\infty + \Gamma^H$, with

$$\Gamma^\infty = \frac{\mu^2}{16\pi}\Omega_r \sum_{\ell m}\left(\omega_+|B_{\ell m}^{H+}|^2 - \omega_-|B_{\ell m}^{H-}|^2\right), \tag{3.60}$$

where $\omega_\pm = m\Omega \pm \Omega_r$; and

$$\Gamma^H = \frac{\mu^2}{16\pi M^2}\Omega_r \sum_{\ell m}\left(\frac{\alpha_\ell^+}{\omega_+}|B_{\ell m}^{\infty+}|^2 - \frac{\alpha_\ell^-}{\omega_-}|B_{\ell m}^{\infty-}|^2\right). \tag{3.61}$$

We also have

$$h(v) = \frac{1 - 12v^2 + 66v^4 - 108v^6}{2(1-2v^2)^2(1-6v^2)}, \tag{3.62}$$

with $v = (M/r_0)^{1/2}$.

Eqs. (3.59) – (3.62) imply that the calculation of $\mu\dot{\varepsilon}/\varepsilon$ is much simpler than the individual computations, to second order in the eccentricity, of $\dot{E}^{(\mathrm{GW})}$ and $\dot{L}^{(\mathrm{GW})}$.

Because of the occurrence of important cancellations, the calculation only requires the computation of $B^{H,\infty\pm}_{\ell m}$, and the leading-order part of $A^{H,\infty}_{\ell m}$. Computation of all other coefficients, as well as the $O(\varepsilon^2)$ part of $A^{H,\infty}_{\ell m}$, is superfluous.

Because of those various cancellations, the calculation of $\mu\dot{\varepsilon}/\varepsilon$ may now proceed in complete ignorance of the $O(\varepsilon^2)$ corrections to the motion of the particle. The only essential correction, the $O(\varepsilon^2)$ part of Ω_ϕ, has already been incorporated into Eq. (3.59). The computation of $B^{H,\infty\pm}_{\ell m}$ only requires a calculation accurate to first order in the eccentricity.

4.5 Calculation of $A^{H,\infty}_{\ell m}$ and $B^{H,\infty\pm}_{\ell m}$

The calculation follows the lines of subsection 4.2 above. We find

$$A^{H,\infty}_{\ell m} = \frac{\pi}{i(\omega_m r_0)^2 Q^{\rm in}_{\omega_m \ell}}\Big({}_0A^{H,\infty}_{\ell m} + {}_{-1}A^{H,\infty}_{\ell m} + {}_{-2}A^{H,\infty}_{\ell m}\Big), \tag{3.63}$$

where (we momentarily remove all unnecessary indices for the sake of clarity)

$$\begin{aligned}
{}_0A &= {}_0a f_0 R,\\
{}_{-1}A &= {}_{-1}a f_0[(2f_0 + i\omega_m r_0)R - f_0 r_0 R'],\\
{}_{-2}A &= {}_{-2}a f_0[i\omega_m r_0(2 - 2v^2 + i\omega_m r_0)R - 2(f_0 + i\omega_m r_0) f_0 r_0 R' + (f_0 r_0)^2 R''].
\end{aligned} \tag{3.64}$$

Here, $\omega_m = m\Omega$, $f_0 = 1 - 2M/r_0 = 1 - 2v^2$, $R = R^{H,\infty}_{\omega_m \ell}(r_0)$, and a prime denotes differentiation with respect to r_0. Also

$$B^{H,\infty\pm}_{\ell m} = \frac{\pi}{i(\omega_\pm r_0)^2 Q^{\rm in}_{\omega_\pm \ell}}\Big({}_0B^{H,\infty\pm}_{\ell m} + {}_{-1}B^{H,\infty\pm}_{\ell m} + {}_{-2}B^{H,\infty\pm}_{\ell m}\Big), \tag{3.65}$$

where

$$\begin{aligned}
{}_0B^{\pm} &= {}_0c^{\pm} R_\pm - {}_0a(f_0 r_0 R'_\pm - 4v^2 R_\pm),\\
{}_{-1}B^{\pm} &= {}_{-1}c^{\pm}[(2 - 4v^2 + i\omega_\pm r_0)R_\pm - f_0 r_0 R'_\pm] +\\
&\quad + {}_{-1}a[(4v^2 - 8v^4 + 6iM\omega_\pm - i\omega_\pm r_0)R_\pm -\\
&\qquad - f_0(1 + i\omega_\pm r_0) r_0 R'_\pm + (f_0 r_0)^2 R''_\pm],\\
{}_{-2}B^{\pm} &= {}_{-2}c_\pm[(f_0 r_0)^2 R''_\pm - 2f_0(1 - 2v^2 + i\omega_\pm r_0) r_0 R'_\pm +\\
&\qquad + i\omega_\pm r_0(2 - 2v^2 + i\omega_\pm r_0)R_\pm] -\\
&\quad - {}_{-2}a[(f_0 r_0)^3 R'''_\pm - 2i\omega_\pm r_0 (f_0 r_0)^2 R''_\pm -\\
&\qquad - f_0(2 - 8v^2 + 8v^4 - 10iM\omega_\pm + 2i\omega_\pm r_0 + {\omega_\pm}^2 {r_0}^2) r_0 R'_\pm +\\
&\qquad + 2i\omega_\pm r_0(1 - 6v^2 + 4v^4 - 4iM\omega_\pm + i\omega_\pm r_0)R_\pm],
\end{aligned} \tag{3.66}$$

with $\omega_\pm = m\Omega \pm \Omega_r$ and $R_\pm = R^{H,\infty}_{\omega_\pm \ell}(r_0)$. We have introduced

$$\begin{aligned} {}_0a_{\ell m} &= [\lambda(\lambda+2)]^{1/2}\, {}_0Y_{\ell m}(\tfrac{\pi}{2},0)\,[2(1-2v^2)(1-3v^2)^{1/2}]^{-1}, \\ {}_{-1}a_{\ell m} &= i\lambda^{1/2}\, {}_{-1}Y_{\ell m}(\tfrac{\pi}{2},0)\, v[(1-2v^2)^2(1-3v^2)^{1/2}]^{-1}, \\ {}_{-2}a_{\ell m} &= -{}_{-2}Y_{\ell m}(\tfrac{\pi}{2},0)\, v^2[2(1-2v^2)^3(1-3v^2)^{1/2}]^{-1}, \end{aligned} \tag{3.67}$$

where $\lambda = (\ell-1)(\ell+2)$, and

$${}_sc^{\pm}_{\ell m} = {}_sa_{\ell m}\Big[2-s-2(3-s)v^2 \pm i(2+s)v(1-6v^2)^{1/2} \pm 2m(1-3v^2)(1-6v^2)^{-1/2}\Big]. \tag{3.68}$$

The previous equations imply the following symmetry properties: $\bar{A}^{H,\infty}_{\ell,-m} = (-1)^\ell A^{H,\infty}_{\ell m}$; $\bar{B}^{H,\infty\mp}_{\ell,-m} = (-1)^\ell B^{H,\infty\pm}_{\ell m}$, and for $m=0$, $\bar{B}^{H,\infty-}_{\ell,0} = B^{H,\infty+}_{\ell,0}$.

4.6 The adiabatic approximation

We conclude this section by formulating the conditions under which the adiabatic approximation holds. The results of this subsection were summarized in Sec. 1.2.

We require that the *inspiral timescale* $r_0/|\dot{r}_0|$ always be much smaller than the *orbital period* $2\pi/\Omega_r$. Using Eq. (3.18), this requirement becomes

$$\mu/M \ll \frac{1}{4\pi}\frac{v^5(1-6v^2)^{3/2}}{(1-3v^2)^{3/2}}\frac{1}{(M/\mu)^2\dot{E}^{(0)}}. \tag{3.69}$$

At large radii, $r_0 \gg 6M$, $(M/\mu)^2\dot{E}^{(0)} \simeq 32v^{10}/5$ and the adiabatic condition (3.69) becomes $\mu/M \ll (5/128\pi)v^{-5}$. This is superseded by a wide margin by the condition $\mu/M \ll 1$, which ensures that the gravitational perturbations are linear. Near $r_0 = 6M$, we may use the numerical results of Sec. 5.3 and put $(M/\mu)^2\dot{E}^{(0)} \simeq 9\times 10^{-4}$, and Eq. (3.69) becomes $\mu/M \ll 2.8(1-6v^2)^{3/2}$. This condition is far more restrictive than $\mu/M \ll 1$.

5 ANALYTICAL AND NUMERICAL RESULTS

5.1 Weak-field, slow-motion case

For $r_0 \gg 6M$ and $v = (M/r_0)^{1/2} \ll 1$, the analytical techniques developed in paper I may be used to calculate, approximately, $R^H_{\omega_\pm \ell}(r)$ and $Q^{\rm in}_{\omega_\pm \ell}$. The expressions for these quantities may then be substituted into the equations of Sec. 4.4 and 4.5, to obtain $\mu\dot{\varepsilon}/\varepsilon$ in the form of a post-Newtonian expansion. As was mentioned

previously, there is no need to calculate $\dot{E}^H$ and $\dot{L}^H$, because they contribute only at order v^8 to the post-Newtonian expansion [27]. The calculations are straightforward and will be presented without much detail.

The calculation of $\mu\dot{\varepsilon}/\varepsilon$ up through order v^3 beyond Newtonian requires the computation of $B^{H\pm}_{\ell m}$ for $\ell = 2$ and $\ell = 3$. We may use the symmetry properties of $B^{H\pm}_{\ell m}$ and only consider nonnegative values of m; for $m = 0$, only $B^{H+}_{\ell,0}$ is required. We find

$$\begin{aligned}
B^{H+}_{2,2} &= (\pi/5)^{1/2}v^2[-18 + 27v^2 - 54\pi v^3 + O(iv^3, v^4)],\\
B^{H-}_{2,2} &= (\pi/5)^{1/2}v^2[6 + \tfrac{221}{7}v^2 + 6\pi v^3 + O(iv^3, v^4)],\\
B^{H+}_{2,1} &= (\pi/5)^{1/2}v^2[-\tfrac{16}{3}iv + \tfrac{176}{21}iv^3 + O(v^4)],\\
B^{H-}_{2,1} &= O(v^6),\\
B^{H+}_{2,0} &= (\pi/30)^{1/2}v^2[-4 + \tfrac{206}{7}v^2 - 4\pi v^3 + O(iv^3, v^4)],\\
B^{H+}_{3,3} &= (\pi/42)^{1/2}v^2[64iv + O(v^3)],\\
B^{H-}_{3,3} &= (\pi/42)^{1/2}v^2[-24iv + O(v^3)],\\
B^{H+}_{3,1} &= (\pi/70)^{1/2}v^2[\tfrac{8}{3}iv + O(v^3)],\\
B^{H-}_{3,1} &= O(v^6),
\end{aligned} \tag{3.70}$$

and $B^{H\pm}_{3,m} = O(v^5)$ for $m = \{0, 2\}$. In the above, the notation $O(iv^3)$ signifies that those terms of order v^3, which are purely imaginary, do not contribute, at order v^3, to $|B^{H\pm}_{\ell m}|^2$. That the coefficients $B^{H-}_{\ell,1}$ are so small is due to the fact that, for $m = 1$, $\omega_- = \Omega - \Omega(1 - 6v^2)^{1/2} = 3v^2\Omega + O(v^4)$; since ω_- is suppressed by a factor v^2 with respect to ω_+, the resulting $B^{H-}_{\ell,1}$ is much smaller than $B^{H+}_{\ell,1}$.

We now substitute Eqs. (3.70) into (3.60) and (3.59), and use the post-Newtonian expansion

$$\dot{E}^{(0)} = \dot{E}_N\Big[1 - \frac{1247}{336}v^2 + 4\pi v^3 + O(v^4)\Big] \tag{3.71}$$

derived in paper I [$\dot{E}_N = \frac{32}{5}(\mu/M)^2v^{10}$ is the leading-order, Newtonian expression]; this yields

$$\dot{\varepsilon} = \dot{\varepsilon}_N\Big[1 - \frac{6849}{2128}v^2 + \frac{985}{152}\pi v^3 + O(v^4)\Big], \tag{3.72}$$

where $\dot{\varepsilon}_N$ is the leading-order, Newtonian expression,

$$\mu\dot{\varepsilon}_N/\varepsilon = -\tfrac{304}{15}(\mu/M)^2v^8. \tag{3.73}$$

Throughout the post-Newtonian regime, $v \ll 1$, $\dot{\varepsilon}$ is negative—radiation reaction therefore reduces the eccentricity.

Substitution of Eq. (3.71) into (3.18), and use of Eqs. (3.72) and (3.73) yields Eq. (3.4).

5.2 Highly relativistic case

Analytical calculations may also be carried out in the case where r_0 approaches $6M$. Because $h(v)$ diverges when $v^2 \to 1/6$, cf. Eq. (3.62), and because both $\dot{E}^{(0)}$ and Γ have well-defined limits when $r_0 \to 6M$, $\mu\dot{\varepsilon}/\varepsilon$ is dominated by the second term on the right-hand side of Eq. (3.59).

Our claim that $\dot{E}^{(0)}$ is well behaved in the vicinity of $r_0 = 6M$ can be substantiated by (i) an inspection of the perturbation formalism, which shows no sign of a singularity at $r_0 = 6M$; in particular, $R^{H,\infty}_{\omega\ell}(r)$ and $Q^{\rm in}_{\omega\ell}$, for $M\omega = mM\Omega = 6^{-3/2}m$, are well behaved. And (ii) with numerical calculations, which confirm the proper behavior of $\dot{E}^{(0)}$ in the vicinity of $r_0 = 6M$.

The proper behavior of Γ can be established as follows. Writing $\delta = (1 - 6M/r_0)^{1/2} \ll 1$, we first infer the various δ-dependence of the relevant quantities. Using the equations of Sec. 4.5, we find that the ${}_sa_{\ell m}$ are independent of δ, while ${}_sc^{\pm}_{\ell m} = \pm m\,{}_sa_{\ell m}\delta^{-1} + O(\delta^0)$. Using the fact that $R^{H,\infty}_{\omega_\pm\ell}(r)$ and $Q^{\rm in}_{\omega_\pm\ell}$ are properly behaved, Eq. (3.65) then implies $B^{\pm}_{\ell m} = \pm k_{\ell m}\delta^{-1} + k^{\pm}_{\ell m} + O(\delta)$, where $k_{\ell m}$ and $k^{\pm}_{\ell m}$ are independent of δ. The fact that, at leading order in δ, $B^{+}_{\ell m}$ and $B^{-}_{\ell m}$ differ only by a sign is an important aspect of this discussion. [The case $m = 0$ requires special thought, since then $\omega_\pm = \pm\delta\Omega$, and Eq. (3.65) suggests that $B^{\pm}_{\ell,0}$ might be more singular than $O(\delta^{-1})$. However, a careful study of the Teukolsky equation reveals that this does not happen.] The final step is to substitute our result for $B^{\pm}_{\ell m}$ into Eq. (3.60), and notice a remarkable cancellation of the leading-order, $O(\delta^{-2})$ terms. Multiplication by $\Omega_r = \delta\Omega$ then ensures that each term in the sum over ℓ and m is $O(\delta^0)$. That Γ has a well-defined limit follows from the fact that the sum converges for every $r_0 \geq 6M$, which was verified numerically.

Having established that Γ and $\dot{E}^{(0)}$ have well-defined limits when r_0 approaches $6M$, Eq. (3.59) reduces to

$$\mu\dot{\varepsilon}/\varepsilon \sim \frac{3}{2\sqrt{2}}\dot{E}^{(0)}|_{r_0=6M}(1 - 6M/r_0)^{-2}, \tag{3.74}$$

for $r_0 \to 6M$.

Substitution of Eq. (3.74) and (3.18) into (3.2) yields Eq. (3.4).

5.3 General case—numerical integration

When r_0 is neither very large nor very close to $6M$, $R^{H,\infty}_{\omega_\pm\ell}(r)$ and $Q^{\rm in}_{\omega_\pm\ell}$ must be calculated numerically. By performing the integration for a wide range of orbital

radii, we obtain $\mu\dot{\varepsilon}/\varepsilon$ as a function of r_0. The numerical results may then be checked against the limiting cases (3.72) and (3.74).

We have carried out the numerical integration using a straightforward generalization of the algorithm presented in paper II [19] (we shall not repeat the discussion of paper II here). We have constructed our integrator upon the Bulirsh-Stoer method, using fortran subroutines given in Ref. [29]; all operations were performed with double precision. We have verified that our numerical results are in agreement with the limiting cases of subsections 5.1 and 5.2; this agreement gives us great confidence in our results, which are summarized in Fig. 1.

It is easy to obtain high numerical accuracy by adjusting the tolerance of our integrator to a very small value; we have typically chosen a tolerance of 10^{-6}. Although it is hard to *prove*, we *believe* our numbers to be accurate to at least six significant digits. Consequently, our estimate of the critical radius r_c (at which $\dot{\varepsilon}$ changes sign) should be accurate to six significant digits; we have chosen to quote only five digits in Eq. (3.1).

The accuracy of our numerical results is also subject to errors of non-numerical origin, which are due to the fact that the infinite sum over ℓ must be truncated. The magnitude of the error thus induced can be controlled by requiring that the terms ignored contribute to a fractional error no greater than a certain value ζ. Since a multipole of order ℓ contributes a fractional amount of order $(M/r_0)^{\ell-2}$ to $\dot{E}$ and $\dot{L}$ [18], we arrive at the following criterion on the maximal value of ℓ which needs be included in the sum,

$$\ell_{\max} \geq 2 - \log\zeta/\log(r_0/M). \tag{3.75}$$

For example, choosing $\zeta = 10^{-6}$ yields $\ell_{\max} = 10$ for $r_0/M = 6$, and $\ell_{\max} = 3$ for $r_0/M = 10^6$.

The graph of Fig. 2 was obtained by numerically integrating Eq. (3.5), in the range between $r_0/M = 6 + 10^{-8}$ and $r_0/M = 100$. The integration was performed using the extended trapezoidal rule, which is accurate enough for our purposes.

6 CONCLUSION

We have established in this paper that a particle in circular motion around a nonrotating black hole remains on a circular orbit under the influence of radiation reaction. Furthermore, we have shown that circular orbits are *stable* only if the

orbital radius is greater than a critical radius $r_c \simeq 6.6792M$, where M is the mass of the black hole.

Also, our analysis permits us to follow the evolution, under radiation reaction, of an orbit's eccentricity, so long as it remains small. We find that the eccentricity is reduced by many orders of magnitude during the post-Newtonian phase of the inspiral, but that it starts increasing once the orbit's radius is smaller than r_c. For reasonable values of μ/M, the eccentricity increases by at most an order of magnitude before the adiabatic approximation breaks down and the particle begins its plunge toward the black hole.

Our analysis is restricted by four major assumptions: (i) the black hole is non-rotating, (ii) the eccentricity is always small, (iii) the gravitational perturbations are linear, and (iv) the adiabatic approximation is valid. On the other hand, our analysis is not limited to weak-field, slow-motion situations; it is valid for particle motion in strong gravitational fields.

We now examine whether any of our four assumptions could be relaxed, and at what cost, in future work.

Assumption (i) could be removed without much effort, that is, our analysis could be extended to the case of a rotating black hole, if and only if the orbit lies in the hole's equatorial plane. In the more general and more interesting situation of non-equatorial orbits, the formulation of the problem of radiation reaction would take a significantly different form. In such cases, the motion possesses a non-vanishing value of the Carter constant, whose rate of change cannot be simply (if at all) related to the rates of change of energy and (vectorial) angular momentum. The general analysis would therefore require techniques more sophisticated than the ones utilized here; for example, a numerical implementation of Gal'tsov's formalism [14].

Assumption (ii) is one of simplicity, and could be removed without introducing additional conceptual difficulties. For example, a calculation valid to higher order in the eccentricity could be carried out, at the price of a modest effort. A calculation valid to all orders in ϵ could also be performed by numerical integration of the geodesic equations; see Ref. [17].

Assumption (iii) cannot be removed easily. Strong-field analyses valid for arbitrary mass ratios would require either the formulation of a higher-order perturbation theory, or the complete numerical solution of Einstein's equations for the two-body problem. Both approaches are still a long way into the future. A recent analysis by Kidder, Will, and Wiseman [30] suggests that the value of the critical

radius r_c should increase with the mass ratio μ/M.

Assumption (iv) could be removed (at least partially) by incorporating, at the very beginning, radiation-reaction effects into the motion of the particle. Thus the motion would be non-geodesic to begin with, and higher-order radiation-reaction effects could then be calculated. These higher-order effects would be quite small at large orbital radii; but for a given mass ratio, there exists an orbital radius r_0 at which the adiabatic approximation breaks down, and at which higher-order effects would become important. The breakdown of the adiabatic approximation, and the transition from slow inspiral to fast plunge, is discussed in Ref. [15].

ACKNOWLEDGMENTS

For numerous discussions, we thank Amos Ori, Kip Thorne, and the members of the Relativity Group at Caltech. We also thank George Djorgovski for the use of his computing facilities, and Julia Smith for much computing help and advice. The work presented here was supported by the NSF Grant AST 9114925, and the NASA Grant NAGW-2897. Eric Poisson acknowledges support from the Natural Sciences and Engineering Research Council of Canada.

Bibliography

[1] J.D. Jackson, *Classical Electrodynamics* (Wiley, New York, 1975), Ch. 17.

[2] F. Rohrlich, *Classical Charged Particles* (Addison-Wesley, Reading, 1965).

[3] C.W. Misner, K.S. Thorne, and J.A. Wheeler, *Gravitation* (Freeman, New York, 1973), Part VIII.

[4] B.S. DeWitt and R.W. Brehme, Ann. Phys. (U.S.A.) **9**, 220 (1960).

[5] A. Krolak and B.F. Schutz, Gen. Relativ. Gravit. **19**, 1163 (1987).

[6] Such as the American LIGO (Laser Interferometer Gravitational-wave Observatory), cf. A. Abramovici, W.E. Althouse, R.W.P. Drever, Y. Gürsel, S. Kawamura, F.J. Raab, D. Shoemaker, L. Siewers, R.E. Spero, K.S. Thorne, R.E. Vogt, R. Weiss, S.E. Whitcomb, and M.E. Zucker, Science **256**, 325 (1992); and the French-Italian VIRGO, cf. C. Bradaschia, E. Calloni, M. Cobal, R. Del Fasbro, A. Di Virgilio, A. Giazotto L.E. Holloway, H. Kautzky, B. Michelozzi, V. Montelatici, D. Pascuello, and W. Velloso, in *Gravitation: a Banff Summer Institute*, ed. R. Mann and P. Wesson (World Scientific, Singapore, 1991).

[7] C. Cutler, T.A. Apostolatos, L. Bildsten, L.S. Finn, E.E. Flanagan, D. Kennefick, D.M. Markovic, A. Ori, E. Poisson, G.J. Sussman, and K.S. Thorne, *The last three minutes: Issues in gravitational wave measurements of coalescing compact binaries*, Caltech preprint (1992).

[8] K.S. Thorne, in *300 Years of Gravitation*, ed. S.W. Hawking and W. Israel (Cambridge University Press, Cambridge, 1987).

[9] Such as the proposed LAGOS (LAser Gravitational-wave Observatory in Space), cf. K.S. Thorne, in *Recent Advances in General Relativity, Proceed-*

ings of a conference in honor of E.T. Newman, ed. A. Janis and J. Porter (Birkhauser, Boston, 1992) and references therein.

[10] T. Damour, in *300 Years of Gravitation*, ed. S.W. Hawking and W. Israel (Cambridge University Press, Cambridge, 1987).

[11] P.C. Peters, Phys. Rev. **136**, B1224 (1964).

[12] C.W. Lincoln and C.M. Will, Phys. Rev. D **42**, 1123 (1990).

[13] B.R. Iyer and C.M. Will, Phys. Rev. Lett. **70**, 113 (1993).

[14] D.V. Gal'tsov, J. Phys. A **15**, 3737 (1982).

[15] L.S. Finn, A. Ori, and K.S. Thorne (unpublished).

[16] S.A. Teukolsky, Astrophys. J. **185**, 635 (1973).

[17] T. Tanaka, M. Shibata, M. Sasaki, H. Tagashi, and T. Nakamura, Kyoto University Report KUNS-1175 (1993).

[18] E. Poisson, Phys. Rev. D **47**, XXXX (1993).

[19] C. Cutler, L.S. Finn, E. Poisson, and G.J. Sussman, Phys. Rev. D **47**, XXXX (1993).

[20] J.N. Goldberg, A.J. MacFarlane, E.T. Newman, F. Rohrlich and E.C.G. Sudarshan, J. Math. Phys. **8**, 2155 (1967).

[21] S.L. Detweiler, Astrophys. J. **225**, 687 (1978).

[22] R.A. Isaacson, Phys. Rev. **166**, 1272 (1968).

[23] K.S. Thorne, Rev. Mod. Phys. **52**, 299 (1980).

[24] P.L. Chrzanowski, Phys. Rev. D **11**, 2042 (1975).

[25] S.A. Teukolsky and W.H. Press, Astrophys. J. **193**, 443 (1974).

[26] B. Carter, in *General Relativity, An Einstein Centenary Survey*, ed. S.W. Hawking and W. Israel (Cambridge University Press, Cambridge, 1979).

[27] For circular orbits, a gravitational-wave mode of given ℓ and m radiates energy in such a way that $\dot{E}^H/\dot{E}^\infty = {\beta_{\ell m}}^2 v^{2(\ell+2)}[1 + O(v^2)]$, where $\beta_{\ell m} = 2\ell!/m^\ell$ if $\ell + m$ is even, and $\beta_{\ell m} = 2(\ell+1)!/\ell m^\ell$ if $\ell + m$ is odd. The dominant contribution to the gravitational power comes from the modes $\ell = |m| = 2$; we therefore have $\dot{E}^H/\dot{E}^\infty = v^8[1 + O(v^2)]$. This behavior is confirmed by our numerical results.

[28] D.V. Galt'sov, A.A. Matiukhin, and V.I. Petukhov, Phys. Lett. **A77**, 387 (1980).

[29] W.H. Press, B.P. Flannery, S.A. Teukolsky, and W.T. Vetterling, *Numerical Recipes* (Cambridge University Press, Cambridge, 1986), Ch. 15.

[30] L.E. Kidder, C.M. Will, and A.G. Wiseman, Class. Quantum Grav. **9**, L125 (1992).

Chapter 4

Spin-induced orbital precession and its modulation of the gravitational waveforms from merging binaries. [Co-authored with Curt Cutler, Gerald J. Sussman, and Kip S. Thorne]

(Originally appeared in Phys. Rev. D **49**, 6274 (1994).)

Abstract

Merging compact binaries are currently regarded as the most promising source of gravitational waves for the planned Earth-based LIGO/VIRGO laser-interferometer detector system, and will be an important source also for similar, lower-frequency detectors that might be flown in space (e.g., the proposed LISA mission). During the orbital inspiral, if one or both bodies are rapidly rotating, the general relativistic spin-orbit and spin-spin coupling (i.e., the "dragging of inertial frames" by the bodies' spins) cause the binary's orbital plane to precess. In this paper we analyze the resulting modulation of the inspiral gravitational waveform, using post^2-Newtonian equations to describe the precession of the orbital plane, but only the leading-order (Newtonian, quadrupole-moment approximation) equations to describe the orbit, the radiation reaction, the inspiral, and the wave generation. We derive all the formulae one needs to readily compute the spin-modulated gravitational waveform (within the post-Newtonian approximation and the approximation that the precession frequency is much smaller than the orbital frequency). We also develop intuition into what the modulated signals "look like," by a variety of means. We provide approximate, analytical solutions for the precessional motion and the modulated waveforms for two important special cases: the case where the bodies have nearly equal masses and the case where one of the bodies has negligible spin. For these cases, for almost all choices of binary parameters, the motion is a *simple precession* of the orbital angular momentum around the nearly fixed direction of the total angular momentum, with a few tens of precession periods as the waves sweep through the LIGO/VIRGO observational band. However, when the spin and orbital angular momenta are approximately anti-aligned, there is a *transitional-precession* epoch during which their near cancellation causes the binary to "lose its gyroscopic bearings" and tumble in space, with a corresponding peculiar sweep of the waveform modulation. We also explore numerically the precessional behaviors that occur for general masses and spins; these typically appear quite similar to our special-case, simple-precession and transitional-precession solutions. An Appendix develops several diagrammatic aids for understanding intuitively the relation between the precessing orbit and the modulated waveform.

1 INTRODUCTION

Merging compact binaries–i.e., neutron star/neutron star (NS-NS), neutron star/ black hole (NS-BH), and black hole/black hole (BH-BH) binaries–are currently regarded as the most promising source of gravitational waves for the planned LIGO/VIRGO laser-interferometer detector system [1, 2, 3]. LIGO/VIRGO will have good sensitivity in the range $\sim$ 10–500 Hz, and hence will observe the last few minutes and last several thousand cycles of the inspiral waveforms.

To lowest order, the inspiral and the resulting waveform are described by the "Newtonian" quadrupole formula. Cutler et. al. [3, 4, 5] have recently pointed out that post-Newtonian corrections to the waveform, though small instantaneously, produce large cumulative effects, which may permit fairly sensitive measurements of certain combinations of the binary's masses and spins. The cumulative effects are of two types [3]: (i) Post-Newtonian corrections to the binary's inspiral rate result in a large, secular correction to the phase of the waveform. Details of this accumulating phase correction have been computed by Lincoln and Will [6], Cutler et. al. [3], Poisson [7], and Kidder, Wiseman, and Will [8], based in part on earlier work of Wagoner and Will [9], and of Blanchet, Damour, and Iyer [10, 11]; and the accuracy of the information that LIGO/VIRGO should be able to extract from the accumulating phase correction has been computed by Cutler and Flanagan [4]. (ii) Post-Newtonian spin-orbit and spin-spin couplings cause the orbital plane to precess tens of times as the waves sweep through the LIGO/VIRGO band, thereby modulating the waves' amplitude, phase, and polarization [3]. For large spins the effects on the waveform can be quite dramatic, as one can see from a brief perusal of Figs. 4.6 and 4.11–4.18 below.

In this paper we explore in detail the modulation of the waveform due to spin-induced precession. This modulation is qualitatively different from other post-Newtonian effects. Since our principal purpose in this paper is to explore this "new" behavior, we will isolate it by neglecting other post-Newtonian corrections to the waveforms. Most especially, we will neglect other effects of the bodies' spins, such as their direct wave emission and their contribution, via radiation reaction, to the waves' cumulative phase correction. These other spin effects have been explored by Kidder, Wiseman, and Will [8], by Kidder [12], and by Cutler and Flanagan [4].

The spin-induced modulation will be important not only for waves from normal-mass compact binaries ($M \sim 1$ to $10^3 M_\odot$), which lie in the LIGO/VIRGO fre-

quency band, but also for waves emitted by supermassive black-hole binaries ($M \sim 10^3 M_\odot$ to $10^7 M_\odot$) and by stars and small black holes spiraling into supermassive black holes. These low-frequency waves are targets for laser-interferometer detectors that might be flown in space in the early 21st century—e.g., the proposed LISA ("Laser Interferometer Space Antenna") mission [13], which is currently the subject of a one-year study funded by the European Space Agency.

The rest of this paper is organized as follows. In Sec. 2 we briefly review the "lowest-order" waveforms that one calculates from the binary's time-varying Newtonian quadrupole moment, neglecting spin effects. In Sec. 3.1 we write down the post-Newtonian equations that describe the precession of the orbital plane. In Sec. 3.2 we derive the equations that describe the corresponding modulation of the gravitational waveform, and in Sec. 3.3 we give a simple expression for the Fourier transform of the modulated waveform. In Sec. 4 we specialize to two important special cases, for which the precession equations simplify greatly and in the same manner: the case where the bodies have nearly equal masses and the case where one of the bodies has negligible spin. In Sec. 4.1 we write down and discuss the precession equations for these two cases, neglecting spin-spin coupling (which is of post^2-Newtonian order) but keeping spin-orbit coupling (which is of post$^{1.5}$-Newtonian order). The precession can take two forms: *simple precession* and *transitional precession. Simple precession*, which is in some sense the norm, occurs whenever the binary's total angular momentum vector is not small compared to the orbital or spin angular momenta—i.e., whenever the orbital and spin angular momenta do not conspire to almost cancel each other. In that case, we shall show, the direction of the binary's total angular momentum vector remains nearly fixed during the inspiral, and the orbital angular momentum vector (i.e., the normal to the orbital plane) precesses about that direction. In Sec. 4.2 we construct analytic expressions for simple precession and the resulting modulation of the gravitational waves. In Sec. 4.3 we examine several explicit examples of simple precession and the corresponding waveforms. In a forthcoming paper [12] he will present an analysis similar to what we present in Secs. 4.1, 4.2, and 4.3; his work will differ from–and improve upon–ours by incorporating all the post-Newtonian corrections to the waveform through post$^{3/2}$-Newtonian order (corrections which we have neglected here for simplicity), in addition to the post$^{3/2}$-Newtonian and post^2-Newtonian precessional effects.

In Sec. 4.4, we discuss the breakdown of simple precession due to near cancellation of the orbital and spin angular momenta, and we analyze the resulting

transitional precession of the orbit (a loss of gyroscopic stability which causes the binary to tumble in space) and the corresponding waveform modulation. In Sec. 5 we discuss the general case, where the bodies have arbitrary spins and masses. The precession and waveforms in the general case are qualitatively quite similar to the special cases considered in Sec. 4, as we illustrate with several numerical examples. An appendix develops concepts and tools for understanding, intuitively, the amplitude and phase modulation produced by any precession of the orbital plane.

An important question *not* addressed in this paper is how well the modulation can be measured, given realistic detector noise, and how accurately one can thereby measure the bodies' spins. We plan to address this issue in future work—in a follow-up paper to Ref. [4].

Throughout we use units where $G = c = 1$.

2 NONPRECESSING BINARIES: ORBITAL INSPIRAL AND THE LOWEST-ORDER WAVEFORM

We consider the gravity wave signal measured by a single L-shaped interferometric detector at some location on Earth. We attach a Cartesian coordinate system to the detector, with x and y axes along the detector's arms and z axis in the vertical direction as shown in Fig. 4.1. We denote unit vectors along these three axes by $\hat{x}$, $\hat{y}$, $\hat{z}$ and we denote by $\hat{N}$ the unit vector pointing towards the the source binary, and by (θ, ϕ) the spherical polar coordinates of $\hat{N}$ with respect to our Cartesian coordinates.

To further establish notation, let us review the lowest-order description of the inspiral waveform measured by such a detector; i.e., the "Newtonian, quadrupole-moment approximation" (as given in numerous references, e.g., [14]), which neglects spins, higher multipoles, and other post-Newtonian corrections. We denote by M_1 and M_2 the masses of the binary's two bodies, and by $\vec{r}(t)$ the vector pointing from M_1 to M_2 at retarded time t. We assume the orbital eccentricity is negligible (which will be true if the compact binary was born with orbital period $P \gtrsim 1$ hour and the orbit has since decayed due to gravitational radiation reaction [15]). Then the orbital angular momentum is given by

$$\vec{L} = \mu M^{1/2} r^{1/2} \hat{L} \,, \tag{4.1}$$

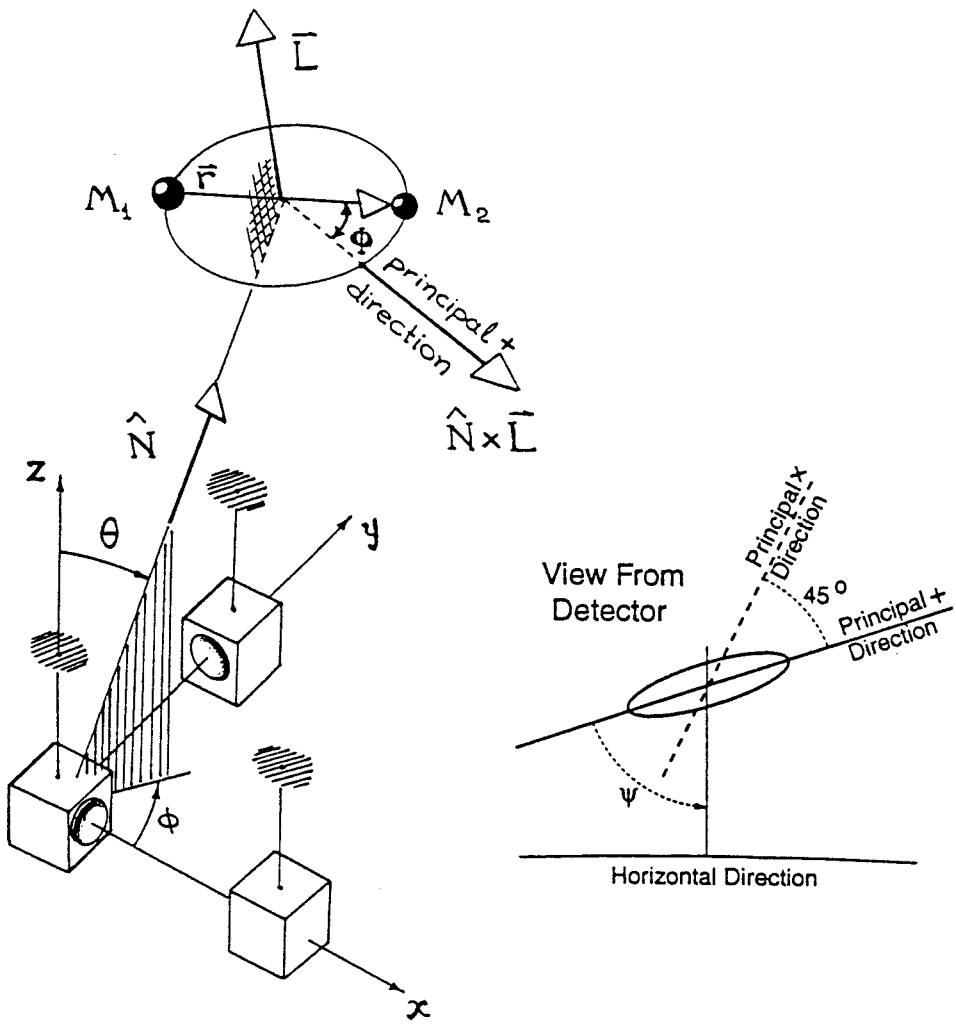

Figure 4.1: A Cartesian coordinate system (x, y, z) attached to a gravitational-wave detector, and the geometry of a coalescing binary relative to these coordinates.

where $M \equiv M_1 + M_2$ is the binary's total mass, $\mu \equiv M_1 M_2/M$ is its reduced mass, $r \equiv |\vec{r}|$ is its orbital diameter, and $\hat{L}$ is the unit vector along $\vec{L}$.

The binary's circular orbit, when projected on the plane of the sky at the detector's location (i.e., projected orthogonal to the waves' propagation direction), looks elliptical; see inset in Fig. 4.1. The principal axis of this orbital ellipse, which points along $\pm\hat{N} \times \hat{L}$, will be called the waves' *principal+ direction*; an axis that is rotated counterclockwise from it by 45° in the plane of the sky will be called the waves' *principal× direction.* We resolve the waves into two polarization states: the *principal+ state* with polarization axes along and perpendicular to the principal+ direction, and the *principal× state* with polarization axes along and perpendicular to the principal× direction. Any plane-fronted gravitational wave traveling in the $-\hat{N}$ direction can be written as some linear combination $h_+(t)\times$ {*principal+ polarization tensor*} plus $h_\times(t)\times$ {*principal× polarizaton tensor*}, where $h_+(t)$ and $h_\times(t)$ are positive, by convention, whenever the tidal deformations along the principal+ and principal× directions are stretches (as opposed to compressions).

With these conventions, in the Newtonian, quadrupole-moment approximation, the gravitational-wave fields $h_+(t)$ and $h_\times(t)$ are given by

$$h_+(t) = -\frac{2\mu M}{rD}\left[1 + (\hat{L}\cdot\hat{N})^2\right]\cos 2\Phi(t)\ , \tag{4.2}$$

$$h_\times(t) = -\frac{2\mu M}{rD}\left[-2\hat{L}\cdot\hat{N}\right]\sin 2\Phi(t)\ . \tag{4.3}$$

Here D is the distance to the source and $\Phi(t)$ is the angle in the orbital plane from the principal+ direction $\pm\hat{N}\times\hat{L}$ to the bodies' separation vector $\vec{r}$; see Fig. 4.1. The overall minus sign in Eqs. (4.2), (4.3) results from the fact that the waves' tidal distortion is a squeeze, not a stretch, along the transverse projection of the stars' retarded separation vector $\vec{r}(t)$; see the Appendix.

The strain $h(t)$ that the waves produce in the interferometric detector is the following linear combination of $h_+(t)$ and $h_\times(t)$,

$$h(t) = F_+(\theta,\phi,\psi)h_+(t) + F_\times(\theta,\phi,\psi)h_\times(t)\ , \tag{4.4}$$

where F_+ and $F_\times$ are "detector beam-pattern" coefficients that depend in the following way on the source direction (θ,ϕ) and on a *polarization angle* ψ:

$$\begin{aligned} F_+(\theta,\phi,\psi) &= \frac{1}{2}(1+\cos^2\theta)\cos 2\phi\cos 2\psi \\ &\quad - \cos\theta\sin 2\phi\sin 2\psi\ , \\ F_\times(\theta,\phi,\psi) &= \frac{1}{2}(1+\cos^2\theta)\cos 2\phi\sin 2\psi \end{aligned} \tag{4.5}$$

$$+\cos\theta\sin 2\phi\cos 2\psi\ . \tag{4.6}$$

The polarization angle ψ (shown in the lower-right inset of Fig. 4.1) is the angle from the principal+ direction, $\pm\hat{N}\times\hat{L}$, clockwise in the plane of the sky to the direction of constant azimuth, $\pm\hat{N}\times(\hat{N}\times\hat{z}) = \pm[-\hat{z}+\hat{N}(\hat{N}\cdot\hat{z})]$. (The $\pm$ signs are included because ψ is defined only modulo π.) In other words, up to an arbitrary multiple of π,

$$\psi = \tan^{-1}\left(\frac{\hat{L}\cdot\hat{z} - (\hat{L}\cdot\hat{N})(\hat{z}\cdot\hat{N})}{\hat{N}\cdot(\hat{L}\times\hat{z})}\right)\ . \tag{4.7}$$

[**Note:** In Figs. 9.2, 9.8, and 9.9 of Ref. [14], ψ is shown with the wrong sign (i.e., opposite to the above). The error is confined to those figures; the equations in Ref. [14] are all in accord with the sign convention used here.]

In the next section we shall divide the precession's modulational effects into an amplitude modulation and a phase modulation. To aid in this, we rewrite the signal strain (4.4) in the conventional amplitude-and-phase form

$$h(t) = -A(t)\cos[2\Phi(t)+\varphi]\ , \tag{4.8}$$

where $A(t)$ and φ (not to be confused with the source's direction angle ϕ) are given by

$$\begin{aligned} A(t) &= \frac{2\mu M}{rD}\Big([1+(\hat{L}\cdot\hat{N})^2]^2 {F_+}^2(\theta,\phi,\psi) \\ &\qquad +4[\hat{L}\cdot\hat{N}]^2 {F_\times}^2(\theta,\phi,\psi)\Big)^{1/2}\ , \end{aligned} \tag{4.9}$$

$$\varphi = \tan^{-1}\left(\frac{2\hat{L}\cdot\hat{N}\ F_\times(\theta,\phi,\psi)}{[1+(\hat{L}\cdot\hat{N})^2]F_+(\theta,\phi,\psi)}\right)\ . \tag{4.10}$$

We will refer to φ as the signal's *polarization phase.* We have defined the amplitude-and-phase decomposition (4.9), (4.10) with an overall minus sign to emphasize the fact that the waves' tidal distortion is a squeeze, not a stretch, along the transverse projection of the stars' separation vector $\vec{r}$; cf. the Appendix.

Equations (4.4)—(4.10) describe the waves in terms of the direction to the source $\hat{N}$ [and its polar angles (θ,ϕ) relative to the detector's Cartesian coordinates], the vertical direction $\hat{z}$ at the detector, the normal $\hat{L}$ to the binary's orbital plane (and the associated polarization angle ψ), and the binary's total mass M, reduced mass μ, orbital diameter r, orbital phase Φ, and distance from Earth D. When we ignore the orbital precession, then all of these quantities are constant in time except the orbital diameter $r(t)$ and orbital phase $\Phi(t)$. We obtain $r(t)$ by

integrating the inspiral rate $dr/dt = (dE/dt)/(dE/dr)$, where we use the Newtonian expression for the energy, $E = -\frac{1}{2}\mu M/r$, and the energy-loss rate given by the quadrupole formula, $dE/dt = -\frac{32}{5}\mu^2 M^3/r^5$. The (well-known) result is

$$r(t) = \left(\frac{256}{5}\mu M^2\right)^{1/4} (t_c - t)^{1/4}, \tag{4.11}$$

where t_c is the "collision time" at which (formally) $r \to 0$.

In the absence of precession, $\dot{\Phi} \equiv d\Phi/dt$ is simply the angular velocity Ω of the two bodies in the orbital plane. However since our definition of Φ depends explicitly on the direction $\hat{L}$ (cf. Fig. 4.1), $\dot{\Phi}$ will not be equal to Ω when $\hat{L}$ is time-varying. To deal with this, whether the orbit is precessing or not we define the *carrier* phase of the waveform by

$$\Phi_C(t) \equiv \int \Omega(t) dt. \tag{4.12}$$

The term "carrier" is intended to recall the carrier signal used in radio transmission —an analogy that we will make clear below, in Sec. 3.3.

We find it convenient to specify the constant of integration in Eq. (4.12) so that $\Phi_C(t_c) \equiv \Phi(t_c)$, whether the orbit is precessing or not. Evaluating the integral in Eq. (4.12) using $\Omega = M^{1/2}/r^{3/2}$ along with Eq. (4.11), we find that to lowest order in M/r,

$$\Phi_C(t) = \Phi(t_c) - \left[\frac{1}{5}\left(\mu^{3/5} M^{2/5}\right)^{-1} (t_c - t)\right]^{5/8}. \tag{4.13}$$

To reiterate, if one ignores precession, then $\Phi(t)$ is simply $\Phi_C(t)$.

Spin-induced precession causes one other quantity besides r and Φ to be time-dependent in the waveform equations (4.4)—(4.10): the direction $\hat{L}$ of the orbital angular momentum. In the next section we describe the motion of $\hat{L}$ and the corresponding modulation of the waveform.

3 SPIN-INDUCED PRECESSION AND WAVEFORM MODULATION

3.1 Equations describing orbital precession and inspiral

We now consider the binary's spin-induced orbital precession. Let the bodies have spin angular momenta $\vec{S}_1$ and $\vec{S}_2$, respectively. For black holes, there is a strict upper limit on the magnitude of the spins: $|\vec{S}_i| \leq M_i^2$. For neutron stars the upper

limit is comparable, but depends somewhat on the (uncertain) nuclear equation of state. Most candidate equations of state yield an upper limit of $|\vec{S}_i| \lesssim \frac{1}{2}M_i^2$ for uniformly rotating neutron stars [16]. To simplify the discussion, below we will assume $|\vec{S}_i| \leq M_i^2$ for all bodies.

Approximate equations of precession for the binary's spins and orbit have been derived in a variety of ways by a number of researchers; see, e.g., Barker and O'Connell [17] for a derivation that assumes gravity is weak throughout the binary, and Hartle and Thorne [18] for a derivation that permits the bodies' internal gravity to be arbitrarily strong but requires their gravitational interaction to be weak. After specializing to circular orbits and after averaging over one orbit, the precession equations take the following form, accurate through post^2-Newtonian order:

$$\begin{aligned}
\dot{\vec{L}} &= \frac{1}{r^3}\left[\frac{4M_1+3M_2}{2M_1}\vec{S}_1 + \frac{4M_2+3M_1}{2M_2}\vec{S}_2\right]\times\vec{L} \\
&\quad -\frac{3}{2}\frac{1}{r^3}[(\vec{S}_2\cdot\hat{L})\vec{S}_1 + (\vec{S}_1\cdot\hat{L})\vec{S}_2]\times\hat{L} \\
&\quad -\frac{32}{5}\frac{\mu^2}{r}\left(\frac{M}{r}\right)^{5/2}\hat{L}\,, \qquad (4.14)\\
\dot{\vec{S}}_1 &= \frac{1}{r^3}\left[\frac{4M_1+3M_2}{2M_1}(\mu M^{1/2}r^{1/2})\hat{L}\right]\times\vec{S}_1 \\
&\quad +\frac{1}{r^3}\left[\frac{1}{2}\vec{S}_2 - \frac{3}{2}(\vec{S}_2\cdot\hat{L})\hat{L}\right]\times\vec{S}_1\,, \qquad (4.15)\\
\dot{\vec{S}}_2 &= \frac{1}{r^3}\left[\frac{4M_2+3M_1}{2M_2}(\mu M^{1/2}r^{1/2})\hat{L}\right]\times\vec{S}_2 \\
&\quad +\frac{1}{r^3}\left[\frac{1}{2}\vec{S}_1 - \frac{3}{2}(\vec{S}_1\cdot\hat{L})\hat{L}\right]\times\vec{S}_2\,. \qquad (4.16)
\end{aligned}$$

Here a '$\cdot$' represents 'd/dt' and to this order of approximation, $r(t)$ is given by Eq. (4.11) and $L(t) = \mu(Mr)^{1/2}$ [Eq. (4.1)]. The first square bracketed terms in Eqs. (4.14)—(4.16), which involve just one spin $\vec{S}$, are due to post$^{1.5}$-Newtonian-order spin-orbit coupling, and the second square-bracketed terms, involving two $\vec{S}$'s, are due to post^2-Newtonian-order spin-spin coupling. The last term in $d\vec{L}/dt$ [Eq. (4.14)] is due to radiation reaction [cf. Eqs. (4.1) and (4.11)]; it is the only term that changes the magnitude of any of the angular momenta. Note that the change in the total vectorial angular momentum $\vec{J} \equiv \vec{L} + \vec{S}_1 + \vec{S}_2$ is entirely due to this radiation-reaction term; Eqs. (4.14)—(4.16) imply that

$$\dot{\vec{J}} = \dot{\vec{L}}^{(\mathrm{react})} = -\frac{32}{5}\frac{\mu^2}{r}\left(\frac{M}{r}\right)^{5/2}\hat{L}\,. \qquad (4.17)$$

In Sec. 4, we will derive approximate, analytic solutions for $\hat{L}(t)$ for special cases. Before doing so, however, we must deal with a few other issues:

In writing the angular-momentum evolution equations in the form (4.14)—(4.16), we have used the fact that, to lowest order, radiation reaction causes $|\vec{L}| = L$ to decrease, but does not affect $|\vec{S}_1|$ and $|\vec{S}_2|$. Since this fact might not be obvious, we now demonstrate it by computing the leading-order radiation-reaction torque on the binary's bodies. We restrict attention to the radiation reaction torque on body 1; the same argument will apply to body 2. Since our goal is an order of magnitude estimate and not an exact equation, we shall simplify the calculation by treating body 1 formally as a Newtonian-order star, and we shall set $\mu \sim M_1 \sim M_2 \sim M$, and let the radius of star 1 (which is actually a neutron star or black hole) be of order its gravitational radius, $R_1 \sim M_1 \sim M$, and let the star's spin be of order its maximum allowed value, $S_1 \sim {M_1}^2 \sim M^2$. The gravitational radiation-reaction potential inside the star is given by [19] :

$$\Phi^{(\text{react})} = \frac{1}{5}\frac{d^5\mathcal{I}_{jk}}{dt^5}x^j x^k \ , \tag{4.18}$$

where $\mathcal{I}_{jk}$ is the binary's quadrupole-moment tensor, and in order of magnitude

$$d^5\mathcal{I}_{jk}/dt^5 \sim \mu r^2\Omega^5 \sim M^{7/2}r^{-11/2} \ . \tag{4.19}$$

Inside star 1 we introduce coordinates $\bar{x}^i \equiv x^i - {x_1}^i$, where ${x_1}^i$ is the star's center of mass. Then the radiation reaction acceleration $-\nabla\Phi^{(\text{react})}$ produces a torque $\vec{\tau}$ on star 1 (about its center-of-mass), whose components are

$$\tau^i = -\epsilon^{ijk}\frac{2}{5}\frac{d^5 I_{kl}}{dt^5}\int(\rho\bar{x}_j\bar{x}^l)dV_1 \ , \tag{4.20}$$

where ρ is the star's density, and the integral is taken over star 1. Because tidal distortions of the shape of the star are extremely small (see below), to high accuracy the star is axisymmetric about its spin axis; this symmetry, together with our assumptions that $R_1 \sim M_1 \sim M$ and that the star is rapidly rotating and thus strongly centrifugally flattened, implies that

$$\int(\rho\bar{x}_j\bar{x}^l)dV_1 = M^3(a\,{\delta_j}^l + b\,\hat{S}_{1j}\hat{S}_1^l) \tag{4.21}$$

for some a and b that are dimensionless and of order unity. The term $a\,{\delta_j}^l$ vanishes when contracted into $\epsilon^{ijk}d^5\mathcal{I}_{kl}/dt^5$, so

$$\begin{aligned}\tau^i &= -\frac{2}{5}b\,\epsilon^{ijk}\frac{d^5\mathcal{I}_{kl}}{dt^5}M^3\hat{S}_{1j}\hat{S}_1^l \\ &\sim M^{13/2}r^{-11/2} \ .\end{aligned} \tag{4.22}$$

Here, in the second line, we have used Eq. (4.19). Notice the following: (i) In order of magnitude, the radiation-reaction torque (4.22) is smaller by $\sim (M/r)^3$, i.e. by three full post-Newtonian orders, than the spin-orbit coupling torque (4.15), and smaller by two full orders than the radiation-reaction-induced loss of orbital angular momentum, dL/dt. (ii) The scalar product of the radiation-reaction torque (4.22) with $\vec{S}_1$ vanishes (by the antisymmetry of ϵ^{ijk}), so at this leading order in the radiation reaction, the magnitude of the body's spin, S_1, remains constant. (iii) To produce a change in S_1, the radiation-reaction acceleration must couple to a nonaxially symmetric piece of $\int(\rho\bar{x}_j\bar{x}^l)dV_1$. The dominant deviation from axisymmetry is due to tidal distortion by the gravity of the star's companion, and it is smaller by $(M/r)^3$ than the axisymmetric part of $\int(\rho\bar{x}_j\bar{x}^l)dV_1$. Correspondingly, the S_1-changing piece of the radiation-reaction torque will be a full five post-Newtonian orders smaller than dL/dt, and we can safely ignore it.

The spin-up of the bodies due to tidal interactions is also negligible for the cases of interest to us, as shown by Bildsten and Cutler [20].

3.2 Equations describing the modulation of the waveform

In this section we describe the modulation of the waveform caused by the orbital precession. A key point is that (as we show below), the orbital period is much shorter than the timescale for $\hat{L}$ to change significantly; i.e., $\hat{L}$ is roughly constant over many gravity wave cycles. Therefore to a good approximation we can simply take over the expressions (4.2)—(4.10) for the wave fields $H_+(t)$ and $h_\times(t)$, and the detector-measured waveform amplitude $A(t)$ and polarization phase $\varphi(t)$, but plug into those expressions the time-varying $\hat{L}(t)$ obtained by solving the precession equations (4.14)—(4.16). This approximation will be correct up to terms of order the precession frequency over the gravity wave frequency.

Note that the expressions for $h_+(t)$, $h_\times(t)$, $A(t)$ and $\varphi(t)$ in Eqs (4.4)—(4.10) depend on $\hat{L}(t)$ explicitly through the $\hat{L}\cdot\hat{N}$ terms and implicitly through ψ. Thus, to be completely explicit, our precession-modulated fields and gravitational waveform are

$$h_+(t) = -\frac{2\mu M}{rD}\left[1+(\hat{L}(t)\cdot\hat{N})^2\right]\cos 2\Phi(t)\,, \tag{4.23}$$

$$h_\times(t) = -\frac{2\mu M}{rD}\left[-2\hat{L}(t)\cdot\hat{N}\right]\sin 2\Phi(t)\,, \tag{4.24}$$

$$h(t) = -A(t)\cos[2\Phi(t)+\varphi(t)]\,, \tag{4.25}$$

where

$$A(t) = \frac{2\mu M}{rD}\Big([1+(\hat{L}(t)\cdot\hat{N})^2]^2 {F_+}^2(\theta,\phi,\psi(t)) + 4[\hat{L}(t)\cdot\hat{N}]^2 {F_\times}^2(\theta,\phi,\psi(t))\Big)^{1/2}, \tag{4.26}$$

$$\varphi(t) = \tan^{-1}\left(\frac{2\hat{L}(t)\cdot\hat{N}\ F_\times(\theta,\phi,\psi(t))}{[1+(\hat{L}(t)\cdot\hat{N})^2]F_+(\theta,\phi,\psi(t))}\right). \tag{4.27}$$

and where

$$\psi(t) = \tan^{-1}\left(\frac{\hat{L}(t)\cdot\hat{z} - (\hat{L}(t)\cdot\hat{N})\,(\hat{z}\cdot\hat{N})}{\hat{N}\cdot(\hat{L}(t)\times\hat{z})}\right). \tag{4.28}$$

Intuitive, diagrammatric methods for visualizing the $\hat{L}(t)$-induced modulation of A and φ, for the special cases where the source is directly underfoot or overhead, are given in the Appendix.

In addition to the modulation of the polarization phase φ discussed above, there is an additional modulation of the waveform phase due to an effect which is akin to the Thomas precession of the electron's spin in a semiclassical model of the hydrogen atom. Recall that in Sec. 2 we introduced a distinction between the carrier phase $\Phi_C(t)$ defined as the integral $\int \Omega dt$ of the bodies' angular velocity in the orbital plane, and $\Phi(t)$, defined as the angle between the orbital separation vector $\hat{r}$ and the principal+ direction $\pm\hat{L}\times\hat{N}$. (The latter definition was required in order for Eqs. (4.2), (4.3) for $h_+(t)$ and $h_\times(t)$ to be valid.) We emphasize that we are *not* presently concerned with corrections to the waveform phase $\Phi(t)$ that are due to post-Newtonian corrections to $\Omega(r)$ or $\dot{\Omega}(r)$. Rather, we are calculating that correction to $\Phi(t)$ which arises from the changing orientation of the orbital plane, *even if we take* Ω *and* $\dot{\Omega}$ *to have their lowest-order, "Newtonian" values.* We define the *precessional correction to the orbital phase* $\delta\Phi(t)$ by

$$\Phi(t) \equiv \Phi_C(t) + \delta\Phi(t)\,, \tag{4.29}$$

and we now proceed to find an expression for $\delta\Phi$ in terms of $\hat{L}(t)$.

By definition, the unit orbital separation vector is

$$\hat{r} = \cos\Phi(t)\,\hat{\zeta} + \sin\Phi(t)\,\hat{L}\times\hat{\zeta} \tag{4.30}$$

where

$$\hat{\zeta} \equiv \frac{\hat{L}\times\hat{N}}{[1-(\hat{L}\cdot\hat{N})^2]^{1/2}} \tag{4.31}$$

is the principal+ direction. We also have

$$\dot{\hat{r}} = \Omega\,\hat{L}\times\hat{r} - (\dot{\hat{L}}\cdot\hat{r})\,\hat{L}\,. \tag{4.32}$$

The first term on the right side of Eq. (4.32) rotates $\hat{r}$ about $\hat{L}$, while the second term insures that $\hat{r}$ remains orthogonal to $\hat{L}$; the second term basically corresponds to "Fermi-Walker transport" of $\hat{r}$ due to the precession of the orbital plane. From Eq. (4.30) we have

$$\cos\Phi(t) = \hat{\zeta}\cdot\hat{r}. \tag{4.33}$$

Taking d/dt of Eq. (4.33) and using Eqs. (4.30) and (4.32), we obtain

$$\begin{aligned} -\dot{\Phi}\sin\Phi &= \dot{\hat{\zeta}}\cdot\hat{r} + \hat{\zeta}\cdot\dot{\hat{r}} \\ &= \dot{\hat{\zeta}}\cdot\hat{r} - \Omega\sin\Phi \end{aligned} \tag{4.34}$$

or [from Eqs. (4.29) and (4.12)]

$$\delta\dot{\Phi} = -\dot{\hat{\zeta}}\cdot\hat{r}/\sin\Phi. \tag{4.35}$$

Using the definition (4.31) of $\hat{\zeta}$ and expression (4.30) for $\hat{r}$, a few lines of algebra allow us to rewrite Eq. (4.35) as

$$\delta\dot{\Phi} = \left(\frac{\hat{L}\cdot\hat{N}}{1-(\hat{L}\cdot\hat{N})^2}\right)(\hat{L}\times\hat{N})\cdot\dot{\hat{L}}\,. \tag{4.36}$$

This equation must be integrated subject to the boundary condition that $\delta\Phi = 0$ at the endpoint of the coalescence [Eq. (4.13) and associated discussion]; therefore,

$$\delta\Phi(t) = -\int_t^{t_c}\left(\frac{\hat{L}\cdot\hat{N}}{1-(\hat{L}\cdot\hat{N})^2}\right)(\hat{L}\times\hat{N})\cdot\dot{\hat{L}}\,dt\,. \tag{4.37}$$

This integral cannot be expressed in terms of $\hat{N}$ and the instantaneous value of $\hat{L}$ at time t; it depends on the full time history of $\hat{L}$ between times t and t_c [as one can readily verify by expressing the integrand as $\vec{F}\cdot d\hat{L}$ and then noting that the curl of $\vec{F}$ (in $\hat{L}$-space) is nonzero].

In summary, our precession-modulated waveform is

$$h(t) = -A(t)\cos[2\Phi_C(t) + 2\delta\Phi(t) + \varphi(t)]\,. \tag{4.38}$$

Here $\Phi_C(t)$ is the integral of $\Omega(t)$, which is given to lowest (Newtonian) order by Eq. (4.13). To determine $A(t)$, $\varphi(t)$, and $\delta\Phi(t)$ one solves Eqs. (4.14)—(4.16) for $\hat{L}(t)$ and plugs the result into Eqs. (4.26), (4.27), (4.28) and (4.37).

We note that $\delta\Phi(t)$ depends on $\hat{L}(t)$ and the location of the binary on the sky, but is independent of the orientation of the detector arms. By contrast, $A(t)$ and $\varphi(t)$ *do* depend on the detector orientation, through the terms F_+ and $F_\times$ in Eqs. (4.26)—(4.28).

3.3 Fourier transform of the modulated signal

In this section we derive a simple expression for the Fourier transform of the precession-modulated signal,

$$\tilde{h}(f) \equiv \int_{-\infty}^{+\infty} df\, e^{2\pi i f t}\, h(t)\,. \tag{4.39}$$

This is useful for the following reason. The process of searching for a merging-binary waveform $h(t)$ in LIGO/VIRGO data will consist of beating the "Wiener-filtered" version of the waveform, $h_W(t)$, against the measured detector strain $s(t)$; i.e., taking the inner product

$$\int_{-\infty}^{+\infty} s(t) h_W(t) dt. \tag{4.40}$$

Here the Wiener-filtered waveform $h_W(t)$ is defined by the equation

$$\tilde{h}_W(f) \equiv \tilde{h}(f)/S_h(f) \tag{4.41}$$

where $S_h(f)$ is the spectral density of the detector noise. (We refer the reader to Ref. [14] for the definition of $S_h(f)$ and for a discussion of noise sources in the LIGO/VIRGO detectors, and to Ref. [1] for estimates of $S_h(f)$ in the first LIGO detectors and more advanced LIGO detectors).

Radio transmission provides a useful analogy for an intuitive understanding of signal modulation. The unmodulated signal is like the radio station's high-frequency *carrier* signal, while the effect of precession on the gravity waveform is like the modulation. [The analogy becomes better in the limit that the smaller mass $M_2 \to 0$, since then the inspiral rate also approaches zero and (the quadrupole piece of) the unmodulated "carrier" waveform becomes truly monochromatic.] In this spirit, let us define a complex "carrier" signal $h_C(t)$ by

$$h_C(t) \equiv \frac{M_1 M_2}{D\, r(t)} e^{-2i\Phi_C(t)} \tag{4.42}$$

where $\Phi_C(t) = \int \Omega dt$ is the carrier phase we defined in Eqs. (4.12) and (4.13). The Fourier transform of the carrier signal can be calculated approximately using the stationary phase method, which yields

$$\tilde{h}_C(f) \approx \begin{cases} \frac{M_1 M_2}{D\, r(t)} (i df/dt)^{-1/2} e^{i[2\pi f t - 2\Phi_C(t)]} & \text{for } f > 0 \\ 0 & \text{for } f < 0\,, \end{cases} \tag{4.43}$$

where $t \equiv t(f)$ is the time at which the carrier frequency, $\dot{\Phi}_C/\pi = \Omega/\pi$, equals f. The difference between expression (4.43) and the actual Fourier transform of $h_C(t)$

is of order the ratio of orbital period to inspiral timescale, which is negligible for cases of interest.

We next define a complex modulation factor

$$\Lambda(t) \equiv A(t)\left[\frac{M_1 M_2}{D\, r(t)}\right]^{-1} e^{-i[2\delta\Phi(t)+\varphi(t)]} . \tag{4.44}$$

Then $h(t) = \Re\left\{\Lambda(t)\,\tilde{h}_C(t)\right\}$, where "$\Re$" means "the real part of". Since $\Lambda(t)$ varies much more slowly than $2\Phi_C(t)$, we can again use the stationary phase method to approximate $\tilde{h}(f)$; the result is

$$\tilde{h}(f) \approx \begin{cases} \frac{1}{2}\Lambda(t(f))\,\tilde{h}_C(f) & \text{for } f > 0 \\ \frac{1}{2}\Lambda^*(t(|f|))\,\tilde{h}_C^*(|f|) & \text{for } f < 0 . \end{cases} \tag{4.45}$$

The factor $\frac{1}{2}$ in Eq. (4.45) arises because the real and imaginary parts of $\Lambda(t)\,\tilde{h}_C(t)$ contribute equally to the Fourier transform, in the stationary phase approximation.

The stationary phase result given above [Eq. (4.45)] differs from the true $\tilde{h}(f)$ by terms of order the ratio of the orbital period to the precession period; i.e., the stationary phase method computes $\tilde{h}(f)$ less accurately than $\tilde{h}_C(f)$, because the precession timescale is much shorter than the inspiral timescale. We can improve our calculation of $\tilde{h}(f)$ as follows. The stationary phase results quoted above can be viewed as merely the lowest-order results in a power series expansion for the true Fourier transform, where the expansion parameter is the ratio of the orbital period to the precession period. We improve Eq. (4.45) by adding the next-order term in the expansion; the result is

$$\tilde{h}(f) \approx \frac{1}{2}\,\Lambda(t)\tilde{h}_C(f) + \frac{1}{4\pi i}\frac{d\Lambda}{dt}\left[\frac{d\tilde{h}_C(f)}{df} - 2\pi i t \tilde{h}_C(f)\right] \tag{4.46}$$

for positive f, and the complex conjugate of this for negative f. Here, again, $t = t(f)$ is the time at which the carrier frequency Ω/π is equal to f. The formula given in Eq. (4.46) differs from the true $\tilde{h}(f)$ by terms of order (orbital period/inspiral timescale) and terms of order (orbital period/precession period)^2.

In this paper, for simplicity, we use only the lowest-order version of the carrier signal $h_C(t)$, and our derivation of $\Lambda(t)$ is of similarly low order. However our formula (4.46) has the virtue that it can be applied essentially without modification to versions of $h_C(t)$ and $\Lambda(t)$ that are correct to higher post-Newtonian order. One just plugs the more accurate versions of $\tilde{h}_C(f)$ and $\Lambda(t)$ into Eq. (4.46), while also using an improved version of $t(f)$. [Actually, the above statement applies only to the dominant, mass-quadrupole piece of the waveform. If one includes the radiation

due to the binary's time-varying current-quadrupole and mass-octupole moments (or other, higher-order moments) then the situation is somewhat more complicated, since different moments emit gravitational radiation at different harmonics of the orbital frequency, and their contributions to h_+ and $h_\times$ have different dependences on $\hat{L}\cdot\hat{N}$ than those given in Eqs. (4.2), (4.3).]

4 BINARIES WITH $M_1 \simeq M_2$ OR $S_2 \simeq 0$

4.1 Orbital evolution equations, and approximate description of the evolution

In this section we construct approximate, analytic solutions of the inspiral and precession equations (4.14)—(4.16) for two important special cases: 1) $M_1 = M_2$ and 2) $\vec{S}_2 = 0$. Both cases are of interest. The prototypical example where $M_1 \simeq M_2$ would be an NS/NS merger, since measured neutron star masses all cluster near $1.4M_\odot$. The prototypical example where $\vec{S}_2$ can be neglected would be a neutron star spiraling into a much larger, rapidly rotating black hole. In that case, the black-hole spin $\vec{S}_1$ will dominate the orbital precession unless $\vec{S}_1$ is nearly parallel or antiparallel to $\vec{L}$.

Our first approximation is that *we neglect the spin-spin terms in the $M_1 = M_2$ case.* These neglected terms are of post^2-Newtonian order and thus will typically be small compared to the post$^{3/2}$-Newtonian spin-orbit terms, which we retain. Given this approximation, the orbital evolution equations (4.14)—(4.16) imply that $\vec{S}_1\cdot\vec{S}_2$ is constant in time and therefore the total spin vector

$$\vec{S} \equiv \vec{S}_1 + \vec{S}_2 \tag{4.47}$$

has constant magnitude. Then, *for both of our special cases*, the inspiral and precession equations (4.14)—(4.16) can be brought into the following simple form:

$$\dot{L} = \frac{-32}{5}\frac{\mu^2}{r}\left(\frac{M}{r}\right)^{5/2}, \tag{4.48}$$

$$\dot{S} = 0, \tag{4.49}$$

$$\dot{\hat{L}} = \left(2+\frac{3M_2}{2M_1}\right)\frac{\vec{J}}{r^3}\times\hat{L}, \tag{4.50}$$

$$\dot{\hat{S}} = \left(2+\frac{3M_2}{2M_1}\right)\frac{\vec{J}}{r^3}\times\hat{S}. \tag{4.51}$$

Here

$$\vec{J} = \vec{L} + \vec{S} \tag{4.52}$$

is the binary's total angular momentum and

$$S = |\vec{S}| \quad \text{and} \quad \hat{S} = \vec{S}/S \tag{4.53}$$

are the magnitude and direction of the total spin.

Let us first describe qualitatively the solutions of the evolution equations (4.48)—(4.51). The orbital evolution can be divided into two pieces: 1) a precession of the plane containing $\vec{L}$ and $\vec{S}$, and 2) the motion of these vectors in this plane. The in-plane evolution is driven by the radiation-reaction-induced orbital shrinkage. This shrinkage causes the length L of $\vec{L}$ to decrease, but leaves constant the length S of $\vec{S}$ [Eq. (4.49)] and the angle $\arccos(\hat{L} \cdot \hat{S})$ between $\vec{L}$ and $\vec{S}$ [cf. Eqs. (4.50), (4.51)]. This evolution is depicted in Fig. 4.2. Note that the angle between $\vec{L}$ and $\vec{J}$ must continually increase.

The precession of the plane containing $\vec{L}$ and $\vec{S}$ can take one of two qualitatively different forms, which we shall call *simple precession* and *transitional precession.* We shall devote four paragraphs to simple precession, and then shall describe transitional precession.

In *simple precession*, $\hat{S}$ and $\hat{L}$ both precess around $\hat{J}$ with an angular velocity

$$\Omega_p = \left(2 + \frac{3M_2}{2M_1}\right)\frac{J}{r^3} \tag{4.54}$$

[cf. Eqs. (4.50), (4.51)] that is fast compared to the orbital inspiral rate $\dot{L}/L$. Because $\vec{L}$ precesses around $\hat{J}$, the value of

$$\dot{\vec{J}} = \dot{L}\hat{L} \tag{4.55}$$

[cf. Eqs. (4.48)—(4.51)], averaged over one precession, is nearly parallel to $\vec{J}$, and therefore to a reasonable approximation $\vec{J}$ changes in magnitude but not in direction; this approximation becomes exact in the limit that $\dot{L}/(\Omega_p J) \to 0$.

We can integrate Eq. (4.54) to obtain a back-of-the-envelope estimate of the number of precessions in the observable inspiral, and to see how the precession rate scales with the frequency of the emitted gravity waves. We define the precession angle α by

$$d\alpha/dt = \Omega_p \, . \tag{4.56}$$

We consider two limiting cases: $L \gg S$ and $S \gg L$. When $L \gg S$, $J \approx L$, so $d\alpha/dt \propto L/r^3 \propto r^{-2.5}$. Eq. (4.11) then implies that $dr/dt \propto r^{-3}$, so $d\alpha/dr \propto r^{1/2}$.

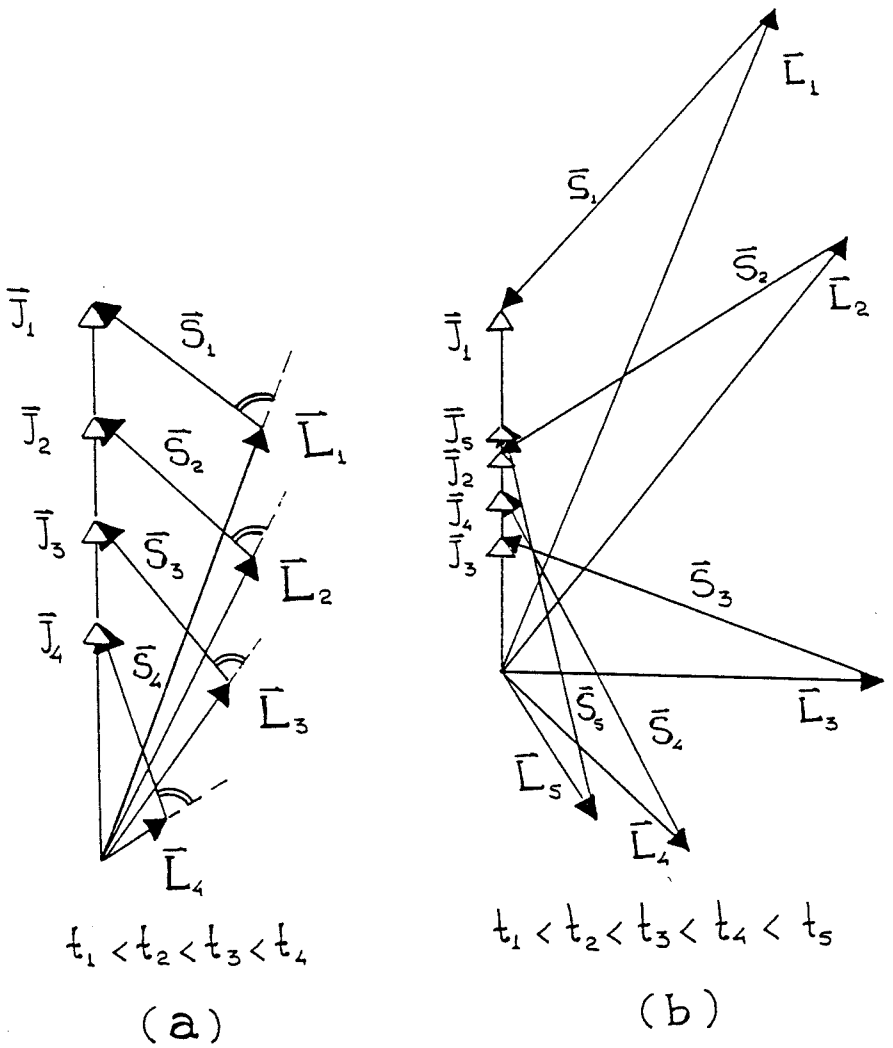

Figure 4.2: The in-plane evolution of the total spin angular momentum $\vec{S}$, orbital angular momentum $\vec{L}$ and total angular momentum $\vec{J}$ for binaries governed by Eqs. (4.48)—(4.51). When $\vec{L}$ and $\vec{S}$ are nearly oppositely directed as in drawing (b), the precession initially is simple, then at times $t \sim t_3$ it becomes transitional, then it returns to simple. In case (a), the precession is always simple.

Since here we are only interested in the change in α, we set $\alpha = 0$ when $r = 0$. Then $\alpha(r) \propto r^{3/2}$, or $\alpha(f) \propto f^{-1}$, where f is the frequency of the emitted gravity waves at orbital separation r. Thus, of all the precessions that occur in the "observable" frequency range $10 - 1000$ Hz, 90% of them occur in the range $10 - 100$ Hz. That is, most of the precessions occur at *low* frequencies. When $S \gg L$, $J \approx S$, so $d\alpha/dt \propto S/r^3$. Hence $d\alpha/dr$ is constant, so $\alpha(r) \propto r$ and $\alpha(f) \propto f^{-2/3}$. Thus, when $S \gg L$, roughly 80% of the precessions in the observable frequency range occur between 10 and 100Hz. Typical cases of simple precession will be intermediate between these two limiting cases, so we can expect $80 - 90\%$ of the "observable" precessions to occur in the $10 - 100$Hz frequency range.

Putting back the constant factors that we omitted in the above scaling analysis, we find

$$\frac{\alpha(f)}{2\pi} \approx \begin{cases} 11\,(1 + \frac{3M_1}{4M_2})\,\frac{10M_\odot}{M}\,\frac{10\text{Hz}}{f} & \text{for } L \gg S, \\ 1.9\,(1 + \frac{3M_1}{4M_2})\,\frac{M_1}{M_2}\,\frac{S}{M_1{}^2}\,(\frac{10M_\odot}{M}\,\frac{10\text{Hz}}{f})^{2/3} & \text{for } S \gg L. \end{cases} \tag{4.57}$$

Note that when $L \gg S$, the number of precessions is independent of S. This is an important point: slowly spinning bodies produce roughly as many precessions as rapidly spinning ones; however the cone of precession is narrow if S is small.

The "simple" precession of $\vec{L}$ and $\vec{S}$ around a nearly constant $\hat{J}$, which we have been discussing, can break down and be replaced by *transitional precession* under just one circumstance: If $\vec{L}$ and $\vec{S}$ initially point in nearly opposite directions and $\vec{L}$ is initially longer than $\vec{S}$ (as in Fig. 4.2b), then the orbital inspiral will bring the binary into an epoch (time $t \sim t_3$ in Fig. 4.2b) where $\vec{L} \simeq -\vec{S}$, and hence J and Ω_p are small and the precession rate is no longer fast compared to the inspiral rate. Before this small-J epoch, $\vec{L}$ and $\vec{S}$ undergo simple precession around $\vec{J}$. Then, during the small-J epoch, the precession becomes transitional: the binary loses its "gyroscopic bearings" and tumbles in space, and that tumbling causes $\vec{J}$ to swing around to a new direction, and causes $\vec{L}$ and $\vec{S}$, locked onto each other, to swing around with $\vec{J}$. Then, after the small-J epoch, $\vec{L}$ and $\vec{S}$ resume their simple precessional motion, but now around the new $\vec{J}$ direction. We shall explore this transitional precession in Subsec. 4.4 below; but first, in Subsecs. 4.2 and 4.3, we give a quantitative analysis of simple precession and present some concrete examples.

4.2 Simple precession

In this section we give a quantitative analysis of simple precession. For ease of analysis, we introduce the notations

$$\kappa \equiv \hat{S} \cdot \hat{L} \,, \quad \gamma(t) \equiv S/L(t) \,. \tag{4.58}$$

The evolution equations (4.48), (4.49) imply that κ is a constant of the motion, whereas (4.50), (4.51) imply that γ grows with time: $\dot{\gamma} > 0$. Note, however, that because $S_1 \lesssim {M_1}^2$ and similarly for body 2, $\gamma(t)$ is bounded above by

$$\gamma \lesssim \frac{{M_1}^2 + {M_2}^2}{M_1 M_2} \left(\frac{M}{r}\right)^{1/2} \,. \tag{4.59}$$

The magnitude and direction of the total angular momentum can be expressed in terms of κ, $\gamma(t)$, $L(t)$, and the directions $\hat{L}$ and $\hat{S}$ as

$$J = L\sqrt{1 + 2\kappa\gamma + \gamma^2} \,, \tag{4.60}$$

$$\hat{J} = \frac{\hat{L} + \gamma \hat{S}}{\sqrt{1 + 2\kappa\gamma + \gamma^2}} \,, \tag{4.61}$$

and correspondingly, the precessional angular velocity (4.54) can be written as

$$\Omega_p = \left(2 + \frac{3M_2}{2M_1}\right)\sqrt{1 + 2\kappa\gamma + \gamma^2}\frac{L}{r^3} \,. \tag{4.62}$$

We now solve for the motion of $\hat{J}$. Differentiating Eq. (4.61) and using the simple precessional equations (4.50), (4.51), we find

$$\dot{\hat{J}} = \frac{\dot{\gamma}\left[\hat{S}(1 + \kappa\gamma) - \hat{L}(\kappa + \gamma)\right]}{(1 + 2\kappa\gamma + \gamma^2)^{3/2}} \,. \tag{4.63}$$

Thus, at any instant, $\hat{J}$ moves on the unit sphere along the great-circle arc from $\hat{L}$ towards $\hat{S}$; see Fig. 4.3. Because $\hat{L}$ and $\hat{S}$ are themselves precessing around $\hat{J}$ with precessional angular velocity Ω_p [Eq. (4.62)], this (tiny) motion of $\hat{J}$ must also be a precession at the same angular velocity. We denote by $\hat{J}_0$ the fixed direction around which $\hat{J}$ and $\hat{L}$ both spiral.

The opening angle of the cone on which $\hat{J}$'s precessional motion takes place is given by

$$\begin{aligned} \lambda_J &= \arcsin\left(\frac{|\dot{\hat{J}}|}{\Omega_p}\right) = \arcsin\left(\frac{1}{\Omega_p}\frac{\dot{\gamma}\sqrt{1-\kappa^2}}{(1 + 2\kappa\gamma + \gamma^2)}\right) \\ &= \arcsin\left(\frac{\frac{16}{5}(M/r)^{3/2}\gamma\sqrt{1-\kappa^2}}{(1 + \frac{3}{4}M_1/M_2)(1 + 2\kappa\gamma + \gamma^2)^{3/2}}\right) \,. \end{aligned} \tag{4.64}$$

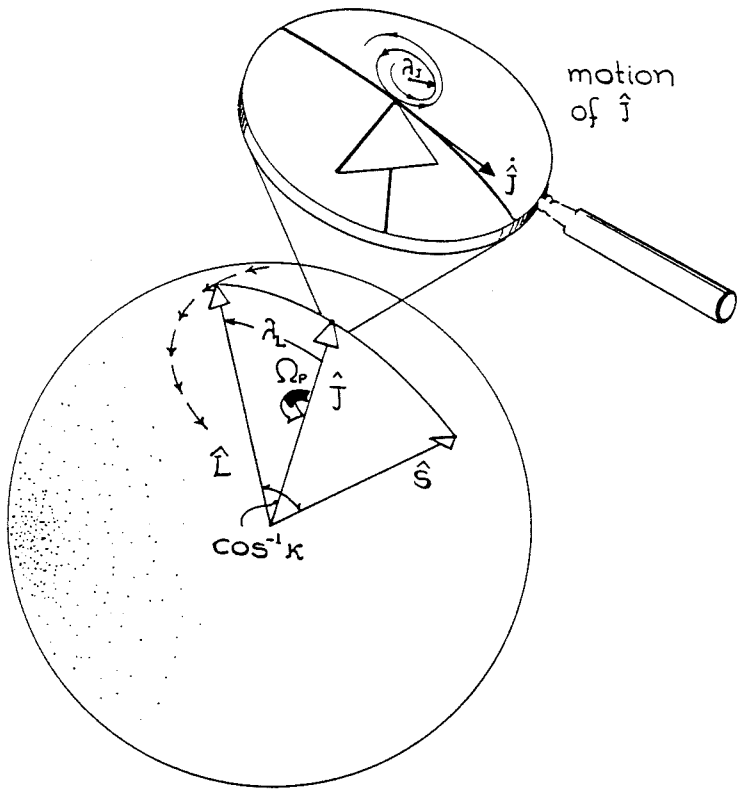

Figure 4.3: Simple precession: $\hat{L}$, $\hat{J}$, and $\hat{S}$ undergo tight-spiral motion on the unit sphere, with precessional opening angles $\lambda_J \ll \lambda_L$ and with λ_L gradually increasing; cf. Fig. 4.2.

Similarly, the opening angle of the cone on which $\hat{L}$ precesses is

$$\lambda_L = \arcsin\left(\frac{|\dot{\hat{L}}|}{\Omega_p}\right) = \arcsin\left(\frac{\gamma\sqrt{1-\kappa^2}}{\sqrt{1+2\kappa\gamma+\gamma^2}}\right) . \tag{4.65}$$

Because of the gradual orbital inspiral, the values of the precessional opening angles λ_J and λ_L gradually change; i.e., $\hat{J}$ and $\hat{L}$ undergo tight spirals on the unit sphere rather than precise circular motions; see Fig. 4.3.

Because $\dot{\lambda}_L > 0$ [cf. Fig. 4.2 or differentiate Eq. (4.65)], the spiral of λ_L is always outward from $\hat{J}$. Note that for $\lambda_L < \pi/2$ this means that the cone on which $\hat{L}$ spirals is opening up around $+\hat{J}$, but for $\lambda_L > \pi/2$ (as at times $t > t_3$ in Fig. 4.2b), the cone is closing down around $-\hat{J}$. The tiny spiral of $\hat{J}$ is outward when $\lambda_L < \pi/2$, and can be either outward or inward when $\lambda_L > \pi/2$, as one can

see by differentiating Eq. (4.64) and comparing with the sign of $\cos\lambda_L = \hat{L}\cdot\hat{J} = (1+\kappa\gamma)/\sqrt{1+2\kappa\gamma+\gamma^2}$ [cf. Eq. (4.61)].

Note that if $S \gg L$ near the end of the inspiral ($\gamma \gg 1$), then the value of $\cos\lambda_L$ must approach κ at late times, since then $\vec{J} \approx \vec{S}$. Thus, while $\hat{J}$ is roughly fixed, $\hat{L}$ and $\hat{S}$ effectively "trade places" during the evolution from early to late times: At early times $\hat{L}$ is close to $\hat{J}$, and $\hat{S}$ orbits them at angle $\cos^{-1}\kappa$ radians away; at late times $\hat{S}$ and $\hat{J}$ are close, and $\hat{L}$ orbits them at an angle $\cos^{-1}\kappa$ away. a Finally, we show how to put our description of simple precession on a more rigorous basis. In so doing, we will isolate the sufficient condition for simple precession. We described above how the approximate constancy of $\hat{J}$ arises when the precession timescale Ω_p^{-1} is much shorter the inspiral timescale $L/\dot{L}$. Actually, even if the ratio of timescales is small, $\hat{J}$ can still change significantly in one precession period if the magnitude of $\vec{J}$ is much smaller than the magnitude of $\vec{L}$ (as can happen if $\vec{L}$ and $\vec{S}$ are roughly anti-aligned and have roughly equal magnitude). These considerations suggest defining a "small parameter" $\epsilon = (L/J) \times$ (ratio of precession timescale to inspiral timescale), i.e.,

$$\epsilon \equiv \frac{L}{J}\frac{\dot{L}/L}{\Omega_p} = \frac{|\dot{\vec{J}}|/J}{\Omega_p}\,, \tag{4.66}$$

and solving the precession equations as an expansion in powers of ϵ.

First we note that ϵ is indeed small for "typical" cases. From Eqs. (4.54) and (4.11), we have

$$\epsilon = \frac{16}{5}\frac{(M/r)^{3/2}}{(1+\frac{3}{4}M_2/M_1)(1+2\kappa\gamma+\gamma^2)}\,. \tag{4.67}$$

Thus, for example, $\kappa > 0 \Rightarrow \epsilon < \frac{16}{5}(M/r)^{3/2}$, which is $\ll 1$ except near final coalescence.

We can now jusify our assertion that, for small ϵ, both $\hat{J}$ and $\hat{L}$ spiral around a single fixed direction, $\hat{J}_0$. We do so by explicitly exhibiting $\hat{J}_0$:

$$\hat{J}_0 = \hat{J} - \epsilon\,\hat{J}\times\hat{L}\,. \tag{4.68}$$

It is straightforward to check that $\dot{\hat{J}}_0$ vanishes up to terms of order ϵ^2. Equivalently, we may write

$$\hat{J} = \hat{J}_0 + \epsilon\,\hat{J}_0\times\hat{L} + O(\epsilon^2)\,. \tag{4.69}$$

To the same order, $\dot{\hat{L}}$ is given by

$$\dot{\hat{L}} = \Omega_p\,\hat{J}_0\times\hat{L} + \epsilon\,\Omega_p\,(\hat{J}_0\times\hat{L})\times\hat{L}\,, \tag{4.70}$$

where the precession frequency Ω_p is given by Eq. (4.62).

Finally, dividing Eq. (4.64) by Eq. (4.65), we find that

$$\frac{\sin\lambda_J}{\sin\lambda_L} = \epsilon. \tag{4.71}$$

Thus ϵ being small implies that $\sin\lambda_J$ is small compared to $\sin\lambda_L$, as well as being small compared to unity.

Algebraic solution to simple-precession equations

We now solve Eq. (4.70); this will provide us with an algebraic expression for $\hat{L}(t)$ which is accurate up to terms of $O(\epsilon^2)$. Referring to Fig. 4.4, let $\hat{J}_0$ point in the (θ', ϕ') direction relative to the detector's Cartesian coordinates (cf. Fig. 4.1); let α be the instantaneous angular location of $\hat{L}$ in its precessional motion around $\hat{J}_0$ with $\alpha = 0$ when $\hat{L}\cdot\hat{z}$ is maximum; and note that, by virtue of Eq. (4.69), the opening angle λ_L of the cone on which $\hat{L}$ precesses can be regarded equally well as the angle between $\hat{L}$ and $\hat{J}_0$, or between $\hat{L}$ and $\hat{J}$, aside from fractional errors of order ϵ^2.

Then the geometry of Fig. 4.4 dictates that

$$\begin{aligned}\hat{L} = \hat{J}_0\cos\lambda_L \;&+\; \frac{(\hat{z} - \hat{J}_0\cos\theta')}{\sin\theta'}\sin\lambda_L\cos\alpha \\ &+\; \frac{\hat{J}_0\times\hat{z}}{\sin\theta'}\sin\lambda_L\sin\alpha\,.\end{aligned} \tag{4.72}$$

Of the quantities appearing in this equation, only λ_L and α change with time during simple precession. By Eq. (4.61), $\cos\lambda_L = \hat{L}\cdot\hat{J}$ is given by

$$\cos\lambda_L(t) = \frac{\mu\sqrt{Mr(t)} + S_{\|}}{\left[(\mu\sqrt{Mr(t)} + S_{\|})^2 + {S_\perp}^2\right]^{1/2}}\,. \tag{4.73}$$

Here $S_{\|} \equiv S\kappa$ is the component of the spin $\vec{S}$ along $\hat{L}$, $S_\perp = S\sqrt{1-\kappa^2}$ is the length of its perpendicular component, and $r(t)$ is given by Eq. (4.11). A similar algebraic expression for the angular position α of $\hat{L}$ can be obtained from its differential equation

$$d\alpha/dt = \Omega_p(t) \tag{4.74}$$

[Eq. (4.70) dotted into $\hat{J}_0\times\hat{L}$]. Changing the independent variable from t to r using (4.11), Eq. (4.74) becomes

$$\frac{d\alpha}{dr} = \frac{-5}{32}\left(\frac{1+\frac{3}{4}M_2/M_1}{\mu M^2}\right)\left[(\mu\sqrt{Mr} + S_{\|})^2 + {S_\perp}^2\right]^{1/2}. \tag{4.75}$$

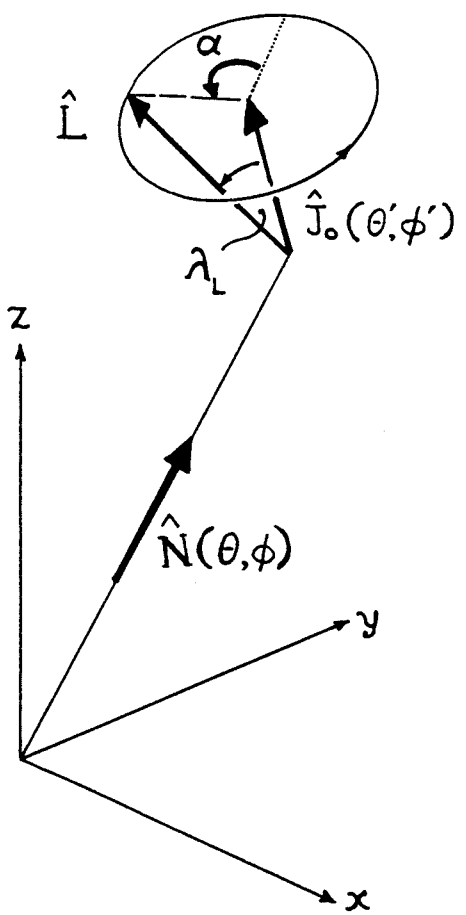

Figure 4.4: Geometry for a binary's simple precession relative to the Earth-based detector's Cartesian axes; cf. Fig. 4.1.

This is easily integrated to give

$$\alpha = \frac{-5(1+\frac{3M_2}{4M_1})}{96\mu^3 M^3}\Big[2Y^{3/2} - 3S_{\|}(\mu\sqrt{Mr}+S_{\|})\sqrt{Y} \\ -3S_{\|}{S_\perp}^2 \sinh^{-1}\Big(\frac{\mu\sqrt{Mr}+S_{\|}}{S_\perp}\Big)\Big] + \text{const}\,, \tag{4.76}$$

where

$$Y \equiv \mu^2 Mr + 2S_{\|}\mu\sqrt{Mr} + S^2. \tag{4.77}$$

This completes our solution for $\hat{L}(t)$ for our two special cases. As a check, we have integrated the orbital evolution equations (4.48)—(4.51) numerically for

a broad range of initial conditions and have found that, whenever the constraint $\epsilon \ll 1$ is satisfied, the evolution is in excellent accord with the "simple"-precession behavior embodied in Eqs. (4.69), (4.72), (4.73) and (4.76).

Algebraic expressions for simple-precession waveforms

The gravitational waveforms emitted by the binary are described by Eqs. (4.23)—(4.29), and (4.13), (4.37), (4.5), (4.6), in which $h_+(t)$, $h_\times(t)$, $A(t)$ and $\varphi(t)$ are represented as simple algebraic functions of $\hat{L}(t)$, and $\delta\Phi$ is represented as an integral of a simple algebraic function of $\hat{L}(t)$. In these formulae, $\hat{L}(t)$ appears in the combinations $\hat{L}\cdot\hat{N}$, $\hat{N}\cdot(\hat{L}\times\hat{z})$ and $\hat{L}\cdot\hat{z}$. Straightforward algebra based on Eq. (4.72) gives for these quantities

$$\hat{L}\cdot\hat{N} = \hat{J}_0\cdot\hat{N}\left[\cos\lambda_L - \frac{\cos\theta'\sin\lambda_L\cos\alpha}{\sin\theta'}\right] + \frac{\cos\theta\sin\lambda_L\cos\alpha}{\sin\theta'} + \hat{N}\cdot(\hat{J}_0\times\hat{z})\frac{\sin\lambda_L\cos\alpha}{\sin\theta'}\,, \tag{4.78}$$

$$\hat{N}\cdot(\hat{L}\times\hat{z}) = \hat{N}\cdot(\hat{J}_0\times\hat{z})\left[\cos\lambda_L - \frac{\cos\theta'\sin\lambda_L\cos\alpha}{\sin\theta'}\right] + (\hat{N}\cdot\hat{z}\cos\theta' - \hat{N}\cdot\hat{J}_0)\frac{\sin\lambda_L\sin\alpha}{\sin\theta'}\,, \tag{4.79}$$

$$\hat{L}\cdot\hat{z} = \cos\theta'\cos\lambda_L + \sin\theta'\sin\lambda_L\cos\alpha\,, \tag{4.80}$$

where

$$\hat{J}_0\cdot\hat{N} = \cos\theta\cos\theta' + \sin\theta\sin\theta'\cos(\phi-\phi')\,, \tag{4.81}$$

$$\hat{N}\cdot(\hat{J}_0\times\hat{z}) = \sin\theta\sin\theta'\sin(\phi-\phi')\,, \tag{4.82}$$

and λ_L and α are given by Eqs. (4.73) and (4.76). This completes the solution for $h_+(t)$, $h_\times(t)$, $A(t)$ and $\varphi(t)$.

As was noted following Eq. (4.37), $\delta\Phi(t)$ cannot be expressed as a function of $\hat{N}$ and the instantaneous value of $\hat{L}$; it depends on the full time history of $\hat{L}$ between time t and the endpoint of coalescence, t_c. However, the growth of this phase shift over one precession period can be described by an approximate analytical expression. That expression turns out to depend on whether the line containing $\hat{N}$ lies outside or inside $\hat{L}$'s cone of precession (i.e., on whether $|\hat{J}_0\cdot\hat{N}|$ is greater or less than $|\hat{J}_0\cdot\hat{L}|$), but is otherwise independent of $\hat{N}$. If we approximate $\cos\lambda_L$ as constant over one precession period, then by changing variables from t to α using

$d\alpha/dt = \Omega_p$, we find (with some effort) that

$$\int_0^{2\pi} \frac{d\,\delta\Phi}{d\alpha}\, d\alpha = \begin{cases} -2\pi\cos\lambda_L & |\hat{J}_0\cdot\hat{L}| < |\hat{J}_0\cdot\hat{N}| \\ 2\pi(-\cos\lambda_L + 1) & \hat{J}_0\cdot\hat{L} > |\hat{J}_0\cdot\hat{N}| \\ 2\pi(-\cos\lambda_L - 1) & \hat{J}_0\cdot\hat{L} < -|\hat{J}_0\cdot\hat{N}| \end{cases} . \tag{4.83}$$

We see from Eq. (4.83) that the "average value" of $\delta\dot{\Phi}$ can be roughly as large as the precessional frequency Ω_p. Thus the term "$2\delta\Phi$" in Eqs. (4.23)—(4.25) can change the total number of cycles in the wave fields and the observed waveform by roughly twice the total number of precessions–a sizeable correction.

This completes our analytic treatment of simple precessional waveforms for our two special cases.

4.3 Examples of simple precession

$1M_\odot$ Neutron star and maximally spinning $10M_\odot$ black hole

As an example of simple precession and the waveform modulation it produces, consider a $M_2 = 1M_\odot$ nonspinning neutron star spiraling into a $M_1 = 10M_\odot$ maximally rotating black hole, so $S = S_1 = {M_1}^2$. (We also gave a brief discussion of this example in Ref. [3].) We shall begin following the binary's evolution at an initial moment $t_c - t_i = 204$ s before the final collision when the orbital radius is $r_i = 63.2M$ and the gravitational-wave frequency (twice the orbital frequency) is $f_i = 11.7$ Hz. This is roughly the time when the gravity wave signal enters the frequency band accessible to the advanced LIGO/VIRGO detectors. We shall follow the evolution up to $t_c - t_f = 0.03$ s, when the orbital radius is $r_f = 6.96M$ and the gravitational-wave frequency is $f_f = 321$ Hz. Because photon shot noise in the broad band detectors rises sharply for $f > 100$ Hz, more than 99% of the signal-to-noise has been accumulated by this point. Note that as the binary spirals in from r_i to r_f, the parameter $\gamma = S/L$ increases from $\gamma_i = 1.258$ to $\gamma_f = 3.79$. Thus, throughout the LIGO/VIRGO observational band, the hole's spin angular momentum is somewhat larger than the orbital angular momentum.

In our example the orbit has a modest inclination to the hole's equatorial plane, $\arccos(\hat{L}\cdot\hat{S}) = 11.3°$ (0.197 radians), so $\kappa = \hat{L}\cdot\hat{S} = 0.9806$. Then, as the binary spirals in from $r_i = 63.2M$ to $r_f = 6.96M$, the opening angle of $\hat{L}$'s precession cone increases from $\lambda_{Li} = 6.30°$ to $\lambda_{Lf} = 8.95°$, and the parameter $\epsilon = \sin\lambda_J/\sin\lambda_L$ that characterizes our simple-precession approximation increases from $\epsilon_i = 1.17\times10^{-3}$ to $\epsilon_f = 7.11\times10^{-3}$. With ϵ so small, our approximation is excellent throughout the inspiral.

In our example, the binary is directly underfoot as seen from the detector, so $\hat{N} = -\hat{z} + \delta\hat{x}$, where δ is an arbitrarily small angle (required because some of our formulas, e.g. Eq. (4.7), become singular for sources that are precisely overhead or underfoot). At the initial time t_i, the orbit is precisely edge-on as seen from Earth, with the orbital plane parallel to the detector's $\hat{x}$ arm and the orbital angular momentum along its $\hat{y}$ arm, so $\hat{L}_i = \hat{y}$; and the black hole's spin is parallel to the detector's plane (perpendicular to our line of sight), so $\hat{S}_i = 0.9806\hat{y} - 0.1960\hat{x}$. These initial conditions are depicted in the upper left portion of Fig. 4.6. The subsequent precessional motion of $\hat{L}$ is shown in Fig. 4.5. The initial position of $\hat{L}$ in this figure is at the origin (since $\hat{L}_i = \hat{y}$), which corresponds to an angular location $\alpha_i = \pi/2$ in the conventions of the previous subsection. The total number of precessions during the inspiral from $r_i = 63.2M$ to $r_f = 6.96M$ is $(\alpha_f - \alpha_i)/2\pi = 23.8$. The opening up of the precession cone from $\lambda_{L\,i} = 6.30°$ to $\lambda_{L\,f} = 8.95°$ is evident in the figure. The center of the precession cone is at $\hat{J}_0 = \hat{J} = -0.1097\hat{x} + 0.9940\hat{y}$ (aside from fractional corrections of order ϵ).

The gravitational-wave signals from this binary are depicted in Figs. 4.6 and 4.7, for two possible orientations of the detector. The first orientation, referred to as $+'$ in Figs. 4.6 and 4.7, is the one assumed until now in all of this paper's formulas and figures: arms along $\hat{x}$ and $\hat{y}$, so $h(t) = \frac{1}{2}(h^{TT}_{xx} - h^{TT}_{yy}) \equiv h_{+'}$ (where h^{TT}_{jk} is the "transverse-traceless," tensorial gravitational-wave field [14]). The second orientation, referred to as $\times'$ in the figures, is rotated 45° relative to the first, so the arms are along $\frac{1}{2}(\hat{x} + \hat{y})$ and $\frac{1}{2}(-\hat{x} + \hat{y})$, and $h(t) = h^{TT}_{xy} \equiv h_{\times'}$.

The amplitudes $A_{+'}(t)$ and $A_{\times'}(t)$ of the signals $h(t)$ measured by these two detectors are shown in Fig. 4.6. Each complete period of the orbit's precession produces one cycle of amplitude modulation; the 23.8 precessions in the LIGO band produce 23.8 modulation periods.

Along the $A_{+'}(t)$ curve is marked the gravitational waves' carrier frequency $f = \Omega/\pi$. Because the radiation reaction grows stronger as the binary spirals inward, the carrier frequency sweeps upward ("chirps") at a gradually growing rate. Also indicated along the $A_{+'}(t)$ curve is the number of carrier-frequency oscillation cycles during one (or, early on, several) modulation periods. Early in the LIGO/VIRGO band there are several hundred carrier cycles per modulation cycle; late, there are several tens. The modulation shapes are explained in the appendix using diagrammatic tools developed there to provide an intuitive understanding of precession-induced modulation.

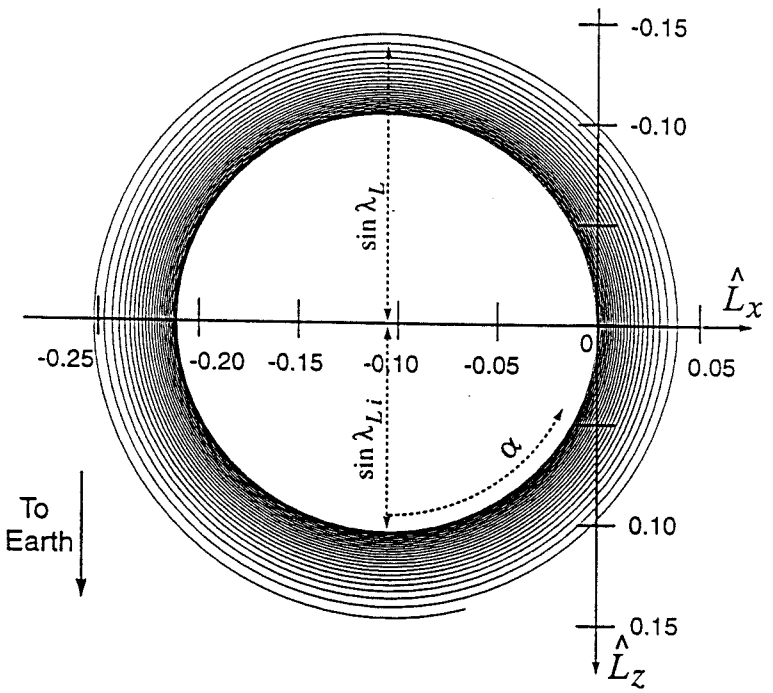

Figure 4.5: The precession of $\hat{L}$ (and hence also of the orbital plane) for the binary whose initial conditions are depicted in the upper left part of Fig. 4.6.

The fundamental modulation frequency [which is equal to the binary's precession frequency $\Omega_p/2\pi \sim (1/\pi)J/r^3$] remains finite in the limit that $\vec{S}$ and $\vec{L}$ are parallel. By contrast, the depth ΔA of the modulation goes to zero in the limit of parallel $\vec{S}$ and $\vec{L}$, because the opening angle λ_L of the orbit's precession cone goes to zero.

Since in our example the precession cone is rather narrow, $\lambda_L \simeq 0.1$ rad, it should not be surprising that the modulation depth is modest for the $+'$-oriented detector: $\Delta A_{+'}/A_{+'} \simeq \lambda_L \simeq 0.1$. Remarkably, by contrast, for the $\times'$ detector, the modulation is very large: $\Delta A_{\times'}/A_{\times'} \simeq 1$. The reason is that once each cycle, the precession carries the binary near a special orientation $\hat{L} \simeq \hat{y}$, which is half-

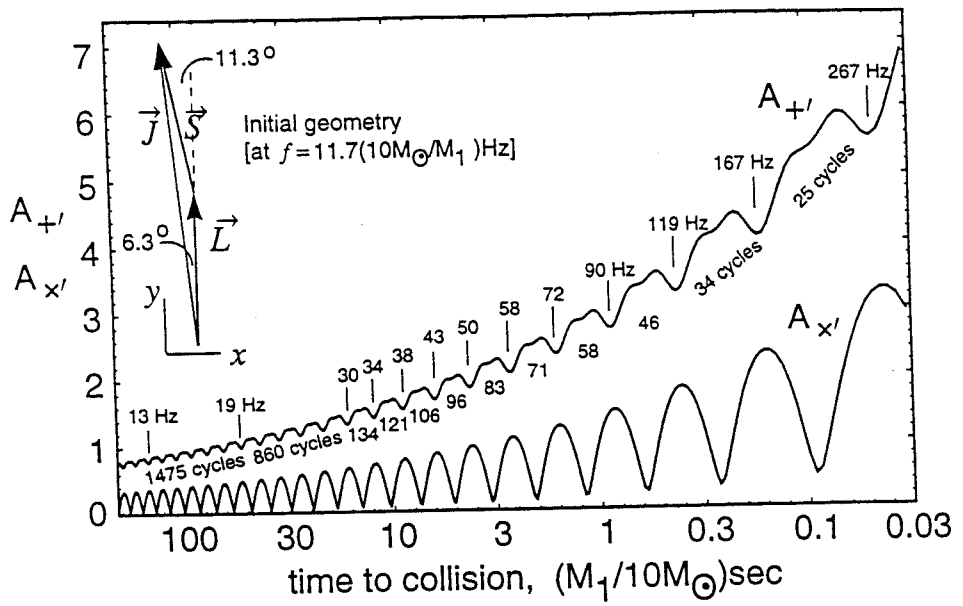

Figure 4.6: Amplitude modulation of the gravitational-wave signals from a non-spinning $M_2 = 1M_\odot$ neutron star spiraling into a maximally spinning $M_1 = 10M_\odot$ black hole. The binary is underfoot as seen from the detector of Fig. 4.1, with its initial spin, orbital, and total angular momenta as shown in the upper left part of this figure (where the direction $\hat{N}$ from Earth to the binary is into the paper). The $+'$ detector, whose measured wave amplitude $A_{+'}$ is shown here as a function of time $t_c - t$ to final collision, has arms oriented along the $\hat{x}$ and $\hat{y}$ directions (as in Fig. 4.1), i.e., along the horizontal and vertical axes of the upper left part of this figure. The $\times'$ detector, with measured wave amplitude $A_{\times'}$, has its arms rotated 45° to the $+'$ detector, i.e., along $\frac{1}{2}(\hat{x} + \hat{y})$ and $\frac{1}{2}(-\hat{x} + \hat{y})$. The signals' amplitude A and phase φ (Fig. 4.7) are defined by Eq. (4.8), where $\Phi(t)$ is the angular position of the binary in its orbit; cf. Fig. 4.1. The vertical scale in this figure is arbitraary, but linear. This figure (and the accompanying Figs. 4.5, 4.7 and 4.8) are also correct for any other binary with the same geometry, same mass ratio $M_2/M_1 = 0.1$, same $S_2 = 0$ and same maximal spin $S_1/M_1^2 \equiv 1$, but different M_1; the only change is an increase in the timescale by a factor $M_1/10M_\odot$ and a decrease in all frequencies by the inverse factor $10M_\odot/M_1$. Setting $M_1 = 10^5 M_\odot$ gives an example relevant to proposed space-based interferometers; see Sec. 4.3.

way between the $\times'$ detector's two arms; by symmetry, the $\times'$ detector's response vanishes for this orientation. One might have expected that, because of the narrowness of the precession cone, the binary would always be near this $\times'$-suppressing orientation, and therefore $A_{\times'}$ would remain always $\lesssim \lambda_L A_{+'} \simeq 0.1 A_{+'}$. Not so. Each cycle of precession carries $\hat{L}$ through an angle of $\Delta\psi \simeq 2\lambda_L \simeq 0.2$ rad in the detector plane; and this drives the signal amplitude up to $A_{\times'} \simeq \sin(2\Delta\psi) A_{+'} \simeq 4\lambda_L A_{+'} \simeq 0.4 A_{+'}$. This explains how, despite the narrow precession cone, the $\times'$ signal manages to have *both* a relatively large maximum amplitude $A_{\times' \max} \simeq \frac{1}{2} A_{+'}$, and a very large depth of modulation, $\Delta A_{\times'} \simeq A_{\times'}$.

Our example also illustrates a general *rule of thumb for simple precession:* The maximum amplitude $A_{\max}$ of a detector's signal during a modulation cycle is generally in the range (0 to 1)$A_{+\max}$, where $A_{+\max}$ is the maximum amplitude of the principal+ mode during the precession; and the depth ΔA of the modulation is generally in the range (0 to 1) $\sin(4\lambda_L) A_{+\max}$ (but of course $\Delta A \leq A$).

Figure 4.7 shows the polarization phases $\varphi_{+'}(t)$ and $\varphi_{\times'}(t)$ for the two detectors. For the $+'$ detector, the modulation of the polarization phase is modest: $\Delta\varphi_{+'} \sim$ 0.1 to 0.2 rad. For the $\times'$ detector, the polarization phase modulation is very large: $\varphi_{\times'}$ grows secularly, though at a somewhat irregular rate, changing by -2π with each cycle of orbital precession. As is discussed in detail in the appendix, this secular growth of $\varphi_{\times'}(t)$ is caused by the fact that each precession takes $\hat{L}$ once around $\hat{y}$, the bisector of the detector's two arms (see Fig. 4.5). If the binary's orientation were shifted away from $\hat{y}$ (leftward in Fig. 4.5) by an additional 3°, then $\hat{L}$ would still pass near the arms' bisector $\hat{y}$ during each precession but would not go around it; as a result, the polarization phase would have the finite-oscillation form that is shown as a dotted line in Fig. 4.7. Although the solid and dotted curves *look* radically different, the effects on the signal $h(t)$ are only slightly different for the two cases: the signal is not sensitive to 2π changes in φ; and modulo 2π, the solid and dotted $\varphi_{\times'}(t)$ are essentially identical, except for the very short time when the dotted curve is flying upward.

Finally, Fig. 4.8 shows the phase correction term $2\delta\Phi$ throughout the inspiral. (We recall that this term is independent of the waves' polarization and independent of detector orientation, and that by convention it vanishes at the end of the inspiral.) In this example, $2\delta\Phi$ accumulates slowly because $\hat{N}$ does not lie inside $\hat{L}$'s precession cone and $\cos\lambda_L$ is close to 1; cf. Eq. (4.83). Moreover the accumulation is very steady, since $\hat{L}$ never comes close to $\hat{N}$.

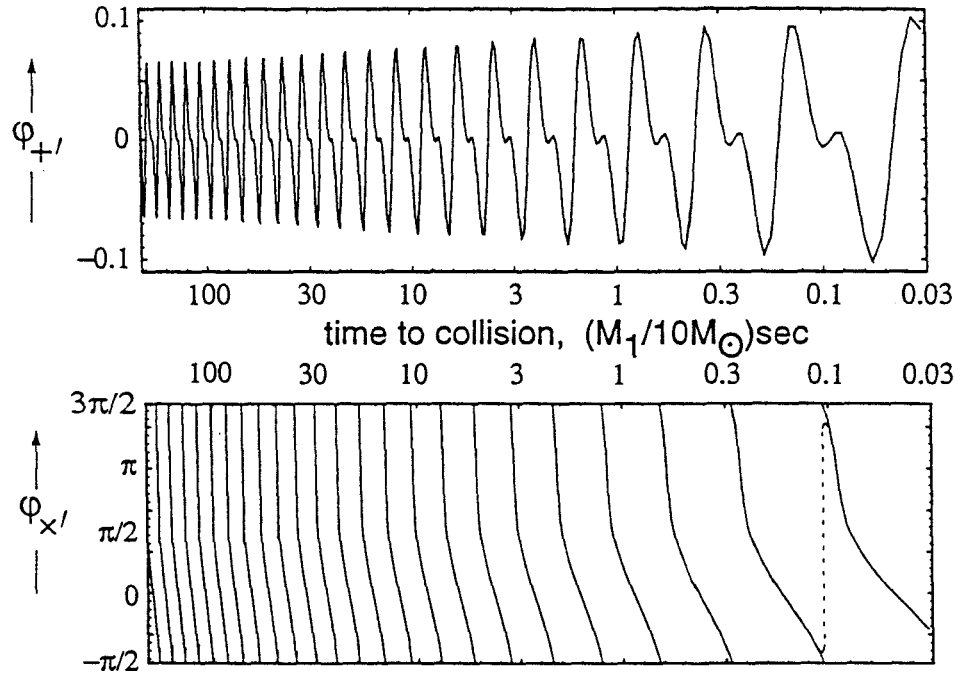

Figure 4.7: Polarization phase of the gravitational-wave signals for the binary and detectors of Fig. 4.6. The phases $\varphi_{+'}$ and $\varphi_{\times'}$ are shown, modulo 2π, as functions of time to collision $t_c - t$.

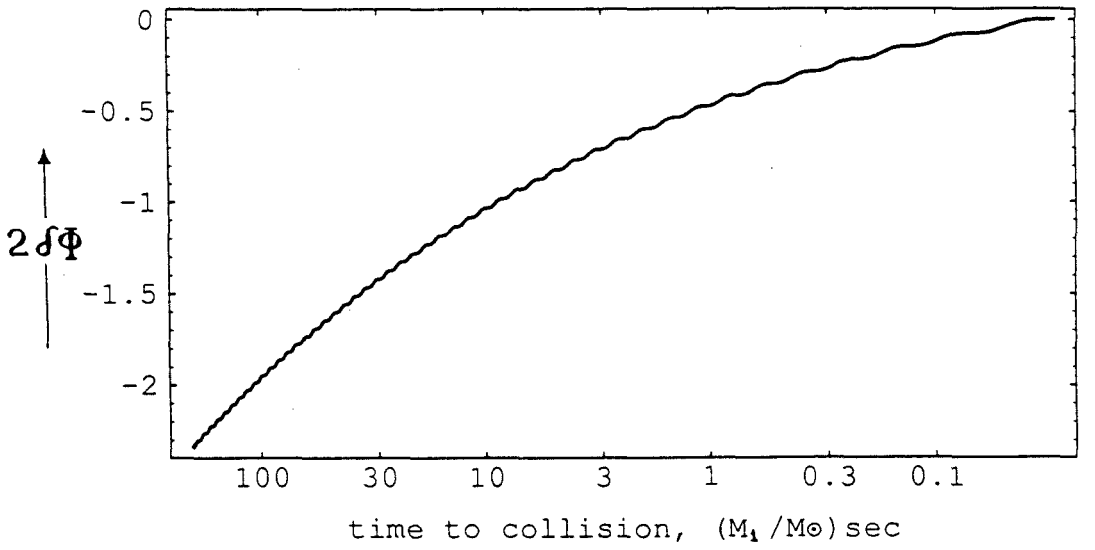

Figure 4.8: The phase correction term $2\delta\Phi$ for the for the binary of Fig. 4.6, shown as a function of time to collision $t_c - t$. This term is independent of detector orientation.

$10^4 M_\odot/10^5 M_\odot$ black-hole binary

Because the equations of orbital dynamics and waveform generation do not contain any intrinsic, binary-independent length scale, the solutions are easily scaled from one binary to another binary with the same values of all dimensionless quantities, but different absolute masses and spins. For example, Figures 4.5–4.8 remain valid if we increase the mass M_1 of the black hole by some arbitrary factor and increase all times and decrease all frequencies by that same factor, while holding fixed the dimensionless quantities $M_2/M_1 = 0.1$, $S_2 = 0$, $S_1/M_1^2 = 1$, $\hat{L} \cdot \hat{S} = \kappa = 0.9806$, and the keeping initial orientations as shown in the upper left of Fig. 4.6.

Most interestingly, if we increase M_1 by a factor 10^4, we obtain an example rel-

evant to space-based interferometric detectors such as the proposed LISA mission [13]. The binary is made of a nonspinning $10^4 M_\odot$ black hole and a maximally spinning $10^5 M_\odot$ black hole; instead of sweeping upward through the LIGO/VIRGO band from $f_i = 11.7$ Hz to $f_f = 321$ Hz, the waves depicted in the figures sweep through the band of space-based interferometers, from $f_i = 0.00117$ Hz to 0.0321 Hz; and instead of lasting for $t_c - t_i = 204$ s, the depicted waves last for 2.04×10^6 s or about a month, which is a reasonable measurement time for a space-based interferometer. (On the other hand, it is not at all obvious whether the event rate for $\sim 10^4 M_\odot / 10^5 M_\odot$ black-hole/black-hole binaries will be interesting, even given that the proposed detectors could see them out to cosmological distances.)

Neutron-star/neutron-star binaries

When the binary's two bodies have equal masses, $M_1 = M_2$, their orbital angular momentum $L = \mu\sqrt{Mr} = \frac{1}{4}M^2\sqrt{r/M}$ is always somewhat larger than their maximum possible total spin, $S_{\max} \simeq M_1^2 + M_2^2 = \frac{1}{2}M^2$. As a result, the total angular momentum $\vec{J}$ is always fairly close to $\vec{L}$, which means that the opening angle λ_L of the precession cone is always small.

For example, consider two equal mass neutron stars, $M_1 = M_2 = 1.4 M_\odot$, each with maximal spin, and with $\hat{S}$ inclined at the same angle to $\hat{L}$ as in our previous $M_1/M_2 = 10$ examples: $\arccos(\hat{S} \cdot \hat{L}) = 11.3°$. Then, as the waves' carrier frequency sweeps through our previously chosen band of 11.7 Hz to 321 Hz, the precession cone grows from $\lambda_L \simeq 1.5°$ to 3.6°. With precession so tight, the modulation is typically quite weak: For the initial spin, orbit, and detectors oriented as in our previous Fig. 4.6, the $+'$ detector has amplitude and phase modulations shaped very much like those of Figs. 4.6 and 4.7, but with modulation amplitudes $\Delta A_{+'}/A_{+'} \sim \Delta\varphi_{+'} \sim 0.01$. As before, the very specially oriented $\times'$ detector shows deep modulation like that in Figs. 4.6 and 4.7, but only at a price of having an amplitude roughly 10 times smaller than that of the $+'$ detector: $A_{\times'}/A_{+'} \sim 4\lambda_L \sim 1/10$.

As another example, let one of the $1.4 M_\odot$ neutron stars be maximally spinning ($S_1 = M_1^2$) and the other be nonspinning ($S_2 = 0$), and open up the angle between $\hat{S}$ and $\hat{L}$ to 60° (so $\kappa = \hat{L} \cdot \hat{S} = 0.5$). For variety, change the initial geometry to that shown in Fig. 4.11 (which is presented in another context in Sec. 5.1): The detector's arms are along the $\hat{x}$ and $\hat{y}$ axis (as in all our formulae); the binary instead of being underfoot is at a zenith angle of 45° along the same azimuth as the $\hat{x}$ arm, i.e., $\hat{N} = (\hat{z} - \hat{x})/\sqrt{2}$; the total angular momentum (and hence the center

of the precession cone) points directly upward, $\hat{J} = \hat{z}$; and $\hat{L}$ and $\hat{S}$ initially are oriented around $\hat{J}$ as shown. The resulting amplitude modulation of the detector's signal is shown in Fig. 4.11 below (where in the horizontal frequency scale we must set $M = 2.8M_\odot$. Although the modulation is modest, growing from roughly 15% to roughly 30% during the inspiral, the number of precessions is rather large: Between 10 Hz and 1000 Hz there are 70 precession periods, with 90% of them occurring between 10 Hz and 100 Hz [in good agreement with Eq. (4.57)].

4.4 Transitional precession

General description

In this section we discuss transitional precession. Our understanding of this behavior is based largely on numerical integrations of our special-case precession equations (4.48)—(4.51) for $S_2 = 0$ or $M_1 = M_2$. We have not been able to derive an approximate analytic solution for $\hat{L}(t)$ during transitional precession, as we could for simple precession, but the main qualitative features of the phenomenon are clear:

Since $L \propto r^{1/2}$ while S is constant during the inspiral, at sufficiently early times L is always much larger than S, $\vec{J} \approx \vec{L}$, $\epsilon \ll 1$, and the binary undergoes simple precession. However, if $\hat{L}$ and $\hat{S}$ are nearly anti-aligned, and if $S > L$ by the end of the inspiral, then the binary must pass through an intermediate stage when $\vec{L}$ and $\vec{S}$ almost cancel and hence J is much smaller than L or S. In this intermediate stage, $\epsilon \equiv \dot{L}/(J\Omega_p) = |\dot{\vec{J}}|/(J\Omega_p)$ is large ($\gtrsim 1$) for two reasons: L/J is large and ${\Omega_p}^{-1} \propto r^3/J$ is large. Now, recall that the "simplicity" of simple precession was due to the smallness of the parameter ϵ. The simple precessional motion that we described in Sec. 4.2 therefore breaks down, and (in numerical examples) $\hat{L}$ and $\hat{S}$ appear to "tumble," while locked in each others' embrace. The tumbling continues until the orbit has shrunk to the point that L is significantly smaller than S. At that point $J \approx S$, and simple precession resumes. Because the tumbling stage represents a short-lived "transition" between two stages of simple precession, we call it *transitional precession.*

In the initial stage of simple precession, $\hat{J}$ moves on a tight outward spiral away from some initial direction $\hat{J}_i = (\hat{J}_0)_{\text{initial}}$, while $\hat{L}$ (which is approximately equal to $\hat{J}$) moves on a looser outward spiral away from $\hat{J}_i$. During transitional precession, $\hat{J}$ "migrates" from the vicinity of $\hat{J}_i$ towards a new, fixed location $\hat{J}_f = (\hat{J}_0)_{\text{final}}$. In the final stage of simple precession, $\hat{J}$ moves on a tight, inward spiral towards $\hat{J}_f$,

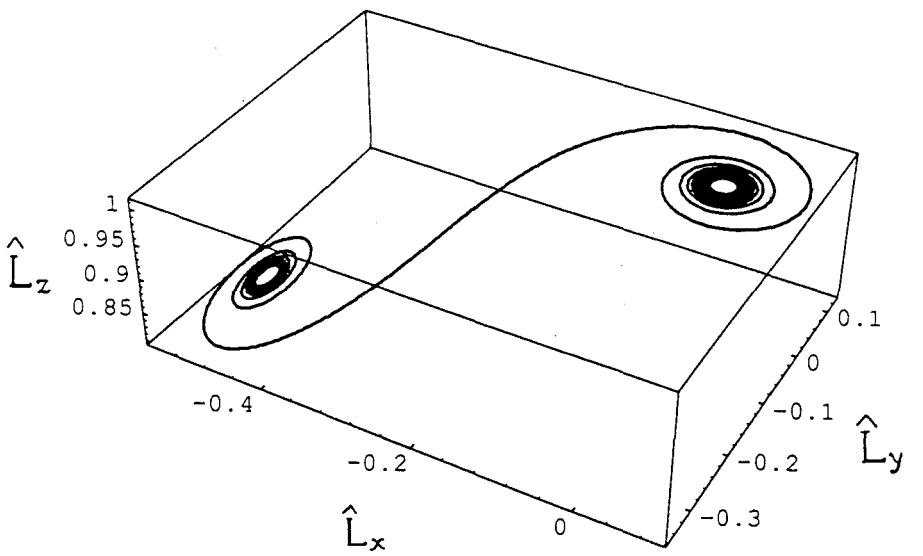

Figure 4.9: An example of the path traced by $\hat{L}(t)$ during the evolution from simple precession to transitional precession and back to simple precession. In this example, $M_1/M_2 = 10$, $\arccos(\kappa) = 179.3°$, r/M decreases from ~ 330 to 6, and f increases from $1(10M_\odot/M_1)$ Hz to $400(10M_\odot/M_1)$ Hz.

while $\hat{L}$ points almost 180° away from $\hat{J}$ and spirals more loosely inwards towards $-\hat{J}_f$.

Figure 4.9 illustrates the evolution of $\hat{L}(t)$ before, during, and after transitional precession. In the example shown, $M_1/M_2 = 10$, $S_1 = {M_1}^2$, $S_2 = 0$, $\cos^{-1}\kappa = 179.3°$, and the epoch of evolution shown begins when $r = 330M$ and $f = 1(10M_\odot/M_1)$ Hz, and ends when $r = 6M$ and $f = 400(10M_\odot/M_1)$ Hz.

The entire sequence that we have just described—from simple to transitional and then back to simple precession—will typically *not* take place during the time that the binary is "visible" to LIGO/VIRGO (or, in the supermassive-binary case, to LISA). It is easy to see why: To include the entire sequence, the binary must

enter the observational band with $L/S \gtrsim 2$ and leave it with $L/S \lesssim 2$, which means that L must change by a factor 4 or more in the observational band. Since $f \propto r^{-3/2} \propto L^{-3}$, this means that f must change by $\gtrsim 4^3 = 64$. However, $f_{\rm max}/f_{\rm min} \sim 64$ is the entire available observational band both for LIGO/VIRGO (with $f_{\rm min} \sim 10$ Hz and $f_{\rm max} \sim 500$ Hz) and for LISA (with $f_{\rm min} \sim 10^{-3}$ Hz and $f_{\rm max} \sim 10^{-1}$ Hz). Therefore, to include the entire sequence, one must carefully adjust M_1, M_2, S_1, and $\kappa = \hat{S} \cdot \hat{L}$ so the spin and orbital angular momenta are nearly anti-aligned, and so $L/S \simeq 2$ when the binary is just entering the observational band, and $L/S \simeq 1/2$ when it is just leaving. Moreover, one must choose M_1/M_2 large enough that, when the binary begins its final coalescence (at $r/M \sim 6$), L/S has gotten at least as small as $1/2$.

Just how precisely anti-aligned must $\hat{L}$ and $\hat{S}$ be, i.e., how close to -1 must $\kappa \equiv \hat{L} \cdot \hat{S}$ be, to produce transitional precession? It is clear from the previous discussion that transitional precession occurs when ϵ becomes of order unity. Let us define

$$\delta \equiv \kappa + 1 \, . \tag{4.84}$$

Using Eq. (4.67) we find that, for small δ, ϵ reaches its maximum value when $\gamma = (1+2\delta)$, which corresponds to an orbital separation $r_{\rm max}/M = (S/M_1M_2)^2(1-4\delta)$; there ϵ is

$$\epsilon_{\rm max} \approx \frac{8}{5}\,\delta^{-1}\left(1+\frac{3M_2}{4M_1}\right)^{-1}\left(\frac{M}{r_{\rm max}}\right)^{3/2} \tag{4.85}$$

for small δ. [Eq. (4.85) assumes that ϵ does in fact reach a maximum at some finite r.] Thus, for transitional precession to occur ($\epsilon \gtrsim 1/2$) at $r_{\rm max}/M \gtrsim 20$ (when there is still a significant number of orbits to go before the binary's final coalescence), δ must be $\lesssim 0.04$ so $\kappa = -1 + \delta$ must lie between -1.0 and -0.96, which means that the angle between $\hat{L}$ and $\hat{S}$ must exceed 164° . Thus, we see that transitional precession will be observed for only a very narrow range of initial conditions.

Even if $\hat{L}$ and $\hat{S}$ are sufficiently anti-aligned to produce transitional precession, the rest of the fine tuning will typically not be achieved in Nature. Either L/S will be somewhat less than 2 when the binary enters the observational band, and the initial period of simple precession will be lost in the detector's low-frequency noise; or else L/S will be somewhat greater than $1/2$ when the binary leaves the observational band, and the final period of simple precession will be lost in the detector's high-frequency noise, or will not occur at all because orbital plunge and final coalescence intervene.

Remarks on the final direction of $\hat{J}$

When the full sequence of simple precession to transitional precession to simple precession occurs, how does the final direction of the binary's total angular momentum, $\hat{J}_f = (\hat{J}_0)_{\rm final}$, depend on its initial direction, $\hat{J}_i = (\hat{J}_0)_{\rm initial}$, and on the binary's masses and spins? We do not have a complete answer to this question, but it is perhaps useful to include here some general remarks and an example. (In this discussion, we ignore the possibility that the inspiral ends before $S \gg L$.)

For this discussion, it is convenient to introduce spherical coordinates (θ', ϕ') on the unit sphere, with $\hat{J}_i$ at the north pole, $\theta' = 0$. We choose the location of the meridian $\phi' = 0$ as follows. We choose some instant of time which is defined in a dimensionless way, such as the moment when $r/M = 100$ or the moment when $L = S$, and we let $\phi' = 0$ correspond to the direction of $\hat{J}$ at that instant. It is then clear by the scale invariance of the problem that the coordinates of $\hat{J}_f$ can depend *only* on the following dimensionless quantities: κ, M_2/M_1, and S/M^2.

We obtain qualitative information about the dependence of $\hat{J}_f$ on these quantities by considering two limiting cases. First consider the case where κ is precisely -1. Then $\hat{J}$ simply "flips" when L becomes smaller than S, so $\hat{J}_f = -\hat{J}_i$. The second, obvious limiting case is that $\hat{J}_f \to \hat{J}_i$ for $\kappa \gg -1$.

By continuity, we see that $\hat{J}_f$ must move from $\theta' = \pi$ to $\theta' = 0$ as we increase κ away from -1. Because typically all this motion occurs as κ changes by only ~ 0.04, $\hat{J}_f$ must be a rather sensitive function of κ.

Fig. 4.10 shows the path traced out by $\hat{J}_f$ as the angle $\arccos(\kappa)$ between $\hat{L}$ and $\hat{S}$ is varied, for one particular choice of mass and spin ratios: $M_2/M_1 = 0.2$, $S = S_1 = {M_1}^2$, and $S_2 = 0$. Each point on the curve is the end result of evolving the precession equations (4.48)—(4.51) from very early to very late times to determine $\hat{J}_f$. In each evolution, $\hat{J}_i$ was taken to be at $\theta' = 0$, and $\phi' = 0$ was defined by the location of $\hat{J}$ at the moment that the gravity wave frequency f swept through $10(M/10M_\odot)$ Hz. For the chosen mass and spin ratios, $r_{\rm max}/M \approx 25$, so from Eq. (4.85) we would expect transitional precession to "turn off" ($\epsilon \lesssim 1/2$) for $\kappa \gtrsim -0.978$, when the angle between $\hat{L}$ and $\hat{S}$ is roughly 168°. This is in reasonable agreement with the numerical results shown in Fig. 4.10.

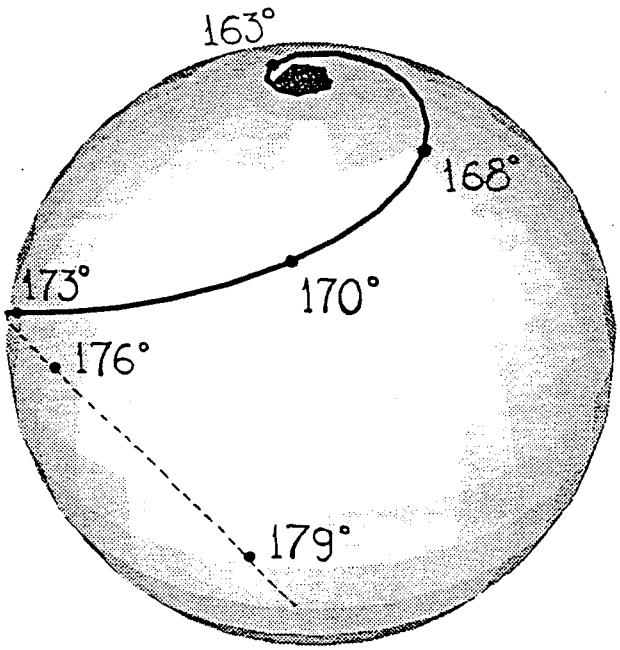

Figure 4.10: The endpoint of transitional precession, i.e., the direction $\hat{J}_f$ of the binary's total angular momentum $\hat{J}$ at asymptotically late times, expressed as a function of the initial direction $\hat{J}_i$ of $\hat{J}$ (which is taken to be the north pole, $\theta' = 0$) and of the angle $\arccos(\kappa)$ between $\hat{L}$ and $\hat{S}$. The mass and spin ratios are chosen to be $M_2/M_1 = 0.2$, $S_1/{M_1}^2 = 1$, and $S_2 = 0$. Each point on the curve is the result of evolving the precession equations (4.48)—(4.51) from early to late times for that point's value of κ. One more piece of initial data, besides $\hat{J}_i$, is needed to fully specify the evolution: the azimuthal direction of $\hat{J}$ at some early, but finite, time. In this figure, $\hat{J}$ is chosen to point in the direction $\phi' = 0$ at the moment when the gravity wave frequency f equals $10(M/10M_\odot)$ Hz.

5 NUMERICAL SOLUTIONS FOR ARBITRARY MASSES AND SPINS

5.1 Relation of the general case to our special cases

In this section we move beyond our two special cases, $M_1 = M_2$ and $S_2 = 0$, and discuss binaries with arbitrary masses and spins (consistent with the requirement that $S_i \leq M_i^2$). In this general case we were unable to solve the precession equations (4.14)—(4.16) analytically, and so had to resort to numerical integrations. One would expect, however, that, for "typical" inspirals, the precessional behavior will qualitatively resemble the simple precession described in Sec. 4, if precession is important to the dynamics at all. That expectation is based on the following argument, which begins by dividing binaries into two categories based on their mass ratio: $M_2/M_1 \ll 1$ and $M_2/M_1 \approx 1$. If $M_2/M_1 \ll 1$, the amplitude of precession will be very small unless $S_1 \gg S_2$, since $S_2/L(t) \leq (M_2/M_1)(M/r(t))^{1/2} \ll 1$. If $S_1 \gg S_2$, the larger spin should dominate the precessional dynamics, and the smaller spin can be treated as a perturbation on the special-case solutions of Sec. 4. Similarly, if $M_1 \approx M_2$, the mass difference can be treated as a perturbation to our special case solutions for $M_1 = M_2$.

The above argument is not very compelling, especially when applied to "intermediate" cases such as $M_2/M_1 = 1/2$. One therefore seeks guidance from numerically generated examples. Now, in principle one could systematically look for qualitatively new types of solutions by integrating the precession equations (4.14)—(4.16) for thousands of randomly chosen values of M_1, M_2, S_1, S_2, and initial directions $\hat{S}_1$ and $\hat{S}_2$. This we have not attempted to do. However, we have integrated equations (4.14)—(4.16) for a wide variety of initial conditions which we "put in by hand"; the results seem to support the conclusion that most cases give "somewhat ragged" versions of the simple precession described in Sec. 4.2. That is, $\hat{J}$ is roughly fixed, and $\hat{L}(t)$ roughly traces an outward spiral from $\hat{J}$.

To illustrate this, Figs. 4.11–4.18 display several examples of numerical solutions to the precession equations (4.14)—(4.16), augmented by the signal-amplitude equations (4.26) and (4.28). The drawing in each figure depicts the initial values of the vectors $\vec{L}$, $\vec{S}_1$, $\vec{S}_2$, and $\vec{S}$ at the moment that the gravity wave frequency sweeps past $10(10M_\odot/M)$ Hz (corresponding to $r/M = 75$). For ease of comparison, we have chosen $\vec{J} = \vec{S} + \vec{L}$ to point initially along the $\hat{z}$-axis in all our examples; the precise details of how the other initial vectors were chosen are spelled out in the

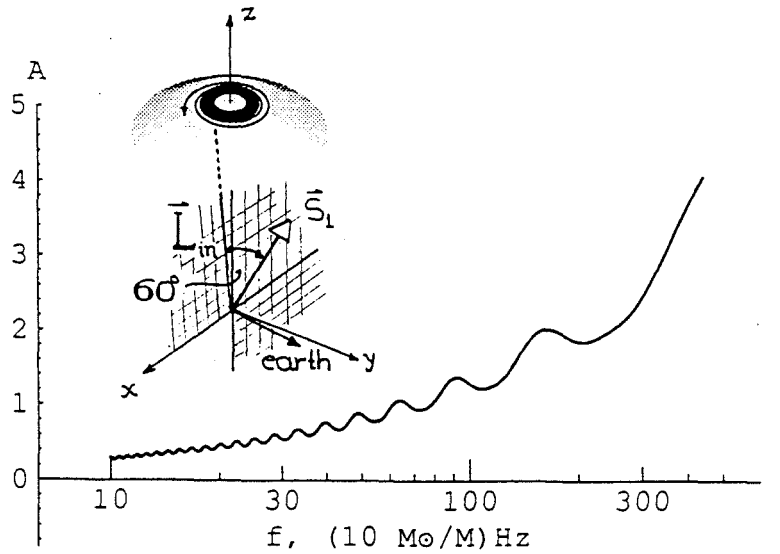

Figure 4.11: This and the next seven figures (Figs. 4.11–4.18) depict the precession of the orbital angular momentum direction $\hat{L}$ and the resulting modulated signal amplitude $A(t)$ in the detector, as computed by numerical integrations of the precession equations (4.14)—(4.16) together with Eqs. (4.26) and (4.28). In all these figures the detector's legs are along the x and y axes, the direction from the detector to the binary is $\hat{N} = (\hat{z}+\hat{x})/\sqrt{2}$, the total spin $\vec{S} = \vec{S}_1 + \vec{S}_2$ has magnitude $S = {M_1}^2$, the angle between the orbital angular momentum $\vec{L}$ and the total spin $\vec{S}$ is 60° so $\kappa = \hat{L}\cdot\hat{S} = 0.5$ (except in Figs. 4.17 and 4.18, where that angle is 178° and $\kappa = -0.99939$), and at the beginning of the integration—when $f = 10(10M_\odot/M)$ Hz, $r/M = 75$, and $L = \sqrt{75}M_1M_2$—the total angular momentum $\vec{J} = \vec{L} + \vec{S}$ points in the z direction, and $\hat{L}$ is in the x-z plane, on the $+x$ side of the z-axis, while $\hat{S}$ is in the x-z plane, on the $-x$ side of the z-axis. When both bodies are spinning (Figs. 4.12, 4.14, 4.16, and 4.18), their spins initially lie in the $\hat{y}$-$\hat{S}$ plane. The figures differ from each other in their mass ratio M_2/M_1 and in the magnitudes of the bodies' spins. In this figure, the masses are equal, $M_2/M_1 = 1$, body 1 is maximally spinning, $S_1 = {M_1}^2$, and body 2 is nonspinning, $S_2 = 0$, so $\vec{S} = \vec{S}_1$ and $\vec{L}$ have the initial values shown in the drawing. The subsequent motion of $\hat{L}$ is shown as an outward-spiraling path on the sphere. The graph shows the amplitude $A(t)$ of the gravitational-wave signal measured by the detector.

caption of Fig. 4.11. In each figure, the curve on the sphere is the time evolution of $\hat{L}(t)$ from the initial moment, when $f = 10(10M_\odot/M)$ Hz and $r/M = 75$ to a final moment, when $f = 440(10M_\odot/M)$Hz and $r/M = 6$. The curve plotted in each figure is the amplitude $A(t)$ of the gravity-wave signal that would be measured by a detector whose arms lie along the $\hat{x}$ and $\hat{y}$ axes, when the binary is in the direction $\hat{N} = (\hat{z} + \hat{x})/\sqrt{2}$. The signal amplitude $A(t)$ is actually plotted against the frequency f of the gravity wave signal at time t; that is, we plot $A(f) \equiv A(t(f))$. (We emphasize that we are *not* plotting the Fourier transform of $A(t)$.) The overall normalization of $A(f)$ is arbitrary.

We have arranged Figs. 4.11–4.18 in pairs: an example with just one body spinning, $S_1 = {M_1}^2$ and $S_2 = 0$ (for which the special-case theory of Sec. 4S is valid), is paired with a corresponding example having the same mass ratio and same initial $\vec{L}$ and $\vec{S}$, but with both bodies maximally spinning, so $S_1 = {M_1}^2$ and $S_2 = {M_2}^2$. We emphasize that when both bodies are spinning (Figs. 4.12, 4.14, 4.16, and 4.18) the precession and signal amplitude depicted are solutions of the full post^2-Newtonian precession equations (4.14)—(4.16), *including the spin-spin terms*; the spin-spin terms either vanished identically or were ignored in our analysis of special cases in Sec. 4.

The first pair of examples, Figs. 4.11 and 4.12, are for a mass ratio $M_2/M_1 = 1.0$ and for $\kappa = 0.5$ (so the angle between $\hat{L}$ and $\hat{S}$ is 60°). Because the two masses are equal, the solutions for $\hat{L}(t)$ and $A(t)$ shown in Figs. 4.11 and 4.12 would be identical, were it not for the spin-spin terms in Eqs. (4.14)—(4.16). We see that the the spin-spin effects are noticeable, but do not change the basic, qualitative behavior of the solution. Quantitatively, the $S_2 = 0$ case contains 0.5 fewer precessions in the observable range than the case where S_2 is maximal.

Figures 4.13 and 4.14 show an example where $M_2/M_1 = 0.3$ and $\kappa = 0.5$; while Figs. 4.15 and 4.16 are for $M_2/M_1 = 0.1$ and $\kappa = 0.5$. Again, the precessional motion of $\vec{L}$ and the signal amplitude are nearly the same in the corresponding cases, i.e., the effect of the second spin is small. This is to be expected, since $S_2/S_1 = {M_2}^2/{M_1}^2$ is 0.09 in Fig. 4.14 and 0.01 in Fig. 4.16.

Finally, in Figs. 4.17 and 4.18 we show an example containing transitional precession. Here $M_2/M_1 = 0.13$ and $\kappa = -0.99939$ (so the angle between $\hat{L}$ and $\hat{S}$ is 178°), and our integrations start [at $f = 10(10M_\odot/M)$ Hz] when the transitional precession is already underway: the figures show the end of transitional precession and the resumption of simple precession. The two solutions for $\hat{L}(t)$ are again qualitatively similar, but, interestingly, the two-spin case (Fig. 4.18) displays a

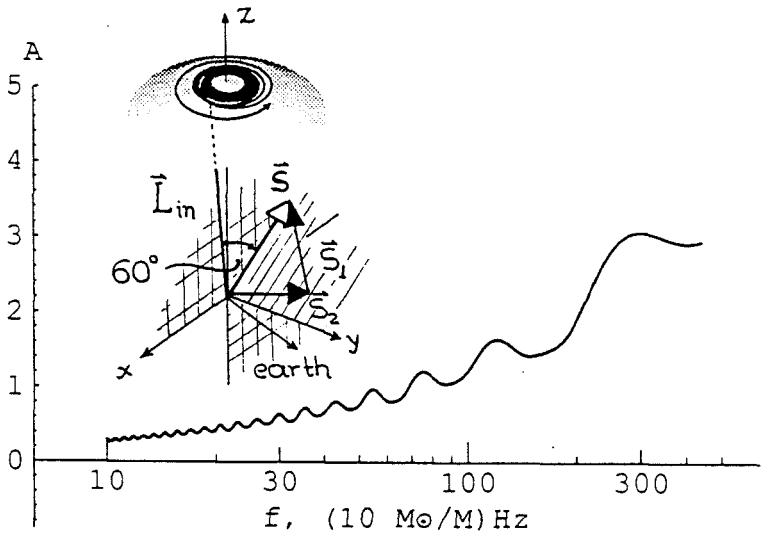

Figure 4.12: Same as Fig. 4.11, and with the same mass ratio $M_2/M_1 = 1$ but with both bodies maximaly spinning,$S_1 = {M_1}^2$, $S_2 = {M_2}^2$, so the initial $\vec{S}_1$, $\vec{S}_2$, $\vec{S}$, and $\hat{L}$ are as shown.

large number of "epicycles" on top of the basic one-spin evolution (Fig. 4.17). The epicycles are reflected in the many little wiggles visible in the waveform's amplitude.

We can understand these epicycles as follows: Since $S_2/S_1 = (0.13)^2 = 0.017$, we can treat the second spin as a perturbation. Actually, the formulation is slightly simpler if we treat $M_2/M_1 = 0.13$ as the expansion parameter rather than S_2/S_1, while regarding M_1 and $S_2/{M_2}^2$ as fixed. Then $\vec{S}_2$ is second-order in the expansion parameter, and $\dot{\vec{S}}_2$ is first order. [The term $\vec{S}_2$ is of higher order than $\dot{\vec{S}}_2$ because the epicyclic frequency diverges as $M_2 \to 0$; see Eq. (4.16).] We define $\vec{L}(t) \equiv \vec{L}_1(t) + \vec{L}_2(t)$, where $\vec{L}_1(t)$ is the "background" solution and $\vec{L}_2(t)$ represents the perturbation in $\vec{L}(t)$ due to $\vec{S}_2$. The term $\vec{L}_2(t)$ is second-order, and $\dot{\vec{L}}_2(t)$ is first order. We now expand the precession equations (4.14)—(4.16) to first-order. Adding Eqs. (4.14) and (4.15), we find

$$\dot{\vec{L}}_2 + \dot{\vec{S}}_2 = 0. \tag{4.86}$$

We can absorb the constant of integration into the definition of $\vec{L}_1$; this leaves

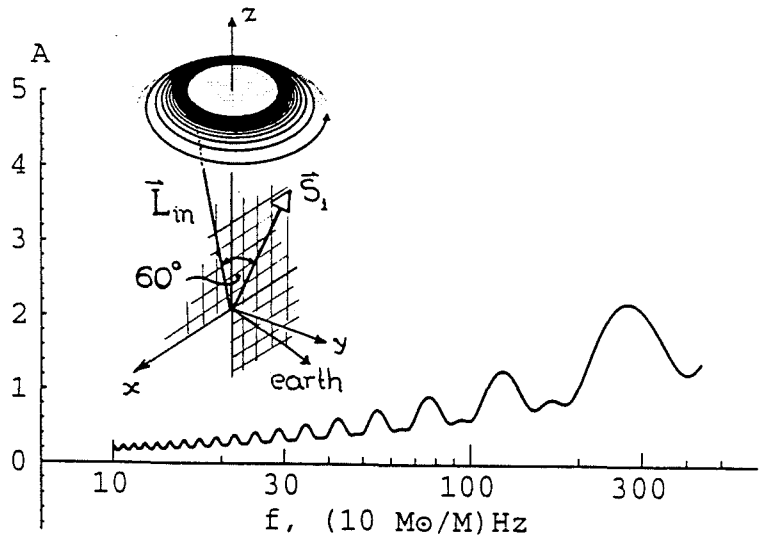

Figure 4.13: Same as Fig. 4.11, but with $M_2/M_1 = 0.3$, $S_1 = {M_1}^2$ and $S_2 = 0$, so the initial $\vec{S}_1$ and $\hat{L}$ are as shown.

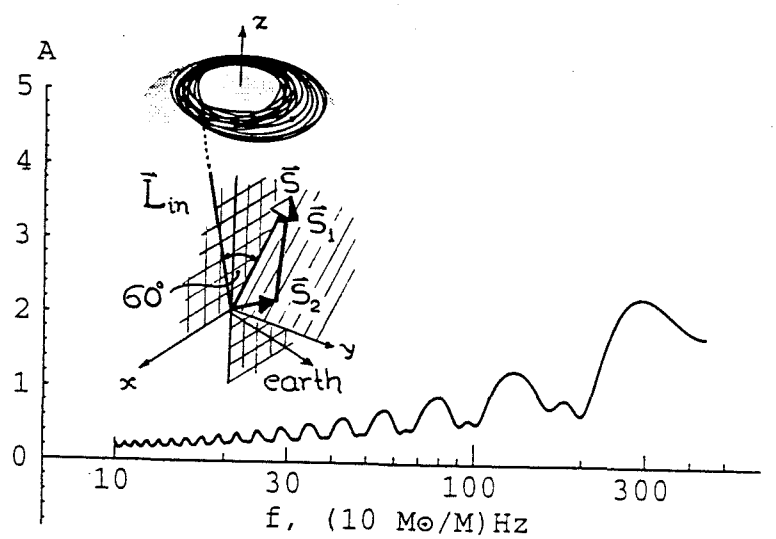

Figure 4.14: Same as Fig. 4.11, but with $M_2/M_1 = 0.3$ (as in Fig. 4.13) and $S_1 = {M_1}^2$, $S_2 = {M_2}^2$, so the initial $\vec{S}_1$, $\vec{S}_2$, $\vec{S}$, and $\hat{L}$ are as shown.

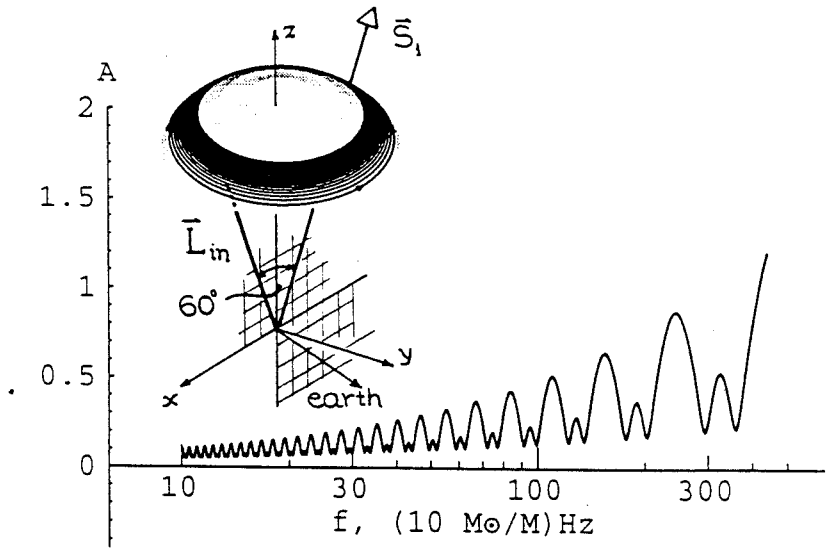

Figure 4.15: Same as in Fig. 4.11, but with $M_2/M_1 = 0.1$, $S_1 = {M_1}^2$ and $S_2 = 0$, so the initial $\vec{S}_1$ and $\vec{L}$ are as shown.

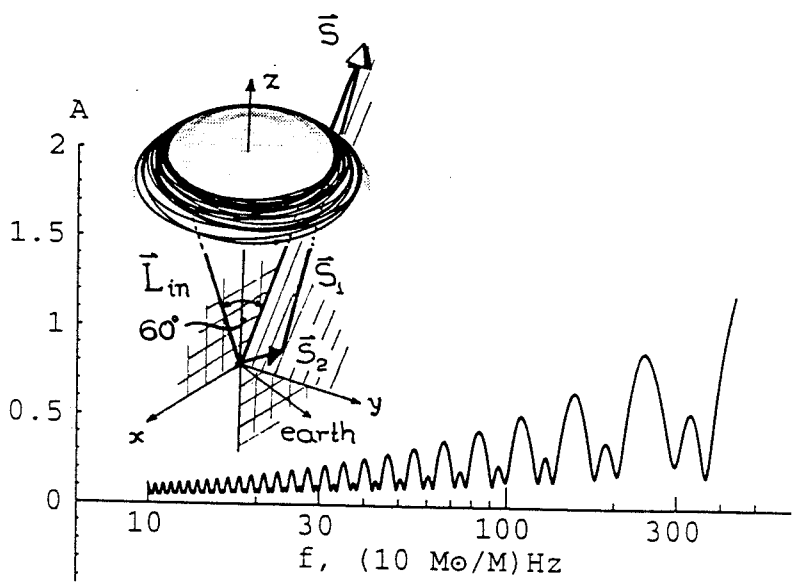

Figure 4.16: Same as in Fig. 4.11, but with $M_2/M_1 = 0.1$ (as in Fig. 4.15) and $S_1 = {M_1}^2$, $S_2 = {M_2}^2$, so the initial $\vec{S}_1$, $\vec{S}_2$, $\vec{S}$, and $\hat{L}$ are as shown.

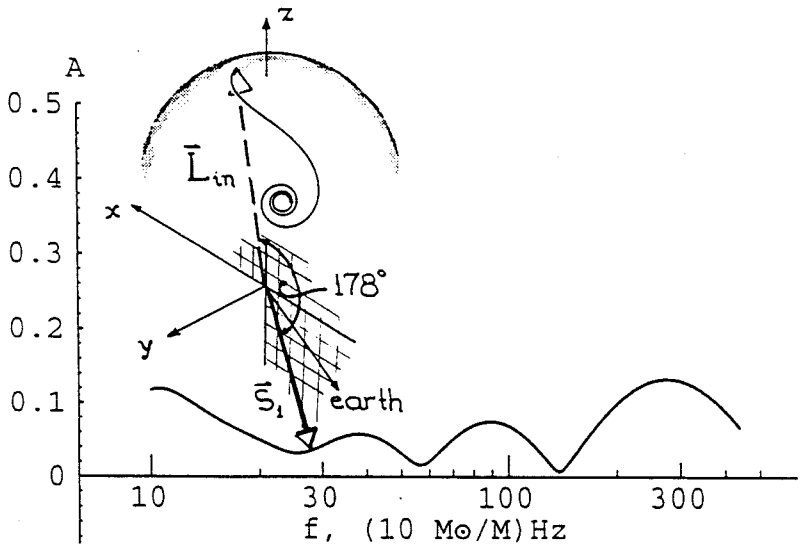

Figure 4.17: Same as in Fig. 4.11, but with $\hat{L}$ and $\hat{S}$ nearly antialigned (i.e., separated by an angle of 178° so $\kappa = -0.99939$), and with $M_2/M_1 = 0.13$, $S_1 = {M_1}^2$ and $S_2 = 0$, so the initial $\vec{S}_1$ and $\vec{L}$ are as shown. The evolution illustrates transitional precession and the subsequent return to simple precession.

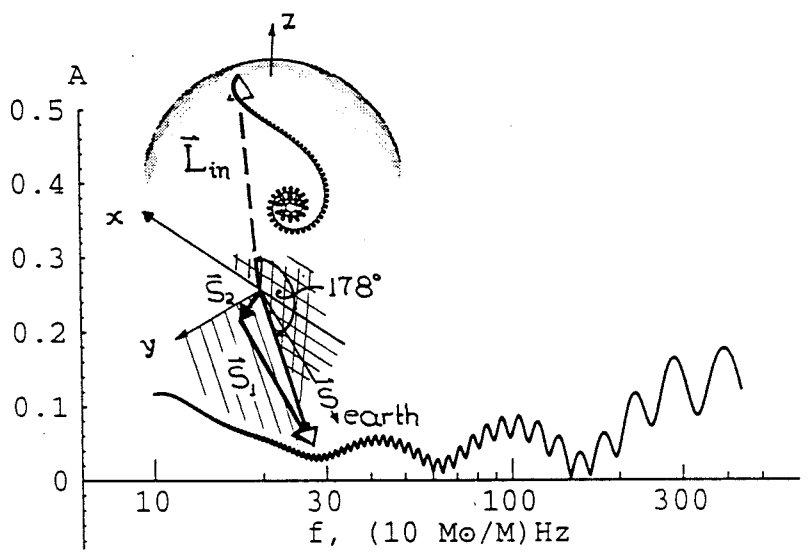

Figure 4.18: Same as in Fig. 4.11, but with the same near antialignment and mass ratio as in Fig. 4.17 (angle 178° between $\hat{L}$ and $\hat{S}$, $\kappa = -0.99939$, $M_2/M_1 = 0.13$), and with and $S_1 = {M_1}^2$, $S_2 = {M_2}^2$, so the initial $\vec{S}_1$, $\vec{S}_2$, $\vec{S}$ and $\vec{L}$ are as shown. The evolution is essentially the same as in Fig. 4.17, but with visible "epicycles" due to the relatively rapid precession of $\vec{S}_2$ around $\vec{L}$.

$\vec{L}_2 = -\vec{S}_2$. The first-order piece of Eq. (4.16) then becomes

$$\dot{\vec{L}}_2 = \left(\frac{1}{r^3}\right)\left(\frac{3M_1}{2M_2}\right)\vec{L}_1 \times \vec{S}_2. \tag{4.87}$$

We see from Eq. (4.87) that $\vec{L}_2$ spirals around $\vec{L}_1$ with an epicyclic frequency

$$\Omega_e = (3M_1/2M_2)\,L/r^3 \tag{4.88}$$

that is larger than the precession frequency Ω_p by a factor $(3M_1/4M_2)L/J$. Using Eq. (4.11) for dr/dt, the total number of epicycles between some large radius r and the final plunge can be estimated to be $\sim (1/80)(M_1/M_2)(r/M)^{3/2}$. This corresponds to ~ 60 epicycles for the case shown in Fig. 4.18, in good agreement with the numerical integration.

Since basically this same perturbation analysis can be applied to the situations shown in Figs. 4.14 and 4.16, one might wonder why epicycles are not visible in those figures. The reason is that in these cases the ratio of epicyclic frequency to precession frequency is much closer to unity than is the case in Fig. 4.18, and also the ratio $|\vec{S}_2 \times \vec{L}|$ to $|\vec{S}_1 \times \vec{L}|$ is much smaller. Therefore it is harder to pick out the epicycles by eye.

In conclusion, it appears that the intuitive pictures that we have derived from the study of special cases in Sec. 4 can be successfully applied to more general values of the mass and spin parameters. The "extra wiggles" that arise in the general case can be understood as perturbations on our special case solutions.

ACKNOWLEDGEMENTS

We thank Eanna Flanagan for helpful conversations. The orbital-precession and wave-generation aspects of this research were supported in part by NSF grant AST-9114925 and, in view of its application to proposed detectors in space, by NASA grant NAGW-2897. The application to ground-based gravitational-wave detection was supported in part by NSF grant PHY-9213508. The last several months of Cutler's contribution to this work were supported by grant AST-9119475 at Cornell University.

6 APPENDIX: FOUNDATIONS FOR AN INTUITIVE UNDERSTANDING OF THE WAVEFORM MODULATION

In leading order (when one ignores orbital inspiral, precession, and post-Newtonian effects), the gravitational waves from a circular binary are monochromatic, and therefore have elliptical polarization. (We regard circular and linear polarizations as special cases of elliptical). In this appendix we develop a set of diagrammatic tools (Figs. 4.19, 4.20, 4.21, and 4.23) for describing such waves and the signals they produce in a detector. These diagrammatic tools are especially useful when the waves come from overhead or underfoot, i.e., when the plane of the detector is orthogonal to the waves' propagation direction. For obliquely inclined detectors, one must apply the tools to each detector arm separately, and then combine the signals.

In Secs. 6.1 and 6.2 of the appendix, we diagrammatically describe the waves alone (without any detector); the culmination of this description is an *elliptical polarization diagram*, which is simply related to the elliptical projection of the binary's orbital plane on the sky. In Sec. 6.3 we show, by examples, how to use this polarization diagram (or, equivalently the orbit's elliptical projection) to deduce the precession-induced modulations of the signal in a detector. In Sec. 6.4 we derive some formulas that underlie another diagrammatic tool, the *cell diagram*, by which one can deduce especially simply the signal's polarization phase φ. In Sec. 6.5 we present the cell diagram and show how to use it. Sections 6.3, 6.4, and 6.5 are restricted to detectors orthogonal to the propagation direction. In Sec. 6.6 we comment on the application of our techniques to obliquely inclined detectors.

6.1 Elliptically polarized gravitational waves

In building our diagrammatic tools, we shall focus initially on an arbitrary, monochromatic, elliptically polarized gravitational wave. Only later, in Sec. 6.2, will we apply these tools to the waves from a circular binary.

For monochromatic waves, the dimensionless gravitational wave fields h_+ and $h_\times$, as they pass through the laboratory, are given by

$$h_+ = H_+ \cos(\omega t), \quad h_\times = \pm H_\times \sin(\omega t) \, . \tag{4.89}$$

Here the + sign corresponds to right-hand polarized waves and the − sign to left-

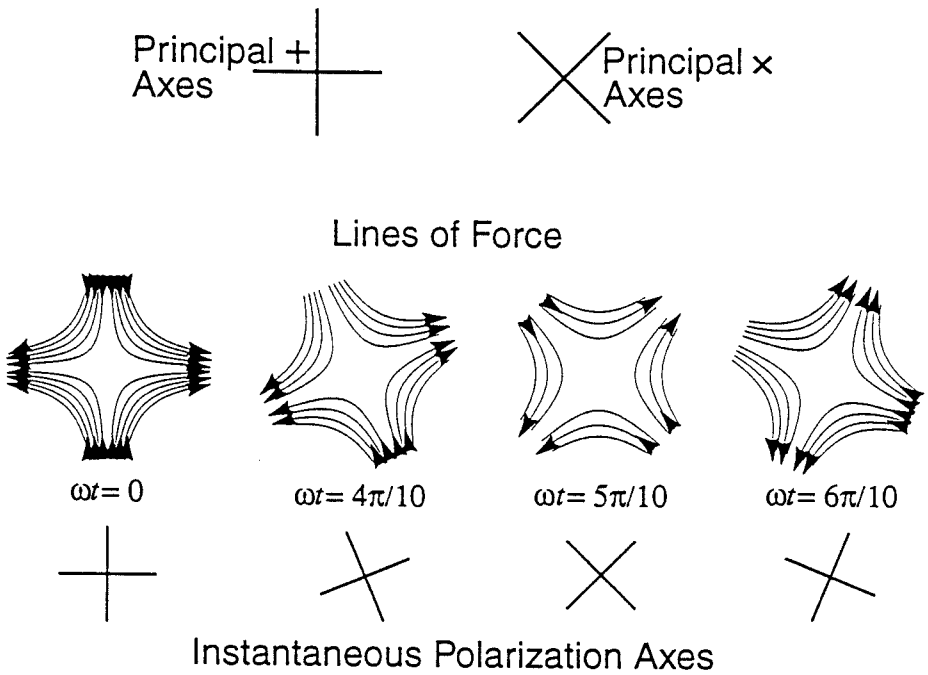

Figure 4.19: Principal axes, instantaneous lines of force, and instantaneous polarization axes for an elliptically polarized gravitational wave with right-hand polarization and amplitude ratio $H_\times/H_+ = 0.5$.

hand; H_+ and $H_\times$ are constants, the amplitudes of the two polarization states, and we have omitted an arbitrary phase by our choice of the zero of time. By convention we shall insist that both amplitudes be positive and that $H_+ \geq H_\times$. The waves will take the form (4.89), with its phase delay of precisely $\pm\pi/2$ radians between the two wave fields and with $H_+ > H_\times$, only for a special, unique choice of the polarization axes with respect to which the "+" and "×" states are defined. We shall call that unique choice the elliptical waves' *principal axes.*

Figure 4.19 shows an example of principal axes for waves that are propagating perpendicularly out of the paper. [To verify that any other ("primed") choice of axes will produce a non$\pm\pi/2$ phase shift between the two fields, one need only insert Eq. (4.89) into the following standard expression [14] for the primed-axis fields in terms of the principal-axis fields

$$h_{+'} + ih_{\times'} = (h_+ + ih_\times)e^{-2i\psi} \tag{4.90}$$

and evaluate the resulting phases of $h_{+'}$ and $h_{\times'}$. In Eq. (4.90), ψ is the angle of rotation to go from the principal axes to the primed axes.]

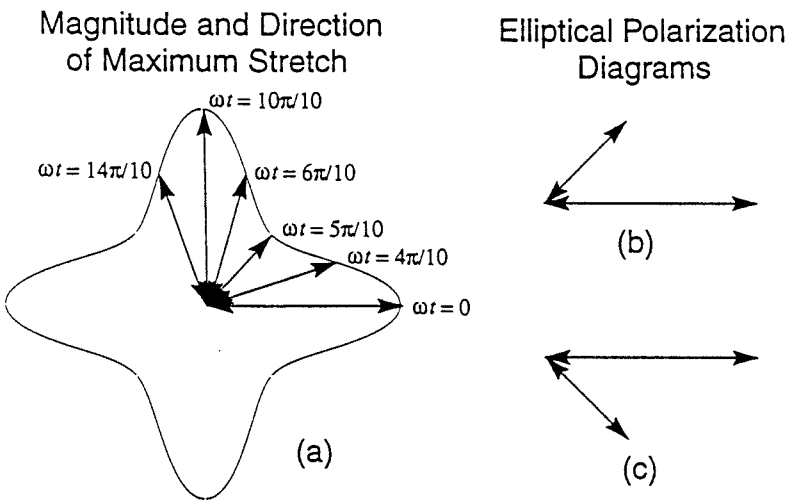

Figure 4.20: (a) The rotating, oscillating stretch line which depicts the direction and magnitude of maximum tidal stretch for the gravitational waves of Fig. 4.1. (b) The elliptical polarization diagram for these same waves. (c) The polarization diagram for these waves but with their handedness changed from right to left.

The instantaneous tidal accelerations exerted on matter by any gravitational wave can be described by electrical-like "lines of force"; see, e.g., Ref. [14]. Figure 4.19 shows the evolution of these lines of force for the monochromatic, right-hand elliptical waves of Eq. (4.89), with $H_\times/H_+ = 0.5$.

Note that the lines of force rotate in a right-hand manner (recall that the waves are propagating out of the paper), and as they rotate, the density of force lines oscillates. Just as in electromagnetic theory, so also here, the density of force lines is proportional to the magnitude of the wave-induced accelerations. The accealerations are strongest at $\omega t = 0$, when only the "principal+" polarization is active, and weakest at $\omega t = \pi/2$ when only the "principal×" polarization is active. Note that the rotation of the force lines is very nonuniform: slow near $\omega t = 0$ when the large principal+ mode is active, and fast near $\omega t = \pi/2$ when the small principal× mode is active.

Figure 4.20a is a simpler way of depicting the rotation and oscillation of the instantaneous force lines. Here we are asked to remember that the shapes of the

force lines are quadrupolar; and at each moment of time we show, via a double-arrowed line, the direction of the instantaneous tidal stretch axis (the direction of maximum tidal stretch), and the magnitude of the tidal acceleration along that axis. As time passes, the stretch axis rotates and the magnitude of the acceleration oscillates (big horizontal stretch at $\omega t = 0$, small 45-degree stretch at $\omega t = \pi/2$, big vertical stretch at $\omega t = \pi$, etc.).

Figure 4.20b (which we shall call an *elliptical polarization diagram* or simply *polarization diagram*) embodies the same information as Fig. 4.20a, but more simply. It shows just two tidal stretch lines, the long one at $\omega t = 0$, which points along a principal+ stretch axis and has length proportional to H_+; and the shorter one at $\omega t = \pi/2$, which points along the principal$\times$ axis and has length proportional to $H_\times$. From this diagram, one can reconstruct both the rotating, oscillating stretch line of Fig. 4.20a and the time-evolving force lines of Fig. 4.19. To do so, one just needs to remember that (i) the quadrupolar-shaped lines of force rotate from the longer stretch line toward the shorter one, (ii) the magnitude of the tidal accelerations is maximum when one of the instantaneous polarization axes coincides with the longer stretch line and then it is proportional to the stretch line's length, and similarly (iii) the magnitude of the accelerations is minimum when an instantaneous polarization axis coincides with the shorter stretch line and then it is proportional to that stretch line's length.

Figure 4.20c is a polarization diagram for the same waves as we have been discussing, but with left-hand polarization rather than right: the lines of force rotate clockwise from the long stretch line toward the short one, rather than counterclockwise as in Fig. 4.20b.

6.2 Specialization to waves from circular binaries

Turn, now, to the leading-order gravitational waves from a circular binary (with inspiral, precession, and post-Newtonian effects ignored). Figure 4.21a depicts the orbit of one of the binary's stars (or black holes), projected onto the plane of the Earth's sky (i.e. projected perpendicular to the incoming waves' propagation direction). Because of the projection, the circular orbit looks elliptical, with a ratio α of minor axis to major axis given by

$$\alpha \equiv |\hat{L} \cdot \hat{N}| \,. \tag{4.91}$$

In Sec. 2 we defined the *principal+ direction* to be the major axis of this orbital ellipse, and the *principal$\times$ direction* to be rotated 45° from it, in a counterclockwise

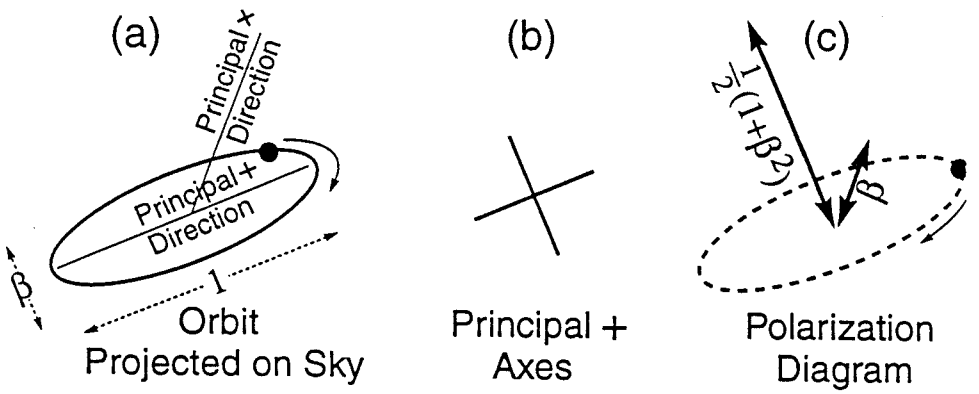

Figure 4.21: (a) The orbit of one of the stars in a circularized binary, projected on the plane of the sky. (b) The principal+ axes of the elliptically polarized waves emitted by this binary; note that these axes coincide with the projected orbit's principal axes; the principal× axes will be rotated 45° to the orbit's axes. (c) The elliptical polarization diagram for the emitted waves.

direction. The binary emits elliptically polarized waves toward Earth. The waves' principal+ axes coincide with the major and minor axes of the projected orbital ellipse as shown in Fig. 4.21b—i.e., one principal+ axis is along the principal+ direction and the other is perpendicular to it; and similarly for principal×. With respect to these principal+ and principal× axes, the waves are described by Eq. (4.89), with amplitudes [cf. Eq. (4.2), (4.3)]

$$H_+ = \frac{4M_1M_2}{rD}\frac{[1+(\hat{L}\cdot\hat{N})^2]}{2}\ ,\quad H_\times = \frac{4M_1M_2}{rD}|\hat{L}\cdot\hat{N}|\ . \tag{4.92}$$

Here, as in the body of this paper, M_1 and M_2 are the masses of the two bodies, r is the orbital diameter, and D the distance of the binary from the Earth. The factor $-\hat{L}\cdot\hat{N}$ in $H_\times$ guarantees that the waves' handedness is the same as the motion of the stars around their projected orbit (left-hand in Fig. 4.21).

From the wave fields (4.2), (4.3), their amplitudes (4.92), and the principal+ axes of Fig. 4.21b, we infer that the elliptical polarization diagram has the form

shown in Fig. 4.21c. Notice the very simple relationship of this polarization diagram to the projection of the orbit on the sky: The longer stretch axis is perpendicular to the projected orbit's major axis, i.e. perpendicular to the principal+ direction (as will always be the case); the shorter stretch axis is rotated 45° *in the direction of the orbital motion* (as will always be the case), i.e. in this case of left-hand polarized waves it is along the principal× direction while for right-hand waves it would be perpendicular to principal×; the length of the shorter stretch is proportional to $\alpha = |\hat{L} \cdot \hat{N}|$ (the orbit's axis ratio); and the length of the longer stretch is proportional to $\frac{1}{2}(1 + \alpha^2)$. At a retarded time when the stars' separation is along the principal+ direction (so one of the stars is at the location shown in Fig. 4.21c), the instantaneous *squeeze* axis is along that principal+ direction, i.e. along the direction from the center of the orbit to the star [cf. the minus sign in Eqs. (4.2), (4.3) and (4.8)], and the instantaneous stretch axis is perpendicular to that direction, i.e., along the long stretch line of Fig. 4.21c. (It is this that dictates our drawing the long stretch axis perpendicular to the principal+ direction rather than along it.) An eighth of an orbit later, when the star in Fig.4.21c has moved from the tail to the tip of the thin orbital arrow, the instantaneous squeeze axis is along the direction to that star, and the instantaneous stretch axis is perpendicular to that direction, i.e. along the short stretch line of Fig.4.21c.

6.3 Signal modulation for detectors orthogonal to the waves' propagation direction

Figure 4.21 provides a simple, intuitive understanding of how a binary's precession modulates its gravitational waves: As the binary precesses, the eccentricity and orientation of its projected orbit (Fig. 4.21a) oscillate, and the polarization diagram (Fig. 4.21c), which describes the waves, oscillates in the obvious, corresponding manner.

It is fairly easy, from the oscillating polarization diagram, to understand the modulation of the amplitude $A(t)$ and polarization phase $\varphi(t)$ of the signal that the wave induces in a detector. As an example, consider the neutron-star/black-hole binary studied in Sec. 4.3, for which $A(t)$ and $\varphi(t)$ were depicted in Figs. 4.6 and 4.7 assuming two different detector orientations, $+'$ and $\times'$. Recall that in this example the source is precisely underfoot; i.e., the detector arms are orthogonal to the direction of wave propagation. In this section and the next two, we shall restrict attention to cases where the detector is directly underfoot or overhead.

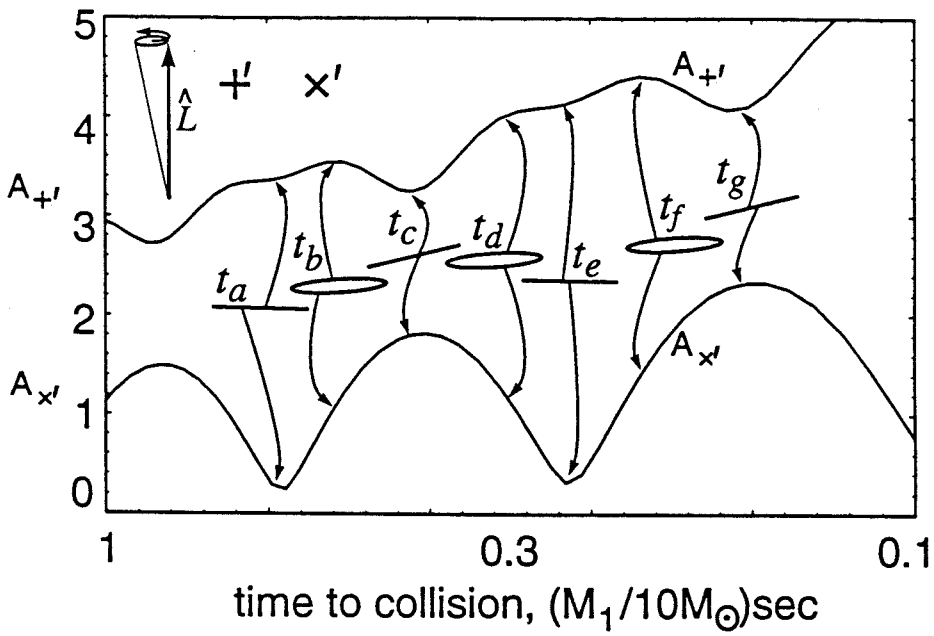

Figure 4.22: Figure used to explain the modulation of the signal amplitudes $A_{+'}(t)$ and $A_{\times'}(t)$ for the binary and detectors of Figs 4.5, 4.6, and 4.7.

Figure 4.22 reproduces a short segment of the amplitudes' time evolution (Fig. 4.6). In the upper left is a schematic picture of the precessing orbital-angular-momentum direction $\hat{L}$ (see also Fig. 4.5). The waves are traveling vertically out of the paper, and the detectors' arms are oriented as indicated by the $+'$ and $\times'$ symbols. The time-evolving projection of the orbit on the plane of the sky is depicted in the center of the figure. When the orbit is edge-on, we see only a line. When $\hat{L}$ is tilted away from Earth, we see the orbit from below (shown as a shaded ellipse); the stars move around the ellipse in a clockwise direction, and the waves therefore are left-hand polarized. When $\hat{L}$ is tilted toward Earth, we see the orbit from above (shown as a white ellipse); the stars move around the ellipse counterclockwise, and the waves are right-hand polarized.

Consider the amplitude $A_{+'}$ measured by the $+'$ detector, and mentally factor out its steady, overall growth due to the steady orbital inspiral. At time t_a, the orbit is edge on, so the waves are concentrated entirely in the principal+ mode; and because the edge-on orbit is almost parallel to one of the $+'$ detector's arms, that detector feels the full force of the principal+ waves. At time t_b, $\hat{L}$ has tilted away from Earth a bit, thereby making the orbit appear somewhat elliptical and giving a bit of added strength to the principal+ waves. [Recall that their strength H_+ is proportional to $\frac{1}{2}(1+\alpha^2)$, where α is the ratio of the minor to major axis of the ellipse.] Because the orbit's major axis is still nearly parallel to a detector arm, the detector still "feels" solely the principal+ mode (even though $H_\times$ is no longer zero), and it feels the mode's full strength; hence, $A_{+'}$ has gone up a bit. At time t_c, the orbit has become edge-on again so $H_\times$ is again zero, but now the orbit is tilted away from the detector's arm by $2\lambda_L \simeq 17°$, thereby reducing somewhat the $+'$ detector's response to the principal+ mode; as a result, $A_{+'}$ has decreased significantly. At time t_d, the orbit is tilted toward Earth and has thus become somewhat elliptical once again, thereby enhancing H_+; and again the orbit is nearly parallel to the detector's arm, so the detector feels nearly the full force of the principal+ mode. As a result, $A_{+'}$ has gone up again. At time t_e, the orbit's major axis is still nearly parallel to the detector arm. Hence the detector still feels nearly the full force of the principal+ mode, but the orbit is now edge-on, so H_+ has been reduced, and $A_{+'}$ has gone down a bit, relative to the steady increase caused by the shrinking orbit.

The evolution of $A_{\times'}$ can be understood similarly: At time t_a, the orbit is edge-on, so $H_\times = 0$; also the orbit is inclined almost 45° to the arms of the detector, so the $\times'$ detector hardly responds at all to H_+. Thus, $A_{\times'}$ is very small. At time t_b,

the orbit's major axis is still almost 45° from the detector's arms, so the detector still responds almost solely to the principal× mode; but now the orbit has become somewhat elliptical, thereby exciting the principal× mode somewhat and driving $A_{\times'}$ upward. At time t_c, the orbit is edge on, so $H_\times = 0$, but now the orbit is tilted to within $45° - 2\lambda_L \simeq 28°$ of the nearest detector arm, so the principal+ mode can drive the detector significantly, thereby pushing $A_{\times'}$ up to its maximum value. At time t_d, the orbit has tilted back to nearly 45° from the arms so only the principal× mode can couple to the detector, and because the orbit is only slightly elliptical, that mode produces a weakened signal $A_{\times'}$. At t_e the orbit is edge-on so $H_\times = 0$, and the orbit's major axis is still about 45° from the arms, so principal+ mode couples hardly at all to the detector, and $A_{\times'}$ has become very small.

We now consider the evolution of the polarization phase $\varphi(t)$ in each of the two detectors. To deduce φ at any moment t, one need only notice how strongly each of the two wave modes (principal+ and principal×) is coupled to the detector, and combine that coupling strength with a knowledge of the phase of the signal put into the detector by each mode. In doing so, one must keep in mind the overall minus signs in Eqs. (4.2), (4.3) and (4.8). As one can verify from Eqs. (4.2)—(4.8) (and as might be obvious),

i. The polarization phase of the principal+ signal is zero (i.e., the signal $h(t)$ goes as $-\cos[2\Phi(t)]$) if the orbit's major axis (i.e. the waves' principal+ direction) is nearer the detector's "first" arm than its "second" arm, and the phase is π (the signal goes as $+\cos[2\Phi(t)]$) if the principal+ direction is nearer the second arm than the first. (The first arm is the one that, by convention, gets stretched when $h > 0$ and squeezed when $h < 0$.)

ii. The polarization phase of the principal× signal is $-\pi/2$, or $3\pi/2$ (so the signal $h(t)$ goes as $-\sin[2\Phi(t)]$) if the waves' principal× direction is nearer the first arm than the second, and the phase is $+\pi/2$ (the signal goes as $+\sin[2\Phi(t)]$) if the principal× direction is nearer the second arm than the first.

Consider, as an example, the polarization phase $\varphi_{\times'}$ in the $\times'$ detector. From the orbital ellipses in Fig. 4.22 and the above phasing rules, we deduce the following: At time t_b the principal× mode is dominant; because the orbit is seen from below and the principal+ and principal× axes are therefore like those of Fig. 4.20c, the principal× direction is nearly along the detector's second arm; therefore, the polarization phase is $\varphi_{\times'} \simeq +\pi/2$. At time t_c only the principal+ mode is felt,

and because the orbit's major axis is near the detector's first arm, the polarization phase is $\varphi_{\times'} \simeq 0$. At time t_d the principal$\times$ mode is dominant, and because the orbit is now seen from above rather than from below, its phase contribution is opposite to that at time t_b: $\varphi_{\times'} \simeq -\pi/2$. At time t_e only the principal+ mode contributes, and although one cannot tell very clearly from the figure, the orbit's major axis is slightly nearer the second arm than the first, so $\varphi_\times = \pi$. Thus, as time passes, the polarization phase grows secularly more negative, decreasing by 2π with each orbital precession—in accord with Fig. 4.7b.

6.4 Some useful formulas for detectors orthogonal to the waves' propagation direction

This procedure for deducing the polarization phase can be embodied in a simple and powerful diagram. As a foundation for that diagram (and as an aid for readers who might wish to explore the signal modulation more quantitatively), we shall now specialize some of the equations of the text to detectors that are orthogonal to the direction of the incoming waves. We shall deal with the same two detectors $+'$ and $\times'$ as above and as in Sec. 4.3 and Fig. 4.6, but we shall allow the binary to be precessing in any manner it wishes, and not necessarily in the simple manner of Secs. 4.2 and 4.3.

For the $+'$ detector with its first arm along $\hat{x}$ and second along $\hat{y}$, and for our underfoot source direction $\hat{N} = -\hat{z} + \delta\hat{x}$ with $0 < \delta \ll 1$ (corresponding to $\theta = \pi - \frac{1}{2}\delta^2$ and $\phi = 0$), Eqs. (4.5), (4.6), and (4.7) reduce to

$$F_+ = \cos 2\psi\ , \quad F_\times = \sin 2\psi\ , \quad \psi = \arctan(\hat{L}_x/\hat{L}_y)\ , \tag{4.93}$$

and Eq. (4.4) then becomes

$$h_{+'} = h_+ \cos 2\psi + h_\times \sin 2\psi\ . \tag{4.94}$$

This is just the real part of the standard law $h_{+'} + ih_{\times'} = (h_+ + ih_\times)e^{-i2\psi}$ by which a gravitational-wave field appears to change when one rotates one's basis axes in the plane orthogonal to the propagation direction [14], i.e. in the plane of our chosen detectors. From the imaginary part of that law, we obtain the expression for the signal measured by our $\times'$ detector [with its first arm along $\frac{1}{2}(\hat{x} + \hat{y})$ and second along $\frac{1}{2}(-\hat{x} + \hat{y})$]:

$$h_{\times'} = -h_+ \sin 2\psi + h_\times \cos 2\psi\ . \tag{4.95}$$

In these equations, h_+ and $h_\times$ are the gravitational-wave fields (4.2), (4.3) defined with respect to the binary's principal+ and principal× axes. By inserting Eqs. (4.93) and $\hat{L}\cdot\hat{N} = -\hat{L}_z$ into the amplitude and phase form (4.9), (4.10) of the measured signals, we obtain the following expressions for the precession-induced modulation of the amplitude and phase:

$$A_{+'} = \frac{2\mu M}{rD}\frac{\sqrt{(1+\hat{L}_z^2)^2(\hat{L}_y^2-\hat{L}_x^2)^2+16\hat{L}_x^2\hat{L}_y^2\hat{L}_z^2}}{1-\hat{L}_z^2}\,, \tag{4.96}$$

$$\varphi_{+'} = -\arctan\left(\frac{4\hat{L}_x\hat{L}_y\hat{L}_z}{(1+\hat{L}_z^2)(\hat{L}_y^2-\hat{L}_x^2)}\right)\,; \tag{4.97}$$

$$A_{\times'} = \frac{2\mu M}{rD}\frac{\sqrt{4(1+\hat{L}_z^2)^2\hat{L}_x^2\hat{L}_y^2+4\hat{L}_z^2(\hat{L}_y^2-\hat{L}_x^2)^2}}{1-\hat{L}_z^2}\,, \tag{4.98}$$

$$\varphi_{\times'} = \arctan\left(\frac{\hat{L}_z(\hat{L}_y^2-\hat{L}_x^2)}{\hat{L}_x\hat{L}_y(1+\hat{L}_z^2)}\right)\,. \tag{4.99}$$

These expressions can be used to verify and quantify the discussion of the previous section. More importantly, we shall now use the phase expressions to construct a powerful diagram for deducing the polarization phase modulation:

6.5 The Cell Diagram for detectors orthogonal to the propagation direction

The detector's polarization phase φ assumes the special values of 0, $\pi/2$, π, and $3\pi/2$ whenever the binary's orbital angular momentum $\vec{L}$ is oriented in one of a set of special directions relative to the detector's arms. These special orientations can be deduced equally well from Eq. (4.97) or Eq. (4.99); and they are depicted in Fig. 4.23. Note that the special orientations comprise boundaries or "walls" in orbital-angular-momentum space. Each wall in the figure is labeled by the value that φ assumes when $\vec{L}$ lies in it. The walls with $\varphi = 0$ or π are shaded; those with $\varphi = \pi/2$ or $3\pi/2$ are white.

We shall call Fig. 4.23 a *cell diagram* because its walls divide the orbital-angular-momentum space into sixteen cells. The values of φ at orientations inside each cell can be deduced, roughly, by interpolation from the values on its three walls.

From the precessional motion of $\vec{L}$ in this cell diagram, one can deduce directly the evolution of the polarization phase φ. Here are a few examples: If the precessional motion of $\vec{L}$ encloses the intersection line between a dark wall and a light

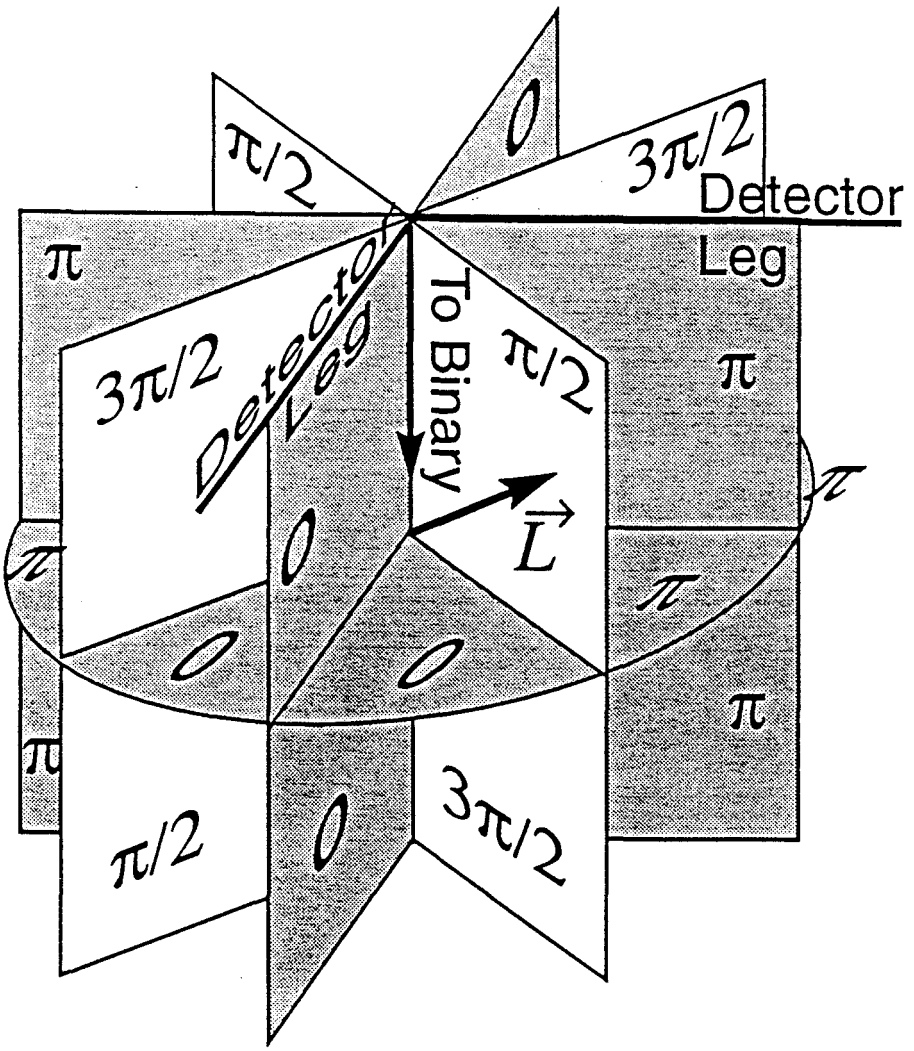

Figure 4.23: The *cell diagram*, which exhibits the polarization phase φ of a detector's gravitational-wave signal as a function of the relative orientation of the detector's arms and the binary's orbital angular momentum vector $\vec{L}$.

one, then φ will grow secularly, gaining or losing 2π with each precessional period (depending on the direction of precession). The $\varphi_{\times'}$ of Fig. 4.7 is an example of this. If the precessional motion almost but not quite encloses such a light/dark intersection, then φ will evolve like the dotted modification of Fig. 4.7. If the precession encloses the vertical direction, where two light and two dark walls intersect, then φ will change secularly by $\pm 4\pi$ with each precessional period. If the precession encloses an intersection of two dark walls, then φ will oscillate up and down around zero, with two oscillations per precession period. The $\varphi_{+'}$ of Fig. 4.7 is an example of this in which the precession is barely encompassing the dark-wall intersection, so one of the two oscillations is tiny while the other is large.

It is important to keep in mind that the total phase of the signal measured by the detector is not φ, but rather $\varphi + \delta\Phi$, and that $\delta\Phi$, like φ, can grow secularly with each precession. For simple precession, that growth is embodied in Eq. (4.83) which, stated in words, says: For simple precession of $\hat{L}$ with opening angle λ_L, if the precession cone encloses the direction $\hat{N}$ to the binary, then $\delta\Phi$ changes secularly with each precession by $\Delta\delta\Phi = -2\pi\cos\lambda_L$; if the precession cone does not enclose $\hat{N}$, then $\Delta\delta\Phi = 2\pi(1-\cos\lambda_L)$ if $\cos\lambda_L > 0$ and $\Delta\delta\Phi = 2\pi(-1-\cos\lambda_L)$ if $\cos\lambda_L < 0$.

6.6 Detectors not orthogonal to the propagation direction

In the last three sections we required that the detector be orthogonal to the waves' propagation direction. By doing so, we guaranteed that each of the two arms experienced precisely the same linear combination of principal+ and principal× modes, and the net signal was just twice that for either arm by itself. If, instead, the detector is inclined to the propagation direction (i.e., if the waves do not come in from directly overhead or underfoot), then the signal in each arm is the same as it would feel if it were projected into the orthogonal plane, and the net signal is the sum of those from the two legs. The projection, unfortunately, changes the lengths of the two legs by amounts that need not be the same and changes the angle between them so it no longer need be 90°. Therefore, it is not trivial to deduce, by the diagrammatic techniques of this appendix, the details of the net signal modulation: One must construct the equivalent, projected interferometer, then use the diagrams to deduce the signal in each leg, and then combine the signals.

Bibliography

[1] A. Abramovici *et al.*, *Science* **256**, 325 (1992).

[2] R. Narayan, T. Piran, and A. Shemi, *Astrophys. J.* **379**, L17 (1991); E.S. Phinney, *Astrophys. J.* **380**, L17 (1991).

[3] C. Cutler, T. A. Apostolatos, L. Bildsten, L. S. Finn, E. E. Flanagan, D. Kennefick, D. M. Markovic, A. Ori, E. Poisson, G. J. Sussman, and K. S. Thorne, *Phys. Rev. Lett* **70**, 2984 (1993).

[4] C. Cutler and E. E. Flanagan, *Phys. Rev. D*, in press.

[5] L. S. Finn and D. Chernoff, *Phys. Rev. D* **47**, 2198 (1993).

[6] C. W. Lincoln and C. M. Will, *Phys. Rev. D* **42**, 1123 (1990).

[7] E. Poisson, *Phys. Rev. D* **47**, 1511 (1993).

[8] L. E. Kidder, C. M. Will, and A. G. Wiseman, *Phys. Rev. D* **47**, 4183 (1993).

[9] R. V. Wagoner and C. M. Will, *Astrophys. J* **210**, 764 (1976), and **215**, 984 (1977).

[10] L. Blanchet and T. Damour, *Ann. Inst. Henri Poincaré* **50**, 377 (1989).

[11] T. Damour and B. R. Iyer, *Ann. Inst. Henri Poincaré* **54**, 115 (1991).

[12] L. Kidder, *Phys. Rev. D*, to be submitted.

[13] K. Danzmann, A. Rüdiger, R. Schilling, W. Winkler, J. Hough, G. P. Newton, D. Robertson, N. A. Robertson, H. Ward, P. Bender, J. Faller, D. Hils, R. Stebbins, C. D. Edwards, W. Folkner, M. Vincent, A. Bernard, B. Bertotti, A. Brillet, C. N. Man, M. Cruise, P. Gray, M. Sandford, R. W. P. Drever, V. Kose, M. Kühne, B. F. Schutz, R. Weiss, and H. Welling, "LISA: Proposal

for a Laser-Interferometer Gravitational Wave Detector in Space," unpublished proposal submitted to the European Space Agency in May 1993; available as document MPQ 177 from the Max-Planck-Institut für Quantenoptik, 8046 Garching bei München, Germany.

[14] K. S. Thorne, in *300 Years of Gravitation*, eds. S. W. Hawking and W. Israel (Cambridge University Press, Cambridge, 1987), p. 330.

[15] P. C. Peters and J. Mathews, *Phys. Rev.* **131**, 435 (1963).

[16] G. B. Cook, S. L. Shapiro, and S. A. Teukolsky, *Astrophys. J.*, in press.

[17] B. M. Barker and R. F. O'Connell, *Gen. Rel. Gravit.* **11**, 149 (1979).

[18] K. S. Thorne, and J. B. Hartle, *Phys. Rev. D* **31**, 1815 (1985).

[19] C. W. Misner, K. S. Thorne, and J. A. Wheeler, 1973, *Gravitation* (Freeman, San Francisco).

[20] L. Bildsten and C. Cutler, *Astrophys. J.* **400**, 175 (1992).

[21] D. Kennefick, D. Laurence, and K. S. Thorne (unpublished).

[22] B. F. Schutz, *Nature* **323**, 310 (1986); B. F. Schutz, Class. Quantum Gravity **6**, 1761 (1989).

[23] Y. Gursel and M. Tinto, *Phys. Rev. D* **40**, 3884 (1990); P. Jaranowski and A. Krolak (unpublished).

[24] H. D. Wahlquist, *Gen. Rel. Gravit.* **19**, 1101 (1987).

[25] A. Krolak, J. A. Lobo, and B. J. Meers, *Phys. Rev. D* **43**, 2470 (1991).

Addendum to Chapter 4

7 ANALYTIC EXPRESSIONS FOR THE INFLUENCE OF SPIN-SPIN COUPLING ON BINARIES WITH $M_1 \simeq M_2$ AND $S_1 \simeq S_2$

7.1 The opening angle of $\hat{\mathbf{L}}$

(This addendum was written by me after the body of the chapter was published.) As we mentioned in Sec. 4.1, the case of a binary with equal masses is an important one, corresponding to $1.4M_\odot, 1.4M_\odot$ NS/NS binaries. We present here a better, than the one used in the main body of the paper, approximation to the equations describing the evolution of the precession of such a binary with almost equal spins. (If one of the spins is much smaller than the other, then the equations for simple precession, as given in Sec. 4.2, describe quite accurately the precession of the orbital plane.)

The assumption of precisely equal masses ($M_1 = M_2$) and spins ($|\mathbf{S_1}| = |\mathbf{S_2}| = S$) makes it possible to solve Eqs. (4.15), (4.16) analytically even if we keep the next higher order terms representing the spin-spin interaction. Then the cosines of the angles between the two spins, $\mathbf{S_1}, \mathbf{S_2}$ and the total angular momentum $\mathbf{J}$ (which, as we have shown is almost constant in direction) evolve as follows:

$$\frac{d}{dt}(\hat{\mathbf{J}}\cdot\hat{\mathbf{S}}_1) = \frac{3S}{2r^3}\left[2-\frac{(\mathbf{S}_2\cdot\mathbf{J})}{L^2}+\mathcal{O}\left(\frac{S^2}{L^2}\right)\right]\hat{\mathbf{J}}\cdot(\hat{\mathbf{S}}_1\times\hat{\mathbf{S}}_2)\,, \tag{4.100}$$

$$\frac{d}{dt}(\hat{\mathbf{J}}\cdot\hat{\mathbf{S}}_2) = -\frac{3S}{2r^3}\left[2-\frac{(\mathbf{S}_1\cdot\mathbf{J})}{L^2}+\mathcal{O}\left(\frac{S^2}{L^2}\right)\right]\hat{\mathbf{J}}\cdot(\hat{\mathbf{S}}_1\times\hat{\mathbf{S}}_2)\,, \tag{4.101}$$

$$\frac{d}{dt}(\hat{\mathbf{S}}_1\cdot\hat{\mathbf{S}}_2) = \frac{3J}{2r^3}\left[\frac{(\mathbf{S}_1\cdot\mathbf{J}-\mathbf{S}_2\cdot\mathbf{J})}{L^2}+\mathcal{O}\left(\frac{S^2}{L^2}\right)\right]\hat{\mathbf{J}}\cdot(\hat{\mathbf{S}}_1\times\hat{\mathbf{S}}_2)\,. \tag{4.102}$$

If we had taken into account the motion of $\hat{\mathbf{J}}$ as described by Eqs. (4.14), (4.15), (4.16), it would have contributed to the $\mathcal{O}(S^2/L^2)$ terms. Therefore the assumption of fixed $\hat{\mathbf{J}}$ is completely justified in our analysis.

Equations (4.101), (4.102), (4.102), have been derived from Eqs. (4.15), (4.16) by using the approximation $\mathbf{L} \simeq \mathbf{J} \times (1 + \mathcal{O}(S/L))$ and then rearranging in terms of successive orders of S^k/L^k. (When $M_1 \simeq M_2$ then $S << L$ throughout the

inspiral; when $M_1 >> M_2$ this need not be so.) By introducing the notation

$$\chi \equiv \hat{\mathbf{S}}_1 \cdot \hat{\mathbf{S}}_2 \,, \quad \xi \equiv \hat{\mathbf{J}} \cdot \frac{\hat{\mathbf{S}}_1 - \hat{\mathbf{S}}_2}{2} \,, \quad \eta \equiv \hat{\mathbf{J}} \cdot \frac{\hat{\mathbf{S}}_1 + \hat{\mathbf{S}}_2}{2} \,, \tag{4.103}$$

Eqs. (4.102) transform to

$$\frac{d\eta}{dt} = \frac{3S}{2r^3}\left[\mathcal{O}\left(\frac{S}{L}\right)\right] w(\eta,\xi,\chi) \,, \tag{4.104}$$

$$\frac{d\xi}{dt} = \frac{3S}{2r^3}\left[2 + \mathcal{O}\left(\frac{S}{L}\right)\right] w(\eta,\xi,\chi) \,, \tag{4.105}$$

$$\frac{d\chi}{dt} = \frac{3S}{2r^3}\left[2\xi + \mathcal{O}\left(\frac{S}{L}\right)\right] w(\eta,\xi,\chi) \,, \tag{4.106}$$

with

$$w(\eta,\xi,\chi) = \sqrt{1 - \chi^2 - 2(\eta^2+\xi^2) + 2\chi(\eta^2 - \xi^2)} \,. \tag{4.107}$$

By ignoring all the $\mathcal{O}(S/L)$ terms, Eqs. (4.104), (4.105), (4.107) simplify to one single differential equation for one of the η, ξ, χ functions while the other two can be expressed as functions of the first one:

$$\eta \simeq \eta(0) = \text{const} \,, \tag{4.108}$$

$$\chi \simeq \chi(0) + \frac{1}{2}(\xi^2 - \xi^2(0)) \,, \tag{4.109}$$

$$\frac{d\xi}{dt} \simeq \frac{3S}{r^3}\sqrt{A + B\xi^2 + \Gamma\xi^4} \,, \tag{4.110}$$

with

$$\begin{aligned} A &\equiv [1 - \eta^2(0)]^2 - [\eta^2(0) - \chi(0) + \xi^2(0)/2]^2 \,, \\ B &\equiv -2 - 3\chi(0) + \eta^2(0) + 3\xi^2(0)/2 \,, \\ \Gamma &\equiv -5/4 \,, \end{aligned} \tag{4.111}$$

where '(0)' means the initial value. Eq. (4.110) can be solved by means of Jacobian Elliptic Integrals [1] leading to

$$\xi = \frac{1}{c_3}\mathrm{sd}\left(c_1 \int \frac{3S}{r^3} dt + c_0 \,\middle|\, c_2\right) \tag{4.112}$$

where

$$\begin{aligned} c_0 &\equiv \mathrm{sd}^{-1}(c_3\,\xi(0)|c_2) \,, & c_1 &\equiv (B^2 - 4A\Gamma)^{1/4} \,, \\ c_2 &\equiv (B + c_1^2)/(2c_1^2) \,, & c_3 &\equiv c_1/\sqrt{|A|} \,, \end{aligned} \tag{4.113}$$

and

$$\int \frac{3S}{r^3}\,dt = \frac{15a}{64}\,Q^2\left[\left(\frac{10\text{Hz}}{f(0)}\right)^{2/3} - \left(\frac{10\text{Hz}}{f}\right)^{2/3}\right], \tag{4.114}$$

where

$$Q = \frac{18.607}{(M/M_\odot)^{1/3}}\,. \tag{4.115}$$

Here a is the spin parameter for the two stars ($S_i = aM_i^2$).

Having analytic expressions for all the angles between the spins and total angular momentum, we can compute the opening angle λ_L of the orbital angular momentum; i.e. the angle between $\hat{\mathbf{L}}$ and $\hat{\mathbf{J}}$ (recall that $\hat{\mathbf{J}}$ is fixed to the level of accuracy used, i.e., $\hat{\mathbf{J}}$ plays the role of the $\hat{\mathbf{J}}_0$ that we used in Sec. 4.2 when analyzing simple precession):

$$\lambda_L = \sin^{-1}\left(\frac{\sqrt{(\mathbf{S}_1+\mathbf{S}_2)^2 - (\mathbf{S}_1\cdot\hat{\mathbf{J}} + \mathbf{S}_2\cdot\hat{\mathbf{J}})^2}}{L}\right) = \sin^{-1}\left(\frac{S}{L}\sqrt{\Delta+\xi^2}\right)\,, \tag{4.116}$$

where

$$\Delta = 2 + 2\chi(0) - 4\eta^2(0) - \xi^2(0)\,. \tag{4.117}$$

In Fig. 4.24 we have plotted the analytic expression (4.116) using the solution (4.112) derived above, versus frequency, for a typical case. (The initial frequency we used is $f(0) = 10$ Hz since this is approximately the frequency of the waves when they enter the detectors' window-band). To show how good our approximate analytic solution is, we have plotted on top of it the corresponding numerical solution of the exact differential equations (4.14), (4.15), (4.16) (dashed line). In the range of frequencies where the detectors are most sensitive (10–200 Hz), the approximate analytic solution is an excellent approximation to the true numerical one. If we had dropped the spin-spin terms from the beginning, we would have missed the ξ^2 term in Eq. (4.116) and hence the "wiggling" shape of Fig. 4.24. This "wiggling" is due to the opening and closing of the spin-spin angle.

As we said earlier Fig. 4.24 corresponds to some set of parameters $\chi(0)$, $\eta(0)$, $\xi(0)$. We have tried several cases with different initial spin and orbital angular momentum orientations, that produced either better or worse results. For the sake of completeness, in Fig. 4.25 we have plotted the corresponding analytic and numerical solutions for the worst case we have found.

7.2 The angular position of $\hat{\mathbf{L}}$

The analysis up to this point gives no information about the angular positions of $\hat{\mathbf{L}}$ and $\hat{\mathbf{S}}_1 + \hat{\mathbf{S}}_2$ in their precession around $\hat{\mathbf{J}}$. The angular velocity of precession

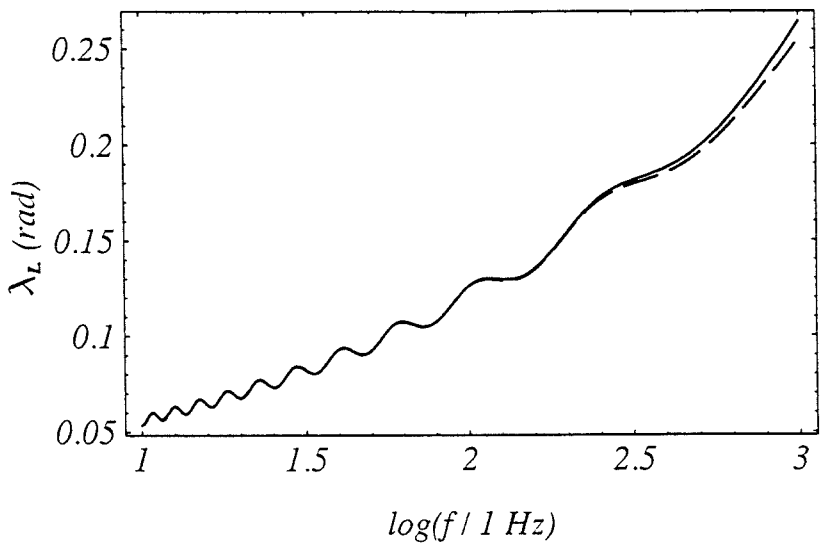

Figure 4.24: Evolution of the opening angle λ_L of $\hat{\mathbf{L}}$ for two $1.4M_\odot$ neutron stars with equal spin magnitudes $0.5M_i^2$ and initial orientations $\hat{\mathbf{S}}_1 = \hat{x}$, $\hat{\mathbf{S}}_2 = \hat{y}$, $\hat{\mathbf{J}} = \hat{z}$. The solid line represents the analytical solution given by Eq. (4.116) and the dashed one, the numerical solution. The approximation is almost perfect within the region $f \lesssim 300$ Hz where the sensitivity of detectors is high.

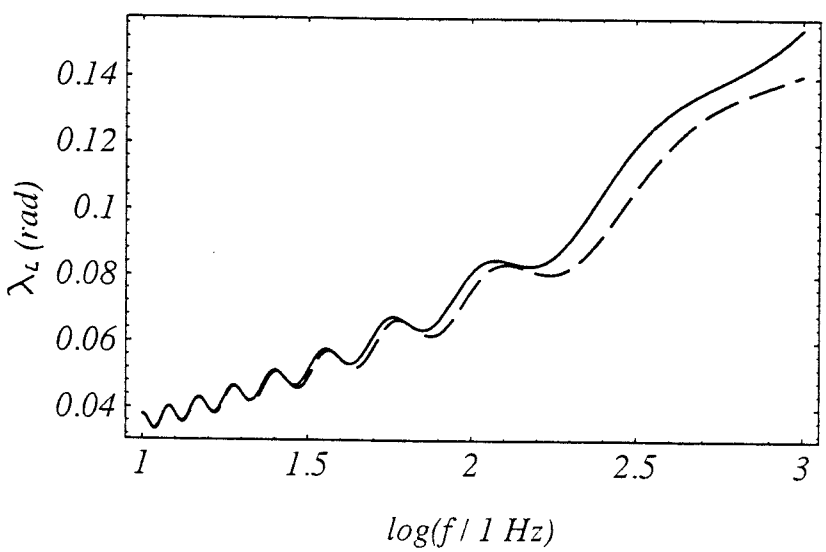

Figure 4.25: Same as Fig. 4.24 but with initial spin and total angular momentum orientations $\hat{\mathbf{S}}_1 = \hat{x}$, $\hat{\mathbf{S}}_2 = \hat{z}$, $\hat{\mathbf{J}} = \hat{z}$.

can be derived from Eqs. (4.14), (4.15), (4.16). Writing these equations in a more suitable form, we get

$$\frac{d\hat{\mathbf{L}}}{dt} = -\frac{1}{L}\frac{d}{dt}(\mathbf{S}_1 + \mathbf{S}_2) = \frac{1}{2r^3}\left[7\,\mathbf{J} - 3\,\mathbf{\Sigma}\right] \times \hat{\mathbf{L}}\,, \tag{4.118}$$

where

$$\mathbf{\Sigma} = \frac{\mathbf{S}_1(\mathbf{S}_2 \cdot \mathbf{L}) + \mathbf{S}_2(\mathbf{S}_1 \cdot \mathbf{L})}{L^2}\,. \tag{4.119}$$

This says that $\hat{\mathbf{L}}$ precesses with instantaneous angular velocity

$$\mathbf{\Omega}_{\mathrm{p}} = \frac{1}{2r^3}\left[7\,\mathbf{J} - 3\,\mathbf{\Sigma}\right]. \tag{4.120}$$

In section 4 in the analysis of *simple precession*, the $\mathbf{\Sigma}$ term was ignored, but now we have to keep it. Although it is of order (S^2/L^2), its effects on the precession angle will be of the same order as these produced by the (S/L) term in

$$\mathbf{J} = \hat{\mathbf{J}}\,L\left(1 + 2\eta(0)\frac{S}{L} + \mathcal{O}(\frac{S^2}{L^2})\right). \tag{4.121}$$

More specifically, $\mathbf{\Sigma}$ expressed in terms of three non-coplanar vectors relevant to the problem

$$\mathbf{\Sigma} = c_J\hat{\mathbf{J}} + c_L\hat{\mathbf{L}} + c_\perp\hat{\mathbf{J}} \times \hat{\mathbf{L}} \tag{4.122}$$

contributes to the revolution of $\hat{\mathbf{L}}$ around $\hat{\mathbf{J}}$ only through c_J ($c_\perp$ produces the change of the opening angle λ_L we found in the previous section, and c_L produces no precession at all). With some effort, from Eqs. (4.108), (4.109), (4.112), (4.119) we find that

$$c_J = S\left[\eta(0)\,\frac{\Delta + 5\xi^2}{\Delta + \xi^2} + \mathcal{O}\left(\frac{S}{L}\right)\right]. \tag{4.123}$$

Therefore Ω_p is given by

$$\Omega_p = \frac{L}{2r^3} \times \left[7 + \eta(0)\frac{11\Delta - \xi^2}{\Delta + \xi^2}\left(\frac{S}{L}\right) + \mathcal{O}\left(\frac{S^2}{L^2}\right)\right], \tag{4.124}$$

and the angular position of $\hat{\mathbf{L}}$, by the time integral of Ω_p

$$\begin{aligned}\alpha \;=\; & \alpha(0) + \frac{35}{192}\,Q^3\left(\left(\frac{10\mathrm{Hz}}{f(0)}\right) - \left(\frac{10\mathrm{Hz}}{f}\right)\right) \\ & + \frac{5a}{128}\,Q^2\,\eta(0)\,W\left(\left(\frac{10\mathrm{Hz}}{f(0)}\right)^{2/3} - \left(\frac{10\mathrm{Hz}}{f}\right)^{2/3}\right) + \mathcal{O}\left(\frac{S^2}{L^2}\right),\end{aligned} \tag{4.125}$$

where W represents the average value of $(11\Delta - \xi^2)/(\Delta + \xi^2)$. This quantity is frequency dependent but has an oscillatory behavior which we choose to approximate by its average value:

$$W = -1 + \frac{12\Delta}{\xi_{max}^2} \ln\left(\frac{\Delta + \xi_{max}^2}{\Delta}\right) , \tag{4.126}$$

where ξ_{max}^2 can be derived by solving

$$A + B\xi_{max}^2 + \Gamma\xi_{max}^4 = 0 \tag{4.127}$$

[cf. Eq. (4.110)]. In Fig. 4.26a we have plotted the analytic expression for α given by Eq. (4.125), along with the corresponding numerical solution of Eqs. (4.14), (4.15), (4.16) for the same typical case as in Fig. 4.24. The approximation is so good that it looks like a single curve! In Fig. 4.26b we show the difference between the numerical and analytical solutions. Other cases, with different set of parameters used, have produced equivalently perfect results.

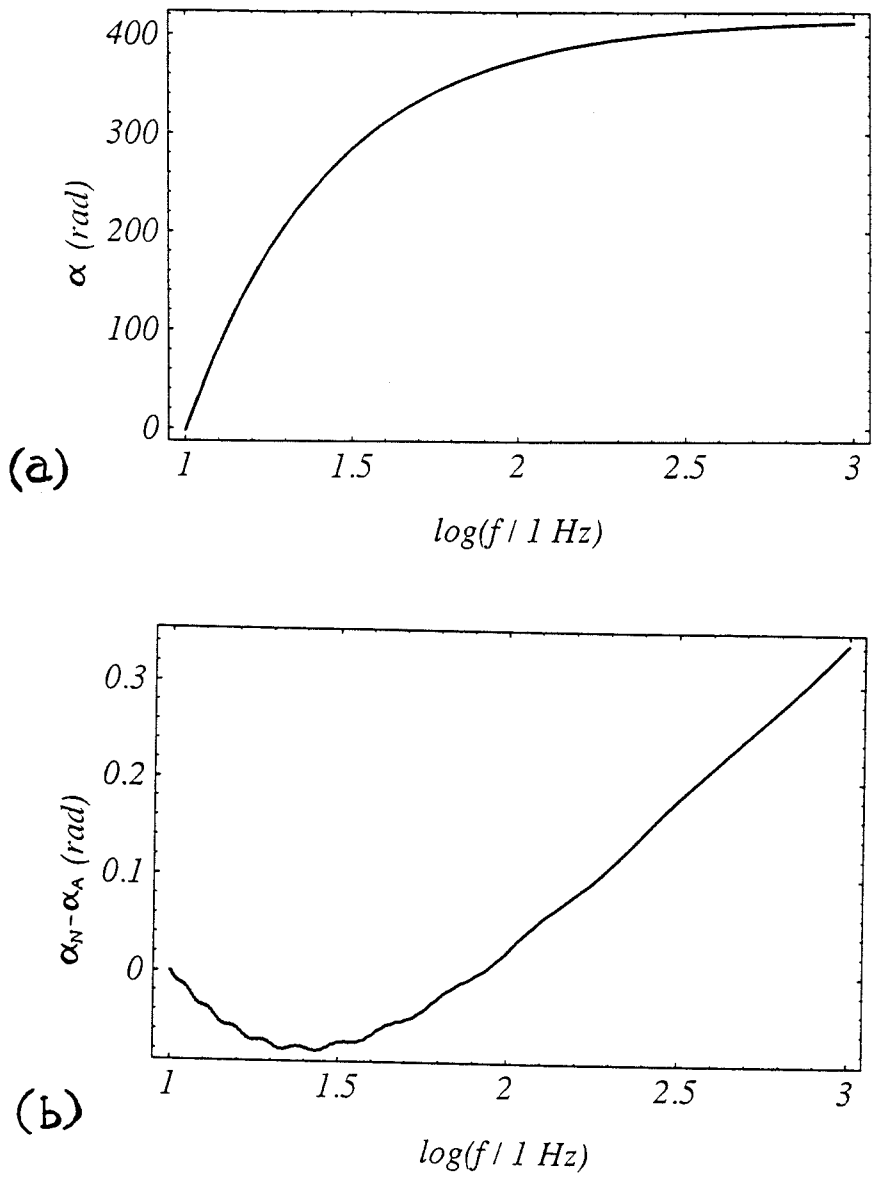

Figure 4.26: (a) Evolution of the angular position α of $\hat{\mathbf{L}}$ for the same neutron stars and initial configuration as in Fig. 4.24. Again the solid line represents the analytical solution given by Eq. (4.125) and the dashed one, the numerical solution. The difference is so tiny that the two lines are hardly distinguishable. (b) The difference of the numerical and the analytical solutions has been plotted to give a feeling for how good the analytical approximation is.

Bibliography

[1] M. Abramowitz, and I. A. Stegun, *Handbook of Mathematical Functions* (Dover, New York, 1972).

Chapter 5

Search templates for gravitational waves from precessing, inspiraling binaries

(Submitted to Phys. Rev. D.)

Abstract

In searching for gravitational waves in the output of the ground-based high-frequency LIGO/VIRGO/GEO detectors, we need a family of "search templates" with which to cross-correlate the noisy detectors' output. This paper introduces a *fitting factor* FF, as a quantitative measure of how well the best template in a family "fits" a hypothetical gravitational waveform, in the presence of a specific detector noise spectrum. More precisely, FF is the reduction in signal-to-noise ratio caused by using the chosen family of templates instead of a template that perfectly matches the hypothetical waveform. It is shown that an $FF < 0.9$ corresponds to a 27% reduction in the event rate of the relevant signals; therefore a family of templates that leads to FF's below 0.9 should be considered inadequate.

The FF is used as a tool to explore the adequateness of several families as search templates for gravitational waves from compact inspiraling binaries. The binaries are taken to move in circular orbits, and the "advanced LIGO noise spectrum" is assumed for the detectors. Although the true waveforms depend on a large number of parameters, we first study the acceptability of the simplest 3-parameter template family, the so called "Newtonian family." This family consists of waveforms predicted by the Newtonian quadrupole formalism. From previous studies by Finn, Królak, Kokotas, Schäfer, Dhurandar, and Balasubramanian, we infer that post-Newtonian effects in the true waveforms of binaries with vanishing spins cause the Newtonian family to have an unacceptable low FF (~ 0.6 to 0.8). We then focus attention on the influence of waveform modulations due to nonzero spins; and we isolate the modulation effects from other post-Newtonian effects by pretending that the true signals are pure Newtonian with modulation. Binaries with many different geometrical and nongeometrical parameters are explored, and intuition is developed into which of the binary's parameters most strongly influence the FF. It is shown that the Newtonian template family works quite well ($FF > 0.9$ for almost all the possible geometries) for the modulational effects of a Newtonian signal from two $1.4M_\odot$ neutron stars (NS) with one of them maximally spinning. By contrast, for a maximally spinning $10M_\odot$ black hole (BH) with a non-rotating $1.4M_\odot$ NS, the Newtonian template family produces $FF < 0.9$ for more than half of all the binaries' orientations, if the spin and orbital angular momenta are misaligned by 30°, and $FF < 0.8$ for almost all the possible orientations, if the misalignment angle exceeds 60°.

We introduce a new four-parameter template family, which has the form of the non-modulated post^1-Newtonian signal from a zero-spin-binary. Although, there

is a substantial improvement of the FF's for a spin-modulated Newtonian signal, the FF's for nonmodulated post$^{1.5}$-Newtonian waveforms are still very poor ($\sim 0.5 - 0.8$). Therefore we propose another four-parameter template family that has the same form as a nonmodulated post$^{1.5}$-Newtonian signal with all the spin related parameters stripped off. This template family works quite well, even for signals with both the modulated and the nonmodulated post$^{1.5}$-Newtonian effects combined. For the NS/NS binary with one NS maximally spinning, this family produces $FF > 0.9$ for almost all the possible geometries; but for the BH/NS binary with the BH maximally spinning and the spin and orbit significantly misaligned, it produces $FF > 0.9$ only for some small, but not negligible, fraction of all the possible geometries (e.g., for 20% of all the possible binary orientations with a 60° misalignment angle). This suggests that, in a few years, when waveforms have been computed up to post^3-Newtonian order, a good template family will be the 4-parameter post^3-Newtonian waveforms for zero-spin binaries, augmented by some appropriate modulations to deal with misaligned black-hole, neutron-star systems.

Finally, we extend our investigations to the space-based low-frequency LISA detector. Due to the similarity in shape of the ground- and space-based detectors' noise spectra, the FF values for the relevant signals and template families are more or less the same as for the low-frequency detectors.

1 INTRODUCTION

The facilities to house the ground-based LIGO/VIRGO laser-interferometer gravitational-wave detectors are already under construction or in the final stage of their design [1], and the GEO600 project for an intermediate scale interferometer has good prospects for approval. At about the turn of the century LIGO/VIRGO/GEO will probably be ready to start searching for gravitational waves coming from the most promising sources: neutron star/neutron star (NS/NS), or neutron star/black hole (NS/BH), or black hole/black hole (BH/BH) binaries.

The detectability of these binaries depends on the family of "search templates" that will be used as matched filters to extract a possible signal buried in the detectors' noise. (For the method of "matched filters" see Ref. [2]). More specifically, the output data stream of each detector will be cross-correlated with each template $T_{\lambda_1,\lambda_2,...}$ of the chosen family, weighted by the inverse of the detector's noise spectrum. If for some combination of the templates' parameters $\lambda_1, \lambda_2, \ldots$ the cross-correlation output is above some threshold level, then a signal will have been detected with great confidence. Therefore, we should make sure that some member of the family of templates used for detection matches very well each of the hypothetical incoming waveforms.

The true general relativistic signals from inspiraling binaries (including post-Newtonian and spin-induced effects) depend on a very large set of parameters (the masses of the two stars, the eccentricity of their orbit, their spin, the relative geometry of their orbit and the detector's location and orientation, and the time and phase of the waves at coalescence). This large set of parameters leads to a huge variety of chirp-like waveform shapes and a corresponding requirement for a huge number of templates in the search family. On the other hand, for two reasons the number of templates should not be allowed to grow too large: (i) The task of computing the cross-correlations can become excessive [2] and (ii) the probability of a false detection can become excessive. Rough estimates [2, 3] suggest that $\sim 10^5 - 10^6$ discrete template shapes might be needed and would be acceptable.

Throughout our analysis and discussion, we assume that the binaries are orbiting around each other in circular orbits when their waves enter the frequency band of the LIGO/VIRGO/GEO detectors. This is justified since long-lived binaries have sufficient time to circularize by radiation reaction, before they reach the LIGO/VIRGO/GEO frequency bands [4] (by contrast with the type of binaries formed by capture events in dense galactic nuclei which might be appropriate

sources for the low-frequency space-based LISA detector [5]).

The most obvious, and perhaps adequate way, to construct a suitable template family is to use approximate waveforms that depend on a small set of parameters related to some special characteristics of the binaries. The simplest such family is the Newtonian family, i.e., the family of waveforms predicted by Newtonian gravity and the quadrupole-moment formalism. These templates (assuming circular orbits) consist of three parameters altogether: the coalescence time t_C, the phase of the waves at coalescence ϕ_C and a certain combination of the masses, called the *chirp mass*: $\mathcal{M} \equiv (M_1 M_2)^{3/5}/(M_1 + M_2)^{1/5}$. The final coalescence time t_C is a special parameter that can be handled directly as an additive phase factor when computing the cross-correlation in the frequency domain [2]. Fortunately only two values of ϕ_C need to be considered, since ϕ_C shows up only as a constant phase in the signal: for convenience $\phi_C = 0$ and $\phi_C = \pi/2$ (see [2]).

As a result, the Newtonian family has only one nontrivial shape parameter: the chirp mass $\mathcal{M}$. The Newtonian family can be handled easily, even with present-day workstations, by spanning the whole range of $\mathcal{M}$'s under consideration with a density $\Delta\mathcal{M}/\mathcal{M}$ of 0.1% [6]. The question that arises is how adequate are the Newtonian templates for identifying realistic waveforms in the noisy detector output? As a tool for answering this question, we introduce the *fitting factor* FF which is a measure of how well any chosen family of templates fits some chosen hypothetical gravitational-wave signal. Several people have used a similar or even the same quantity for the same purpose [7, 8]; but they have given it other names and have discussed it from other viewpoints.

The noise spectrum of the detector plays a significant role in the FF, since a good resemblance between the template and the incoming waveform is needed only at frequencies where the noise is low. In this paper the "advanced-LIGO-detector" noise spectrum will be used. This spectrum has been introduced by the LIGO team [1] as a guess of what the noise might look like some years after LIGO goes into operation.

As we will show later, the FF is the reduction in signal-to-noise ratio that comes from using some chosen inaccurate family of templates instead of a larger family that includes the true signal. Since the event rate for the true signal scales like the cube of the signal-to-noise ratio, the fractional reduction in event rate due to using the chosen template family is $1 - FF^3$. A value of 0.9 for a family's FF thus means a 27% loss in the event rate. This loss could be recovered by increasing the interferometers' arm length by 10%, but the cost would be roughly 6 million

dollars! It should be clear from the numbers that FF values below ~ 0.9 mean that the chosen template family is **inadequate**; and one might want to insist on $FF \gtrsim 0.95$ or even 0.98 when designing a template family.

Several people [7, 8] have recently investigated the effectiveness of the Newtonian template family in searches for the nonmodulated waveforms produced by inspiraling binaries with vanishing spins and circular orbits. The numbers obtained in these studies correspond FF well below 0.9. I have confirmed these numbers, and I present them together with the results of some additional computations (discussed later in this paper) in Table 1. The signals discussed in this table are Newtonian, post^1-Newtonian, or post$^{1.5}$-Newtonian approximations to the exact, general relativistic waveforms. (The waveforms have not yet been computed to higher than post$^{1.5}$-Newtonian order, though an ongoing effort [9] should ultimately bring them up to and including post^3-Newtonian order — which is about the accuracy required for LIGO/VIRGO/GEO [Ref. [10]].)

The main conclusion of Table 1 is that for the post$^{1.5}$-Newtonian signal, with vanishing modulation (because the spin and orbital angular momenta are aligned), the Newtonian template family is completely inadequate. To achieve an acceptable $FF \gtrsim 0.9$ requires the post$^{1.5}$-Newtonian family of templates (templates described by the post$^{1.5}$-Newtonian waveforms with zero spins).

In all previous template investigations, and in all entries in Table 1, the binary's spin and orbital angular momenta are assumed aligned, or the spins are assumed to vanish, so the binary does not precess and the waveforms are not modulated. The principal objective of this paper is to study the effects of spin-induced precession and modulation on the acceptability of unmodulated template families. In these modulational studies, as in most previous studies [7, 8] (but not all [6]), the discreteness of the template families is ignored; i.e., the chirp mass $\mathcal{M}$ and other parameters that determine the template waveforms are allowed to vary continuously rather than taking on a discrete set of values.

In this continuum approximation, we begin by investigating the detectability of a modulated waveform with the (unmodulated) Newtonian template family. The resulting FF values are unacceptable low, not just because of post-Newtonian effects, but also because of the modulational effects. To rectify this, we introduce the spin-free, unmodulated post$^{1.5}$-Newtonian family described in the previous paragraph, which has 4 parameters by contrast with 3 for the Newtonian family. The extra parameter is related to the binary's reduced mass. The new template family fits better the modulated waveforms than the Newtonian one. From the

Table 1: We present here the FF values for a Newtonian, a post^1-Newtonian, and a post$^{1.5}$-Newtonian signal with maximal spin (maximal β; where β is given in Eq. (5.46)) but no precession, being searched for by 3 families of templates: the Newtonian family [Eq. (5.10)], the post^1-Newtonian family [Eq. (5.41)], and the post$^{1.5}$-Newtonian family [Eq. (5.47)]. Note that the post$^{1.5}$-Newtonian templates are assumed to have $\beta = 0$ in order to keep the number of parameters low. The post$^{1.5}$-Newtonian signals though are chosen to have the maximum possible β parameter by aligning the big object's maximal spin with the angular momentum of the binary (the small object is assumed to have no spin). For every case, two FF values are given, corresponding to a $10M_\odot - 1.4M_\odot$ BH/NS binary and a $1.4M_\odot - 1.4M_\odot$ NS/NS binary. Since modulational effects are absent (the spin and angular momenta are aligned), the binary's orientation does not affect the FF values. The numbers quoted in this Table are discussed more extensively in Sec. 7.

	N signal	**P^1-N signal**	**P$^{1.5}$-N signal** (β maximal)
N template:	1.000 (BH/NS) 1.000 (NS/NS)	0.559 (BH/NS) 0.465 (NS/NS)	0.692 (BH/NS) 0.594 (NS/NS)
P^1-N template:		1.000 (BH/NS) 1.000 (NS/NS)	0.699 (BH/NS) 0.546 (NS/NS)
P$^{1.5}$-N template: ($\beta = 0$)			0.987 (BH/NS) 0.985 (NS/NS)

sets of FF values that we compute, we suspect that an adequate template family, for *almost*, but not quite all binary signals (modulated and unmodulated) that LIGO/VIRGO/GEO seek, will be the 4-parameter post^3-Newtonian waveforms of spin-free binaries – waveforms that will likely have been computed within the next $\sim$ 3 years [9].

The rest of this paper is organized as follows. In Sec. 2 we briefly review the equations for the spin-induced simple precession and its modulation of the relevant waveforms, based on the stationary phase method, from the work of Apostolatos, Cutler, Sussman, and Thorne [11]. More specifically, we express the waveforms as Newtonian signals with amplitude and phase modulation. We assume for simplicity that the precessing binaries consist of one spinning object and one nonspinning object; this permits us to use the analytic forms derived in Ref. [11] for the simple precession. This is not a very restrictive assumption since the general case with two spins leads to similar precession trails for the orbital plane. We assume that the spinning object is the more massive one; this maximizes the strength of the precession.

In Sec. 3.1 we define the fitting factor (FF) and show its physical significance as a measure of the reduction of the signal-to-noise ratio due to the use of an inaccurate family of templates that cannot perfectly match the signal. In Sec. 3.2 we derive a simple formula for the FF when the template family is Newtonian and the signal is Newtonian with precession. In Sec. 3.3 we discuss separately the effects of amplitude modulation (AM) and phase modulation (PM) on the Fitting Factor and show some analytic and numerical examples.

In Sec. 4.1 we briefly discuss the code we have used to compute the FF, and its numerical errors, as well as the difficulties underlying our search for the FF's maximum value over our template family. In Sec. 4.2 we begin our study of the FF for the Newtonian template family and precessing Newtonian signal by exploring the dependence of FF on the binary's location on the sky and the orientation of the detector arms. We show that a knowledge of the FF for a binary directly overhead (or underfoot) is adequate to determine the complete distribution of the FF for all other directions to the source. In Sec. 4.3 we discuss the effect on the FF of the direction of the binary's total angular momentum $\mathbf{J}$, around which the orbital plane precesses. In Sec. 4.4 we show how the non-randomly distributed parameters – the binary's masses M_1, M_2 and the opening angle $\widehat{\mathbf{LS}}$ between its orbital and spin angular momenta – affect the FF .

In Sec. 5, for a few representative values of these non-randomly distributed pa-

rameters, we compute the probability, over all the random parameters of Secs. 4.2, 4.3, 4.4, to achieve FF values above some critical level. We find that, for a $1.4M_\odot, 1.4M_\odot$ NS/NS binary, with one of the NS's spinning near breakup, the FF is pleasingly large (> 0.9) for most ($\gtrsim 90\%$) of the geometries. But for a $10M_\odot, 1.4M_\odot$ BH/NS binary with the BH spinning at its maximal rate, the FF can be unpleasantly low and is very sensitive to the opening angle $\hat{\mathbf{L}}\mathbf{S}$. For example, for moderate and high values of $\hat{\mathbf{L}}\mathbf{S}$ (above 30°) the FF's are well below 0.9 in more than half of the random geometries.

In Sec. 6 we suggest the addition of one more parameter to the Newtonian template family, to improve its ability to detect precessing waveforms. This extra term has the same form as arises from the non-precessional post^1-Newtonian correction to the waveform's phase, and it turns out to improve substantially the FF values for precessionally modulated Newtonian signals. For the $1.4M_\odot$, $1.4M_\odot$ NS/NS binary, the FF values remain above 0.9 for at least 90% of all the geometries. By contrast, for the BH/NS binary, the FF values still depend strongly on the misalignment angle $\hat{\mathbf{L}}\mathbf{S}$, but now for a 30° angle, there is $\sim 75\%$ probability to get an FF value above 0.9 (an improvement from $< 50\%$).

In Sec. 7 we review, in the language of our FF, what other people have already published for the detectability of post-Newtonian nonmodulated signals by various template families. The Newtonian template family is completely inadequate (FF generally well below 0.9). Far better FF's are achieved by a template family based on the waveforms for non-spinning post$^{1.5}$-Newtonian-order binaries.

In Sec. 8 we explore the fitting ability of these post$^{1.5}$-Newtonian templates for post$^{1.5}$-Newtonian signals to which spin-induced modulation has been added. The results were improved at least as much as in section 6, where spin-modulated Newtonian signals and unmodulated post^1-Newtonian templates were considered (i.e., for the NS/NS binary FF is above 0.9 for at least 90% of all the geometries, and for the BH/NS binary there is a $\sim 75\%$ probability to get an FF value above 0.9 if the misalignment angle is 30°).

Finally, in Sec. 9 we summarize our results and suggest future research directions on the issue of search templates for detecting inspiraling binaries.

All of this analysis assumes the noise spectrum of "advanced" high-frequency ground-based LIGO detectors. In an Appendix, we extend the analysis to various kinds of signals and templates in the context of the low-frequency, space-based LISA gravitational-wave detector. The extrapolation to this type of detector and its relevant binary sources (supermassive black holes with smaller-mass black holes

or neutron stars) is straightforward, since the corresponding noise spectrum, has the same shape as the LIGO noise spectrum, but shifted to much lower frequencies (10^{-4} — 1 Hz compared with 10 — 1000 Hz for LIGO). This similarity suggests the use of the same kind of search templates for LISA as for the ground-based detectors, but with parameters corresponding to much more massive objects.

Throughout we use units where $G = c = 1$.

2 REVIEW OF FORMULAE FOR SIMPLE PRECESSION AND ITS WAVEFORM MODULATION

As was shown in the work of Apostolatos, Cutler, Sussman, and Thorne [11], a binary consisting of a spinning object with mass M_1 and spin $\mathbf{S}$, and a non-spinning object M_2 orbiting around each other with angular momentum $\mathbf{L}$ will conserve the angle $\widehat{\mathbf{LS}}$ between $\mathbf{L}$ and $\mathbf{S}$ through the whole inspiral phase. The binary's orbital plane will precess around the total angular momentum $\mathbf{J} = \mathbf{L} + \mathbf{S}$, which remains almost fixed in direction. By using the notation

$$\kappa \equiv \hat{\mathbf{L}} \cdot \hat{\mathbf{S}} \ , \quad \cos\lambda_L \equiv \hat{\mathbf{L}} \cdot \hat{\mathbf{J}} \ , \tag{5.1}$$

the opening angle for the precession of $\hat{\mathbf{L}}$ was shown to evolve due to radiation reaction and hence shrinkage of $\mathbf{L}$ according to

$$\cos\lambda_L(t) = \frac{\mu\sqrt{Mr(t)} + S_{\|}}{\left[(\mu\sqrt{Mr(t)} + S_{\|})^2 + {S_\perp}^2\right]^{1/2}} \ . \tag{5.2}$$

Here hats denote unit vectors (e.g., $\hat{\mathbf{L}} = \mathbf{L}/|\mathbf{L}|$), M, μ are the total and reduced masses respectively, $r(t)$ is the distance between the two stars, and $S_{\|} \equiv S\kappa$ and $S_\perp \equiv S\sqrt{1-\kappa^2}$ are the components of $\mathbf{S}$ parallel and perpendicular to the angular momentum $\mathbf{L}$ respectively. The evolution of the angular position α of $\hat{\mathbf{L}}$ (see Fig. 5.1) around the constant $\hat{\mathbf{J}}$ is given by

$$\alpha = \frac{-5(1+\frac{3M_2}{4M_1})}{96\mu^3 M^3} \quad \left[2Y^{3/2} - 3S_{\|}(\mu\sqrt{Mr} + S_{\|})\sqrt{Y} \right.$$
$$\left. -3S_{\|}{S_\perp}^2 \sinh^{-1}\left(\frac{\mu\sqrt{Mr} + S_{\|}}{S_\perp}\right)\right] + \text{const} \ , \tag{5.3}$$

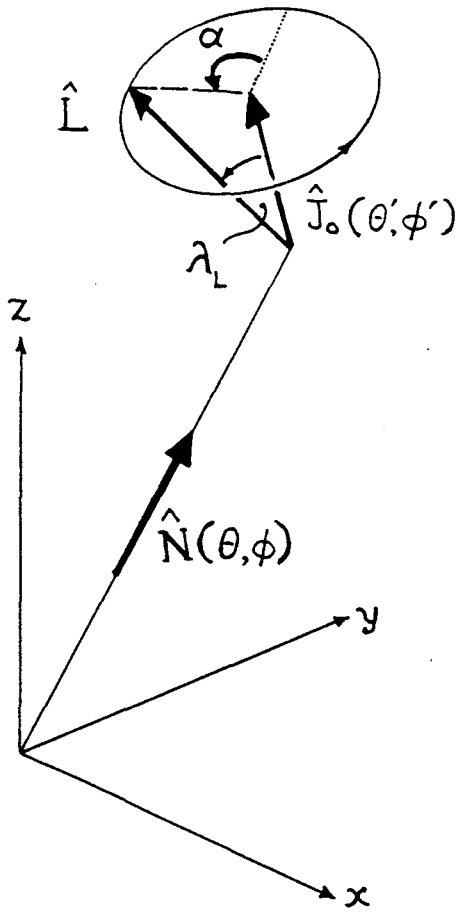

Figure 5.1: The geometry for a binary's simple precession relative to an Earth-based detector's Cartesian axes.

where

$$Y \equiv \mu^2 M r + 2S_{\|}\mu\sqrt{Mr} + S^2. \tag{5.4}$$

Because the computational search for the modulated signal will take place in the frequency domain, it will be useful to know the dependence of the binary's orbital diameter on the frequency f of the gravitational waves:

$$r = \left(\frac{M}{\pi^2 f^2}\right)^{1/3}. \tag{5.5}$$

This completes the formulae needed to describe the *simple precession* of the orbital plane of a binary when M_1, M_2, S, κ, and $\hat{\mathbf{J}}$ are given. It should be noted, however, that if the quantity

$$\epsilon = \frac{16}{5}\frac{(M/r)^{3/2}}{(1+\frac{3}{4}M_2/M_1)(1+2\kappa\gamma+\gamma^2)} \tag{5.6}$$

(where $\gamma = S/L$) is *not* $\ll 1$ then all the above expressions for the simple precession break down and instead the binary undergoes a different type of precession, called *transitional precession* [11]. Fortunately (for this paper), this happens only for a tiny, presumably rare range of parameters: $\hat{\mathbf{L}}\cdot\hat{\mathbf{S}} \lesssim -0.94$ ($\widehat{\mathbf{LS}} \gtrsim 160°$) and a rather restrictive combination of masses (see Fig. 10 of Ref. [11]). In the following examples we avoid any situation where transitional precession is involved, since no analytic expressions exist then.

We now move on to present the equations that describe the modulation of the waves due to simple precession. We write down directly the Fourier transform $\tilde{h}(f)$ of the modulated waveforms, since our calculations will be performed in the frequency domain. As shown in Eq. (38) of Ref. [11], by following the stationary phase method this $\tilde{h}(f)$ is given by

$$\tilde{h}(f) \approx \frac{1}{2}\Lambda(t)\tilde{h}_C(f) + \frac{1}{4\pi i}\frac{d\Lambda}{dt}\left[\frac{d\tilde{h}_C(f)}{df} - 2\pi i t\tilde{h}_C(f)\right] \tag{5.7}$$

for positive f, and the complex conjugate of this for negative f. Whenever we write t we simply mean $t(f)$, the time at which the carrier frequency is f, given by

$$t(f) = t_C - 5(8\pi f)^{-8/3}\mathcal{M}^{-5/3}. \tag{5.8}$$

In Eq. (5.7), $\tilde{h}_C(f)$ is the Fourier transform of the unmodulated "carrier" signal

$$h_C(t) \equiv \frac{2M_1M_2}{D\,r(t)}e^{-2i\Phi_C(t)}, \tag{5.9}$$

where $\Phi_C(t) = \int \Omega dt$ is the carrier phase and Ω is the orbital angular velocity, and D is the distance to the binary. This Fourier transform is

$$\tilde{h}_C(f) = \text{const} \times f^{-7/6} e^{i[2\pi f t_C - \phi_C + \frac{3}{4}(8\pi\mathcal{M}f)^{-5/3}]}, \tag{5.10}$$

where the 'const' represents everything that does not depend on frequency, such as the geometry, the masses etc.; ϕ_C, not to be confused with Φ_C, stands for the phase of the waveform at coalescence, t_C for the time of coalescence, and $\mathcal{M}$ for the *chirp mass*. $\Lambda(t)$ in Eq. (5.7) is the modulation factor defined as

$$\Lambda(t) \equiv \text{AM} \times \text{PM}\,, \tag{5.11}$$

where AM and PM are the following *amplitude modulation factor* and *phase modulation factor*

$$\text{AM} = \left(4[\hat{\mathbf{L}}\cdot\hat{\mathbf{N}}]^2 {F_\times}^2(\theta,\phi,\psi) + [1+(\hat{\mathbf{L}}\cdot\hat{\mathbf{N}})^2]^2 {F_+}^2(\theta,\phi,\psi)\right)^{1/2}, \tag{5.12}$$

$$\text{PM} = e^{-i[2\delta\Phi(t)+\varphi(t)]}\,. \tag{5.13}$$

Here, as before, $t = t(f)$, and

$$\varphi = \tan^{-1}\left(\frac{2\hat{\mathbf{L}}\cdot\hat{\mathbf{N}}\, F_\times(\theta,\phi,\psi)}{[1+(\hat{\mathbf{L}}\cdot\hat{\mathbf{N}})^2]F_+(\theta,\phi,\psi)}\right), \tag{5.14}$$

$$\delta\Phi(t) = -\int_{\hat{\mathbf{L}}}^{\hat{\mathbf{L}}_{final}} \left(\frac{\hat{\mathbf{L}}\cdot\hat{\mathbf{N}}}{1-(\hat{\mathbf{L}}\cdot\hat{\mathbf{N}})^2}\right)(\hat{\mathbf{L}}\times\hat{\mathbf{N}})\cdot d\hat{\mathbf{L}}\,. \tag{5.15}$$

The two phases in Eqs. (5.14), (5.15) represent phase modulations that have different physical origins: φ arises from changes in the polarization axes due to precession of the orbital plane, and $\delta\Phi$ is something similar to the Thomas precession of the electron's spin in a semiclassical model of the hydrogen atom. The rest of the parameters in Eqs. (5.12)—(5.15) are connected to the orientation of the detector and the direction to the binary. Thus $\hat{\mathbf{N}}$ is the unit vector pointing to the source and θ and ϕ are its spherical polar coordinates (see Fig. 5.1), F_+ and $F_\times$ are the detector's "beam-pattern" coefficients given by

$$F_+(\theta,\phi,\psi) = \frac{1}{2}(1+\cos^2\theta)\cos 2\phi\cos 2\psi - \cos\theta\sin 2\phi\sin 2\psi\,, \tag{5.16}$$

$$F_\times(\theta,\phi,\psi) = \frac{1}{2}(1+\cos^2\theta)\cos 2\phi\sin 2\psi + \cos\theta\sin 2\phi\cos 2\psi\,, \tag{5.17}$$

and ψ is the polarization angle given up to an arbitrary multiple of π by

$$\psi = \tan^{-1}\left(\frac{\hat{\mathbf{L}}\cdot\hat{\mathbf{p}} - (\hat{\mathbf{L}}\cdot\hat{\mathbf{N}})(\hat{\mathbf{p}}\cdot\hat{\mathbf{N}})}{\hat{\mathbf{N}}\cdot(\hat{\mathbf{L}}\times\hat{\mathbf{p}})}\right), \tag{5.18}$$

where $\hat{\mathbf{p}}$ is the normal to the detector plane.

By combining Eqs. (5.7), (5.10), (5.11), (5.13), $\tilde{h}(f)$ turns out to be

$$\tilde{h}(f) \approx \frac{1}{2}\tilde{h}_C(f) \times \mathrm{AM} \times \mathrm{PM} \times \left[1 + \frac{7}{12\pi f}(2\delta\dot{\Phi} + \dot{\varphi}) + \frac{7i}{12\pi f}\frac{\dot{\mathrm{AM}}}{\mathrm{AM}}\right], \tag{5.19}$$

where a ' ˙ ' represents 'd/dt'. Expressions for AM and PM can be read from Eqs. (5.12), (5.13). The quantity in the square bracket in Eq. (5.19) can be approximated by 1 since the remaining terms are corrections of order (orbital period)/(precession period) $\approx \Omega_p/\pi f$ (see Eq.(42) of Ref. [11]), which is a very small quantity except maybe at high frequencies near the final stages of inspiral, where the detectors are almost "deaf" due to large shot noise.

3 THE FITTING FACTOR (FF)

3.1 Definition and physical significance

Let us imagine a detector receiving a gravitational signal from a precessing binary with a waveform represented by $W(t)$. Then because of the detector's noise $n(t)$, the output $s(t)$ of the detector will be

$$s(t) = W(t) + n(t)\,. \tag{5.20}$$

If we had used the exact waveform $W(t)$ as our search template, then we would have achieved the highest possible signal to noise ratio, given by Eq. (2.5) of Ref. [12]:

$$\left(\frac{S}{N}\right)_{max} = (W \mid W)^{1/2}\,, \tag{5.21}$$

where the inner product of two waveforms $(h_1 \mid h_2)$ is defined by Eq. (2.3) of Ref. [12]

$$(h_1 \mid h_2) = 2\int_0^\infty \frac{\tilde{h}_1^*(f)\tilde{h}_2(f) + \tilde{h}_1(f)\tilde{h}_2^*(f)}{S_n(f)}\,df\,. \tag{5.22}$$

Here $S_n(f)$ is the spectral density of the detector's noise. Henceforth we will assume for $S_n(f)$ the following analytic fit to the "advanced" LIGO noise spectrum, which

has been published by the LIGO team as an estimate of what might be achieved some years after LIGO turns on: (see Refs. [1, 12])

$$S_n(f) = \begin{cases} \infty & \text{for } f < 10 \text{ Hz}, \\ S_0 \left[\left(\frac{f_0}{f}\right)^4 + 2 \left(1 + \left(\frac{f}{f_0}\right)^2\right) \right] & \text{for } f > 10 \text{ Hz} \end{cases} \tag{5.23}$$

where $S_0 = 0.6 \times 10^{-48} \text{Hz}^{-1}$ and $f_0 = 70\text{Hz}$.

The signal-to-noise ratio will be reduced below $(S/N)_{\max}$ whenever the template is not the exact waveform but some other approximate one. In this paper we are interested in searches performed with some family of templates $T_{\lambda_1,\lambda_2,\ldots}(t)$ that depend on a set of parameters $\lambda_1, \lambda_2, \ldots$ Then by definition the signal-to-noise achieved in the search will be

$$\left(\frac{S}{N}\right) = \max_{\lambda_1,\lambda_2,\ldots} \frac{(s \mid T_{\lambda_1,\lambda_2,\ldots})}{\text{rms}\,(n \mid T_{\lambda_1,\lambda_2,\ldots})} \,. \tag{5.24}$$

For an ensemble of realizations of the detector noise, the expectation values of $(n \mid T_{\lambda_1,\lambda_2,\ldots})$ and $(n \mid T_{\lambda_1,\lambda_2,\ldots})$ $(n \mid T_{\lambda_1,\lambda_2,\ldots})$ are 0 and $(T_{\lambda_1,\lambda_2,\ldots} \mid T_{\lambda_1,\lambda_2,\ldots})$ respectively. Thus the ensemble-averaged signal-to-noise ratio turns out to be

$$\begin{aligned} \left(\frac{S}{N}\right) &= \max_{\lambda_1,\lambda_2,\ldots} \frac{(W \mid T_{\lambda_1,\lambda_2,\ldots})}{\sqrt{(T_{\lambda_1,\lambda_2,\ldots} \mid T_{\lambda_1,\lambda_2,\ldots})}} \\ &= \left[\max_{\lambda_1,\lambda_2,\ldots} \frac{(W \mid T_{\lambda_1,\lambda_2,\ldots})}{\sqrt{(T_{\lambda_1,\lambda_2,\ldots} \mid T_{\lambda_1,\lambda_2,\ldots})(W \mid W)}} \right] \left(\frac{S}{N}\right)_{max} \,. \end{aligned} \tag{5.25}$$

We give the name *Fitting Factor* (FF) to the reduction in signal-to-noise that results from using the chosen template family, rather than the true signal W, in the search:

$$FF \equiv \max_{\lambda_1,\lambda_2,\ldots} \frac{(T_{\lambda_1,\lambda_2,\ldots} \mid W)}{\sqrt{(T_{\lambda_1,\lambda_2,\ldots} \mid T_{\lambda_1,\lambda_2,\ldots})(W \mid W)}} \,. \tag{5.26}$$

This FF or its square root is a quantity that has already been used by various authors (see [7, 8])as a measure of the adequateness of a template family; but previous discussions have not shown explicitly how this intuitively well formed function is connected with detectability. Previously this FF has sometimes been called the "correlation" – a name that is often used in so many different ways that we prefer to avoid it. The new name we have adopted comes from the fact that, by maximizing the quantity in Eq. (5.26), we essentially adjust the parameters of the templates to best *fit* the true waveform.

3.2 The form of FF for the Newtonian template family searching for a precessionally modulated Newtonian signal

In this section we will construct an explicit expression for the FF when a "Newtonian template family" is used to search for the modulated Newtonian waveforms of Sec. 2.

The *Newtonian template family* has been introduced and studied previously by a number of researchers [7, 8]. Each Newtonian template is the waveform predicted in the Newtonian, quadrupole moment approximation, for some circular, inspiraling binary; and it therefore has the same form $h_C(t)$ [or $\tilde{h}_C(f)$] as the carrier signal (5.9). Of course the parameters const, t_C, ϕ_C, and $\mathcal{M}$ of the Newtonian template are not in general the same as these of the "true", modulated signal's carrier. Rather, the template parameters must be adjusted to make the Newtonian template resemble as well as possible the modulated waveform.

By using Eq. (5.19), the FF for a Newtonian filter takes the following form

$$FF = \max_{\Delta t_C, \Delta\phi_C, \Delta(\mathcal{M}^{-5/3})} \frac{\Re\left[\int_0^\infty df \frac{f^{-7/3}}{S_n(f)} e^{i\Psi(f)} \mathrm{AM} \times \mathrm{PM}\right]}{\sqrt{\left[\int_0^\infty df \frac{f^{-7/3}}{S_n(f)}\right]\left[\int_0^\infty df \frac{f^{-7/3}}{S_n(f)} (\mathrm{AM})^2\right]}} , \tag{5.27}$$

where '$\Re$' means "the real part of",

$$\Psi(f) = 2\pi f \Delta t_C - \Delta\phi_C + \frac{3}{4}(8\pi f)^{-5/3} \Delta(\mathcal{M}^{-5/3}) , \tag{5.28}$$

and $\Delta t_C, \Delta\phi_C$, and $\Delta(\mathcal{M}^{-5/3})$ are the differences in the parameters between a chosen template and the modulated signal's carrier. Note that all multiplicative factors not depending on frequency, such as the distance to the binary, have been cancelled out because of the specific form of the FF, which automatically normalizes the template and the signal. Fortunately, one of the maximization parameters, $\Delta\phi_C$, affects the FF value trivially, and there is no need to fine-tune it. To maximize FF over $\Delta\phi_C$, one need only compute the values for FF with $\Delta\phi_C = 0$ and $\Delta\phi_C = \pi/2$ and then add them in quadrature. Therefore Eq. (5.27) for the FF simplifies to

$$FF = \max_{\Delta t_C, \Delta(\mathcal{M}^{-5/3})} \frac{\left|\int_0^\infty df \frac{f^{-7/3}}{S_n(f)} e^{i\Psi(f)} \mathrm{AM} \times \mathrm{PM}\right|}{\sqrt{\left[\int_0^\infty df \frac{f^{-7/3}}{S_n(f)}\right]\left[\int_0^\infty df \frac{f^{-7/3}}{S_n(f)} (\mathrm{AM})^2\right]}} , \tag{5.29}$$

where $\Psi(f)$ is the same as in Eq. (5.28) but with $\Delta\phi_C$ eliminated

$$\Psi(f) = 2\pi f \Delta t_C + \frac{3}{4}(8\pi f)^{-5/3}\Delta(\mathcal{M}^{-5/3}) \,. \tag{5.30}$$

This is the expression that we have used in a computer code, described later in Section 4.1, to compute the FF for various modulated signals. In addition to the obvious parameters in the FF, shown explicitly in Eqs. (5.29), (5.30), there are a few others hidden inside the AM, PM functions: the four angles θ, ϕ, w, g (see Fig. 5.3) defining the orientation and direction of the binary on the sky and the direction of its total angular momentum, the angle $\cos^{-1}\kappa$ between the orbital angular momentum and the spin, the masses M_1 and M_2 of the two objects, and the magnitude S of the spin.

3.3 How do the amplitude and phase modulation affect the FF?

Before we present the numerical results that we have obtained for the FF in various cases, it will be helpful to seek some intuition into the roles that AM and PM play in the value of FF. We will begin with the effect of AM alone without any phase modulation. For vanishing PM, the FF takes a much simpler form than Eqs. (3.2)

$$FF = \frac{\int_0^\infty df \frac{f^{-7/3}}{S_n(f)} \mathrm{AM}}{\sqrt{\left[\int_0^\infty df \frac{f^{-7/3}}{S_n(f)}\right]\left[\int_0^\infty df \frac{f^{-7/3}}{S_n(f)} (\mathrm{AM})^2\right]}} \,. \tag{5.31}$$

The $e^{i\Psi(f)}$ term has disappeared because, with PM=0, the FF is maximized by $\Delta t_C = \Delta(\mathcal{M}^{-5/3}) = 0$. It is straightforward to see that if AM were also a constant (no amplitude modulation), FF would be 1, meaning no signal-to-noise reduction at all. But what if the amplitude has a large depth of modulation like the $A_{x'}$ in Fig. 6 of Ref. [11]? For the sake of simplicity, we will assume that the form of AM during one binary precession is approximately given by $AM = \mid \sin(kf) \mid$ for some k, which very much resembles the plot of $A_{x'}$ in Fig. 6 of Ref. [11]. Bearing then in mind that $f^{-7/3}/S_n(f)$ changes rather slowly during one precession (see Fig. 2 of Ref. [12]), one can infer that

$$FF \approx \frac{\int_0^\pi \sin(x)\, dx}{\sqrt{\left[\int_0^\pi dx\right]\left[\int_0^\pi \sin^2(x)\, dx\right]}} = \frac{2\sqrt{2}}{\pi} = 0.900 \,. \tag{5.32}$$

Of course this is a lower limit on the FF due to AM, since it corresponds to the deepest possible modulation.

To get a feeling for *realistic* minimum values of FF due to AM, consider a binary with a maximally spinning $10M_\odot$ black hole and a non-spinning $1.4M_\odot$ neutron star with an $\hat{\mathbf{LS}}$ angle of 30° and choose its location and orientation to produce the worst possible amplitude modulation. Then the FF with no PM turns out to be 0.907 in very good agreement with our rough approximate value of Eq. (5.32).

Turn, now, from AM with vanishing PM, to PM with vanishing AM. The analysis in this case is somewhat more complicated, since the two parameters $\Delta t_C, \Delta(\mathcal{M}^{-5/3})$ have to be suitably tuned, to cancel out as well as possible the effects of φ, and $\delta\Phi$ given in Eqs. (5.14), (5.15). It can be easily verified that a perfect cancellation is not possible: the simple frequency dependence of $\Psi(f)$ [Eq. (5.30)] **cannot** perfectly correct for the oscillating behaviors of φ and $\delta\Phi$. If the amplitude of phase modulation is high, then $\Psi(f)$ is totally unable to keep the FF at high levels (> 0.9).

There is another effect (for some cases the main effect) that causes PM to produce low values of the FF. As has been shown in Eq. (45) of Ref. [11], the number of precessions for the two extreme cases $L \gg S$, $S \gg L$, can be inferred from the following expression for the precession angle

$$\frac{\alpha(f)}{2\pi} \approx \begin{cases} 11\left(1+\frac{3M_2}{4M_1}\right)\frac{10M_\odot}{M}\frac{10\text{Hz}}{f} & \text{for } L \gg S, \\ 1.9\left(1+\frac{3M_2}{4M_1}\right)\frac{M_1}{M_2}\frac{S}{M_1^2}\left(\frac{10M_\odot}{M}\frac{10\text{Hz}}{f}\right)^{2/3} & \text{for } S \gg L. \end{cases} \tag{5.33}$$

Now, in the case of secular evolution of φ (see Fig. 7 of Ref. [11]), φ varies like $\alpha(f)$ on top of the additional oscillation we talked about in the last paragraph. But the frequency dependence of $\alpha(f)$ is very different ($\propto f^{-2/3}$ to f^{-1}) from that of $\Psi(f)$. Therefore, $\Psi(f)$ cannot follow the evolution of $\varphi+2\Delta\Phi$ for long frequency intervals, and the FF remains at low levels.

Finally, there is a third PM effect that can lead to low FF values. If the PM changes behavior, from oscillatory to secular or conversely, especially at a frequency near ~ 50Hz where $f^{-7/3}/S_n(f)$ is maximal (see Fig. 2 of Ref. [12]), then $\Psi(f)$ can only attempt to follow the PM evolution during *one* of the two evolution phases; it will fail during the other. This leads to even lower values of the FF. Later on, in Section 4, we will check with realistic examples how important these three factors are in lowering the FF and what are the chances for each one of them to play an important role.

For the moment, we will give an example of the FF due to PM alone. For the same BH/NS binary as we discussed a few paragraphs above, when we were examining the effect of the AM on the FF, the lowest value the FF can take for the worst kind of PM is 0.564. This is much lower than the worst FF for the AM alone. It should be noted that the FF values due to PM alone and AM alone cannot be trivially combined to obtain the FF value when both PM and AM are present. For instance, for the above example, where PM alone gives $FF = 0.564$, if the AM alone had been used then the FF would have been 0.922, but with both AM and PM on, the FF would have been 0.653! Instead of driving FF to lower values (below 0.564), the AM effect has reduced the bad behavior of the PM effect by strongly suppressing some parts of deep PM modulation. But this is not a general rule. Sometimes the AM combines with the PM constructively and sometimes destructively.

4 NUMERICAL INVESTIGATIONS OF FF

4.1 The numerical code

The code written to compute the FF is based on Eqs. (5.29), (5.30). The integrands are numerically integrated from 10Hz up to the frequency of the final stable orbit, $4383.45\,(M_\odot/M)$ Hz. Actually this upper limit is rather unimportant for binaries with small total mass ($< 30M_\odot$) because the detector's high shot noise $S_n(f)$ at high frequencies strongly suppresses the integrand. The number of steps used is such that the precession angle α does not change by more than 0.1 rad in each step; this keeps the error in the calculated FF smaller than 10^{-3} and therefore negligible since we compute FF only to three significant digits.

We have also checked the error due to approximating the square bracket in Eq. (5.19) by unity. As we expected, the extra factors next to the 1 change the FF by a tiny amount ($< 10^{-4}$) even for rapidly modulated phases and amplitudes.

The only difficulty in computing the FF is to guess the right pair of parameters $\Delta t_C, \Delta(\mathcal{M}^{-5/3})$ that produces the maximum in Eqs. (5.29), (5.30). Of course, the code is able to climb up at a maximum, but there is no guarantee that this is *the global maximum.* The form of the function to be maximized on the 2-parameter Δt_C, $\Delta(\mathcal{M})^{-5/3}$ space is very complicated; see Fig. 5.2. We have roughly guessed the region of the global maximum by computing the average value of d(modulating phase)$/df$ around 50 Hz and adjusting the parameters of $d\Psi(f)/df$

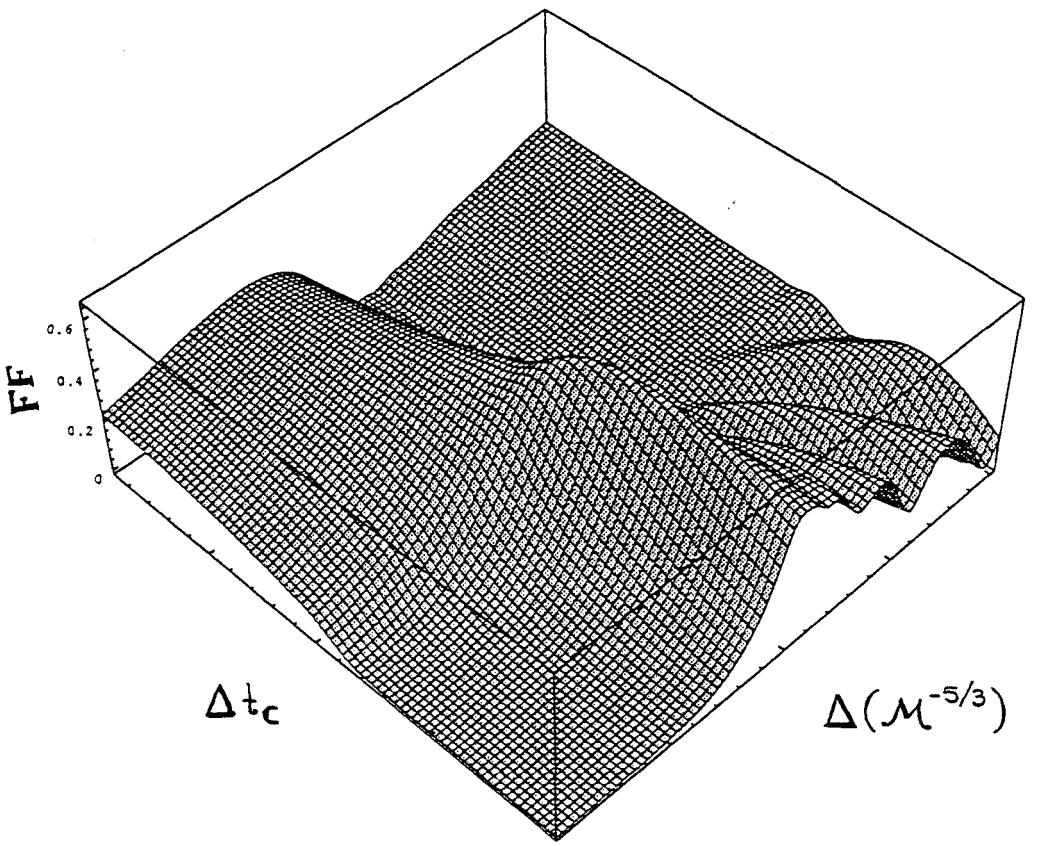

Figure 5.2: This is an example of the complicated landscape of the FF on the parameter space of $\Delta t_C, \Delta(\mathcal{M}^{-5/3})$ where many local maximums can be observed. The geometry used here is the one that provided the overall lowest FF value for the case of a maximally spinning $10M_\odot$ black hole and a $1.4M_\odot$ neutron star with $\widehat{\mathbf{LS}} = 30°$.

so that the two slopes are almost opposite. Then, starting from this point the code climbs up to the neighboring maximum. By searching a little bit around this peak we can be quite sure that it is the highest peak.

This procedure becomes more complicated in cases like the one where the PM changes behavior at some frequency. Then, there may be more than one candidate place for a global maximum. In the examples that follow we have carefully examined all such candidate places.

It is worthwhile to note that the improved template families we introduced in Sections 6 and 7 produce lower values of $|\Delta t_C|$, $|\Delta(\mathcal{M}^{-5/3})|$ than the Newtonian family because the extra parameter itself corrects for the PM and AM.

Throughout, we have used a grid on the 2-parameter space with a spacing of 1 msec for Δt_C and $2 \times 10^{-5} M_\odot^{-5/3}$ for $\Delta(\mathcal{M}^{-5/3})$. This choice is such that the difference for two nearby grid points in the overall change of $\int d\Psi(f)$, over the band of low detector noise (10 - 100 Hz), is less than 1 rad. Hence the FF changes very smoothly from point to point.

4.2 Dependence of the FF on the direction to the binary

In order to study the dependence of the FF on the binary's direction we performed the following search. We assumed that the merging compact binary is located directly above the North Pole of the Earth (of course this choice is only a matter of convention since any other point on Earth would be equivalent). We fixed the direction of the binary's total angular momentum **J** and let it precess. Then we filled the whole Earth's surface with identical detectors having the same noise spectrum, described by Eq. (5.23), and computed the FF for their outputs.

There are three angles related to the location of the detector: the standard θ' and ϕ' spherical coordinates related to the geographic longitude and latitude of the detector's location (not to be confused with the angles θ and ϕ used in Eqs. (5.16), (25.17)) and an angle w defining the orientation of its arms. In the following we define w to be the angle that one has to rotate the detector on the Earth's surface, for the arms to coincide with the local parallel and meridian (see Fig. 5.3). Note that w is only defined modulo $\pi/2$ due to the quadrupolar behavior of gravitational waves.

By keeping w fixed and moving the "rotated" detector around the Earth, we notice the following features of the FF. (i) The FF has the same form, as a function of longitude at any latitude, but with some shift γ that depends on the

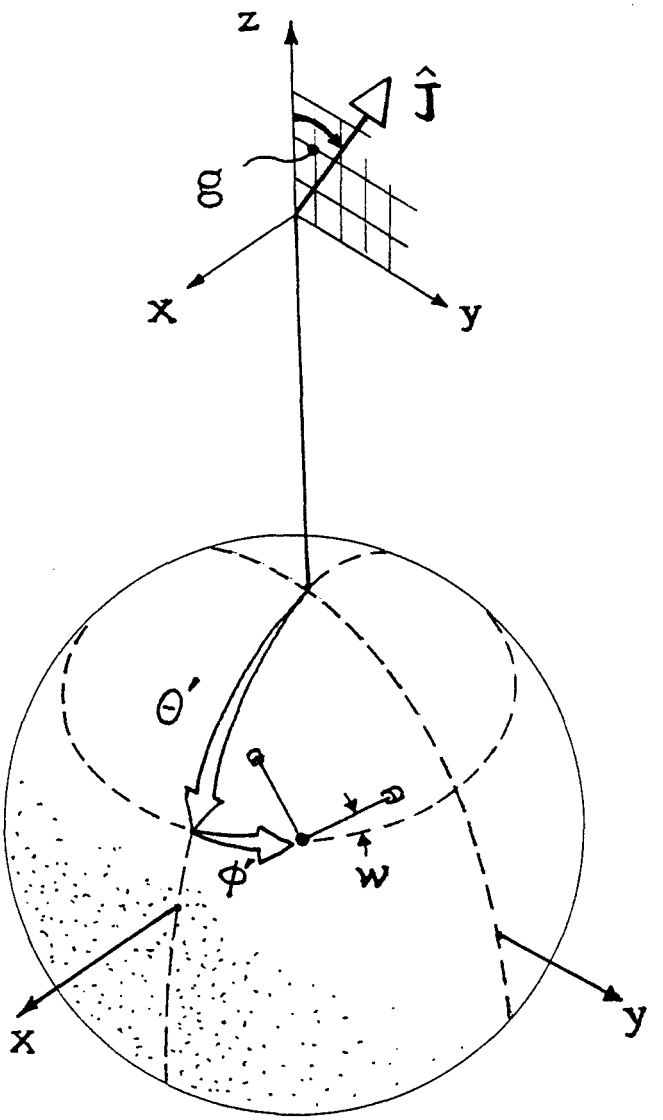

Figure 5.3: This is the geometry that we have used to investigate the dependence of FF on the various random angles, θ', ϕ', w, g.

latitude and on the rotation angle w:

$$FF(\theta', \phi', w) \cong FF(\theta' = 0, \phi' + \gamma, w) \,, \tag{5.34}$$

where

$$\gamma = \gamma(\theta', w) \,. \tag{5.35}$$

This dependence is depicted in Fig. 5.4 for three different θ' values. It can be explained by the following argument. If the detector's plane is not perpendicular to the waves' propagation direction, then the signal is the same as if the two arms were the projections of the original ones on the plane perpendicular to the propagation direction. The equivalent arms, orthogonal to the direction of the binary, are no longer equal to each other and they form some angle between 90° and 180°. If we now lengthen the shorter arm to give them equal lengths and move them by equal amounts toward the bisector to make them perpendicular, we will change the linear combination of $h_+(t)$ and $h_\times(t)$ (the two waveforms) that they measure; but this change is not important because we could get all the different combinations of polarizations, even with orthogonal detectors (detectors at the North pole in our case) by rotating the detector in its plane. (ii) For the two special cases of detectors at the North pole (and equivalently at the South pole) and at the Equator it is easy to verify analytically that

$$FF(\theta' = 0, \phi'_1, w_1 = 0) = FF(\theta' = 0, \phi'_2 = 0, w_2 = \phi'_1) \,, \tag{5.36}$$

and

$$FF(\theta' = \pi/2, \phi'_1, w_1) = FF(\theta' = 0, \phi'_1, w_2 = 0) \,. \tag{5.37}$$

The former corresponds to the fact, easily seen in Fig. 5.4, that for $\theta' = 0$ the detector's orientation depends only on $\phi' + w$ and not separately on ϕ' and w. The latter can be easily understood, since at the Equator a detector is equivalent to a one-arm detector perpendicular to the incoming waves.

This dependence of the FF on the location of the detector on Earth simplifies our investigation of the FF a lot. Eq. (5.34) makes it possible to restrict ourselves to detectors orthogonal to the propagation direction (detectors at the North pole) without any loss of generality.

4.3 Dependence of FF on the direction of the binary's total angular momentum J

We assume, now, that the binary is overhead at the detector and we move the total angular momentum $\mathbf{J}$ around to see how its direction $\hat{\mathbf{J}}$ affects the FF.

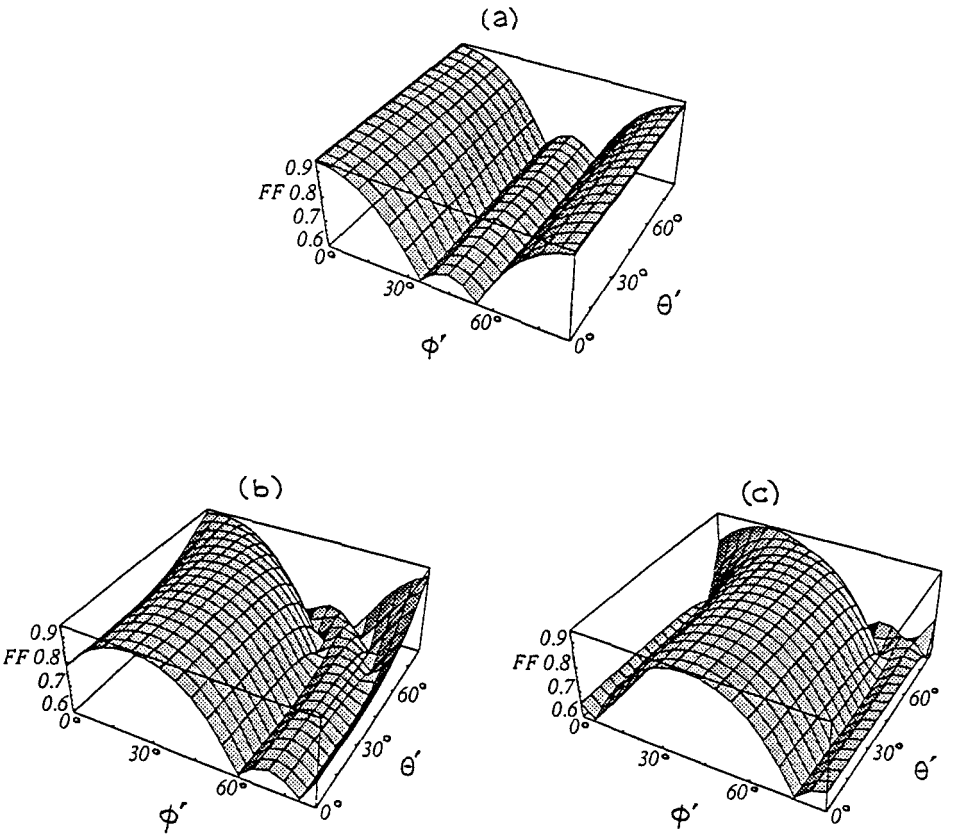

Figure 5.4: This is a series of 3 three-dimensional plots showing the FF for a binary of fixed orientation as one moves a detector on the Earth's surface keeping w fixed. (a) $w = 0°$, (b) $w = 25°$, (c) $w = 40°$. The plots verify Eqs (5.34), (5.35), (5.36), (5.37).

Recall that the modulational phase is the sum of two terms, $\mathrm{PM} = e^{-i[2\delta\Phi(t)+\varphi(t)]}$ [cf. Eq. (5.13)]. From Eq. (65) of Ref. [11] we know that during one precession $\delta\Phi$ changes by

$$\int_0^{2\pi} \frac{d\,\delta\Phi}{d\alpha}\, d\alpha = \begin{cases} -2\pi\cos\lambda_L & \text{if } |\hat{J}_0\cdot\hat{L}| < |\hat{J}_0\cdot\hat{N}| \\ 2\pi(-\cos\lambda_L+1) & \text{if } \hat{J}_0\cdot\hat{L} > |\hat{J}_0\cdot\hat{N}| \\ 2\pi(-\cos\lambda_L-1) & \text{if } \hat{J}_0\cdot\hat{L} < -|\hat{J}_0\cdot\hat{N}| \end{cases} . \tag{5.38}$$

As for φ, its evolution can be deduced using an intuitive tool introduced in Ref. [11], the *cell diagram* (which is reproduced in Fig. 5.5). There are six special "singular" directions in the cell diagram: the six intersections of the black and white cell walls. If the binary's precession cone (the cone on which its orbital angular momentum $\hat{\mathbf{L}}$ precesses) encloses one of the singular directions, then φ evolves secularly; otherwise it oscillates. We expect φ to behave in the most irregular way and thus cause the FF to assume its lowest values for the cases where $\hat{\mathbf{L}}$'s spiraling precession barely touches one of these singular directions at a frequency near 50 Hz, where $f^{-7/3}/S_n(f)$ is maximum (see Figs. 5.6).

Actually, for the two singular directions where φ changes by 4π with each precession that encloses them, $2\,\delta\Phi$ changes by $-4\pi\cos\lambda_L$ (which is $\simeq -4\pi$ if $\widehat{\mathbf{LS}}$ is small) thus moderating the total phase modulation. Correspondingly, as we will see later, these two directions produce fairly high values for the FF, when $\widehat{\mathbf{LS}}$ is small.

By contrast, for the other four singular directions, around which φ changes by 2π with each precession, $2\,\delta\Phi$ changes only by $4\pi(1-\cos\lambda_L)$, a small angle if the opening angle $\widehat{\mathbf{LS}}$ is small. Thus these four directions will typically produce the lowest values of the FF.

It should be emphasized that it is **not** $\hat{\mathbf{J}}$ itself that leads to low FF values by pointing along these singular directions, but $\hat{\mathbf{L}}$. Thus, to produce low FF's $\hat{\mathbf{J}}$ should find itself in ring-like areas around these singular points ; see Figs. 5.6.

The situation is much more complicated if the opening angle $\widehat{\mathbf{LS}}$ is big than if it is small (but excluding the extreme value of $\approx 180°$ which would lead to transitional precession). In this case the cone of $\hat{\mathbf{L}}$ can encompass more than one singular direction, leading to multiple behavior of the phase evolution and low values of the FF.

In general in the parameter space $[\Delta t_C, \Delta(\mathcal{M}^{-5/3})]$ there are at most as many candidate regions, for expression (5.27) for the FF to acquire its global maximum, as the number of singular directions encompassed by the cone of $\hat{\mathbf{L}}$. This happens

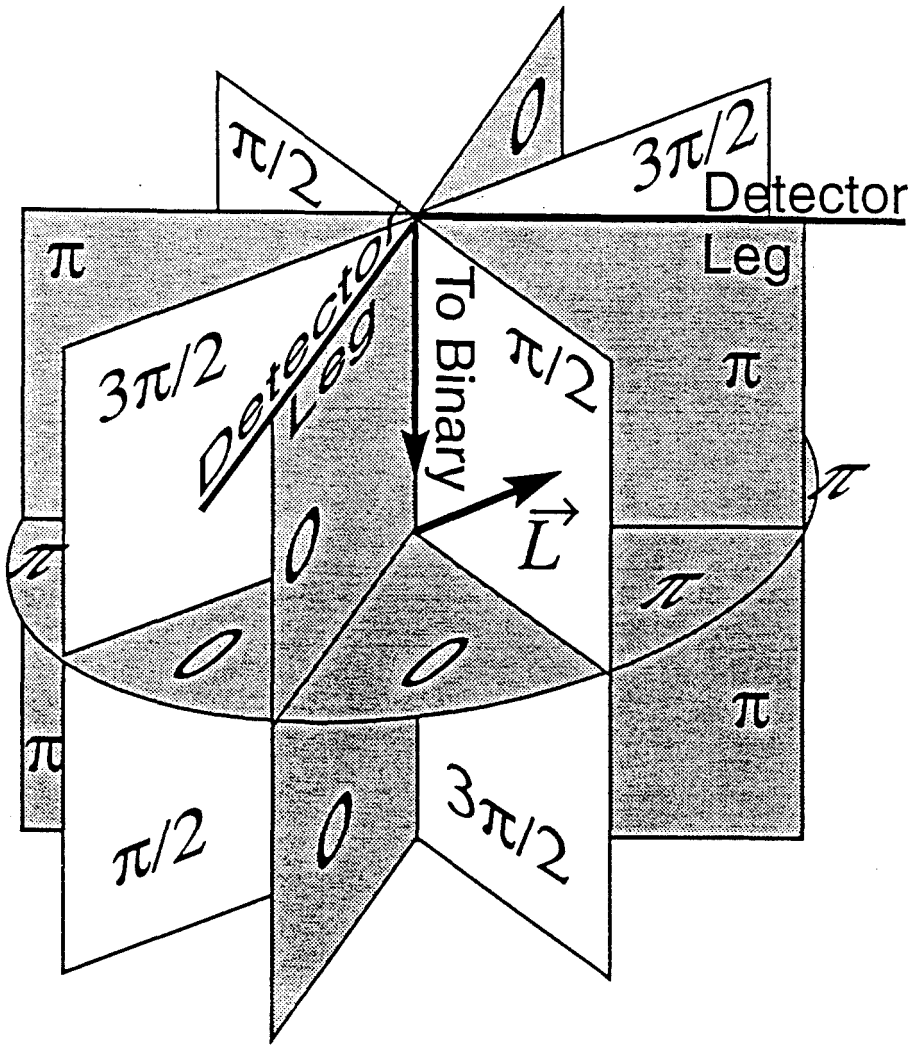

Figure 5.5: This *cell diagram*, reproduced from Ref. [11], is a useful tool for understanding how the phase φ evolves while $\hat{\mathbf{L}}$ precesses, for a detector positioned as shown in the diagram. Each wall in the diagram is labeled by the value that φ takes when $\hat{\mathbf{L}}$ lies in that wall. The lines at which black and white walls intersect are singular directions; when $\hat{\mathbf{L}}$ passes near such a line, φ changes rapidly.

because, when the evolving precession cone passes through each of the singular directions, the behavior of the phase evolution changes. This information enables us to initiate our numerical search for FF for various geometries.

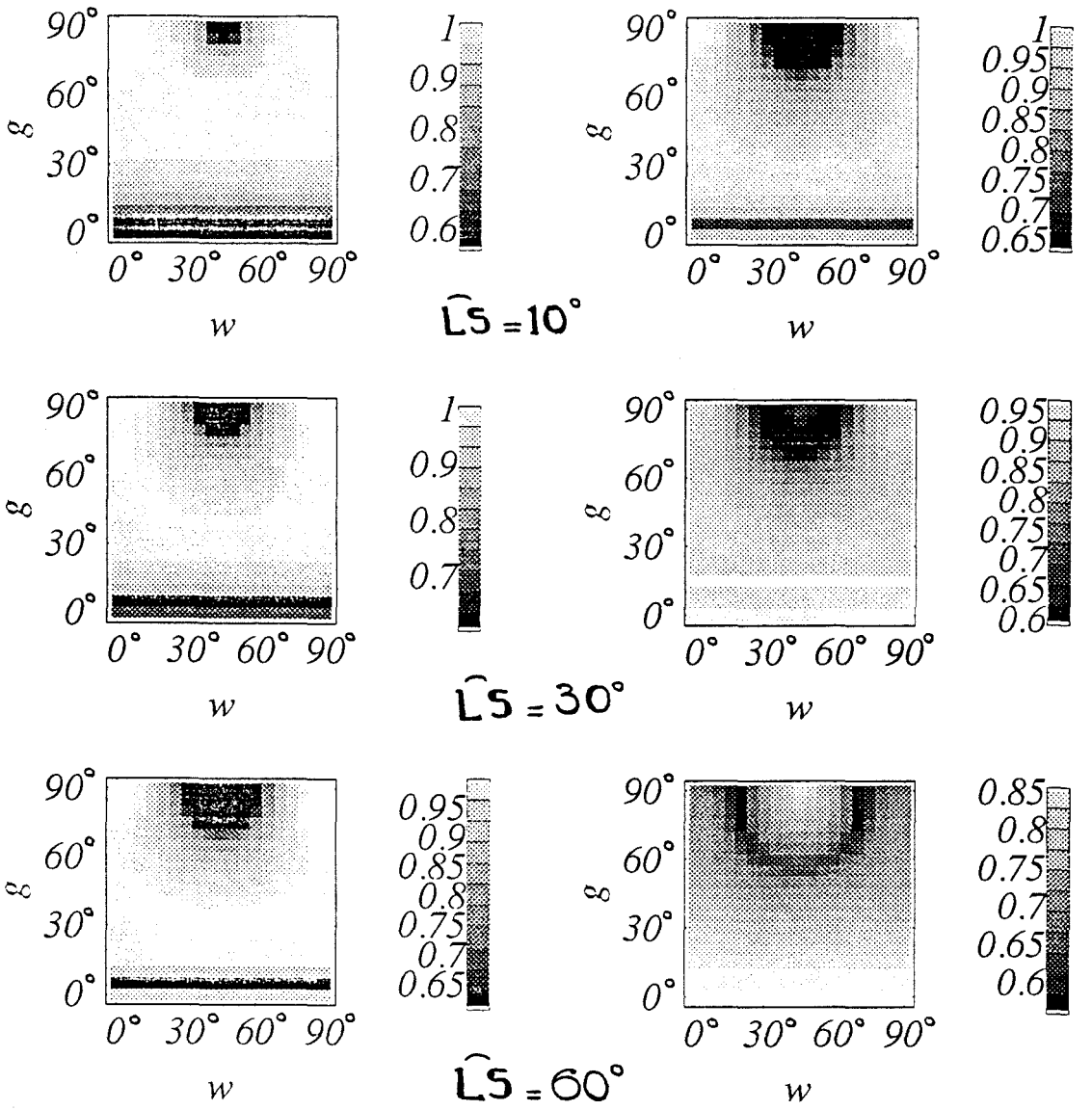

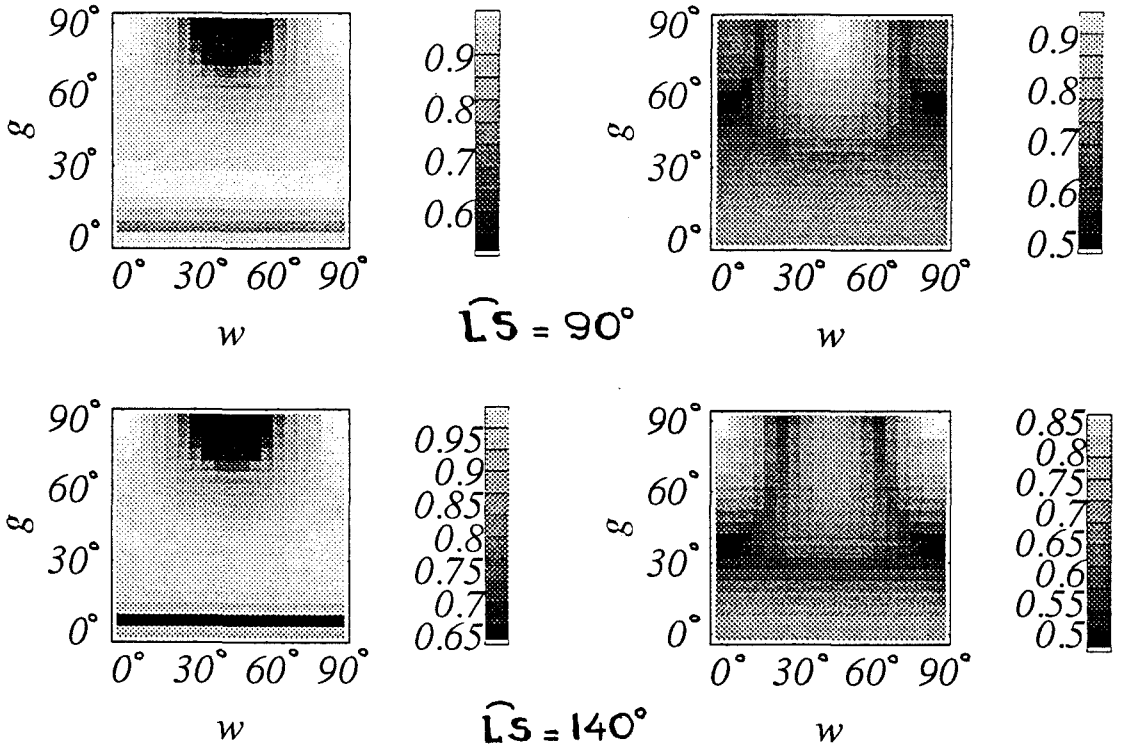

Figure 5.6: This is a series of density plot diagrams showing the FF distribution in grey-scale (black represents the lowest values) for a detector at the North pole as one rotates its arms (variable w) and changes the inclination g of the binary's total angular momentum $\mathbf{J}$ to the z-axis (the Earth's rotation axis) while keeping $\mathbf{J}$ in the $y-z$ plane (see Fig. 5.3). We have arranged the Figures in pairs. The left column corresponds to a $1.4M_\odot$, $1.4M_\odot$ NS/NS binary and the right column to a $10M_\odot$, $1.4M_\odot$ BH/NS binary. For both types of binaries the more massive object is maximally spinning ($S_i = M_i^2$). The ring with the low FF around the singular direction ($g = 90°$, $w = 45°$) can be easily recognized. Actually only one eighth of the whole (g, w) space is displayed here since the same pattern is repeated.

4.4 Dependence of FF on the masses and the $\hat{\mathbf{LS}}$ angle

Up to this point, we have investigated the dependence of the FF on all the randomly distributed variables defining the geometry of the source-detector system. These are the variables over which we must average to obtain a probabilistic picture of the FF. In the present section, we discuss the effect of the other, non-randomly distributed, variables M_1, M_2, S, and $\hat{\mathbf{LS}}$. In the following, as in Sec. 4.3, we assume that the larger mass is maximally spinning,

$$S = M_1^2 \,. \tag{5.39}$$

As we showed in Sec. 4.3 the FF value depends greatly on the opening angle λ_L of the precession cone, and the singular points it encompasses. The angle λ_L itself is a function of the binary's masses, the $\hat{\mathbf{LS}}$ angle, and the gravity wave frequency [cf. Eqs. (5.2), (5.5)]. It is easy to show that

$$\frac{L}{S} = 40.088 \left(\frac{M_2}{M_1}\right) \left(\frac{M}{M_\odot}\frac{f}{\mathrm{Hz}}\right)^{-1/3} \,. \tag{5.40}$$

From Eq. (5.2) with $L = \sqrt{Mr}$ we see that the opening angle λ_L is larger if L/S is lower, i.e., [Eq. (5.40)] if the total mass M is higher and the ratio of masses is lower. Restricting ourselves to our two typical combinations of masses, one with a $10M_\odot$ black hole and a $1.4M_\odot$ neutron star and the other with two $1.4M_\odot$ neutron stars, we can see that in the NS/NS case the λ_L opening angles are much smaller than in the BH/NS case; cf. Figs. 5.7. Hence we expect, and it is true as we shall see in examples in Sec. 5, that the NS/NS binaries produce overall higher values of FF than NS/BH or BH/BH binaries with unequal masses.

Of course the $\hat{\mathbf{LS}}$ angle plays also a crucial role. If $\hat{\mathbf{LS}}$ is small the values of FF stay at a high level for most of the various geometries, whatever the masses may be.

5 DETECTABILITY OF PRECESSING BINARIES

We have thoroughly analyzed how the various random variables, such as the position on the sky and the orientation of the binary's plane, affect the FF values. We have also checked how the non-random variables like the masses and the $\hat{\mathbf{LS}}$ angle affect the worsening or improvement of the FF. But ultimately what is important

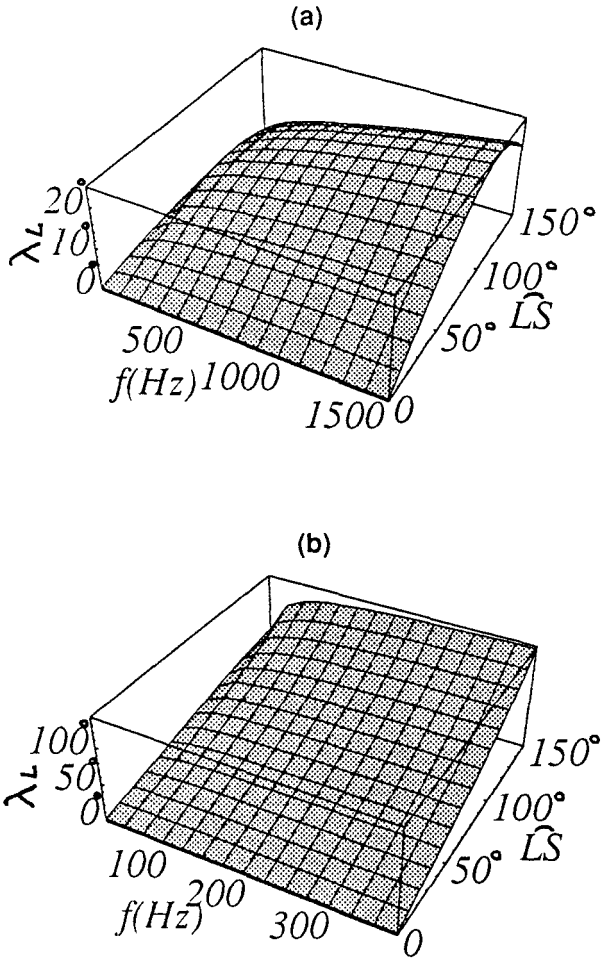

Figure 5.7: (a) This three-dimensional plot shows how the opening angle λ_L of $\hat{\mathbf{L}}$ changes with frequency (from 10 Hz up to the frequency of the last stable orbit) for various $\hat{\mathbf{L}}\hat{\mathbf{S}}$ angles, for two representative binaries: (a) a $1.4M_\odot$, $1.4M_\odot$ NS/NS binary with one of the stars maximally rotating, $S_i = M_i^2$; (b) a $10M_\odot$, $1.4M_\odot$ BH/NS binary with the black hole maximally rotating.

is the probability of detecting these modulating signals. In this spirit, for a number of typical values of the nonrandom parameters, we have integrated all the random variables to investigate what is the probability to have an FF value above some level and therefore to be able to detect the gravitational waves coming from (Newtonian) precessing binaries using the nonprecessing Newtonian template family. In Fig. 5.8, the probability $P(FF < FF_0)$ of getting an FF value below some level FF_0 is depicted. Part (a) of the figure shows this probability for our standard $1.4M_\odot$, $1.4M_\odot$ NS/NS binary for various $\hat{\mathbf{L}}\mathbf{S}$ angles. Things look very optimistic in this case; only a very small portion of the geometries produce FF's below 0.9 with a corresponding reduction in the event rate. In Figs. 5.8b by contrast, one can see that for our standard $10M_\odot$, $1.4M_\odot$ BH/NS binary, if the $\hat{\mathbf{L}}\mathbf{S}$ angle is large enough ($> 30°$) the FF is below 0.9 for more than half of the various randomly distributed geometries!

6 POST-NEWTONIAN TEMPLATE FAMILY

Of course an obvious way to improve the detectability is to use the full family of modulated theoretical waveforms in the search for signals; then the FF would be unity and we would obtain the maximum possible signal-to-noise. But this solution is rather undesirable since the modulated waveforms are a very large family containing many parameters, and this would greatly increase the computational task and seriously reduce the statistical significance of any discovered signal. What we need is a variation of the Newtonian filter with only one or two extra parameters that can improve the FF values by better matching the complicated phase evolution of the signals.

As we have seen in Sec. 3.3, the main reason that a Newtonian template cannot follow the evolution of the PM, is that the only frequency evolution of its phase $\Psi(f)$ is $(3/4)(8\pi\mathcal{M}f)^{-5/3}$ [cf. Eq. (5.30)], while $\alpha(f)$ (the precession angle; see Eq. (5.33)) evolves $\propto f^{-2/3}$ or f^{-1} depending on the relative sizes of L and S. A simple way, then, to solve our problem is to add an extra term onto the phase evolution of the Newtonian template, a term with a softer than $f^{-5/3}$ dependence on f; for example an $A f^{-1}$ term, where A is the new template parameter:

$$\tilde{T}_{PN}(f) = \text{const} \times f^{-7/6} e^{i\Psi_{PN}(f)}, \tag{5.41}$$

with

$$\Psi_{PN}(f) = 2\pi f t_C - \phi_C + \frac{3}{4}(8\pi\mathcal{M}f)^{-5/3} + A f^{-1} . \tag{5.42}$$

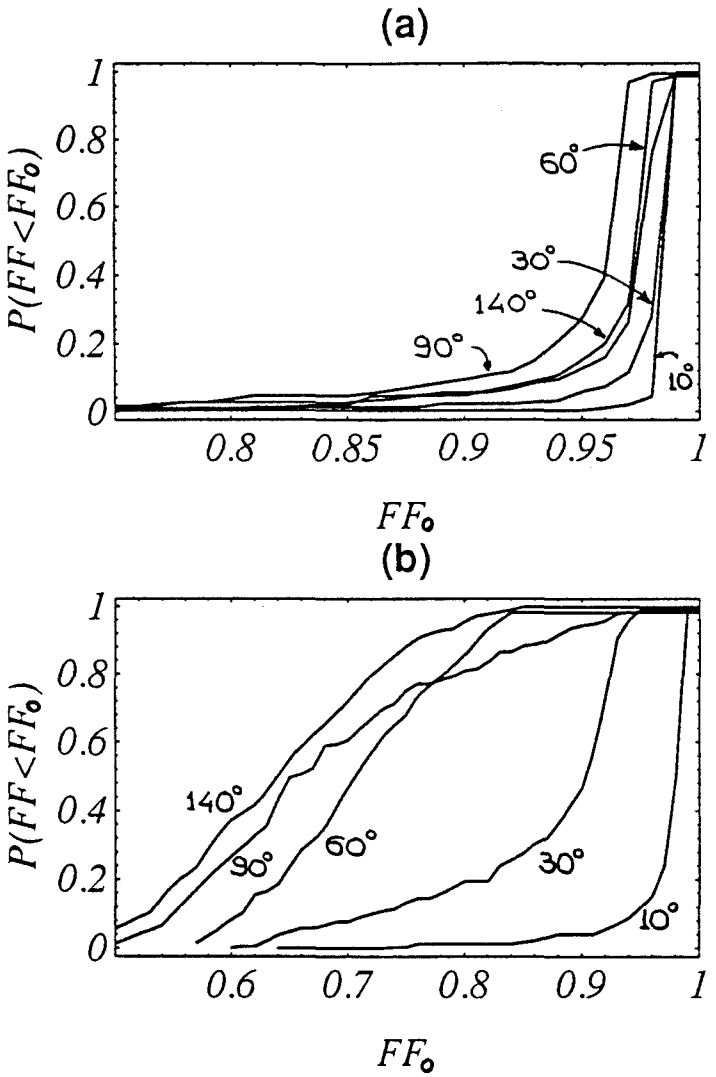

Figure 5.8: By compiling the values of the FF for all the cases shown in Figs. 5.6, we obtain the probability over all the random variables for the FF to stay below some critical value FF_0. The curves in this figure show that probability, for various values of the opening angle $\widehat{\mathbf{LS}}$. Plot (a) is for NS/NS binaries and (b) for BH/NS binaries with the same masses and spins as in Fig. 5.7.

Since this $A f^{-1}$ term is also exactly the correction to the phase that is required to match the binary's nonmodulated post^1-Newtonian effects in the waveform [12], this template family (henceforth, we shall call it the "post^1-Newtonian template family") might well be the best one can construct with four parameters $(t_C, \phi_C, \mathcal{M}, A)$ altogether. Our code is able to handle the new parameter in the maximization process to compute the FF. We have attempted a few runs with the extra term for the worst cases we presented in the previous section. It turns out [see Fig. 5.9] that this extra term helps a lot in matching the modulated Newtonian waveforms, but it still leaves the FF below 0.9 for most of the geometries of our standard BH/NS binary when $\hat{\mathbf{L}}\mathbf{S}$ is greater than $\sim 45°$.

7 NONMODULATIONAL POST-NEWTONIAN EFFECTS AND A POST$^{1.5}$-NEWTONIAN FAMILY

Up to this point we have assumed modulated Newtonian waveforms as signals. But what about the nonmodulational post-Newtonian effects? We neglected them so as to explore the influence of precession-induced modulation on the FF in isolation from other post-Newtonian effects. Now we are ready to consider these other effects.

As we said in the Introduction, Kokotas, Kròlak, and Schäfer [7], and Balasubramanian, and Dhurandhar [8] have investigated the importance of all the higher nonmodulational post-Newtonian corrections currently available, namely the post^1- and post$^{1.5}$-Newtonian corrections in the signal, and have found that the Newtonian template family produces rather low FF values for such signals. We have repeated their calculations and confirmed their results. In addition, we have calculated the FF values for all the possible combinations between Newtonian and post-Newtonian nonmodulated signals and templates, and have incorporated the effects of spins, with $\hat{\mathbf{L}}\mathbf{S}$ =0 (and thus no precession), into the calculations. Of course, when we use signals and templates of the same post-Newtonian accuracy, we get FF values equal to 1.

Before we present our general results, let us write down the form of the most accurate nonmodulated waveform currently available (see Refs. [12, 14]), with all the post-Newtonian effects in the amplitude ignored:

$$\tilde{h}_{P1.5N}(f) = \text{const} \times f^{-7/6} e^{i\Psi_{P1.5N}(f)}, \tag{5.43}$$

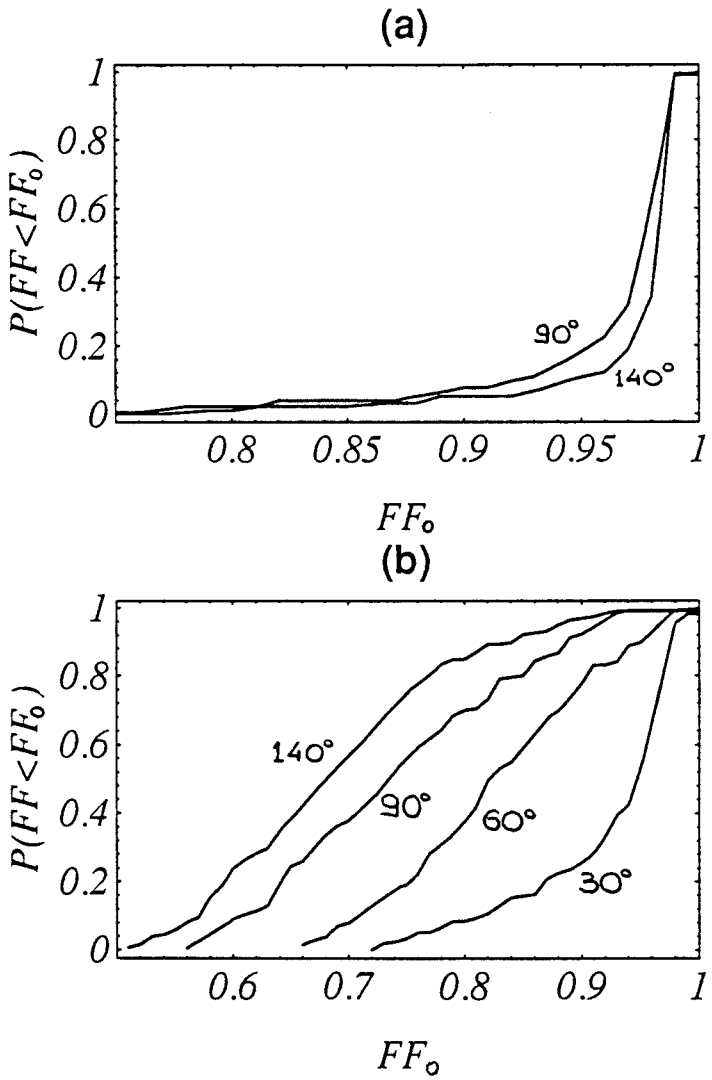

Figure 5.9: The same kind of plots as in Fig. 5.8 but for the (unmodulated) post^1-Newtonian family of templates used to search for modulated Newtonian signals. Again (a) is for NS/NS and (b) for BH/NS. Only a few (the worst) cases are shown here, for comparison with the ones in Figs. 5.8.

where

$$\Psi_{P1.5N}(f) = 2\pi f t_C \;-\; \phi_C + \frac{3}{128}(\pi\mathcal{M}f)^{-5/3} \times \left[1 + \frac{20}{9}\left(\frac{743}{336} + \frac{11\mu}{4M}\right)x - (16\pi - 4\beta)\,x^{3/2}\right], \quad (5.44)$$

and

$$x \equiv (\pi M f)^{2/3}, \quad (5.45)$$

$$\beta \equiv M^{-2}\hat{\mathbf{L}}\cdot\left[\left(\frac{113}{12} + \frac{25M_2}{4M_1}\right)\mathbf{S}_1 + \left(\frac{113}{12} + \frac{25M_1}{4M_2}\right)\mathbf{S}_2\right]. \quad (5.46)$$

One can easily identify the $\mathcal{O}[x]$ post^1-Newtonian correction in (5.45) as the $A\,f^{-1}$ post^1-Newtonian term that we introduced in the previous section as an improvement to the Newtonian family.

Table 1 shows the results of our calculations. Here, by contrast with Secs. 4 and 5, the signal in each column is unique. The many signal parameters that we faced in Secs. 4 and 5 ($\hat{\mathbf{L}}\hat{\mathbf{S}}$, detector orientation, direction of $\hat{\mathbf{J}}$, direction to source) vanish from the signal in this section's non-precessing limit, $\hat{\mathbf{L}}\hat{\mathbf{S}}$=0. From Table 1, one can see that the FF values for the post$^{3/2}$-Newtonian signal (without precession) and the Newtonian or the post^1-Newtonian template family are much too low for these families to be adequate for detection. These low FF's can be explained by the fact that the signal term $x^{3/2}$ (which is left out of the templates) is comparable with the x term (which the post^1-Newtonian templates include), and has the opposite sign.

Because the Newtonian and post^1-Newtonian families are so inadequate, it is necessary to include higher-order, nonmodulational effects in the waveforms. This can (and should) be done up to the highest available post-Newtonian order, without introducing any new parameters, in the case of vanishing spins. However the waveforms are not yet known beyond post$^{1.5}$-Newtonian order; so for now we only go that high.

More specifically, we introduce a post$^{1.5}$-Newtonian template family whose form is that of Eqs. (5.43)—(5.46) but with the new spin parameter β set to zero:

$$\tilde{T}_{P1.5N}(f) = \text{const} \times f^{-7/6} e^{i\Psi'_{P1.5N}(f)}, \quad (5.47)$$

where

$$\Psi'_{P1.5N}(f) = 2\pi f t_C - \phi_C + \frac{3}{128}(\pi\mathcal{M}f)^{-5/3}\left[1 + \frac{20}{9}\left(\frac{743}{336} + \frac{11\mu}{4M}\right)x - 16\pi x^{3/2}\right]. \quad (5.48)$$

Again we ignore all the post-Newtonian effects in the amplitude. Note that the $\mathcal{O}[x]$ correction is equivalent to the $A f^{-1}$ term of the post^1-Newtonian template.

We have explored the adequacy of this 4-parameter $(t_C, \phi_C, \mathcal{M}, A)$ family in searches for waves from non-precessing but maximally spinning ($\hat{\mathbf{L}}\mathbf{S}$=0) post$^{1.5}$-Newtonian binaries. The resulting FF (0.987 for BH/NS, 0.985 for NS/NS; see Table 1) is excellent. The unimportance of the spin effects (the β factor in the signal), is due to the small value of β compared to 4π (see Eq. (5.43)). The situation becomes worse (lower FF) for an extreme ratio of masses ($FF \simeq 0.895$ for $M_2/M_1 = 0.05$), since for a maximally rotating large black hole (with mass M_1) and a small nonrotating black hole or neutron star (with mass M_2) β grows like the ratio $M_1^2/(M_1+M_2)^2$. [The FF values quoted in Table 1, for a post$^{1.5}$-Newtonian signal and template assume that only the more massive body is spinning with $\mathbf{S}_i = M_i^2 \hat{\mathbf{L}}$; the more massive was chosen in order to obtain the maximum value for β.]

8 MODULATED POST$^{1.5}$-NEWTONIAN SIGNALS SEARCHED FOR WITH THE POST$^{1.5}$-NEWTONIAN FAMILY

We now consider the suitability of this post$^{1.5}$-Newtonian family (5.47) for detection of spin-modulated signals. For this purpose we have used as signals the nonmodulated post$^{1.5}$-Newtonian signals for our typical NS/NS and BH/NS binaries and have modulated them according to the AM and PM introduced in Sec. 2:

$$\tilde{h}(f) = \mathrm{AM} \times \mathrm{PM} \tilde{h}_{P^{1.5}N}(f) \,. \tag{5.49}$$

Although the modulational effects are based on Newtonian orbits and quadrupole wave generation, this artificial composition of signal will surely give us a more realistic kind of signals than just the nonmodulated post-Newtonian or the modulated Newtonian signal.

The FF values we have obtained with our 4-parameter post$^{1.5}$-Newtonian templates and the modulated post$^{1.5}$-Newtonian signals were at least as good as the values we obtained in the previous section for unmodulated post^1-Newtonian templates and modulated Newtonian signals; see Fig. 5.10. This was to be expected since the two terms $x^{3/2}$ and x in the templates' phase [Eq. (5.48)] have the exact

frequency dependences that the precession follows for the two extreme cases of Eq. (5.33).

9 CONCLUSIONS

This paper is an initial exploratory work on the issue of search templates which will be used by the ground-based LIGO/VIRGO/GEO and space-based LISA detectors, for detecting gravity wave signals from inspiraling black hole and/or neutron star binaries. We have introduced a measure of adequateness of a template family (the Fitting Factor) and have shown (in agreement with other people's work) that the Newtonian and the post^1-Newtonian template family are inadequate to detect non-modulated post$^{1.5}$-Newtonian signals. We have then suggested the use of the post$^{1.5}$-Newtonian family with one more parameter than the Newtonian family. The post$^{1.5}$-Newtonian family produces higher FF's than the Newtonian family not only for non-modulated post$^{1.5}$-Newtonian signals but for precessionally modulated signals too.

The understanding of FF's gained from our study suggests that for most binaries, but not all, an adequate family of search templates will be the 4-parameter family (ϕ_C, t_C, $\mathcal{M}$, A), or equivalently (ϕ_C, t_C, $\mathcal{M}$, μ/M), based on the waveforms for circular-orbit, zero-spin binaries at the highest post-Newtonian order $n_{\max}$ that is available when the searches begin. This is likely to be post^3-Newtonian order, i.e., $n_{\max} = 3$. It may well be, however, that as at present ($n_{\max} = 1.5$), so also then, binaries with moderately large mass ratios and moderately large $\hat{\mathbf{L}}\mathbf{S}$, i.e., with large precessions, will have unacceptably low FF's when this 4-parameter family is used. In preparation for that possibility, an effort is needed now to expand the $n_{\max} = 1.5$, 4-parameter family to include some form of modulation that raises FF above 0.9 in these large-precession cases. This also might be done for the extreme mass-ratio $\mu/M << 1$, $n_{\max} = 8$, 4-parameter template family based on the Teukolsky-formalism waveforms of Sasaki and Tagoshi [15].

Throughout this paper we have restricted ourselves to template families with continuously varying parameters. Now is the time to abandon that restriction and focus on discrete template families. The goal must be, building on the continuous-family insights of this paper and on Refs [7, 8] to device a discrete family with as small a number of members as possible, which gives $FF > 0.9$ (or some other threshold) for all plausible binary waveforms. A first exploration of discrete template families has been carried out by Sathyaprakash and Dhurhandhar [6].

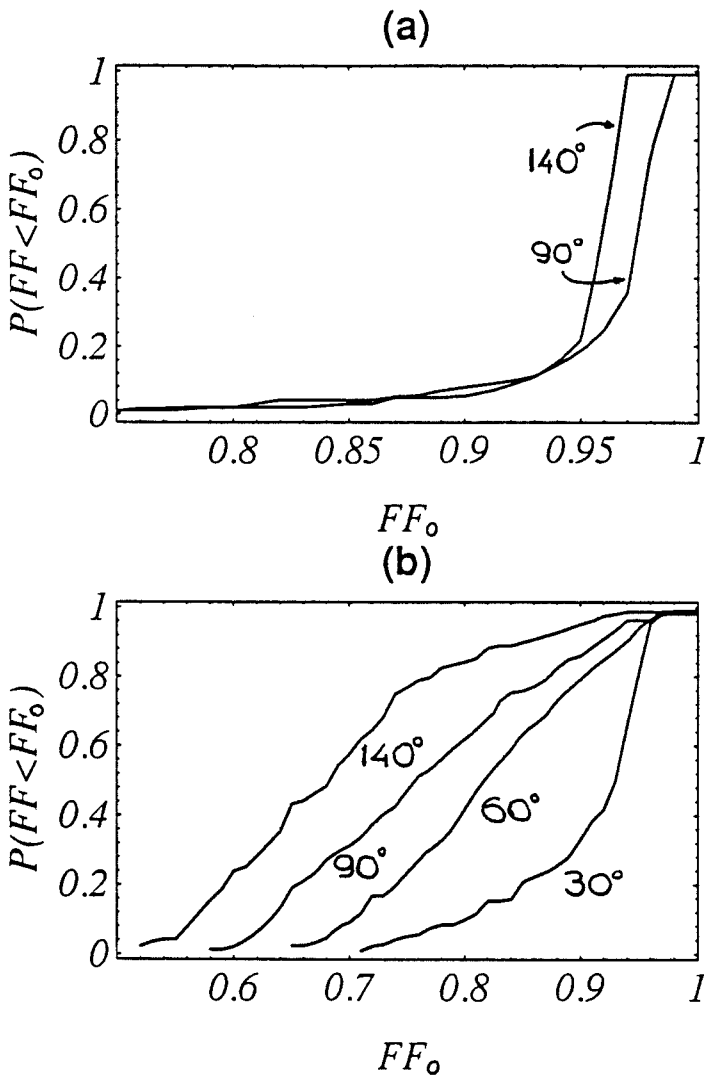

Figure 5.10: The same kind of plots as in Fig 5.9 but for the zero-spin post$^{1.5}$-Newtonian family of Eq. (5.47), and a signal in which the Newtonian-order precession effects are added on top of the more realistic post$^{1.5}$-Newtonian signal. Again (a) is for NS/NS and (b) for BH/NS. Only a few (the worst) cases are shown here, for comparison with the ones in Figs. 5.8.

Acknowledgments

I am grateful to Kip Thorne for suggesting this problem, and for many helpful discussions and comments. I would also like to thank Éanna Flanagan for many helpful discussions with respect to signal analysis and Eric Poisson for pointing out that the extra term A/f introduced to improve the Newtonian filter is the same as the post^1-Newtonian nonmodulational correction to the waveform. This work was supported in part by NSF grant PHY-92135082 and (in view of its auxiliary implications for space-based gravitational-wave detectors) by NASA grant NAGN-2897.

APPENDIX: Extension of the results to low-frequency space-based detectors

Preliminary designs for a space-based antenna (LISA) to detect gravitational waves from supermassive black holes have been developed, and LISA has been proposed for a future space mission(see Refs. [16]). The noise spectrum for such a detector has been estimated to have roughly the following shape; this is an analytic fit to Fig. 2 of Ref. [16]:

$$S_n(f) = S_0 \times \begin{cases} (f/1\text{mHz})^{-4} & \text{for } f < 1 \text{ mHz}, \\ 1 & \text{for } 1 \text{ mHz} < f < 0.1 \text{ Hz}, \\ 10^{-4}(f/1\text{mHz})^2 & \text{for } f > 0.1 \text{ Hz} \end{cases} \tag{5.50}$$

with $S_0 = 10^{-42}$ Hz^{-1}. Actually, there is one more branch of the noise spectrum for frequencies below 10^{-5} Hz, which grows with decreasing f even faster than $\propto f^{-4}$; but since the noise levels are already so high at these low frequencies, we can ignore this branch and restrict ourselves to the above approximation when computing the FF for binary signals.

There is a great similarity between the shapes of the noise spectra of the ground-based [Eq. (5.23)] and the space-based [Eq. (5.50)] detectors. There is a big difference, however, in the range of frequencies over which these detectors have high sensitivity: 5 orders of magnitude. The equations describing the precession of a binary and its waveforms depend only on the ratio of masses and the product fM [see Eqs. (5.2), (5.3), (5.40)]. Therefore, if we use as examples binaries with masses 10^5 times larger than for the binaries considered for the ground-based detectors, and keep the same mass ratios, we should get approximately the same FF values

as for the LIGO/VIRGO/GEO detectors. The only differences will come from the modest differences in the shapes of the noise spectra (5.23) and (5.50); and since the spectra are so similar, the FF's should be nearly the same.

We verify this in Fig. 5.11 for the case of a Newtonian template family and a maximally rotating $10^6 M_\odot$ and a nonrotating $1.4 \times 10^5 M_\odot$ BH/BH binary, with $\widehat{\mathbf{LS}} = 60^0$ and a noise spectrum given by Eq. (5.50). The corresponding plot of the FF probability distribution over the random variables for a $10 M_\odot$, $1.4 M_\odot$ BH/NS binary, with $\widehat{\mathbf{LS}} = 60^0$ and a noise spectrum given by Eq. (5.23), is copied here from Fig. 5.8 for comparison. The fairly good agreement is obvious. Thus, all the results derived in this paper for LIGO/VIRGO/GEO search templates can be carried over essentially without change to LISA; and this paper can be regarded as an initial exploratory study of templates for LISA as well as for LIGO/VIRGO/GEO.

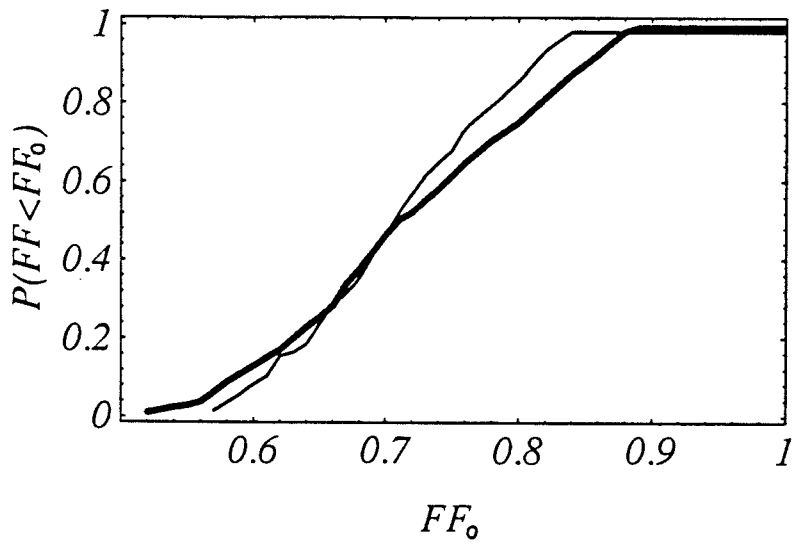

Figure 5.11: The same kind of plot as in Fig. 5.8 but for a $10^6 M_\odot$, $1.4 \times 10^5 M_\odot$ BH/BH binary, with $\hat{\mathbf{L}}\mathbf{S} = 60^0$ and a noise spectrum given by Eq. (5.50) (thick line). The corresponding plot for a $10 M_\odot$, $1.4 M_\odot$ BH/NS binary, with $\hat{\mathbf{L}}\mathbf{S} = 60^0$ and a noise spectrum given by Eq. (5.23) is copied here from Fig. 5.8 for comparison (thin line).

Bibliography

[1] A. Abramovici *et al.*, *Science* **256**, 325 (1992).

[2] B. F. Schutz, in *The Detection of Gravitational Waves*, ed. D. G. Blair (Cambridge University Press, Cambridge, 1991), pp. 406-452.

[3] K. S. Thorne, *private communication.*

[4] T. A. Apostolatos, D. Kennefick, A. Ori, E. Poisson, *Phys. Rev. D* **47**, 5376 (1993).

[5] G. Quinlan, and S. L. Shapiro, *Astrophys. J.* **321**, 199 (1987).

[6] S. V. Dhurhandhar, and B. S. Sathyaprakash, *Phys. Rev. D* **49**, 1707 (1994).

[7] K. Kokkotas, A. Kròlak, G. Schäfer, *Proceedings of the Moriond 94 Workshop.*

[8] R. Balasubramanian, and S. V. Dhurandhar, *Phys. Rev. D.*, in press.

[9] M. Will, to be published in *Proceedings of the Eighth Nishinomiya-Yukawa Symposium on Relativistic Cosmology*, ed. M. Sasaki (Universal Academy Press).

[10] C. Cutler and E. Flanagan, in preparation

[11] T. A. Apostolatos, C. Cutler, G. J. Sussman, and K. S. Thorne, *Phys. Rev. D* **49**, 6274 (1994).

[12] C. Cutler, and E. Flanagan, *Phys. Rev. D* **49**, 2658 (1994).

[13] E. Flanagan, *Phys. Rev. D* **46**, 1429 (1992).

[14] A. G. Wiseman, *Phys. Rev. D* **46**, 1517 (1992).

[15] H. Tagoshi, and M. Sasaki, *Phys. Rev. D*, in press.

[16] K. Danzmann, A. Rüdiger, R. Schilling, W. Winkler, J. Hough, G. P. Newton, D. Robertson, N. A. Robertson, H. Ward, P. Bender, J. Faller, D. Hils, R. Stebbins, C. D. Edwards, W. Folkner, M. Vincent, A. Bernard, B. Bertotti, A. Brillet, C. N. Man, M. Cruise, P. Gray, M. Sandford, R. W. P. Drever, V. Kose, M. Kühne, B. F. Schutz, R. Weiss, and H. Welling, "LISA: Proposal for a Laser-Interferometer Gravitational Wave Detector in Space," unpublished proposal submitted to the European Space Agency in May 1993; available as document MPQ 177 from the Max-Planck-Institut für Quantenoptik, 8046 Garching bei München, Germany.